



***An Investigation into the Electrogenenerated
Chemiluminescence of Near-Infrared Quantum Dots for
Application in Biomedical Sensing***

Alasdair J. Stewart MSci.

A thesis submitted for the degree of Doctor of Philosophy

**University of Strathclyde
Department of Pure and Applied Chemistry
Centre for Forensic Science**

2014

Supervisor – Dr Lynn Dennany

This thesis is the result of the author's original research. It has been composed by the author and has not been previously submitted for examination which has led to the award of a degree. The copyright of this thesis belongs to the author under the terms of the United Kingdom Copyright Acts as qualified by the University of Strathclyde Regulation 3.50. Due acknowledgement must always be made of the use of any material contained in, or derived from, this thesis.

Signed:

Date:

Acknowledgments

Firstly, I would like to thank my supervisor, Lynn, for her constant encouragement, support and advice over the past three years. Your approachability and easy-going style have been crucial in guiding me towards completion of this PhD.

I would also like to thank all of the staff in the CFS for their help throughout this PhD, particularly Jim, Lynn and Andrew for their help around the lab.

To all the FFBs I have worked with over the past three years, thank you for being so welcoming back in 2011 and for your support and distractions since then!

To my family and friends, thank you for taking my mind away from the lab and bench, to Gordon for your proof reading and guidance, and to Mum & Dad for your support and encouragement over the past 25 years.

And finally, thank you to Rachel for putting up with me during this PhD and for being so dedicated when times were tough. Without your continual support, reassurance and grammatical skills I would not have been able to get to where I am. I will never be able to thank you enough for what you have done for me, but I hope you know how much I appreciate it all.

Abstract

The objective of this work is two-fold; investigation of the electrochemical and electrochemiluminescent (ECL) properties of near-infrared (NIR) quantum dots (QDs) in buffer and whole blood; and their subsequent incorporation into ECL biosensing systems with potential application in whole blood analysis. QDs exhibited size-dependent optical and electrochemical properties with the largest QDs demonstrating ECL emission in the NIR region (811 nm). This should improve light penetration through whole blood, a prediction that has not yet been investigated for the ECL process.

NIR QDs were shown to be flexible ECL emitters and optimisation of system parameters was implemented to obtain maximum ECL performance. This was achieved using a QD-chitosan film on a glassy carbon electrode with potassium persulfate co-reactant in phosphate buffered saline at pH 7.4. Intense reductive and oxidative ECL signals were generated directly in whole blood, which was at least ten times more intense than that achieved using visible region emitting QDs. The response exhibited sensitivity to blood samples spiked with clinically relevant analytes, homocysteine and dopamine, establishing the viability of NIR ECL as a detection method from whole blood.

To expand the integration of NIR QDs into biosensing systems, a selective biosensor for cholesterol was developed that exhibited good stability, specificity and a clinically relevant linear range (1-5 mM). Detection in human serum was possible, however, radical quenching in whole blood limited its use as a biosensor in this environment in its current form, demonstrating the complications that can arise with analysis from such a complex matrix. For that reason, an alternative biosensor design that used conditions optimised in earlier work was used to improve system sensitivity. Fabrication of an immunosensor for IgG resulted in an ECL signal that was detected in whole blood. Following significant development, it is envisaged such a system can form the basis of a new generation of NIR ECL biosensors capable of detection directly from whole blood.

Table of Contents

Chapter 1 - Introduction and review of the literature	1
1.1 <i>Electrogenerated Chemiluminescence (ECL)</i>	2
1.1.1 <i>General principles</i>	2
1.1.2 <i>Heterogeneous electron transfer - Precursor formation</i>	4
1.1.2.1 <i>Annihilation pathway</i>	4
1.1.2.2 <i>Co-reactant Pathway</i>	5
1.1.2 <i>Homogeneous electron transfer – Excited state formation</i>	8
1.1.3 <i>Energetics of homogeneous electron transfer</i>	12
1.1.4 <i>Analytical applications and recent advances</i>	15
1.1.4.1 <i>Traditional applications</i>	15
1.1.4.2 <i>Enhanced ECL – Incorporation of nanomaterials</i>	18
1.2 <i>Electrochemical biosensors</i>	21
1.2.1 <i>Overview</i>	21
1.2.2 <i>Integration of QDs</i>	22
1.2.2.1 <i>QD overview</i>	23
1.2.2.2 <i>QD biosensing systems</i>	24
1.2.2.3 <i>NIR-based systems</i>	29
1.3 <i>Cyclic Voltammetry (CV)</i>	30
1.3.1 <i>General principles</i>	30
1.3.1.1 <i>Theoretical response</i>	31
1.3.1.2 <i>Semi-infinite diffusion control</i>	34
1.4 <i>Differential Pulse Voltammetry (DPV)</i>	36
1.4.1 <i>General principles</i>	36
1.5 <i>Conclusions</i>	38
1.6 <i>References</i>	40
Chapter 2 - Characterisation of 800 nm CdSeTe/ZnS quantum dots	46
2.1 <i>Introduction</i>	47
2.2 <i>Experimental</i>	48
2.2.1 <i>Apparatus</i>	48
2.2.2 <i>Materials</i>	49
2.2.3 <i>Methods</i>	49
2.3 <i>Characterisation</i>	51
2.3.1 <i>Optical characterisation</i>	51
2.3.1.1 <i>UV/Visible spectroscopy</i>	51

2.3.1.2 Emission spectroscopy	57
2.3.1.3 ECL emission spectroscopy.....	61
2.3.2 Electrochemical characterisation.....	65
2.3.2.1 CV.....	65
2.3.2.2 DPV.....	71
2.4 Conclusions	77
2.5 References	79

Chapter 3 - Electrogenerated chemiluminescent behaviour of 800 nm CdSeTe/ZnS

quantum dots.....	81
3.1 Introduction.....	82
3.2 Experimental.....	83
3.2.1 Apparatus	83
3.2.2 Materials.....	83
3.2.3 Methods.....	84
3.3 Estimation of QD HOMO and LUMO energy levels.....	85
3.4 ECL behaviour	88
3.4.1 Anodic ECL characteristics	88
3.4.1.1 Elucidation of anodic ECL mechanisms	89
3.4.2 Cathodic ECL characteristics	98
3.4.2.1 Elucidation of cathodic ECL mechanisms	100
3.5 Conclusions	115
3.6 References	118

Chapter 4 - Optimisation of electrogenerated chemiluminescent performance of 800 nm CdSeTe/ZnS quantum dots

800 nm CdSeTe/ZnS quantum dots	121
4.1 Introduction.....	122
4.2 Experimental.....	123
4.2.1 Apparatus	123
4.2.2 Materials.....	123
4.2.3 Methods.....	124
4.3 Optimisation of ECL performance.....	126
4.3.1 Film composition.....	126
4.3.1.1 Polymer type	126
4.3.1.2 Polymer concentration	130
4.3.1.3 QD concentration	132
4.3.1.4 QD/chitosan film volume	135

4.3.2 Co-reactant	137
4.3.2.1 Co-reactant selection	137
4.3.2.2 Co-reactant concentration	145
4.3.3 Buffer	147
4.3.3.1 Buffer selection	147
4.3.3.2 Buffer pH	149
4.3.4 Electrochemical System	154
4.3.4.1 Electrode material	154
4.3.4.2 Scan rate	158
4.4 Conclusions	159
4.5 References	161

Chapter 5 - Electrogenerated chemiluminescence of 800 nm CdSeTe/ZnS quantum dots in whole blood 164

5.1 Introduction	165
5.2 Experimental	167
5.2.1 Apparatus	167
5.2.2 Materials	167
5.2.3 Methods	168
5.3.1 CV and DPV	170
5.4 NIR QD ECL in whole blood	175
5.4.1 Detection of a cathodic ECL response	175
5.4.1.1 Co-reactant free system	175
5.4.1.2 $K_2S_2O_8$ system	177
5.4.2 Detection of an anodic ECL response	180
5.4.2.1 Co-reactant free system	180
5.4.2.2 TPA system	181
5.4.3 NIR vs visible region ECL - Light penetration through whole blood	182
5.5 Development of whole blood ECL biosensors	186
5.5.1 A cathodic ECL system	187
5.5.1.1 QD concentration	187
5.5.1.2 Response variability	188
5.5.1.3 Homocysteine detection	189
5.5.2 Co-reactant free detection	197
5.5.2.1 QD concentration	197
5.5.2.2 Response variability	198
5.5.2.3 Dopamine detection	199

5.6 Conclusion.....	205
5.7 References	206
Chapter 6 – Development of a cholesterol biosensor based on electrogenerated chemiluminescence of 800 nm CdSeTe/ZnS quantum dot.....	208
6.1 Introduction.....	209
6.2 Experimental.....	211
6.2.1 Apparatus	211
6.2.2 Materials.....	211
6.2.3 Methods.....	212
6.3 Cholesterol detection using NIR QD ECL	215
6.3.1 Viability of the biosensor	215
6.3.2 Mechanism and kinetics of H ₂ O ₂ production	217
6.3.3 Optimisation of experimental conditions.....	220
6.3.4 Dependence of NIR QD ECL on cholesterol concentration	223
6.3.6 Biosensor stability.....	227
6.3.7 Effect of interferences on response.....	229
6.3.8 Detection from human serum samples.....	230
6.3.9 Summary.....	231
6.4 Towards whole blood analysis.....	232
6.4.1 Viability of the system.....	232
6.4.2 Enzyme immobilisation	234
6.4.2.1 Immobilisation via adsorption	234
6.4.2.2 Immobilisation via glutaraldehyde cross-linking.....	236
6.4.2.3 Enzyme immobilised biosensor – whole blood analysis	241
6.4.3 Future developments	243
6.5 Conclusions	243
6.6 References	245
Chapter 7 – Designing an immunoassay for whole blood analysis	248
7.1 Introduction	249
7.2 Experimental.....	251
7.2.1 Apparatus	251
7.2.2 Materials.....	251
7.2.3 Methods.....	252
7.3 Immunoassay development.....	257
7.3.1 Viability of response.....	257

7.3.2 Selection of immunoassay design	258
7.3.2.1 'Switch off' design – The steric hindrance model	260
7.3.2.2 'Switch off' design – An alternative approach to the steric hindrance model	263
7.3.2.3 'Switch on' design – A sandwich type immunoassay	270
7.4 Future developments	281
7.5 Conclusions	284
7.6 References	286
Chapter 8 – Conclusions and future work	288
8.1 Conclusions and future work	289
Appendix	295
Appendix 1	296

Chapter 1 - Introduction and review of the literature

1.1 Electrogenerated Chemiluminescence (ECL)

1.1.1 General principles

ECL is a form of chemiluminescence in which the light emitting chemiluminescent reaction is preceded by an electrochemical reaction.¹ Excited states are produced through rapid ($\sim 10^{10} \text{ M}^{-1} \text{ s}^{-1}$), energetic (2-4 electron volts (eV))² homogeneous electron transfer between electrogenerated precursor species (Figure 1.1), which emit light at a wavelength characteristic of the band gap energy of the emitting species.

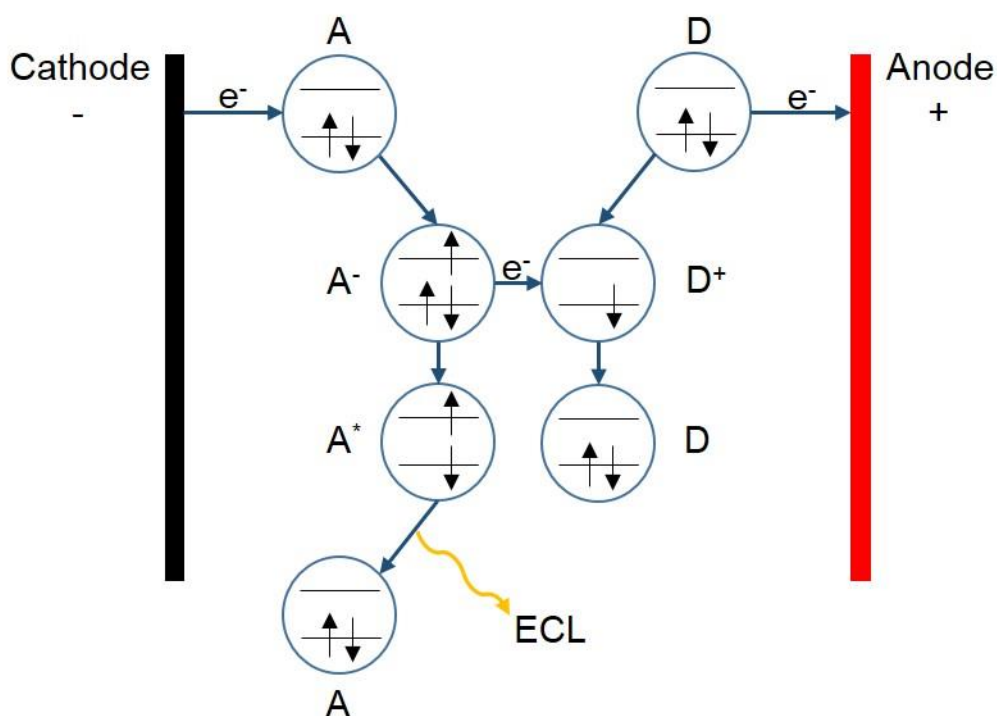


Figure 1.1 - Outline of the ECL process. Adapted from Miao *et al.*³

ECL first appeared in the literature in 1964,⁴ laying the groundwork for expansion into a variety of well-documented and reviewed analytical applications as both a stand-alone and combined technique.^{3, 5-10} The basis of such applications is reliant upon the inherent advantages of the ECL process over more conventional chemiluminescence techniques. ECL is operated

through application of a suitable potential at the electrode surface allowing unprecedented control over the position and timing of ECL reactions.¹¹ Delayed emission, maximisation of signal to noise ratio and multi-analyte detection are all possible as a result.¹¹ As is improved selectivity as a specific ECL reaction can be controlled by altering the electrode potential.¹¹ No external light source is required permitting simple instrumentation, minimising background signals¹² and avoiding problems linked to scattered light and interferences from emission by impurities.¹³ This contributes to the superb sensitivity associated with ECL, which is further improved through regeneration of electroactive species that allows a single species to take part in several ECL reactions.¹¹ Combining these assets with the fact that highly unstable species and reactants can be electrogenerated *in situ*, allowing their analysis when other techniques would not, results in a system that is capable of ultra-sensitive detection of a vast array of analytes with wide dynamic ranges.¹⁴⁻¹⁹ These benefits have enabled the use of ECL across a multitude of disciplines, including food and water testing, clinical diagnostics and bio-warfare agent detection.²⁰⁻²²

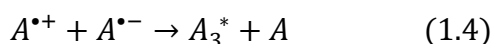
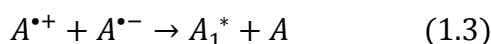
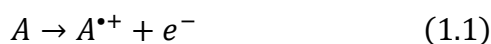
Three fundamental factors are required for production of an efficient ECL signal, specifically, the generation of stable precursor species within the system, sufficient energetics of the homogeneous electron transfer reactions to create an excited state and good photoluminescent efficiency of this excited species.¹¹ Both organic²³ and inorganic^{24, 25} ECL systems exist, which differ in their respective precursor species. Organic precursors tend to exist as radical ions, whilst inorganic precursors are usually the reduced and/or oxidised forms of the parent complex. The key element dictating the efficiency of ECL production is the kinetics of the electron transfer reactions leading to precursor and excited state formation.^{11, 26} The energetics of these processes are also important to consider when investigating the ECL behaviour of a system.

1.1.2 Heterogeneous electron transfer - Precursor formation

Heterogeneous transfer of electrons from the electrode to the electroactive species is essential for the generation of ECL precursors that are formed following this initial oxidation or reduction process. In most cases, the electro-generation of these species follows an annihilation or co-reactant pathway.¹

1.1.2.1 Annihilation pathway

This mechanism (equations (1.1) – (1.6)) involves sequential generation of the oxidised and reduced forms of a parent molecule through rapid switching of the potential between values where these processes can occur. Initially, the electrode potential is pulsed at a voltage capable of producing radical cations within the system (equation (1.1)), which remain within the diffusion layer surrounding the electrode. The potential is then rapidly switched to a voltage capable of producing the corresponding radical anion (equation (1.2)), which diffuses away from the electrode following Fick's first law, as its concentration at the electrode surface increases. At this secondary potential, radical cations (produced during the initial voltage pulse) within the immediate vicinity of the electrode are reduced and their concentration at the electrode surface diminishes. A concentration gradient is formed, resulting in back diffusion of the same species from within the diffusion layer towards the electrode surface. These then interact with electrogenerated radical anions (produced during the second voltage pulse) that are diffusing in the opposite direction.³



The excited singlet state is formed directly by the interaction of two electrogenerated species (equation (1.3)) or through triplet-triplet annihilation following the formation of two excited triplet states (equations (1.4) and (1.5)); this is discussed further in the following section. Radiative relaxation of the excited state is accompanied by light emission (equation (1.6)) at a wavelength characteristic of the emitting species.

An alternative method for precursor formation involves the use of rotating ring-disk electrodes, with one species formed at the ring and the other at the disk. These species are then swept together by diffusion and convection, allowing them to interact.³

The major advantage of the annihilation pathway is that only the ECL species, solvent and electrolyte are required to generate light so the system is simple and cost-effective. However, this system also has some limitations; for emission in the visible region (~400-700 nm), the excited singlet energy lies between 1.8 and 3.1 eV (from the Planck Relation) and for annihilation ECL to occur, the potential window of the system must be sufficiently wide (up to ~3.3 V) to allow generation of both radical anions and cations.³ Organic solvents are required (hazardous and expensive) as the potential window of aqueous media is often insufficient (the edge of most aqueous systems potential window is ~1.5 V)³ to satisfy this criteria. Moreover, quenching of excited states by dissolved O₂ can significantly affect annihilation ECL and as such must be removed from the system prior to analysis.²⁷

1.1.2.2 Co-reactant Pathway

This mechanism involves the addition of a reagent, often referred to as the co-reactant, to the system. The co-reactant must satisfy a selection of criteria in order to be suitable. It must be both soluble and stable (ideally within aqueous media), be easily oxidised and reduced, and be able to form strongly oxidising or reducing intermediates. The kinetics of these processes should be rapid and

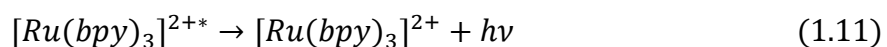
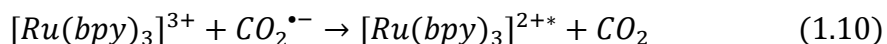
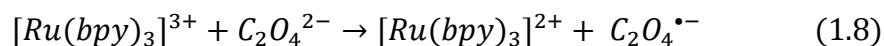
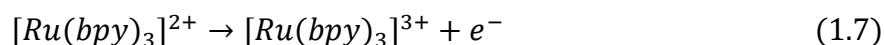
none of the species involved should themselves generate ECL or quench the ECL signal of the luminophore.¹¹

A potential is applied at an electrode to oxidise or reduce (depending on the polarity of the potential) both the luminophore and the co-reactant using a one-directional voltage scan. The electrogenerated co-reactant radical rapidly decomposes to a powerful reducing or oxidising intermediate,³ which has a standard redox potential that permits rapid electron or hole injection into the electrogenerated luminophore species with sufficient energy to generate an excited state. Following light emission, the luminophore can often be regenerated, whilst the co-reactant is normally consumed during the electrochemical reactions.¹¹ The co-reactant pathway has four main stages that are outlined in Table 1.1.

Table 1.1 - The co-reactant mechanism. Adapted from Miao *et al.*³

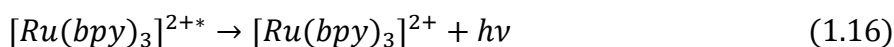
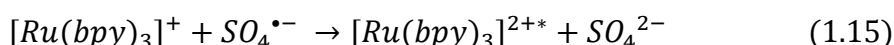
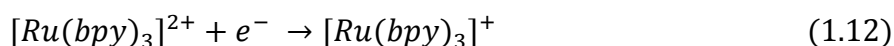
Reaction process	Oxidative ECL	Reductive ECL
Heterogeneous electron transfer	$A \rightarrow A^{\bullet+} + e^-$ $C \rightarrow C^{\bullet+} + e^-$	$A + e^- \rightarrow A^{\bullet-}$ $C + e^- \rightarrow C^{\bullet-}$
Homogeneous electron transfer	$A^{\bullet+} + C \rightarrow A + C^{\bullet+}$ $C^{\bullet+} \rightarrow C_{red}^{\bullet}$ $A + C_{red}^{\bullet} \rightarrow A^{\bullet-} + P$	$A^{\bullet-} + C \rightarrow A + C^{\bullet-}$ $C^{\bullet-} \rightarrow C_{ox}^{\bullet}$ $A + C_{ox}^{\bullet} \rightarrow A^{\bullet+} + P$
Excited state formation	$A^{\bullet+} + A^{\bullet-} \rightarrow A^* + A$ $A^{\bullet+} + C_{red}^{\bullet} \rightarrow A^* + P$	$A^{\bullet-} + A^{\bullet+} \rightarrow A^* + A$ $A^{\bullet-} + C_{ox}^{\bullet} \rightarrow A^* + P$
Light emission	$A^* \rightarrow A + h\nu$	$A^* \rightarrow A + h\nu$
A=luminophore, C=co-reactant, C_{red}^{\bullet} =reducing co-reactant intermediate, C_{ox}^{\bullet} =oxidising co-reactant intermediate, P=product of co-reactant reactions.		

The oxidative route involves initial oxidation of the luminophore and co-reactant to create radical cations, with excited state formation following homogeneous electron transfer reactions, as outlined in Table 1.1. A common example of this mechanism is the ruthenium/oxalate system, illustrated in equations (1.7) – (1.11).¹⁴



This shows the oxidation of tris(2,2'-bipyridine)ruthenium(II) ($[Ru(bpy)_3]^{2+}$) (equation (1.7)) followed by oxidation of oxalate in the presence of $[Ru(bpy)_3]^{3+}$ (equation (1.8)) to create $C_2O_4^{\bullet-}$. This rapidly decomposes to CO_2 and $CO_2^{\bullet-}$ (equation (1.9)), which is a strong reducing agent key in the production of an ECL signal. $CO_2^{\bullet-}$ injects an electron into $[Ru(bpy)_3]^{3+}$ to form CO_2 and the excited state luminophore (equation (1.10)) that returns to the ground state with emission of light (equation (1.11)).

The reductive ECL process involves reduction of the luminophore and co-reactant, which can then generate the excited state following interaction of the oxidising co-reactant intermediate with the reduced luminophore (Table 1.1). An example of this is the ruthenium/persulfate system, shown in equations (1.12) – (1.16).²⁸



Reduction of both $[Ru(bpy)_3]^{2+}$ and $S_2O_8^{2-}$ (equations (1.12) and (1.13)) occurs directly at the electrode surface with strong oxidising agent $SO_4^{\bullet-}$ formed from decomposition of $S_2O_8^{\bullet 3-}$ (equation (1.14)). This is capable of removing an electron from $[Ru(bpy)_3]^{2+}$ to generate the excited state (equation (1.15)) that can emit light (equation (1.16)).

One of the major benefits of this co-reactant pathway is that it allows ECL generation in aqueous solution as the luminophore and co-reactant can be reduced or oxidised during the same potential step. Therefore, a solvent with a wide potential window (i.e. an organic solvent) is not required. This is ideal for biomedical applications where an aqueous solution and maintenance of physiological pH help maximise biocompatibility.^{29, 30} Co-reactants also allow generation of ECL from a system in which the radical cation or anion of the luminophore is so unstable that it would break down before an excited state could be formed through ion annihilation.³

It must be noted that ECL intensity can be affected by dissolved O₂, which can interact with excited states causing non-radiative relaxation to the ground state, quenching the ECL signal.²⁷

1.1.2 Homogeneous electron transfer – Excited state formation

The interaction and subsequent electron transfer between electrogenerated precursor species are pivotal reactions in the ECL process. Formation of an excited state that can relax radiatively to the ground state is essential for observation of an ECL response. However, a competition exists between this route and one in which ground state species are formed directly from these electron transfer reactions. These alternative routes are shown in Figure 1.2.

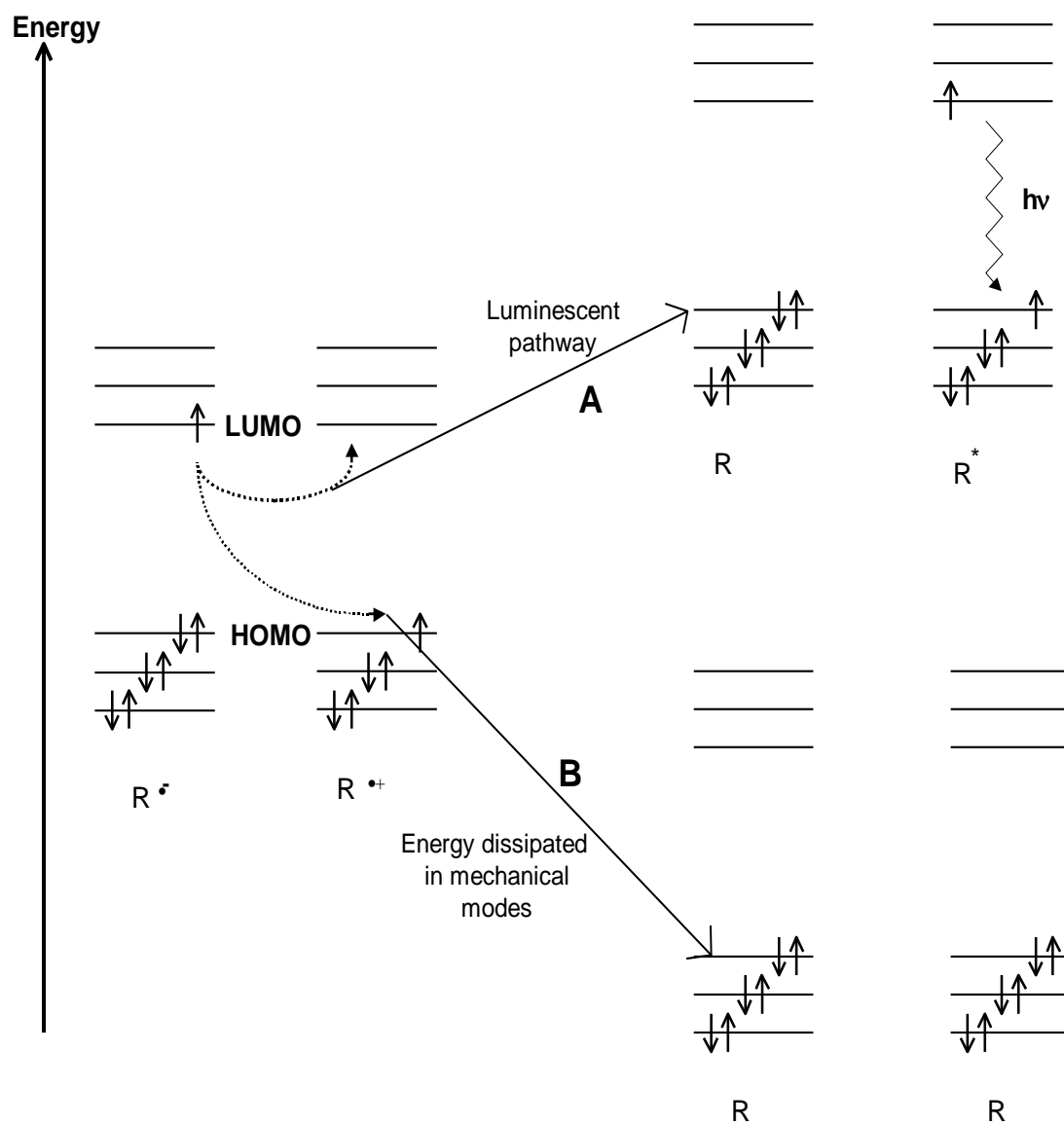


Figure 1.2 - The competing routes of homogeneous electron transfer reactions in the ECL process.

Route A involves transfer of an electron from the Lowest Unoccupied Molecular Orbital (LUMO) of the reduced precursor to the LUMO of the oxidised precursor. This results in formation of one ground state molecule and one excited state molecule, which can then relax via the emission of a photon to the ground state. Route B involves electron transfer from the LUMO of the reduced precursor to the Highest Occupied Molecular Orbital (HOMO) of the oxidised precursor to produce two molecules in the ground state. The latter pathway is clearly favoured thermodynamically as it results in two ground state molecules; however, if electron transfer is rapid enough, a large amount of energy has to be dissipated in vibrational modes over a very short period of time, which is unfavourable. In this situation, a kinetic manifestation of the Frank-Condon principle appears. The Frank-Condon principle states that the relative positions and momenta of atoms involved in a specific transition are preserved because the movement of an electron is exponentially faster than that of a nucleus.³¹ Thus, the most probable transition will obey this principle and will be that with the fastest electron transfer. Relating this to the ECL process, route B results in the formation of two ground state molecules and is therefore thermodynamically favourable as a large amount of energy is released from the system. However, this energy must be dissipated vibrationally, which is not a favourable process due to disruption of the system. Route A results in the formation of one excited state molecule and one ground state molecule, which is a less exergonic process overall and so less thermodynamically favoured. However, this means less energy must be dissipated through vibrational modes, so the process becomes more kinetically favourable and electron transfer occurs more rapidly.

This process can be related to the Marcus theory for electron transfer, which correlates the rate of electron transfer to both electronic and nuclear (Frank-Condon principle, discussed above) considerations through equation (1.17).³²

$$K_{ET} = \nu \exp\left(-\frac{\Delta G^\ddagger}{RT}\right) \quad (1.17)$$

Where K_{ET} is the rate of electron transfer, ν is the frequency factor, ΔG^\ddagger is the Marcus free energy of activation, R is the gas constant and T is the absolute temperature.

ΔG^\ddagger can then be related to the standard free energy of the reaction, ΔG^0 , through equation (1.18).³²

$$\Delta G^\ddagger = \frac{(\Delta G^0 + \lambda)^2}{4\lambda} \quad (1.18)$$

Where λ is the total reorganisation energy (the energy required to distort the system to attain the equilibrium configuration of the product state), which comprises an outer sphere component (reorganisation of solvent and surrounding media) and an inner sphere component (reorganisation of the molecular geometry of the reactant as it reaches the product state).

This equation predicts a parabolic relationship between ΔG^\ddagger and ΔG^0 that can be used to explain the rate of electron transfer in relation to the standard free energy of the reaction. It predicts that as ΔG^0 increases so does the rate of electron transfer. K_{ET} reaches a maximum when $\lambda = \Delta G^0$ and $\Delta G^\ddagger = 0$, with any further increases in ΔG^0 resulting in a decrease in the electron transfer rate in what is known as the Marcus inverted region.³² This can be related to the competing processes in Figure 1.2, where the highly exergonic nature of route B means that it lies in this inverted region and thus the rate of electron transfer is slower than for route A, which is less exergonic. Therefore, route A will experience a more instantaneous type electronic transition (due to faster electron transfer) and, from the Frank-Condon principle, will be the most probable transition.²

1.1.3 Energetics of homogeneous electron transfer

An excited state can be formed via the singlet or triplet route, which is dictated by the energetics of homogeneous electron transfer reactions and the energies of the excited state. The energy of the electron transfer reaction can be determined from the redox potentials for the oxidation and reduction of the species involved (equation (1.19)).¹¹

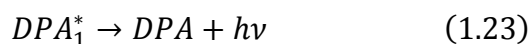
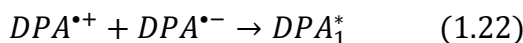
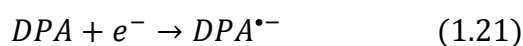
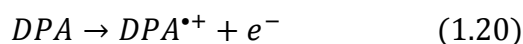
$$-\Delta H^0 = E_p(D^{\bullet+}/D) - E_p(A/A^{\bullet-}) - T\Delta S^0 \quad (1.19)$$

Where $-\Delta H^0$ is the enthalpy for the electron transfer reaction in eV, $E_p(D^{\bullet+}/D)$ is the peak potential for reduction of precursor D and $E_p(A/A^{\bullet-})$ is the peak potential for reduction of precursor A, in eV. $T\Delta S^0$ is an entropy term that is usually estimated at 0.1 eV (at 25°C)^{33, 34} and is combined with the peak separation of a reversible redox couple (0.057 eV for a 1-electron transfer process) to give a final estimated value of 0.16 eV.³⁵

Typically, there are four pathways via which ECL can occur;³

i) The S-route

The reaction is said to be energy sufficient when $-\Delta H^0$ is greater than the energy required to promote an electron into the lowest excited singlet state. Therefore, excited singlet states can be produced directly from electron transfer between ECL precursors; this mechanism of excited state formation is said to follow the S route. An example of this route is the 9, 10-diphenylanthracene (DPA) system shown in equations (1.20) – (1.23).³⁶



ii) The T-route

If there is insufficient energy in the system to generate excited singlet states, an alternative mechanism is responsible for creating the ECL signal. Provided the free energy of the system is greater than that required for production of the excited triplet state, an ECL signal can be generated via the T route; the triplet-triplet annihilation of triplet species formed during the electron transfer reaction to produce an emissive singlet state. ECL emission directly from a triplet state is expected to be very low due to quenching of these long lived states by O₂ and other species in solution.³⁷ An example of this is the N, N, N', N'-tetramethyl-*p*-phenylenediamine (TMPD)/DPA system (equations (1.24) – (1.27)).³⁶



Figure 1.3 outlines the energetics of the DPA and TMPD/DPA systems. It shows that equation (1.22) is capable of populating the excited singlet state directly, whereas equation (1.25) only has sufficient energy to generate an excited triplet state. In general, the energy gap between the triplet state and the ground state is greater than the energy gap between the triplet and singlet states. As such, the interaction between two of these triplet species should provide sufficient electronic energy to create one excited singlet species, provided the second species relaxes to the ground.³⁸

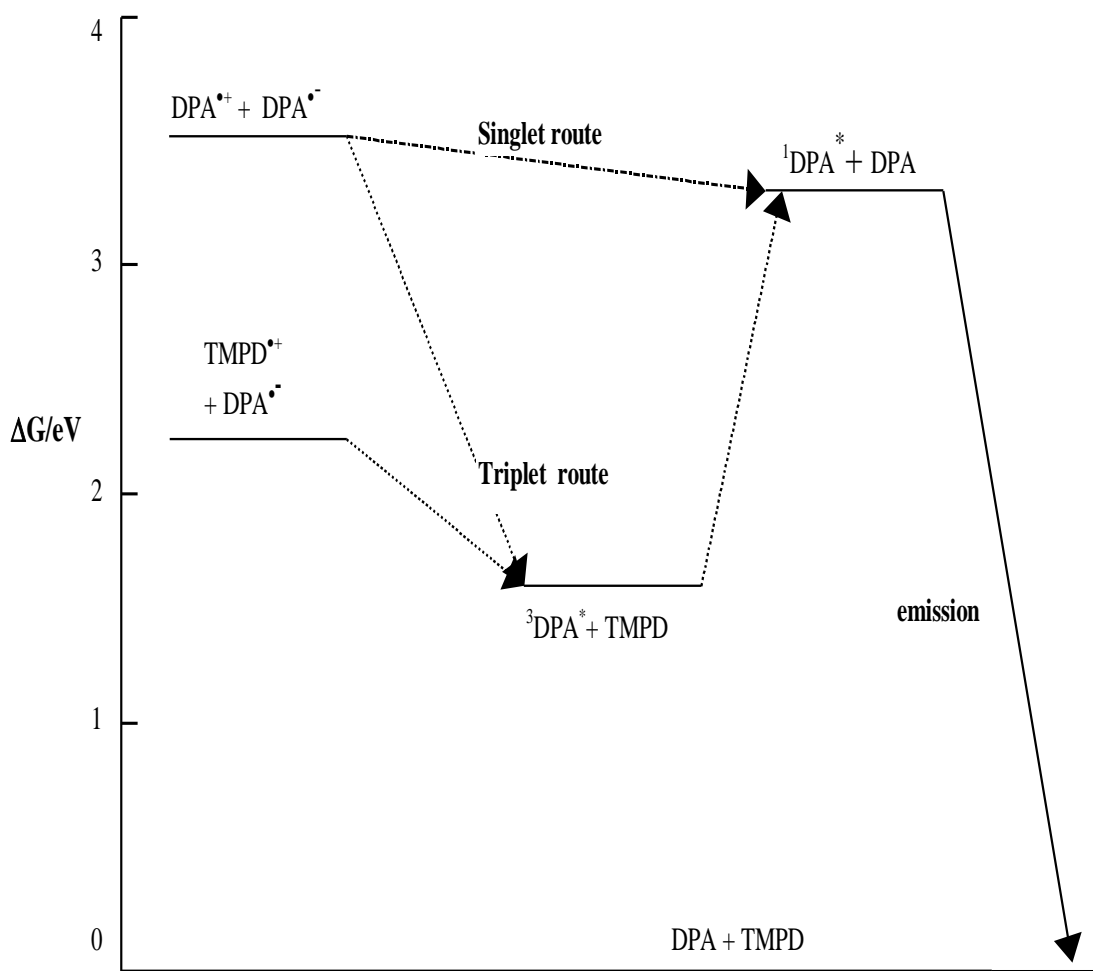
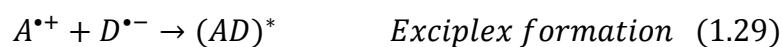
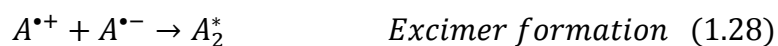


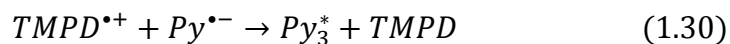
Figure 1.3 - The free energies involved in the DPA and DPA/TMPD ECL systems.

iii) and iv) The ST and E-routes

An alternative mechanism for excited state generation combines both the S and T-routes (the ST-route). When the energy available in the system is close to that of the excited singlet state, both the S and T routes contribute to the formation of the excited singlet species. An example of this is the Rubrene anion-cation annihilation.³⁹ Ion annihilation reactions can also result in the formation of excited dimers (excimers) and excited complexes (exciplexes), as shown in equations (1.28) and (1.29).³



These excimers and exciplexes can then emit light directly; this is known as the E route. E route emission is broad, featureless and lower in energy than the corresponding singlet emission.³ This type of emission occurs in the Pyrene/TMPD system (equations (1.30) – (1.32)).⁴⁰



OR



Where Py_1^* and Py_3^* represent the excited singlet and triplet states of pyrene respectively, and Py_2^* represents the excimer. The ECL emission profile contains a double peak, one at ~400 nm corresponding to the singlet, and one at ~480 nm corresponding to the excimer.


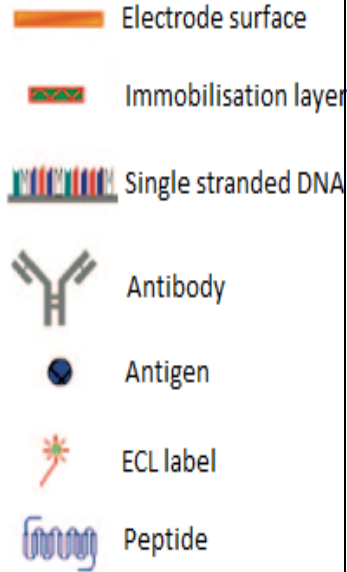
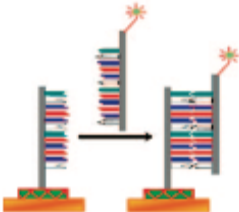

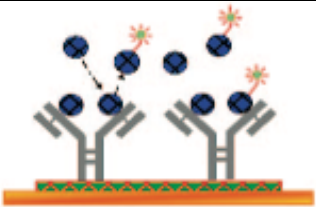
1.1.4 Analytical applications and recent advances

1.1.4.1 Traditional applications

ECL has a range of analytical,⁴¹⁻⁴³ clinical⁴⁴⁻⁴⁶ and biological⁴⁷⁻⁴⁹ applications following extensive research over the past 30-40 years. A combination of the high sensitivity, selectivity and flexibility of the ECL technique and the commercial availability of reagents and instrumentation has resulted in the development of numerous assay formats for a variety of functions. The majority of these applications involve detection of clinically relevant analytes either in combination with a separation technique (HPLC,⁴² capillary electrophoresis⁴³) or more commonly as a stand-alone technique. This is achieved by linking the target analyte to an ECL active label. $[Ru(bpy)_3]^{2+}$ and its derivatives are the most widely used ECL labels⁵⁰ owing to their ease of functionalisation with biomolecules, efficient ECL production in aqueous solution and stability of their reduced and oxidised species. As a result they can be used in conjunction with a number of co-reactant systems, such as

tripropylamine (TPA), oxalate ($C_2O_4^{2-}$) and hydrogen peroxide (H_2O_2).⁵¹⁻⁵³ Selectivity can be inferred by using a label that binds specifically to the target analyte, such as a labelled antibody (Ab). ECL from these labels can then be induced through application of a potential and the response monitored. In most cases, the intensity of generated luminescence is proportional to the concentration of the ECL label on or very close to the working electrode surface.⁵⁰ The most commonly developed and utilised ECL assay formats are based on immunoassays, which are biochemical tests used to determine the presence and concentration of a particular molecular structure.⁵⁴ They often rely on the specific interaction between an Ab and antigen that, in the case of immunoassays utilising ECL detection, permits the electrochemical ECL reactions to occur by bringing the ECL label into contact with the working electrode.³ Common immunoassay formats are outlined in Table 1.2.

Table 1.2 - Commonly used ECL immunoassay formats. Adapted from Miao *et al.*³

Assay format	Schematic	System	Example	Key
Sandwich-type		-One Ab immobilised on solid substrate (electrode), other labelled with ECL active species. -Response detected following antigen and labelled Ab binding.	Cardiac troponin I, ⁵⁵ prostate specific antigen, ⁵⁶ anthrax. ⁵⁷	
DNA hybridisation		-Capture strand immobilised on solid substrate (electrode), target strand labelled with ECL active species. -Response detected following DNA hybridisation with labelled target strand.	Variety of DNA sequences. ^{48, 58, 59}	
Direct		-Ab immobilised on solid substrate (electrode). -Response detected following binding of antigen labelled with ECL active species.	G-protein coupled receptor binding. ²⁶	
Competitive		-As above, except competition exists between labelled and un-labelled target antigen. -Response dependent upon degree of labelled antigen binding.	Intracellular cGMP and cAMP. ³	

These various formats provide a range of platforms from which ECL detection based systems can be developed. Sandwich-type immunoassays are by far the most commonly reported in the literature as they do not require modification of the sample with an ECL label. The alternative assay formats all require a degree of sample pre-treatment that could result in contamination or loss of binding affinity between complementary species. These factors can affect assay performance, therefore, these assays are used to a lesser extent than sandwich-type systems.

1.1.4.2 Enhanced ECL – Incorporation of nanomaterials

ECL immunoassay detection limits have reached ultrasensitive levels (fM-aM)^{60, 61}, mainly due to signal enhancement through incorporation of nanomaterials that exhibit excellent electrical and optical properties.^{9, 62} Although $[\text{Ru}(\text{bpy})_3]^{2+}$ is traditionally the most commonly used label in ECL detection, recent enhancements in ECL have been observed through integration of nanomaterials as both immobilisation matrices and ECL emitters.

Carbon nanotubes (CNTs), graphene and gold nanoparticles (Au NPs) are ideal candidates as immobilisation matrices due to their large surface-to-volume ratio and ease of surface functionalisation, permitting high antibody loading.⁶³ These materials have shown great promise in their ability to increase electron transfer kinetics and improve ECL detection limits. Wang *et al.* improved film conductivity and the resulting ECL intensity by coating the electrode surface with a Au NP-graphene composite; this was attributed to the excellent electron transfer properties of this nanocomposite film.⁶⁴ Li *et al.* used graphene modified CdSe quantum dots (QDs) to enhance the rate of electron transfer within their system, allowing development of a highly sensitive biosensor for human immunoglobulin G (HIgG) with a detection limit of 5 fg/mL.⁶⁵ A comparative system using $[\text{Ru}(\text{bpy})_3]^{2+}$ ECL had an LOD of 0.035 ng/mL⁶⁶ and thus nanomaterial induced enhancement allowed an increase in sensitivity of 7000 times.

CNTs have excellent electrical conductivity properties as they are comprised solely of sp_2 -hybridised carbon and can exist in either a single-wall (SWCNTs) or multi-wall (MWCNTs) configuration. SWCNTs are nanocylinders created from rolled up sheets of graphene, whereas MWCNTs consist of assemblies of these cylinders inside one another.⁷ The unique electrical properties of these materials have been exploited to increase ECL intensities. A biosensor combining Au NPs and CNTs was developed by Li *et al.* for the detection of thrombin.⁶⁷ The superb electronic conductivity properties of this system allowed detection down to 3 fM. This LOD was 66 times lower than that achieved using an aptasensor for thrombin with a ruthenium label.⁶⁸ Cao *et al.* exploited the functionality of carboxylated MWCNTs for attachment of Au NPs, secondary α -1-fetoprotein (AFP) Ab and glucose oxidase (GOD).⁶⁹ Formation of an immunocomplex between this label, AFP antigen and the primary-Ab modified electrode catalysed the enzymatic production of H_2O_2 in the presence of glucose, resulting in enhancement in luminol ECL. The Au NP modified MWCNTs permitted high secondary Ab and GOD loading with excellent biocompatibility. This resulted in efficient catalysis of glucose and so the biosensor had a detection limit for AFP of 0.03 pg/mL.⁶⁹ An immunosensor using $[Ru(bpy)_3]^{2+}$ -labelled anti-AFP without the incorporation of nanomaterials exhibited a detection limit of 0.4 ng/mL,⁷⁰ over 13000 times more concentrated than that achieved above.

A similar approach was used by Cheng *et al.* for the detection of carcinoembryonic antigen (CEA), using graphene rather than CNTs as the immobilisation matrix.⁷¹ Enhancement in luminol ECL was again achieved through efficient loading and excellent stability of the graphene-ZnO NPs-GOD-secondary Ab composite, which was brought into contact with the Au NPs-primary-Ab modified electrode through the immunoreaction with CEA antigen. This NP-graphene amplified strategy allowed detection to 3.3 pg/mL and a wide linear range from 10 pg/mL to 80 ng/mL.⁷¹ An LOD of 0.2 ng/mL was demonstrated using a nanomaterial free ECL biosensor with a

[Ru(bpy)₃]²⁺-label.⁷⁰ An enhancement in sensitivity of over 60 times was thus achieved through incorporation of nanocomposites.

The electrical and physical properties of these nanomaterials can also be used to enhance ECL through attachment of multiple ECL labels onto a single nanostructure.^{62, 72, 73} Shen *et al.*⁷⁴ developed a nanocomposite based biosensor for the detection of cardiac troponin I (cTnI), a cardiac marker released as a result of cardiac muscle damage.⁷⁵ Au NPs were coated with streptavidin and then linked to a Au electrode. Primary Ab were then attached to the Au NPs and secondary Ab to N-(aminobutyl)-N-(ethylisoluminol) (ABEI) functionalised Au NPs. The formation of an immunocomplex in the presence of cTnI resulted in an increase in ECL intensity. In this case, the NP itself is not the ECL emitter, rather it acts as a carrier of the ECL probe, ABEI. The Au NPs provide an opportunity for signal enhancement in three ways. Firstly, the high surface-to-volume ratio of the NP allows higher loading of secondary Ab, therefore increasing the probability of immunocomplex formation. Secondly, they permit higher loading of the ECL emitting species, ABEI. Thirdly, the Au NPs may catalyse the reaction of ABEI radicals with the co-reactant, H₂O₂. This catalysis has already been reported for the luminol-H₂O₂ chemiluminescence system.⁷⁶ A working linear range between 2.5 and 10,000 pg/mL and an LOD of 2 pg/mL was reported. A peptide-based method for the detection of cTnI was developed by Wang *et al.* that used a ruthenium bipyridine complex as ECL label.⁷⁷ This system did not incorporate nanomaterials into its design and exhibited an LOD (0.16 µg/mL) that was 60000 times less sensitive than that achieved using nanocomposite enhanced emission.

ECL enhancement of simple nanomaterial systems has also been demonstrated through integration within more sophisticated nanocomposite designs. A seven-fold enhancement in ECL intensity was reported by Guo *et al.* following creation of a QD-graphene-agarose composite when compared to a film of pure QDs.⁷⁸ This was thought to be related to improved conductivity

of the composite film. Au NPs have also been used to improve the ECL response from QDs due to their efficient charge transport properties. Surface passivation of QDs with Au NPs has been used to enhance the ECL response from CdSe/CdS QDs by 17 times because of amplified electron transfer kinetics of this nanocomposite.⁷⁹ Another Au NP modified CdSe/ZnS QD film exhibited a 13 times enhancement in ECL intensity compared to a film of bare QDs, which was the result of improved electron transfer rates.⁸⁰ These examples illustrate the benefits of creating nanocomposite materials that exhibit enhanced electron transfer rates and subsequent improvements in ECL performance.

1.2 Electrochemical biosensors

1.2.1 Overview

Electrochemical biosensors combine the inherent sensitivity of electro-analytical detection methods with the superb biological selectivity associated with biological components.⁸¹ These biological components contain a specific recognition element that can selectively recognise and interact with their target analyte, leading to a physical, chemical or biological change.⁸² These recognition elements include enzymes, proteins, Ab, tissues and receptors. The selective nature of these interactions helps to minimise interferences from the sample matrix, improving both the accuracy and precision of the biosensors.⁸¹ The change resulting from an interaction between a biological component and a target analyte is monitored by a transducer, which converts the response into a measurable signal that is collected and amplified by a signal processor.

Biosensors are divided into two main categories, biocatalytic devices and affinity devices, depending on the nature of the biological recognition process occurring within the device.⁸³ Biocatalytic devices incorporate a biorecognition element that interacts with its target analyte to produce an electroactive species. For example, enzyme electrodes used for the detection of glucose.⁸⁴

Affinity devices are based on the selective binding interactions between a biological component and its target analyte. For example, the Ab-antigen interactions exploited in numerous immunoassays.

Electrochemical biosensors routinely use amperometric and potentiometric transducers that allow development of sensitive, simple devices for analyte detection.⁸⁵ In recent years, ECL has been used extensively as a detection method in biosensing as it possesses advantages over other detection techniques. The excellent sensitivity and specificity of the ECL reaction produces a technique that is very well suited for detecting low concentration target analytes in complex matrices with a good signal to noise ratio.⁶² Combining the selectivity of a biological recognition element with the enhanced sensitivity of ECL provides an excellent platform from which novel biosensors can be designed.

1.2.2 Integration of QDs

The miniaturisation of biosensors has been of particular interest in recent years as it allows the construction of biosensor arrays that can be used for the simultaneous detection of multiple analytes with pico- and femto-molar detection using minimal (μL or mL) sample volumes. Currently, there is extensive research into the incorporation of nanomaterials into these ECL biosensors to improve their detection limits, stability and overall performance.⁸⁶⁻⁹⁰ QDs are ideal in this capacity as they possess a large surface-to-volume ratio that is well-suited to high biomolecule loading, and rapid electron transfer kinetics, which allows generation of intense ECL and the use of smaller overpotentials. This minimises background signals from electro-active interferences.⁹¹ The presence of reactive functional groups on their surface provides immobilisation sites for biomolecules.⁹²

1.2.2.1 QD overview

As ECL emitters, semiconductor QDs have exhibited excellent optical properties for the production of intense ECL signals.⁹³ QDs are typically classified on the periodic table group of their principal elements, most commonly groups 12 and 16. They consist of a small cluster of semiconductor atoms (e.g. CdTe, CdS) and are typically less than 10 nm in size. When the radius of the QD is comparable or smaller than the materials exciton Bohr radius (the natural separation distance between the electron and hole, which is material dependent) their excitons experience quantum confinement in all 3 dimensions.⁹⁴ The continuous energy bands in a bulk semiconductor split into discrete energy levels, much like atomic orbitals, with QDs existing in a form somewhere between the molecular and bulk material (Figure 1.4). This change in electronic structure results in an increase in the band gap energy (E_g) compared to the bulk material, caused by localisation of excitons as a consequence of their quantum confinement, and a unique dependence of E_g on QD size.⁹⁴ A decrease in E_g is observed as the QDs become larger and exciton confinement becomes less severe.

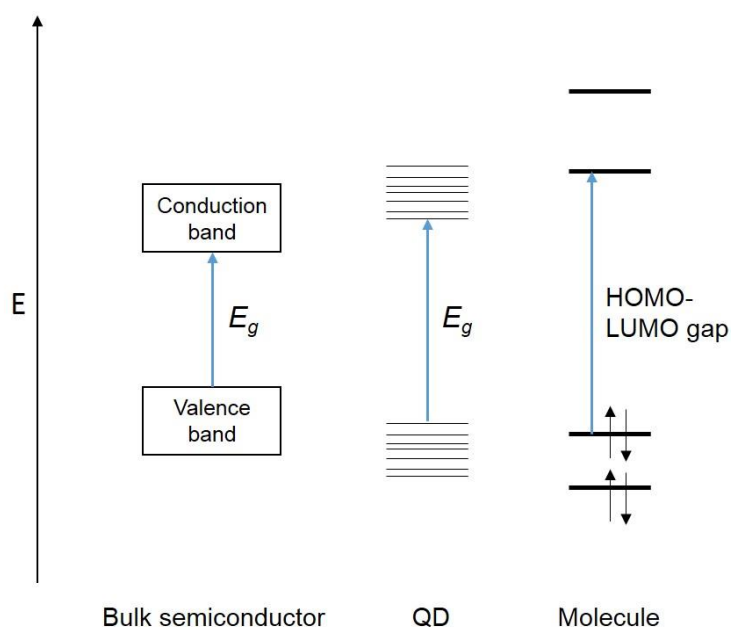


Figure 1.4 - The electronic structure of a bulk semiconductor, a semiconductor QD and a typical molecule.

The benefits of QD ECL lies in their unique optical and electronic properties, specifically high quantum efficiencies, resistance to photo-bleaching and size-tunable emission.⁹⁵

Originally, the ECL of silicon QDs in acetonitrile was investigated, with both annihilation and co-reactant systems (oxalate and persulfate) generating ECL.⁹⁶ Now, a number of elemental and compound semiconductor QDs have been shown to produce ECL through co-reactant and annihilation pathways (Ge, CdS, CdTe).⁹⁷⁻⁹⁹ More recently, ECL from QD films has been reported, which generates stronger ECL signals than solution phase QDs that exhibit low solubility and instability of their reduced and oxidised forms.^{100, 101} QD ECL has been used to detect a number of analytes including catechol derivatives,⁹⁹ thiols,¹⁰² HlgG,¹⁰³ and the human immunodeficiency virus-1 gene.¹⁰⁴

Initially, the ECL of QDs was most sensitive to their surface chemistry and the presence of surface states, rather than their size.¹⁰⁵ However, application of a shell of larger E_g material around the QD core results in effective passivation of these surface states, improving photoluminescent efficiency and ensuring the majority of ECL emission originates from the QD core.¹⁰⁶

1.2.2.2 QD biosensing systems

QDs are used extensively in ECL biosensor development^{21, 87, 107, 108} as they can emit intense ECL signals at a wavelength governed by their size.¹⁰⁹ These size tunable properties can be used to separate analyte emission from background interferences, improving biosensor performance. Liu *et al.*¹¹⁰ used CdSe QDs to detect AFP, elevated levels of which are linked to a variety of cancers.¹¹¹ Anti-AFP was covalently linked to a Au electrode, with secondary AFP Ab labelled with CdSe QDs. Immunoreaction between the electrode bound Ab, AFP and the QD labelled Ab allowed contact to be made between the electrode surface and ECL emitter (QDs) (Figure 1.5).

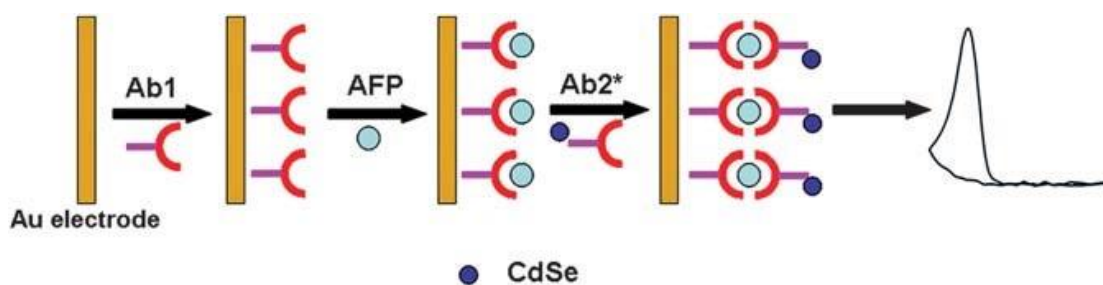


Figure 1.5 - Biosensor fabrication for the detection of AFP using CdSe QDs (reprinted with permission).¹¹⁰

Application of a potential resulted in the reduction of CdSe to produce CdSe^- , which then reacted with the co-reactant, H_2O_2 , producing excited states (CdSe^*) that emit light following relaxation to the ground state.¹¹² The ECL intensity increased with an increase in AFP concentration, with a linear range from 0.002 to 32 ng/mL.¹¹⁰ Detection limits for AFP were further improved using a label-free method developed by Guo *et al.*⁷⁸ A CdS QD-graphene-agarose composite coated onto a glassy carbon (GC) electrode was created with immobilisation of Anti-AFP via glutaraldehyde cross-linking. ECL was observed through the interaction of the reduced forms of CdS and the co-reactant, $\text{K}_2\text{S}_2\text{O}_8$ (CdS^- and $\text{SO}_4^{\cdot-}$ respectively) to produce the excited state (CdS^*) through electron transfer.¹¹³ The ECL intensity of the QD-graphene-agarose composite was 7 times greater than that of the pure CdS QD film, owing to the improved porosity and conductivity of the composite. Complexation of anti-AFP with AFP resulted in a logarithmic decrease in the ECL intensity, allowing the concentration of AFP to be determined with a detection limit of 0.2 fg/mL and a dynamic working range of 0.0005 to 50 pg/mL. This decrease in ECL intensity was attributed to the formation of a blocking layer following immunocomplexation, which hindered the diffusion of $\text{K}_2\text{S}_2\text{O}_8$ to the electrode surface and decreased the rate of electron transfer in the ECL reaction. A similar system was developed that used a CdS QD-graphene-alginate composite coated onto a GC electrode, however, in this case, CdSe/ZnS core shell QDs were utilised.¹¹⁴ Anti-AFP was attached to the QD-graphene-alginate system, with secondary AFP Ab bound to the CdSe/ZnS QDs. AFP was allowed to complex with the composite bound anti-

AFP and then secondary Ab were allowed to bind to the formed immunocomplex (Figure 1.6).

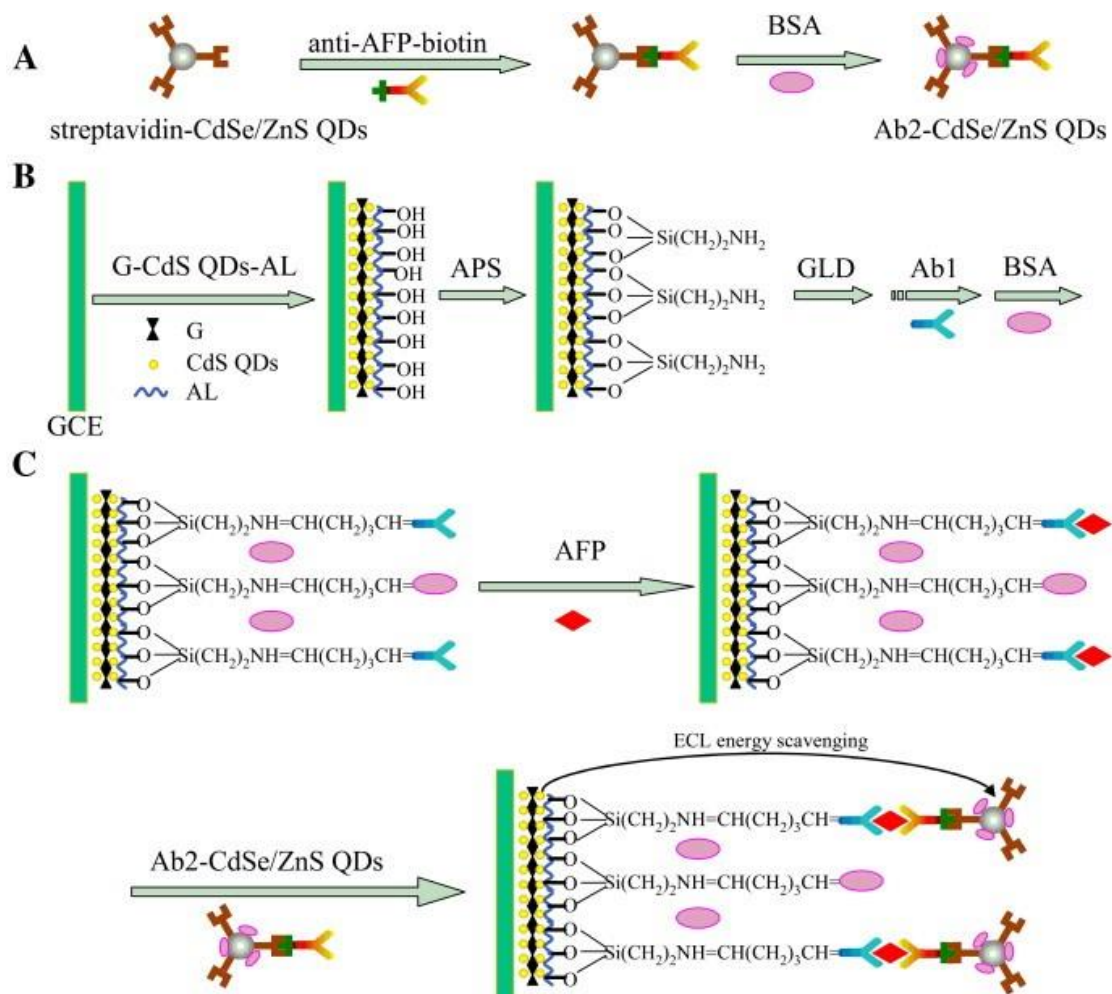


Figure 1.6 - Fabrication of a dual QD biosensor with detection based on the quenching of CdS QD ECL by the CdSe/ZnS QD label (reprinted with permission).¹¹⁴

The formation of this complex resulted in a decrease in ECL intensity of the CdS QD-graphene-alginate composite due to energy transfer with the CdSe/ZnS QD label. This prevented formation of excited states and resulted in extremely efficient quenching of the ECL signal following binding of the anti-AFP CdSe/ZnS QD label.¹¹⁴ This allowed very low limits of detection, down to 20 ag/mL, with a working range of 0.05 to 500 fg/mL. All of these detection systems were successfully used in the determination of AFP from clinical samples (serum and saliva) and were not affected by the presence of other

biomarkers (carbohydrate antigen 19–9 (CA19-9), CEA, human chorionic gonadotropin (HCG) and Hepatitis B surface antigen (HBsAg)), highlighting the specificity of this technique. This system is 5 million times more sensitive for AFP detection than an equivalent system that does not use nanomaterials in its set-up.¹¹⁵ Additionally, when compared to a standard ECL enzyme-linked immunoassay (ELISA)¹¹⁶, which has a limit of detection of 2 ng/mL, a significant improvement in sensitivity was observed. These systems illustrate the vast improvements in sensitivity associated with QD ECL and highlight the flexibility of such materials for use in a variety of designs.

Biosensors have been developed for a number of cancer biomarkers, including CEA and HCG. Jie *et al.*⁷⁹ developed a system for the detection of CEA using a composite nanostructure comprising Au/silica/CdSe-CdS core-shell QDs. CdSe-CdS QDs were surface passivated with silica coated Au NPs and immobilised on an electrode. Ab bound Au NPs were then attached. The ECL intensity of this nanostructure was 17 times greater than that of pure CdSe-CdS QDs.⁷⁹ This amplification was caused by an increase in the rate of electron transfer in the ECL reaction, due to the high concentration of Au NPs coated onto the surface of the QDs, and an improvement in structure porosity, allowing improved diffusion of the co-reactant, $K_2S_2O_8$, towards the electrode.⁷⁹ Formation of the immunocomplex in the presence of CEA resulted in a decrease in the ECL intensity due to an increase in steric hindrance, which impeded electron transfer and diffusion of $K_2S_2O_8$ in the ECL reaction. A linear range for CEA of 0.32 pg/mL to 10 ng/mL was achieved, with an LOD of 0.064 pg/mL. This system was not tested with clinical samples and the effect of interferences were not determined.

Zhang *et al.*¹¹⁷ created a novel biosensor using CdTe QD functionalised PtRu alloys for the detection of α -HCG. CdTe QDs were immobilised within the nanoporous structure of the PtRu alloy followed by attachment of anti-HCG. Chitosan coated Fe_3O_4 magnetic nanoparticles were coated with primary anti-

HCG and, in the presence of HCG, these formed an immunocomplex with the QD modified alloy (Figure 1.7).

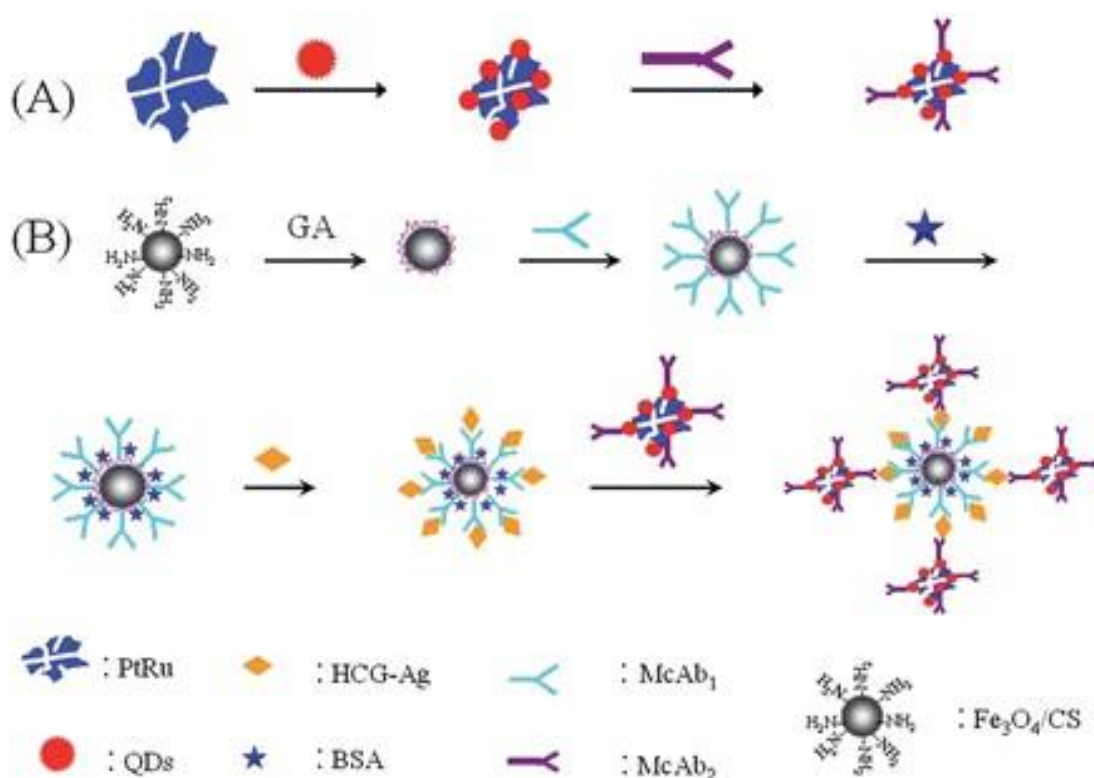


Figure 1.7 - Fabrication of the immunosensor based on QD modified PtRu alloys and magnetic beads (reprinted with permission).¹¹⁷

Formation of the immunocomplex resulted in an increase in ECL intensity as it allowed QD driven signal amplification to occur. ECL detection using a single QD label was 4.7 times less intense due to the decrease in signal enhancement associated with the decrease in QD loading.¹¹⁷ A working linear range of 0.005 to 50 ng/mL and detection limit of 0.8 pg/mL were obtained.¹¹⁷ Specificity of this system was confirmed through application in human serum samples. These systems help to reinforce the versatile nature of QDs, as they are efficient ECL luminophores both by themselves and when combined with other species to form nanocomposites.

1.2.2.3 NIR-based systems

An important advantage of QD-based systems is their flexibility and versatility, which enables numerous modifications to be made that can improve biosensor performance. One such modification is alteration of their size to achieve emission in the near infra-red (NIR) region. QDs with NIR emission (780-2500 nm)¹¹⁸ are becoming increasingly important in the field of biosensors as whole blood absorption and biological autofluorescence are minimised in this region.¹¹⁹⁻¹²¹ The improved signal penetrability of these QDs should provide an opportunity for development of biosensors that can directly analyse whole blood samples without the requirement for sample preparation. This is ideal for use in point of care (POC) type detection. A variety of QDs have been shown to emit in the NIR region, including CdSeTe,¹²⁰ CuInSe,¹²² InAs¹²³ and CdP.¹²⁴ The majority of NIR QD research has focused on their use in imaging applications due to their excellent penetrability through biological specimens.¹²⁵⁻¹²⁸ Currently, research into the ECL applications of NIR QDs is fairly limited, however, it is believed they have huge potential in the development of ECL biosensors.¹²⁹ CdSeTe/ZnS core-shell QDs have been shown to emit a strong NIR ECL signal with good biocompatibility.¹²⁰ Similarly, Ag₂Se QDs exhibited a strong cathodic NIR ECL response with K₂S₂O₈ co-reactant.¹³⁰ This system was used to detect dopamine in the low pM range through the decrease in ECL intensity associated with excited state quenching by energy transfer. Wang *et al.* developed a NIR biosensor for the detection of HlgG using CdTe/CdS QDs.⁶⁴ A sandwich immunoassay approach was used, with a secondary Ab-NIR QD conjugate generating the NIR ECL response with K₂S₂O₈ co-reactant. The system showed excellent sensitivity (87 fg/mL LOD) and was successfully used for analyte detection from human serum samples. Li *et al.* developed an immunoassay for CEA detection based on the quenching of CdSeTe/CdS/ZnS QD NIR ECL signal by Au nanorods.^{64, 131} A secondary Ab-Au nanorod conjugate was used, which was optimised to efficiently quench the NIR ECL signal from a QD-CNT film. Detection to 0.5 fg/mL was achieved and the system showed good stability in human serum samples. Research in

this area has focused on ECL sensing in buffer and human serum. Therefore, it has yet to be shown that NIR QDs can generate an ECL signal directly from a whole blood sample that is both detectable and stable. This is an area of research that requires more comprehensive investigation.

1.3 Cyclic Voltammetry (CV)

1.3.1 General principles

CV is used extensively in the investigation of electrochemical reactions and for the measurement of electrode reaction kinetics. Direct estimation of electrode reversibility is possible because the potentials at which oxidation and reduction occur are observed directly. Kinetic information regarding electron transfer reactions can be obtained by increasing the frequency of the potential sweeps to a point at which the kinetics of electron transfer are competitive with the rate of potential change.¹³²

CV utilises a three-electrode setup, combining a counter, working and reference electrode. This system is used to overcome a decrease in the working electrode potential compared to the applied potential, as a result of internal resistance of the electrolyte.¹³³ These electrodes are stationary and CV is performed in an unstirred solution. An initial potential, E_i , is applied to the working electrode and is ramped linearly with time, followed by the inversion of this sweep once the switching potential, E_λ , has been reached. Sweep rates can be varied but are typically in the region of 5 mV/s to 1 V/s. During these potential scans, the current is measured between the working and counter electrodes, and a cyclic voltammogram is created by plotting this current versus the applied potential. A peak in a cyclic voltammogram represents an electron transfer reaction between the redox species and the electrode.¹³⁴

Initially, no current is detected, as there are no oxidised or reduced species present at that potential. As the potential approaches that at which reduction

of the electroactive species occurs, a cathodic current develops due to the reduction of the species. The current is dependent on two steps: the movement of the redox species to the electrode surface and the electron transfer reaction. Upon potential scanning, the reduction of the reactant results in a rapid decrease in the concentration of the non-reduced species at the electrode surface, causing a sharp increase in the observed current. This results in the formation of a gradient due to the difference in concentration of the species at the electrode surface (where the electron transfer reaction is occurring), compared to the bulk. Therefore, diffusion-controlled mass transport occurs along this gradient. As CV is carried out using a stationary electrode in an unstirred solution, the reactant is transported to the electrode surface primarily through this diffusion process, a relatively slow mode of transport. As the electron transfer reactions occur, the depletion zone around the electrode increases as diffusion cannot maintain a steady state concentration at the electrode surface. The rate of mass transport decreases as reactant molecules must travel further to reach the electrode and eventually becomes the rate determining process. Once this occurs, the current reaches a maximum value and, as the rate of diffusion continues to decrease, the current decays.¹³⁴ During the reverse sweep, an anodic peak is produced as a result of oxidation of the reduced species that have accumulated at the electrode surface during the forward sweep. The current returns to its initial value as the reduced species is depleted at the electrode surface.¹³⁵

1.3.1.1 Theoretical response

The typical theoretical response for an electrochemically reversible couple confined on the electrode surface is a cyclic voltammogram comprising peaks that are Gaussian in shape with no peak-to-peak separation (Figure 1.8).¹³⁶ This is due to the presence of a fixed amount of the redox active species at the electrode surface, which is not influenced by diffusion. This type of behaviour is observed for reversible electrochemical reactions at sufficiently slow scan rates when the redox composition of the layer is in thermodynamic

equilibrium with the electrode potential. For these ideally responding surface-confined systems, the following features are apparent (equations (1.33) – (1.36)).¹³⁶

$$i_p = \frac{n^2 F^2}{4RT} \nu A \Gamma \quad (1.33)$$

$$FWHM = \frac{90.6}{n} mV \quad (1.34)$$

$$E_{p,a} = E_{p,c} \quad (1.35)$$

$$\frac{i_{p,c}}{i_{p,a}} = 1 \quad (1.36)$$

Where i_p is the peak current, n is the number of electrons passed, F is the Faraday constant, ν is the scan rate, Γ is the total electroactive coverage, A is the electrode area, R is the gas constant, T is the temperature, $FWHM$ is the full width at half maximum, $E_{p,a}$ is the anodic peak potential, $E_{p,c}$ is the cathodic peak potential, $i_{p,c}$ is the cathodic peak current and $i_{p,a}$ is the anodic peak current.

Under these conditions the peak current is dependent on the scan rate.¹³⁶ This is because a slower scan rate results in an increase in the overall scan time and thus the charge passed per unit time is smaller, while the total amount of charge is the same. As a result, peak current decreases.¹³⁷

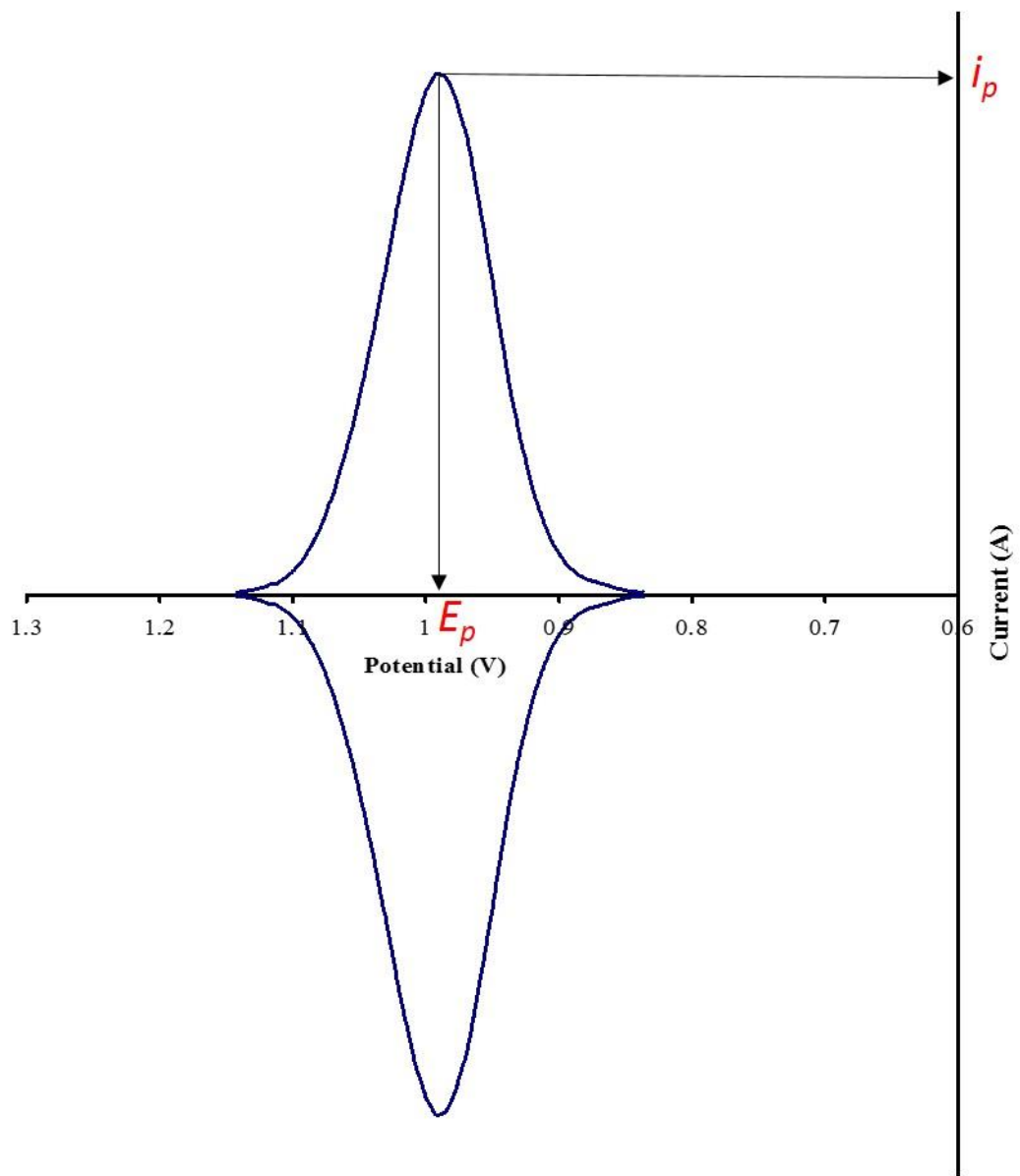


Figure 1.8 - The theoretical response for an electrochemically reversible redox couple confined on the electrode surface.

1.3.1.2 Semi-infinite diffusion control

The voltammogram is affected when higher scan rates are used or the rate of heterogeneous electron transfer is slow. Higher scan rates only allow partial electrolysis to occur within the time frame of each linear scan, whilst slow electron transfer affects the concentrations of electroactive species at the electrode surface. Under such circumstances, semi-infinite diffusion control is observed, resulting in an increase in peak-to-peak separation and peak current no longer increasing in proportion to scan rate.¹³⁶ Instead, peak current is dependent on $v^{1/2}$ and peak separation (ΔE_p) is given by equation (1.37) (at 25°C). The value of ΔE_p tends to increase with an increase in scan rate.¹³⁴ A typical cyclic voltammogram observed for a system under semi-infinite diffusion control is shown in Figure 1.9.

$$\Delta E_p = \frac{57}{n} mV \quad (1.37)$$

Under these conditions, the Randles-Sevcik equation is used to determine peak current (equation (1.38)).^{138, 139}

$$i_p = 2.69 \times 10^5 n^{3/2} A D_{CT}^{1/2} C v^{1/2} \quad (\text{at } 25^\circ\text{C}) \quad (1.38)$$

Where C is the concentration of electroactive sites within the film and D_{CT} is the diffusion coefficient.

With slow electron transfer, the potential at which the peak anodic current is reached shifts to more positive potentials. This is because the concentration of reduced species at the electrode surface decreases at a slower rate than if electron transfer was rapid. Therefore, the largest concentration gradient is not reached until more positive potentials and, as such, the shape of the voltammogram is altered.¹⁴⁰

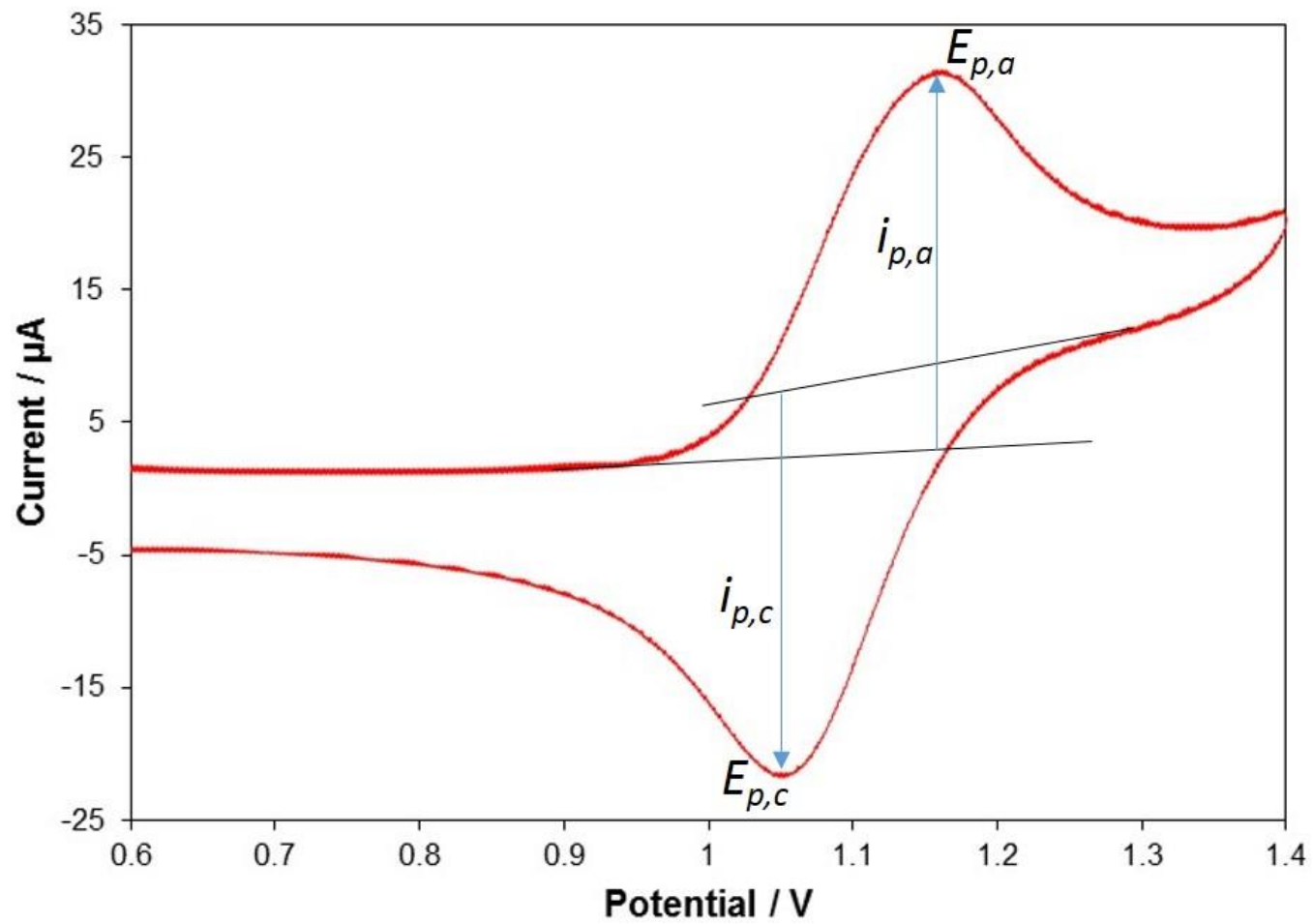


Figure 1.9 - A typical cyclic voltammogram for a reversible redox couple under semi-infinite diffusion control.

The concentration profile of electroactive sites in a polymer film is governed by $D_{CT} \tau / d^2$, where τ is the experimental timescale and d is the polymer layer thickness. When $D_{CT} \tau / d^2 \gg 1$, then all electroactive sites within the polymer film are in equilibrium with the electrode potential and finite diffusion conditions are observed. However, when $D_{CT} \tau / d^2 \ll 1$, then reduced sites furthest from the electrode surface have not been oxidised prior to switching the oxidising scan direction. Here, semi-infinite diffusion conditions are observed.¹³⁶

An alternative situation can arise in which there is considerable peak separation or only a single peak is observed. This can occur when the system is chemically irreversible,¹³⁴ the oxidised or reduced species are unstable¹ or when the rate of heterogeneous electron transfer is very slow and fast scan rates are used. Reactions in which the reactants cannot be rejuvenated electrochemically from the products are said to be chemically irreversible and usually involve extensive bond breaking or change of conformation. This causes a loss of molecules into the electrolyte. As such, these types of reactions yield no return peak. If the forward scan yields ions that are unstable in the time it takes to traverse the wave at a particular scan rate then the reverse peak will not be present, as the ion will decompose before it can be returned to its parent state.

The characteristic features of a cyclic voltammogram can be used to determine a number of characteristics of a redox system. Formal redox potentials, ion stabilities, diffusion co-efficients and kinetics of electron transfer reactions can all be determined using this simple technique and, as such, CV is used extensively in the characterisation of electrochemical systems.^{134, 141}

1.4 Differential Pulse Voltammetry (DPV)

1.4.1 General principles

DPV is routinely used as a technique for electrochemical characterisation of species that require greater sensitivity than can be achieved using CV. DPV is

very effective at correcting for the background current, which is a consequence of the electric double-layer (EDL) effect and impurities in solution.¹⁴² Application of a potential at a solid-liquid interface (i.e. electrode-solution interface) causes this EDL effect as counter-ions in solution are attracted to the charged solid surface, becoming immobilised due to electrostatic forces (the Stern layer).¹⁴³ A mobile diffuse layer (Gouy-Chapman layer) forms above this immobilised layer and can move relative to the charged solid substrate under an electric field (application of a potential).¹⁴³ This means as the potential is changed, a current is required to charge these layers at the electrode-solution interface. This charging current is the major contributor to background current,¹⁴² which can also be affected by redox reactions of impurities in solution.¹⁴² Very small changes in current resulting from electron transfer between the electrode and electroactive species may be masked by this charging current. To correct for this DPV employs potential pulses and current subtraction.

DPV uses fixed magnitude pulses that are applied to the working electrode and superimposed on a stepped potential ramp (Figure 1.10).

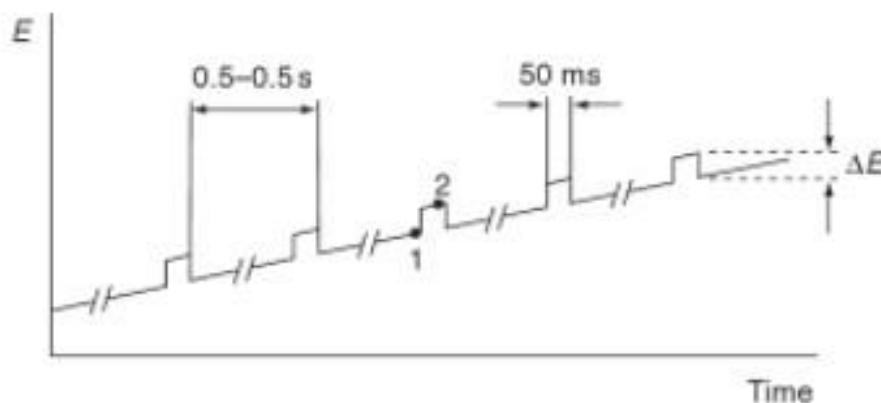


Figure 1.10 - Electronic process for signal generation in DPV.⁸³

The current is measured at two points with regard to this pulse: immediately prior to its application (point 1 in Figure 1.10) and after approximately 40 ms (~80 % of pulse width, point 2 in Figure 1.10). Within this time, the charging current associated with application of the pulse should have decayed.⁸³ The

first current is subtracted from the second and this difference is an effective measure of the differential current. A differential pulse voltammogram (current difference vs. applied potential) is plotted and contains peaks that have i_p , E_p and peak shape that are characteristic of the concentration (equation (1.39)), species (equation (1.40)) and electron stoichiometry (equation (1.41)), respectively.⁸³

$$i_p = \frac{n F A D_{CT}^{\frac{1}{2}} C}{\sqrt{\pi t_m}} \left(\frac{1 - \sigma}{1 + \sigma} \right) \quad (1.39)$$

$$E_p = E_{1/2} - \frac{\Delta E}{2} \quad (1.40)$$

$$FWHM = \frac{3.52 R T}{n F} \quad (1.41)$$

Where t_m is the time after application of the pulse that the current is measured, $\sigma = \exp\left[\left(\frac{nF}{RT}\right)\left(\frac{\Delta E}{2}\right)\right]$, and ΔE is the pulse amplitude.

At 25 °C, equation (1.41) predicts a value of 90.1 mV for a 1-electron transfer process, showing similar resolution of this technique when compared to CV (FWHM = 90.6 mV under same conditions, equation (1.34)). Irreversible systems exhibit broader peaks with lower i_p compared to reversible systems.⁸³

1.5 Conclusions

The desire for sensitive, selective and simplistic biosensors for monitoring and detecting clinically relevant analytes has driven research and development within the ECL field. Its inherent sensitivity, biocompatibility and control over the light-emitting reactions create a technique that is extremely well suited for such applications. The incorporation of nanomaterials into these devices has allowed improvements in sensitivity that are unrivalled compared to classical ECL emitters and their versatility has permitted the development of a vast array of biosensor systems.

QDs have been used extensively in the development of novel biosensors due to their unique optical and electrochemical properties. They have been designed to work at physiological pH, which can be a problem with other luminophores, such as luminol.⁶ Their ability to both enhance the ECL signal of certain systems and effectively quench the ECL of others, highlights the flexibility of these QD based systems. This flexibility is further improved through the ability to incorporate QDs into a number of other matrices, which combine to form nanocomposites that often give rise to enhancements in performance through increased surface area and improved conductivity. The use of NIR emitting QDs is becoming increasingly important in the field of ECL biosensors, as detection in this region should result in minimal signal interference from biological fluids and tissue. However, the ECL viability of these QDs in such samples has yet to be proven.

The future of biomedical diagnostics lies in POC testing, which requires rapid, sensitive biosensing systems with no sample preparation. Incorporating NIR emitters into these ECL systems combines their respective benefits and these devices will likely be at the forefront of development in this area for the foreseeable future.

1.6 References

1. A. J. Bard, *Electrogenerated Chemiluminescence*, 1 edn., Marcel Dekker, Inc., New York, 2004.
2. L. R. F. Allen J. Bard, *Electrochemical Methods: Fundamentals and Applications*, 2nd edn., John Wiley and Sons, Inc., Hoboken, NJ, 2001.
3. W. Miao, *Chemical Reviews*, 2008, **108**, 2506-2553.
4. D. M. Hercules, *Science*, 1964, **145**, 808-809.
5. A. W. Knight, *Trends in Analytical Chemistry*, 1999, **18**, 47-62.
6. K. A. Fahrnich, M. Pravda and G. G. Guilbault, *Talanta*, 2001, **54**, 531-559.
7. P. Bertonecello, A. J. Stewart and L. Dennany, *Analytical and bioanalytical chemistry*, 2014, 1-15.
8. M. Mirasoli and E. Michelini, *Analytical and bioanalytical chemistry*, 2014, 1-2.
9. S. Deng and H. Ju, *Analyst*, 2013, **138**, 43-61.
10. J. Wang and H. Han, *Reviews in Analytical Chemistry*, 2013, **32**, 91-101.
11. S. Parveen, M. S. Aslam, L. Hu and G. Xu, *Electrogenerated Chemiluminescence: Protocols and Applications*, Springer, 2013.
12. A. Arora, J. C. T. Eijkel, W. E. Morf and A. Manz, *Analytical Chemistry*, 2001, **73**, 3282-3288.
13. F.-R. F. Fan, *Electrogenerated Chemiluminescence*, 1 edn., Marcel Dekker, Inc., New York, 2004.
14. L. Hu and G. Xu, *Chemical Society reviews*, 2010, **39**, 3275-3304.
15. H. Qi, X. Qiu, D. Xie, C. Ling, Q. Gao and C. Zhang, *Analytical Chemistry*, 2013, **85**, 3886-3894.
16. Z. Li, L. Sun, Y. Zhao, L. Yang, H. Qi, Q. Gao and C. Zhang, *Talanta*, 2014, **130**, 370-376.
17. Y. Li, C. Huang, J. Zheng and H. Qi, *Talanta*, 2013, **103**, 8-13.
18. J. Liang, S. Yang, S. Luo, C. Liu and Y. Tang, *Microchimica Acta*, 2014, **181**, 759-765.
19. G. Liang, S. Liu, G. Zou and X. Zhang, *Analytical chemistry*, 2012, **84**, 10645-10649.
20. Y. Shan, J. J. Xu and H. Y. Chen, *Nanoscale*, 2011, **3**, 2916-2923.
21. J. Qian, C. Y. Zhang, X. D. Cao and S. Q. Liu, *Analytical chemistry*, 2010, **82**, 6422-6429.
22. N. Gan, J. Zhou, P. Xiong, F. Hu, Y. Cao, T. Li and Q. Jiang, *Toxins*, 2013, **5**, 865-883.
23. S. P. Forry and R. M. Wightman, *Electrogenerated chemiluminescence. Marcel Dekker, New York*, 2004, 273-320.
24. H. S. White and A. J. Bard, *Journal of the American Chemical Society*, 1982, **104**, 6891-6895.
25. H. D. Abruña, *Journal of electroanalytical chemistry and interfacial electrochemistry*, 1984, **175**, 321-326.
26. A. J. Bard, *Electrogenerated Chemiluminescence*, Marcel Dekker, Inc., New York, 2004.
27. H. Zheng and Y. Zu, *The Journal of Physical Chemistry B*, 2005, **109**, 12049-12053.

28. G. B. Xu and S. J. Dong, *Electroanalysis*, 2000, **12**, 583-587.
29. Y.-P. Dong, H. Cui and Y. Xu, *Langmuir*, 2007, **23**, 523-529.
30. Y. Wang, J. Lu, L. Tang, H. Chang and J. Li, *Analytical chemistry*, 2009, **81**, 9710-9715.
31. H. Kuhn, H. D. Försterling and D. H. Waldeck, *Principles of Physical Chemistry*, Wiley, 2009.
32. J. G. Vos, R. J. Forster and T. E. Keyes, *Interfacial Supramolecular Assemblies*, Wiley, 2003.
33. A. Weller and K. Zachariasse, *The Journal of Chemical Physics*, 1967, **46**, 4984-4985.
34. L. R. Faulkner, H. Tachikawa and A. J. Bard, *Journal of the American Chemical Society*, 1972, **94**, 691-699.
35. C. G. Zoski, *Handbook of electrochemistry*, Elsevier Science, 2007.
36. A. W. Knight and G. M. Greenway, *Analyst*, 1994, **119**, 879-890.
37. M. M. Sartin, F. Camerel, R. Ziessel and A. J. Bard, *The Journal of Physical Chemistry C*, 2008, **112**, 10833-10841.
38. N. J. Turro, V. Ramamurthy and J. C. Scaiano, *Principles of molecular photochemistry: an introduction*, Univ Science Books, 2009.
39. H. Tachikawa and A. J. Bard, *Chemical Physics Letters*, 1974, **26**, 246-251.
40. A. K. Campbell and A. K. Campbell, 1988.
41. R. D. Gerardi, N. W. Barnett and S. W. Lewis, *Analytica Chimica Acta*, 1999, **378**, 1-41.
42. D. R. Skotty, W.-Y. Lee and T. A. Nieman, *Analytical chemistry*, 1996, **68**, 1530-1535.
43. J. Liu, W. Cao, H. Qiu, X. Sun, X. Yang and E. Wang, *Clinical chemistry*, 2002, **48**, 1049-1058.
44. W. Zhan and A. J. Bard, *Analytical chemistry*, 2007, **79**, 459-463.
45. H. Qi and C. Zhang, *Analytica chimica acta*, 2004, **501**, 31-35.
46. H. Qi, M. Li, M. Dong, S. Ruan, Q. Gao and C. Zhang, *Analytical chemistry*, 2014, **86**, 1372-1379.
47. R.-P. Liang, C.-Y. Xiang, H.-F. Zhao and J.-D. Qiu, *Analytica chimica acta*, 2014, **812**, 33-40.
48. J. Zhang, H. Qi, Y. Li, J. Yang, Q. Gao and C. Zhang, *Analytical chemistry*, 2008, **80**, 2888-2894.
49. Y. Li, H. Qi, Q. Gao and C. Zhang, *Biosensors and Bioelectronics*, 2011, **26**, 2733-2736.
50. N. D. Danielson, *Electrogenerated Chemiluminescence*, 1 edn., Marcel Dekker, Inc., New York, 2004.
51. I. Rubinstein and A. J. Bard, *Journal of the American Chemical Society*, 1981, **103**, 512-516.
52. W. Miao, J.-P. Choi and A. J. Bard, *Journal of the American Chemical Society*, 2002, **124**, 14478-14485.
53. J.-P. Choi and A. J. Bard, *Analytica chimica acta*, 2005, **541**, 141-148.
54. E. P. Diamandis and T. K. Christopoulos, *Immunoassay*, Elsevier Science, 1996.
55. W. Stockmann, W. Bablok and P. Lupp, *Wiener Klinische Wochenschrift*, 1998, **110**, 10.

56. X. H. Xu, R. B. Jeffers, J. Gao and B. Logan, *Analyst*, 2001, **126**, 1285-1292.
57. J. G. Bruno and J. L. Kiel, *Biotechniques*, 2002, **32**, 178-+.
58. W. Miao and A. J. Bard, *Analytical chemistry*, 2003, **75**, 5825-5834.
59. Z. Chang, J. Zhou, K. Zhao, N. Zhu, P. He and Y. Fang, *Electrochimica Acta*, 2006, **52**, 575-580.
60. X.-B. Yin, Y.-Y. Xin and Y. Zhao, *Analytical chemistry*, 2009, **81**, 9299-9305.
61. F. Yu, G. Li, B. Qu and W. Cao, *Biosensors and Bioelectronics*, 2010, **26**, 1114-1117.
62. H. Qi, Y. Peng, Q. Gao and C. Zhang, *Sensors*, 2009, **9**, 674-695.
63. S. G. Hazelton, X. Zheng, J. X. Zhao and D. T. Pierce, *Sensors*, 2008, **8**, 5942-5960.
64. J. Wang, H. Han, X. Jiang, L. Huang, L. Chen and N. Li, *Analytical chemistry*, 2012, **84**, 4893-4899.
65. L. L. Li, K. P. Liu, G. H. Yang, C. M. Wang, J. R. Zhang and J. J. Zhu, *Advanced Functional Materials*, 2011, **21**, 869-878.
66. J. Qian, Z. Zhou, X. Cao and S. Liu, *Analytica chimica acta*, 2010, **665**, 32-38.
67. Y. Li, H. Qi, Q. Gao, J. Yang and C. Zhang, *Biosensors and Bioelectronics*, 2010, **26**, 754-759.
68. Z. Lin, L. Chen, X. Zhu, B. Qiu and G. Chen, *Chemical Communications*, 2010, **46**, 5563-5565.
69. Y. Cao, R. Yuan, Y. Chai, L. Mao, H. Niu, H. Liu and Y. Zhuo, *Biosensors and Bioelectronics*, 2012, **31**, 305-309.
70. G. F. Blackburn, H. P. Shah, J. H. Kenten, J. Leland, R. A. Kamin, J. Link, J. Peterman, M. J. Powell, A. Shah and D. B. Talley, *Clinical chemistry*, 1991, **37**, 1534-1539.
71. Y. Cheng, R. Yuan, Y. Chai, H. Niu, Y. Cao, H. Liu, L. Bai and Y. Yuan, *Analytica chimica acta*, 2012, **745**, 137-142.
72. Y. Li, H. Qi, F. Fang and C. Zhang, *Talanta*, 2007, **72**, 1704-1709.
73. X. Wang, J. Zhou, W. Yun, S. Xiao, Z. Chang, P. He and Y. Fang, *Analytica chimica acta*, 2007, **598**, 242-248.
74. W. Shen, D. Tian, H. Cui, D. Yang and Z. Bian, *Biosensors and Bioelectronics*, 2011.
75. J. E. Adams, 3rd, G. S. Bodor, V. G. Davila-Roman, J. A. Delmez, F. S. Apple, J. H. Ladenson and A. S. Jaffe, *Circulation*, 1993, **88**, 101-106.
76. Z. F. Zhang, H. Cui, C. Z. Lai and L. J. Liu, *Analytical Chemistry*, 2005, **77**, 3324-3329.
77. C. Wang, H. Qi, X. Qiu, Q. Gao and C. Zhang, *Analytical Methods*, 2012, **4**, 2469-2474.
78. Z. Guo, T. Hao, J. Duan, S. Wang and D. Wei, *Talanta*, 2011, **89**, 27-32.
79. G. F. Jie, P. Liu and S. S. Zhang, *Chemical Communications*, 2010, **46**, 1323-1325.
80. G. Jie, L. Wang, J. Yuan and S. Zhang, *Analytical chemistry*, 2011, **83**, 3873-3880.
81. N. J. Ronkainen, H. B. Halsall and W. R. Heineman, *Chemical Society Reviews*, 2010, **39**, 1747-1763.
82. B. R. Eggins, *Chemical sensors and biosensors*, Wiley, 2002.
83. J. Wang, *Analytical Electrochemistry*, Wiley, 2006.

84. G. Li, J. Lian, X. Zheng and J. Cao, *Biosensors and Bioelectronics*, 2010, **26**, 643-648.
85. J. Wang, *Biosensors and Bioelectronics*, 2006, **21**, 1887-1892.
86. X. F. Wang, Y. Zhou, J. J. Xu and H. Y. Chen, *Advanced Functional Materials*, 2009, **19**, 1444-1450.
87. M. Zhang, M. Yan, J. Yu, S. Ge, F. Wan and L. Ge, *Analytical Methods*, 2012, **4**, 460-466.
88. M. Zhang, W. Dai, M. Yan, S. Ge, J. Yu, X. Song and W. Xu, *Analyst*, 2012.
89. B. Haghighi, S. Bozorgzadeh and L. Gorton, *Sensors and Actuators B: Chemical*, 2011, **155**, 577-583.
90. G. J. Zhang, M. J. Huang, J. A. J. Ang, E. T. Liu and K. V. Desai, *Biosensors and Bioelectronics*, 2011, **26**, 3233-3239.
91. M. L. Lozano, M. C. Rodríguez, P. Herrasti, L. Galicia and G. A. Rivas, *Electroanalysis*, 2010, **22**, 128-134.
92. G. A. Rivas, M. D. Rubianes, M. C. Rodríguez, N. F. Ferreyra, G. L. Luque, M. L. Pedano, S. A. Miscoria and C. Parrado, *Talanta*, 2007, **74**, 291-307.
93. J. Lei and H. Ju, *Trends in Analytical Chemistry*, 2011, **30**, 1351-1359.
94. T. Pradeep, *Nano: the essentials*, Tata McGraw-Hill Education, 2007.
95. W. W. Yu, L. H. Qu, W. Z. Guo and X. G. Peng, *Chemistry of Materials*, 2003, **15**, 2854-2860.
96. Z. F. Ding, B. M. Quinn, S. K. Haram, L. E. Pell, B. A. Korgel and A. J. Bard, *Science*, 2002, **296**, 1293-1297.
97. N. Myung, X. Lu, K. P. Johnston and A. J. Bard, *Nano letters*, 2004, **4**, 183-185.
98. S. K. Haram, B. M. Quinn and A. J. Bard, *Journal of the American Chemical Society*, 2001, **123**, 8860-8861.
99. X. Liu, H. Jiang, J. Lei and H. Ju, *Analytical Chemistry*, 2007, **79**, 8055-8060.
100. R. Hikmet, D. Talapin and H. Weller, *Journal of applied physics*, 2003, **93**, 3509.
101. S. K. Poznyak, D. V. Talapin, E. V. Shevchenko and H. Weller, *Nano letters*, 2004, **4**, 693-698.
102. H. Jiang and H. Ju, *Analytical Chemistry*, 2007, **79**, 6690-6696.
103. G. Jie, J. Zhang, D. Wang, C. Cheng, H. Y. Chen and J. J. Zhu, *Analytical Chemistry*, 2008, **80**, 4033-4039.
104. S. Ruan, Z. Li, H. Qi, Q. Gao and C. Zhang, *Microchimica Acta*, 2014, **181**, 1293-1300.
105. A. J. Bard, Z. Ding and N. Myung, *Semiconductor Nanocrystals and Silicate Nanoparticles*, 2005, **118**, 1-57.
106. N. Myung, Y. Bae and A. J. Bard, *Nano Letters*, 2003, **3**, 1053-1055.
107. H. Wang, Q. Chen, Z. Tan, X. Yin and L. Wang, *Electrochimica Acta*, 2012, **72**, 28-31.
108. C. Yu, J. Yan and Y. Tu, *Microchimica Acta*, 2011, **175**, 347-354.
109. S. K. Poznyak, D. V. Talapin, E. V. Shevchenko and H. Weller, *Nano Letters*, 2004, **4**, 693-698.
110. Q. Liu, M. Han, J. Bao, X. Jiang and Z. Dai, *Analyst*, 2011, **136**, 5197-5203.
111. J. H. Chow and C. Chow, *The Encyclopedia of Hepatitis and Other Liver Diseases*, Facts On File, Incorporated, 2006.

112. G. Z. Zou and H. X. Ju, *Analytical Chemistry*, 2004, **76**, 6871-6876.
113. G. Jie, P. Liu, L. Wang and S. Zhang, *Electrochemistry Communications*, 2010, **12**, 22-26.
114. Z. Guo, T. Hao, S. Wang, N. Gan, X. Li and D. Wei, *Electrochemistry Communications*, 2012, **14**, 13-16.
115. M. Xue, T. Haruyama, E. Kobatake and M. Aizawa, *Sensors and Actuators B: Chemical*, 1996, **36**, 458-462.
116. W. Q. E. Zhuang H.S., *Chemical Journal of Chinese Universities*, 1999, 1194.
117. Y. Zhang, S. Ge, S. Wang, M. Yan, J. Yu, X. Song and W. Liu, *Analyst*, 2012, **137**, 2176-2182.
118. C. Burgess and J. Hammond, *Spectroscopy*, 2007, **22**, 40-48.
119. Q. Ma and X. Su, *Analyst*, 2010, **135**, 1867-1877.
120. G.-X. Liang, L.-L. Li, H.-Y. Liu, J.-R. Zhang, C. Burda and J.-J. Zhu, *Chemical Communications*, 2010, **46**, 2974-2976.
121. W. Jiang, A. Singhal, J. Zheng, C. Wang and W. C. W. Chan, *Chemistry of materials*, 2006, **18**, 4845-4854.
122. P. M. Allen and M. G. Bawendi, *Journal of the American Chemical Society*, 2008, **130**, 9240-9241.
123. P. M. Allen, W. Liu, V. P. Chauhan, J. Lee, A. Y. Ting, D. Fukumura, R. K. Jain and M. G. Bawendi, *Journal of the American Chemical Society*, 2009, **132**, 470-471.
124. S. Miao, S. G. Hickey, B. Rellinghaus, C. Waurisch and A. Eychmüller, *Journal of the American Chemical Society*, 2010, **132**, 5613-5615.
125. S. Kim, Y. T. Lim, E. G. Soltesz, A. M. De Grand, J. Lee, A. Nakayama, J. A. Parker, T. Mihaljevic, R. G. Laurence and D. M. Dor, *Nature biotechnology*, 2003, **22**, 93-97.
126. W. Cai, D.-W. Shin, K. Chen, O. Gheysens, Q. Cao, S. X. Wang, S. S. Gambhir and X. Chen, *Nano letters*, 2006, **6**, 669-676.
127. E. G. Soltesz, S. Kim, R. G. Laurence, A. M. DeGrand, C. P. Parungo, D. M. Dor, L. H. Cohn, M. G. Bawendi, J. V. Frangioni and T. Mihaljevic, *The Annals of thoracic surgery*, 2005, **79**, 269-277.
128. N. Y. Morgan, S. English, W. Chen, V. Chernomordik, A. Russo, P. D. Smith and A. Gandjbakhche, *Academic radiology*, 2005, **12**, 313-323.
129. L. Chen and H. Han, *Microchimica Acta*, 2014, 1-11.
130. R. Cui, Y.-P. Gu, L. Bao, J.-Y. Zhao, B.-P. Qi, Z.-L. Zhang, Z.-X. Xie and D.-W. Pang, *Analytical chemistry*, 2012, **84**, 8932-8935.
131. L. Li, Y. Chen, Q. Lu, J. Ji, Y. Shen, M. Xu, R. Fei, G. Yang, K. Zhang and J.-R. Zhang, *Scientific reports*, 2013, **3**.
132. Nicholso.Rs, *Anal Chem*, 1965, **37**, 1351-&.
133. J. Heinze, *Angewandte Chemie*, 1984, **23**, 831-847.
134. G. A. Mabbott, *J Chem Educ*, 1983, **60**, 697-702.
135. J. Wang, *Analytical Chemistry*, 3rd edn., John Wiley and Sons, Inc., Hoboken, NJ, 2006.
136. J. G. Vos, R. J. Forster and T. E. Keyes, *Interfacial supramolecular assemblies*, Wiley Online Library, 2003.
137. R. G. Compton and C. E. Banks, *Understanding voltammetry*, Imperial College Pr, 2011.

138. J. Randles, *Transactions of the Faraday Society*, 1948, **44**, 327-338.
139. A. Sevcik, *Czech Chemical Communications*, 1948, **13**, 349-377.
140. A. H. C.H. Hamann, W. Vielstich, *Electrochemistry*, 2nd edn., Wiley VCN, 2007.
141. R. M. Wightman and D. O. Wipf, *Accounts of Chemical Research*, 1990, **23**, 64-70.
142. J. Wang, *Electroanalytical Techniques in Clinical Chemistry and Laboratory Medicine*, Wiley, 1988.
143. P. Abgrall and N. T. Nguyen, *Nanofluidics*, Artech House, Incorporated, 2009.

Chapter 2 - Characterisation of 800 nm CdSeTe/ZnS

quantum dots

2.1 Introduction

The electrochemical and optical properties of a species can be used to confirm they are behaving as expected and provide an insight into their electronic structure and properties. Analysis of data obtained from these investigations can help identify the characteristic behaviour of a species following optical or electrochemical stimulation. This can aid in determining the pathways and energetics involved in ECL generation and provide a greater understanding of the species in an electrochemical environment. For this reason, the electrochemical and optical properties of NIR QDs were examined to obtain a preliminary idea of their electronic structure and its role in the ECL process.

The vast majority of work with these QDs has focused on their use in imaging,¹⁻⁴ owing to the increased ability of their emitted light to penetrate biological samples. This characteristic was crucial for selection and integration of NIR QDs within ECL systems, as it should allow detection of an intense signal directly from whole blood samples. Although their use in imaging applications has been well-documented, there does not appear to be any significant electrochemical characterisation of these QDs, with the majority of work focusing on optical and elemental spectroscopy and nano-scale imaging techniques.

The main objective of this work was to evaluate the electrochemical behaviour of NIR QDs and compare this with QDs that emit in the visible region. Together with this, examination of their optical properties was required to ensure these are not affected by ligand exchange procedures used to create water-soluble QDs. The electronic properties of these QDs can then be inferred from this data.

2.2 Experimental

2.2.1 Apparatus

Ultraviolet (UV)-visible spectrometry was carried out in water or decane and samples were prepared at 0.1 μM (800 QDs) and 0.1 mg/mL (560 and 640 nm QDs) concentrations and analysed in a 1 cm quartz cell. Emission spectra were recorded on a Cary Eclipse Fluorescence Spectrophotometer with an excitation and emission slits of 5 nm, 800 V PDA power and a scan rate of 120 nm/min. Samples were prepared as for UV-visible spectroscopy and were analysed on a 96-well plate. The excitation wavelengths used were 450 (800 nm QDs), 625 (640 nm QDs) and 540 (560 nm QDs) nm.

Electrochemical measurements were carried out using a CH instrument model 760D electrochemical analyser. All experiments were carried out using a conventional three-electrode assembly, consisting of a 3 mm diameter GC working electrode, Pt wire counter electrode and Ag/AgCl reference electrode. GC electrodes were cleaned by successive polishing using 1, 0.3 and 0.05 μM alumina slurry, followed by sonication in ethanol and water, respectively, for 30 mins. The electrodes were then dried under a flow of N_2 gas. CV was carried out at a scan rate of 100 mV s^{-1} and sample interval of 1 mV across a potential range outlined in each figure. For DPV, the increment potential was 4 mV, amplitude 50 mV, pulse width 50 ms, sample width 16.7 ms and pulse period 0.5 s across a potential range outlined in each figure. Measurements involving simultaneous detection of light and current utilised a CH instrument model 760D connected to a Hamamatsu H10723-20 PMT. The input voltage to the PMT was + 5 V and the control voltage was set between 0.5 and 1.05 V depending on the required sensitivity. During electrochemical experiments, the cell was kept in a light-tight Faraday cage in a specially designed holder configuration where the working electrode was positioned directly above the PMT window. All measurements were made at room temperature.

2.2.2 Materials

Core-shell CdSeTe/ZnS QDs (Qdot® 800 ITK™ organic quantum dots, 1 μM in decane) were purchased from Invitrogen. Core-shell CdSe/ZnS QDs (Lumidot™ 560 and 640 nm QDs, 5 mg/mL in toluene), chitosan (medium molecular weight, 75-85% de-acetylated), phosphate buffered saline (PBS, pH 7.4), 2-(dimethylamino)ethanethiol (DAET) and hydrogen peroxide (H₂O₂) were all purchased from Sigma-Aldrich and used as received. All other reagents used were of analytical grade, and all solutions were prepared in milli-Q water (18 mΩ cm).

2.2.3 Methods

Preparation of water soluble CdSeTe/ZnS and CdSe/ZnS core-shell QDs

The method followed was similar to that developed by Woelfle and Claus.⁵ 0.5 mL of 0.5 M DAET in methanol was mixed with 0.25 mL of the CdSeTe/ZnS QDs in decane (1 μM) / CdSe/ZnS QDs in toluene (5 mg/mL). N₂ was bubbled through the solution for 5 mins, which was then sealed and left stirring overnight in the dark at room temperature. The QDs were then precipitated with an excess of acetone followed by centrifugation at 5000 rpm for 6 mins. The filtrate was removed and the precipitate was re-dispersed in 0.25 mL of distilled water. These water-soluble QDs were centrifuged for a further 6 mins at 3000 rpm to remove any impurities and then stored in darkness at 4°C.

Preparation of CdSeTe/ZnS and CdSe/ZnS core-shell QD-chitosan composite films

A 0.1 % chitosan solution was prepared in 1 % acetic acid and sonicated for 5 mins. The QD/chitosan composite was prepared by mixing aliquots of the water-soluble QDs with the chitosan solution in a 1:1 (v/v) ratio and mixing for 30 s. 3 μL of this composite was then carefully cast onto the electroactive

portion of a GC electrode, with mixing of the composite for 10 s between electrodes. The film was allowed to dry for 1 h at 4°C. A film of bare QDs was prepared in the same manner, with water used instead of chitosan.

QD concentration in the film was altered by mixing the water-soluble QDs with a suitable volume of water prior to mixing in a 1:1 (v/v) ratio with chitosan.

2.3 Characterisation

2.3.1 Optical characterisation

2.3.1.1 UV/Visible spectroscopy

Typically, QDs have a very broad, featureless absorption spectra with a small peak at a wavelength related to its band gap energy and thus governed by its size.⁶ The absorption spectrum of 800 nm QDs in decane (manufacturer's stock solution) and water-soluble QDs following ligand exchange are shown in Figure 2.1.

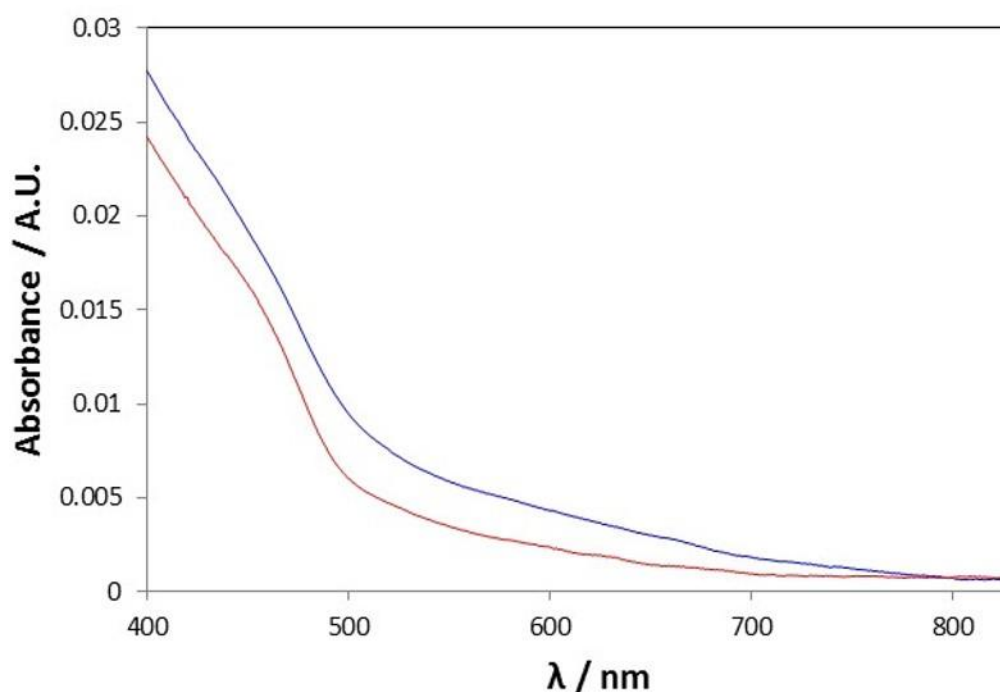


Figure 2.1 - Absorption spectra of 800 nm QDs in decane (red) and in water (blue) following ligand exchange.

The QD absorbance spectrum does not change following ligand exchange. This indicated a successful procedure without QD aggregation or disruption to its electronic structure. Both exhibit classic QD absorption behaviour, with decreasing absorbance accompanying increasing wavelength. The typical electronic structure and allowed optical transitions of a QD are shown in Figure

2.2. With this size of QD, a peak at approximately 1.55 eV (800 nm), corresponding to the 1S(h)-1S(e) transition would be expected. Neither spectra exhibit this peak, however, this is in agreement with spectra obtained from the manufacturer.⁷ It appears that transitions occurring at this specific energy are very weak and are below the detection limits for the spectrometer. Both spectra have a broad, shallow peak around 450 nm, indicative of a specific electron transition with an energy of 2.75 eV. This energy is too great to result from a 1S(h)-1S(e) transition in the core material and is not sufficiently energetic to originate from the 1S(h)-1S(e) ZnS shell, which has a band gap of 3.54 eV in its cubic form at 25°C.⁸ It is possible is associated with either a transition into a ZnS surface state or an allowed transition from deeper within the valence band (1P(h), 1D(h) or 2S(h)) to its corresponding energy level in the conduction band of the QD core.

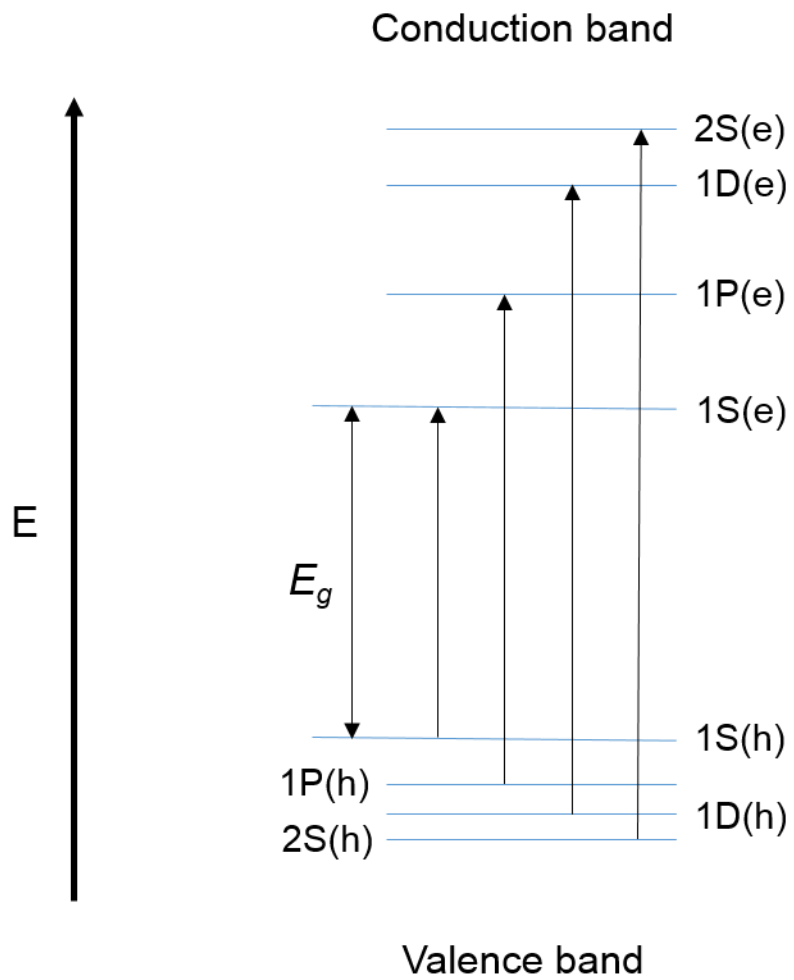


Figure 2.2 - Typical QD energy levels with allowed optical transitions shown. Adapted from Pradeep *et al.*⁹

The electronic structure of QDs consists of discrete energy levels that are separated by an appreciable amount of energy (Figure 2.2).⁹ It is the outermost energy levels within the valence and conduction bands that have the most significant influence on the optical and electronic properties of the species. The difference in energy between the valence and conduction bands is known as the band gap energy (E_g) and determines the photon energy required to excite an electron from the valence into the conduction band. Typically, this transition is seen as a defined peak in the QD absorption spectrum. The large number of discrete energy levels (and possible transitions) in the electronic structure of QDs tends to result in broad absorption across the visible region. The molar extinction co-efficient of QDs increases with decreasing wavelength, resulting in a profile with gradient towards shorter wavelengths, observed in Figure 2.1, which is characteristic of QD absorption behaviour.

Electron excitement into the conduction band leaves behind a positively charged particle in the valence band, known as a hole. An electron has a considerably smaller mass than a hole, which results in greater splitting of the electron energy levels compared to the hole energy levels, as is shown in Figure 2.2. This is because the energy of an electron or hole is related to the inverse of its mass through equation (2.1).¹⁰

$$E_{e/h} = \frac{h^2 n^2}{8\pi^2 m_{e/h} d^2} \quad (2.1)$$

Where h is Planck's constant, n is the quantum number of the conduction or valence band states, $m_{e/h}$ is the effective mass of the electron or hole and d is the diameter of the QD.

This equation also dictates that the electron and hole energy levels, and hence the band gap energy, are influenced by the diameter of the QDs. The energies are dependent upon the inverse of the diameter squared so will increase as the QD diameter decreases. This explains the size-tunable E_g of QDs, which

manifests itself as an increase in 1S(h)-1S(e) transition energy as particle size decreases. This was confirmed experimentally by examining the absorption spectra of 560 (3.4 nm particle size) and 640 (6.3 nm particle size) nm CdSe/ZnS QDs in H₂O (Figure 2.3).

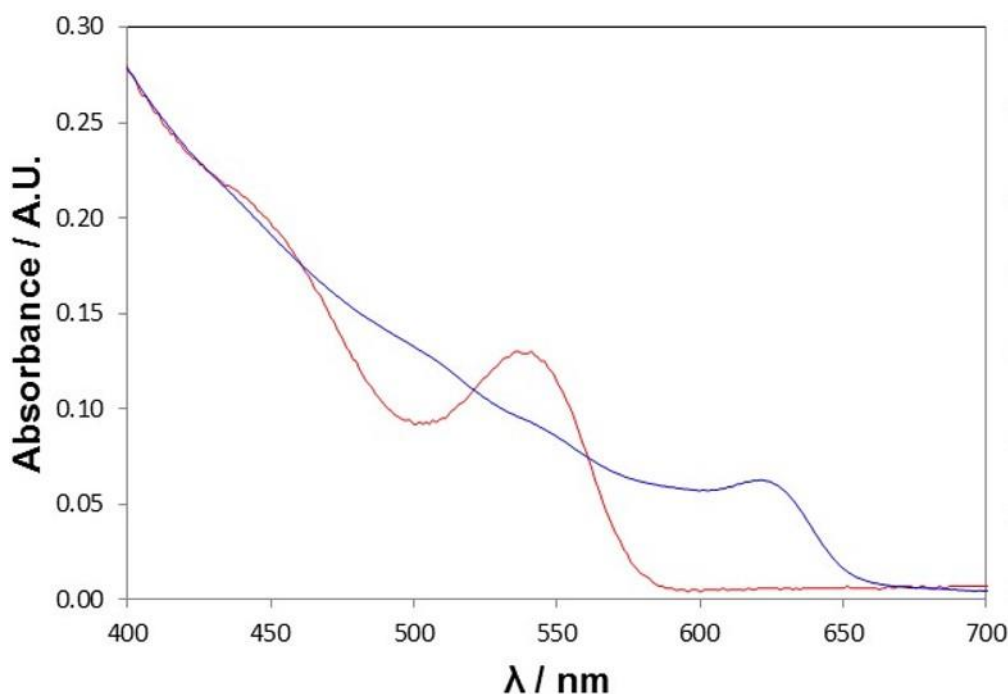


Figure 2.2 - Absorption spectra of 560 (red) and 640 (blue) nm CdSe/ZnS QDs in H₂O.

The spectra of 560 nm QDs contains a small peak around 450 nm that is related to a deep electron transition. A large peak is observed at 540 and 625 nm respectively for the 3.4 and 6.3 nm QDs, which is consistent with the energetics of their 1S(h)-1S(e) transitions.

The tail of the absorption spectra can be used to estimate the QD E_g as this represents the minimum photon energy required for a transition to occur (i.e. the 1S(h)-1S(e) transition). It must be noted that precise determination of QD E_g cannot be accomplished using this method as exciton binding energies must be taken into account, which incorporates a coulombic interaction energy term and a kinetic energy term related to the relative motion of the exciton.¹¹ As a consequence, the energy required to excite an electron in a QD is not simply dictated by E_g , but also by these additional energy contributions, which

are known to decrease with increasing QD size and have a magnitude in the low meV range.¹²

However, an estimation of E_g can be made from the absorption profile using the Planck-Einstein relation, which relates photon energy to Planck's constant and the photon's frequency ($E = h\nu = hc/\lambda$, where h is Planck's constant, c is the speed of light and λ is the photon wavelength). This calculated photon energy can then be used to infer E_g for the QD, which is shown in Table 2.1.

Table 2.1 – Optical E_g calculated from absorption spectra of different size QDs.

QD size (emission λ) / nm	λ_{tail} for transition to occur / nm	E_g / eV
3.4 (560)	575	2.156
6.3 (640)	650	1.907
~20 (800)	n/a	n/a

This data denotes the minimum photon energy required to excite an electron from 1S(h) to 1S(e) and illustrates that a reduction in QD size is accompanied with an increase in E_g . The excited electron and resultant hole remains in the core material of the QD, a consequence of the significantly larger E_g of the shell material compared to the core material. This confines the charge carriers in the core due to the larger chemical potential of the passivating material. Passivation of QDs with a shell material (ZnS, in this case) not only confines excitons in the core but is essential for limiting the formation of surface states. QDs are prone to these surface states due to their large surface area relative to bulk size.¹³

The relatively broad nature typical of QD absorption peaks are a consequence of these surface states, which exist at an energy found within the band gap of the material.¹⁴ Surface states develop due to the lower coordination number of QD surface atoms compared to atoms in the bulk. These atoms have free atomic orbitals ('dangling orbitals') that point away from the surface and usually

have a slight positive or negative charge.¹⁴ Provided their energy lies within the semiconductor E_g , they can act as surface traps for charge carriers, which can lead to a decrease in quantum yields and electron transfer kinetics.¹⁴ Passivation of QDs with a shell and protective ligand layer removes the majority of these dangling orbitals through coordination with surface atoms. Full passivation of QD surfaces is not possible due to surface defects and as such surface states influence the optical and electrochemical behaviour and characteristics of QDs. A photon with insufficient energy to excite an electron into the conduction band may have sufficient energy to excite an electron into one of these surface states, resulting in a low energy electron transition and broadening of the absorption profile. E_g calculated from QD absorption spectra will be influenced by surface states as the minimum photon energy at the tail of the profile may be the result of a transition from the valence band into a surface state. This will underestimate the energy of E_g and indicates that an alternative method, less susceptible to influence from surface states, would provide a more accurate estimation of the true value of E_g .

2.3.1.2 Emission spectroscopy

QD emission is related to radiative recombination of an excited electron in the 1S(e) energy level with a hole in the 1S(h) energy level. Energy separation of an exciton in a QD is minimised through relaxation of the excited electron to the lowest energy level of the conduction band and migration of the hole to the top of the valence band (Figure 2.4). Any excess energy is usually dissipated through inelastic collisions with solvent molecules. The specific value of these discrete energy levels results in emission profiles with a defined, narrow peak at a wavelength corresponding to the energy difference between these two levels. The majority of surface states are dark states that result in nonradiative recombination of trapped charge carriers.¹³ Thus, the wavelength of maximum emission ($\lambda_{\max}(\text{emission})$) should not be affected by these states and corresponds to 1S(e)-1S(h) radiative recombination. Therefore, emission spectroscopy can be used to obtain a more accurate estimation of E_g .

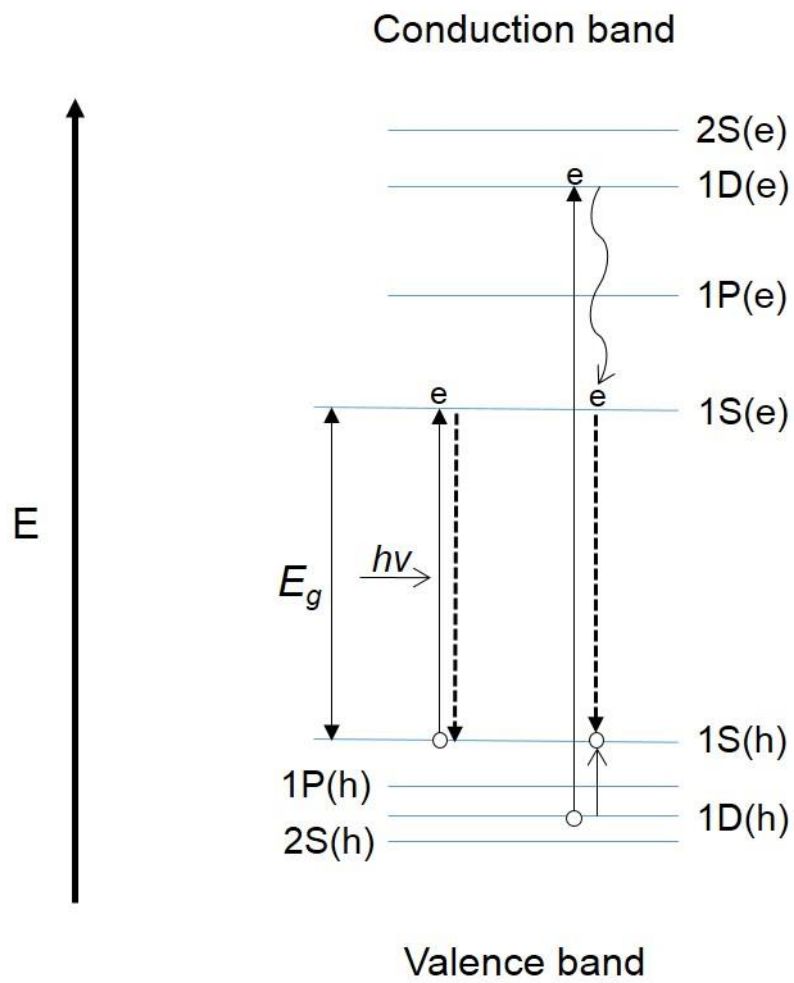


Figure 2.3 – Radiative recombination resulting in band-edge emission in QDs.

A comparison of the 800 nm QD emission profiles before and after ligand exchange is shown in Figure 2.5.

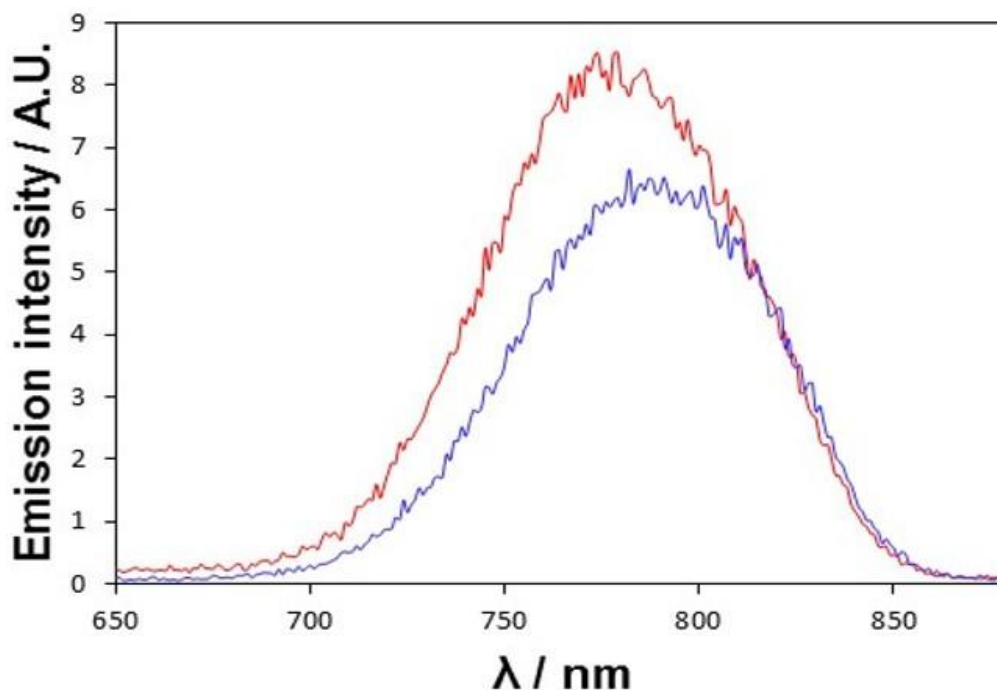


Figure 2.4 - Emission spectra of 800 nm QDs in decane (red) and in water (blue) following ligand exchange. Excitation wavelength = 450 nm.

A single emission peak with λ_{\max} at 784 and 790 nm is observed in the profile of organic and water-soluble QDs respectively, the outcome of radiative recombination in the QD core between 1S(e) and 1S(h). This confirms these QDs emit in the NIR region. The close to identical nature of these profiles designates a successful ligand exchange procedure has occurred with no significant disruption to electronic structure. The emission profiles of 560 and 640 nm QDs are shown in figure 2.6.

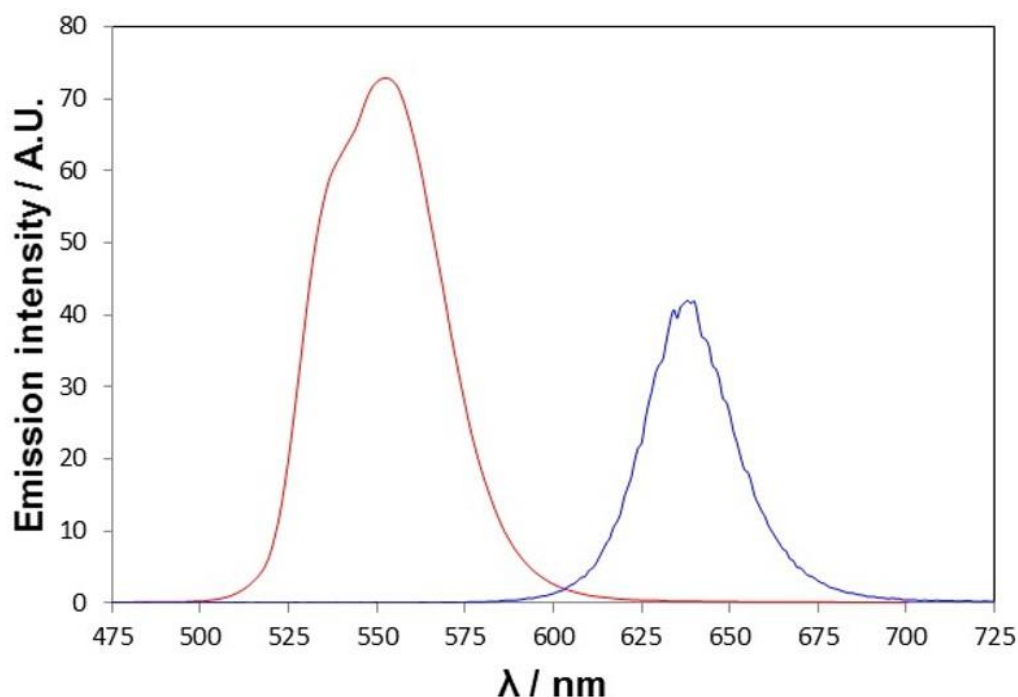


Figure 2.5 - Emission spectra of 560 (red) and 640 (blue) nm CdSe/ZnS QDs in H₂O. Excitation wavelength = 540 and 625 nm respectively.

The 560 and 640 nm QDs exhibit a single emission peak corresponding to band-edge emission from 1S(e) to 1S(h) at 553 and 638 nm respectively. From this it can be seen that the absorption (Figure 2.3) and emission profiles of QDs overlap extensively, which is a consequence of the defined nature of their electronic structure and permits high quantum yields for these materials.¹⁵ The optical E_g of these QDs, calculated from $\lambda_{\max}(\text{emission})$ (Figure 2.4 and 2.5), are shown in Table 2.2.

Table 2.2 – Optical E_g calculated from emission λ of different size QDs.

QD λ_{\max} (emission) / nm	E_g / eV
553	2.242
638	1.943
790	1.569

As expected, an increase in QD size is accompanied by a decrease in E_g . These values are greater than those obtained from absorption spectra (Table 2.1), illustrating the influence of surface states on those calculations.

Assuming $\lambda_{\max}(\text{emission})$ and $\lambda_{\max}(\text{absorption})$ correspond to 1S(h)-1S(e) transitions, and recognising that exciton binding energy must be overcome for excitation, a comparison of E_g calculated from these values should give an estimate of exciton binding energy in each QD. (Table 2.3)

Table 2.3 – Comparison of optical E_g calculated from $\lambda_{\max}(\text{emission})$ and $\lambda_{\max}(\text{absorption})$ of different size QDs.

QD λ_{\max} (emission) / nm	E_g / eV	QD λ_{\max} (absorption) / nm	E_g / eV	Exciton binding energy / eV
553	2.242	541	2.291	0.049
638	1.943	627	1.977	0.034
790	1.569	n/a	n/a	n/a

This data shows an increase in exciton binding energy from 34 to 49 meV as QD size decreases from 6.3 to 3.4 nm. This trend is in good agreement with that accepted in the literature.^{11, 12}

These results have highlighted the size-dependent optical and electronic properties of QDs, confirming they were behaving as expected. Ligand exchange with organic 800 nm QDs was successful and did not disrupt their optical and electronic properties. Confirmation of NIR emission was attained from 800 nm CdSeTe/ZnS QDs and permitted calculation of QD E_g . This provided fundamental information for future electrochemical characterisation of these QDs.

2.3.1.3 ECL emission spectroscopy

The key optical characteristic of these QDs is their ECL emission wavelength, which should closely relate to the optically-induced emission wavelength as the final radiative process in both techniques involves the same process.¹⁶ The optically-induced emission profile is dominated by recombination of electrons

and holes in the QD core, whereas it has been found that ECL emission can be strongly influenced by surface states.¹⁷ This can affect the wavelength of emitted photons, which have been observed to red shift by over 200 nm compared to the optical emission maxima.^{17, 18} This can be useful for investigating these surface states, however, it is difficult to control the formation and energies of these states, which will affect the ECL emission profile. ECL emission from surface states tends to be more problematic with QDs that are not passivated with a protective shell coating. Suitable passivation of QDs with a shell and ligand layer limits the formation of these surface state energy levels and ensures that the majority of ECL emission mimics that of the photoluminescence, which originates from the core.¹⁸ The major benefit of this is that emission wavelength from the core is entirely controllable owing to the unique size-tunable properties of QDs. The ECL spectrum of water-soluble NIR QDs is shown in Figure 2.7.

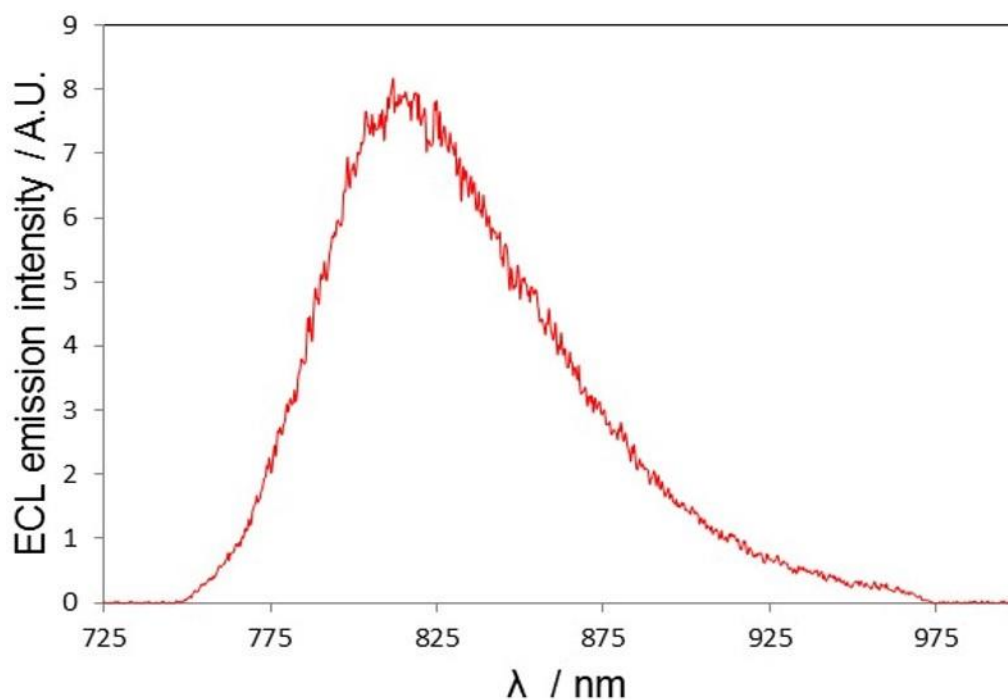


Figure 2.6 - The ECL spectrum of CdSeTe/ZnS QDs in 2mM H₂O₂ at a potential of -1.4 V vs. Ag/AgCl.

This profile displays an ECL emission peak with maximum at 811 nm, red-shifted by 21 nm compared to the QD photo-induced emission peak. The shift

in emission wavelength associated with surface-confined electrochemical reactions leading to emission in the ECL process is most likely due to the difference in reorganisation energy of this route when compared to optically-induced emission.^{19, 20} Injection of an electron into a QD, as occurs during the ECL process, means significant reorganisation of the system will be required. Reorganisation energy typically consists of an inner and outer sphere component. The inner sphere component is associated with changes within the QD that must occur to accommodate this additional electron. The outer sphere component is associated with reorganisation of the solvent and surrounding media and is the most significant contribution to the reorganisation energy.²¹ Upon electron injection, dipoles in the solvent must rapidly re-align in order to accommodate this negative charge, consuming energy from the system in the process. The result of this reorganisation is a red-shift in ECL emission maximum compared to optically induced emission (Figure 2.5). Thus, ECL emission at this wavelength indicates it originated from the QD core rather than any surface states.

Comparison of the optically-induced and ECL emission profiles (Figure 2.8) indicates that these are influenced by different processes.

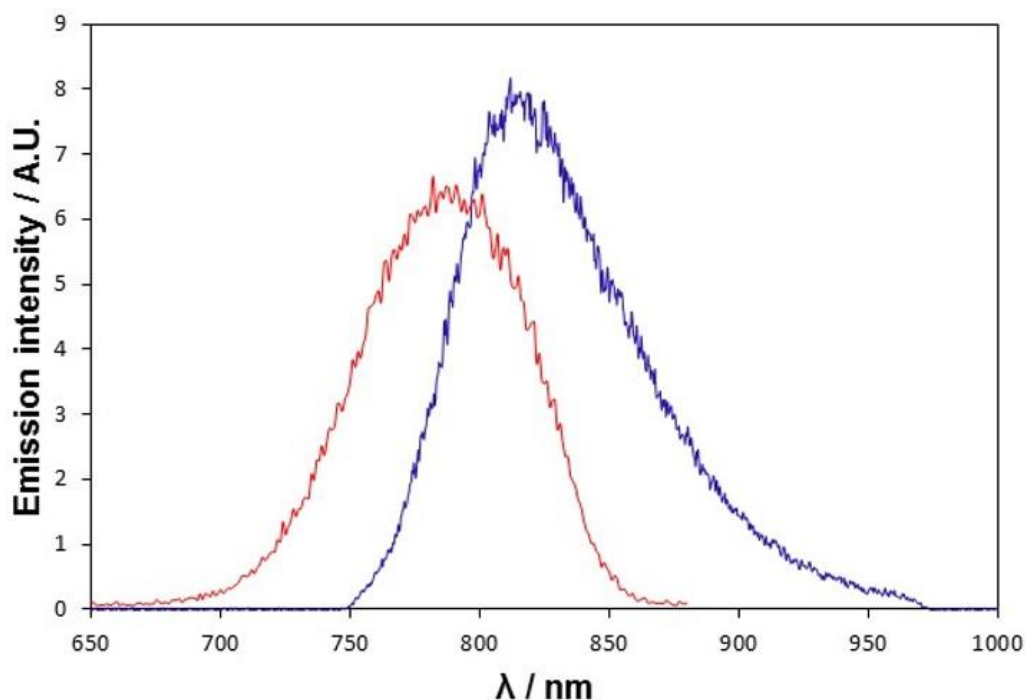


Figure 2.7 – Emission profiles of 800 nm QDs from optically-induced (red) and ECL (blue) processes.

λ_{\max} for both processes corresponds to 1S(e)-1S(h) radiative recombination leading to band-edge emission (with variations between the two explained above). The optically-induced emission profile exhibits a fronting peak, suggesting electron transitions from higher in the conduction band (1P(e), 1D(e) etc.) to the ground state resulting in emission of higher energy photons. The ECL emission profile has a tailing peak that is caused by radiative recombination of excitons trapped within surface states (trapped electron, trapped hole, or both). This results in a broader ECL emission profile compared to optically-induced emission. Therefore, surface states have a greater influence on the overall ECL emission profile, however, the most significant transition involved in both processes is the 1S(e)-1S(h) exciton recombination.

This work has confirmed that ECL emission from these QDs originates from the core material and is within the NIR region.

2.3.2 Electrochemical characterisation

2.3.2.1 CV

Electrochemical characterisation of NIR QDs focused on their behaviour in an aqueous environment as these are the conditions in which the majority of their applications are based. The anodic behaviour of a blank glassy carbon (GC) electrode, solution phase QDs, a film of bare QDs and a QD/chitosan composite film are shown in Figure 2.9. The oxidative voltammograms for each of these is broad and featureless with no defined peaks. The introduction of QDs into the system, in either the solution or film phase, does not result in the appearance of any significant oxidative peaks, highlighting the difficulties associated with visualising these processes when using QDs.

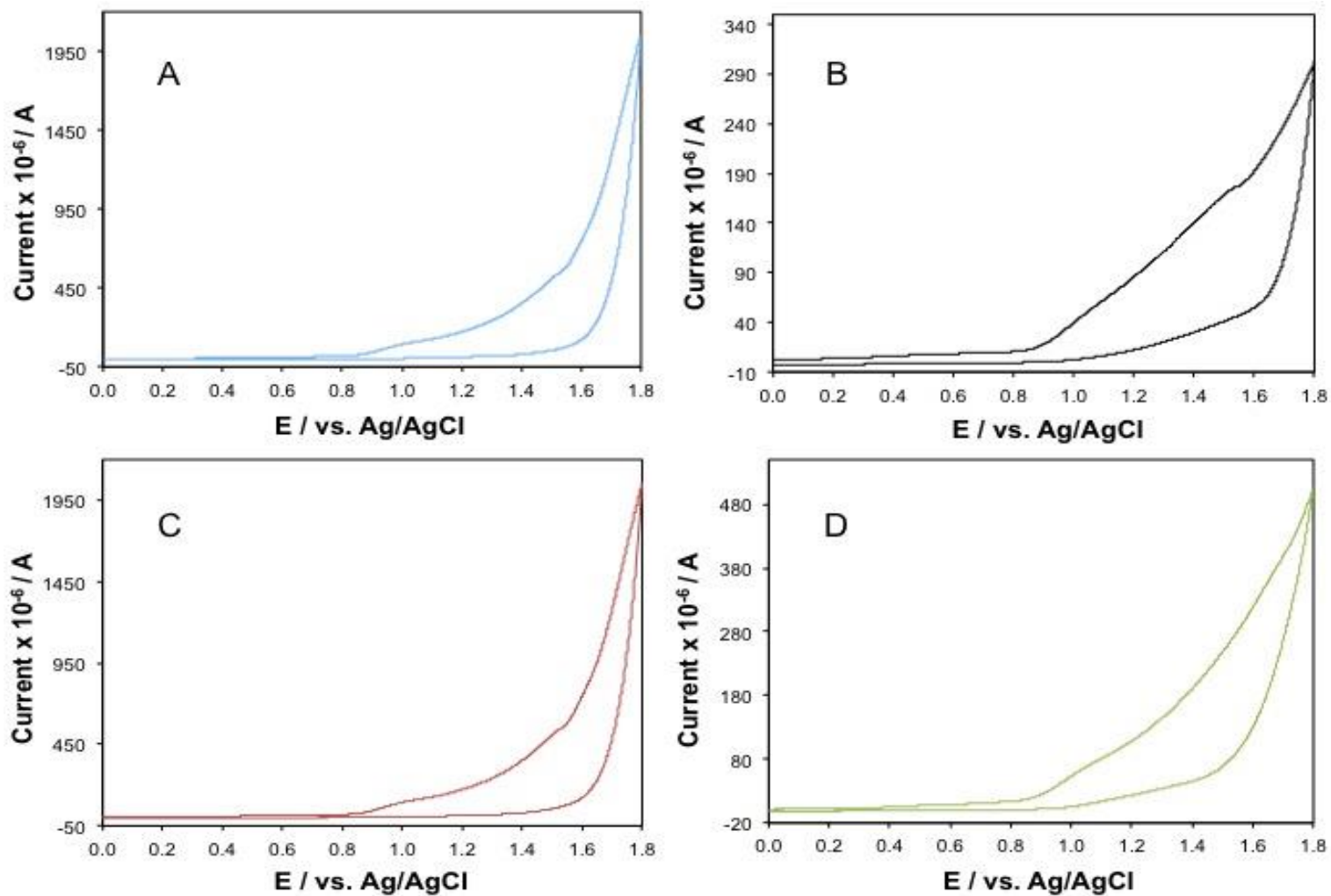
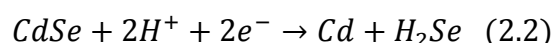


Figure 2.8- Current response for blank GC electrode (a), solution phase 800 nm QDs (b), bare 800 nm QD film (c) and a 800 nm QD/chitosan film (d) at a scan rate of 100 mV s^{-1} over the potential range $0 \text{ V} \leq v \leq 1.8 \text{ V}$ vs. Ag/AgCl in 0.1 M PBS.

Figure 2.10 shows the cathodic voltammograms of a blank GC electrode, solution phase QDs, a film of bare QDs and a QD/chitosan composite film. The blank GC electrode contains a very small, irreversible reduction peak that is hard to discern from the background, with the appearance of one further reduction peak with solution phase QDs and two further peaks with the QD films. Reduction peak onset with the blank GC is at approximately -0.45 V, with a peak potential of -0.65 V. This irreversible peak is consistent with the reduction of dissolved O₂ at a blank GC electrode.²²

Introduction of solution phase QDs into the system yields a second irreversible reduction peak in the voltammograms at approximately -1.50 V that is likely related to direct electron injection into the 1S(e) energy level of QDs as it is only observed in their presence. Application of a QD film onto the electrode surface generated a third irreversible reduction peak at -1.80 V, which was sensitive to QD concentration (Figure 2.11). This indicated it was associated with a secondary QD electron injection process, likely involving injection of a second electron into the 1S(e) orbital or electron injection into a higher energy conduction band level (1P(e), 1D(e), 2S(e)). It has been shown that QD reduction in this manner can result in their destruction due to irreversible chemical reactions following charge injection (equation (2.2)).^{23, 24}



The disappearance of reduction peaks at -1.50 and -1.80 V following sequential voltammetric scans (Figure 2.12) indicates this secondary reduction process is indeed destroying the QDs. Electrochemical behaviour of the QDs is clearly influenced by this process, signifying the cathodic potential window in which they are stable is limited to potentials below that at which this secondary electron injection occurs. The larger band gap of smaller QDs should permit an increase in stability at lower potentials as the energy required for electron injection into the conduction band is greater.

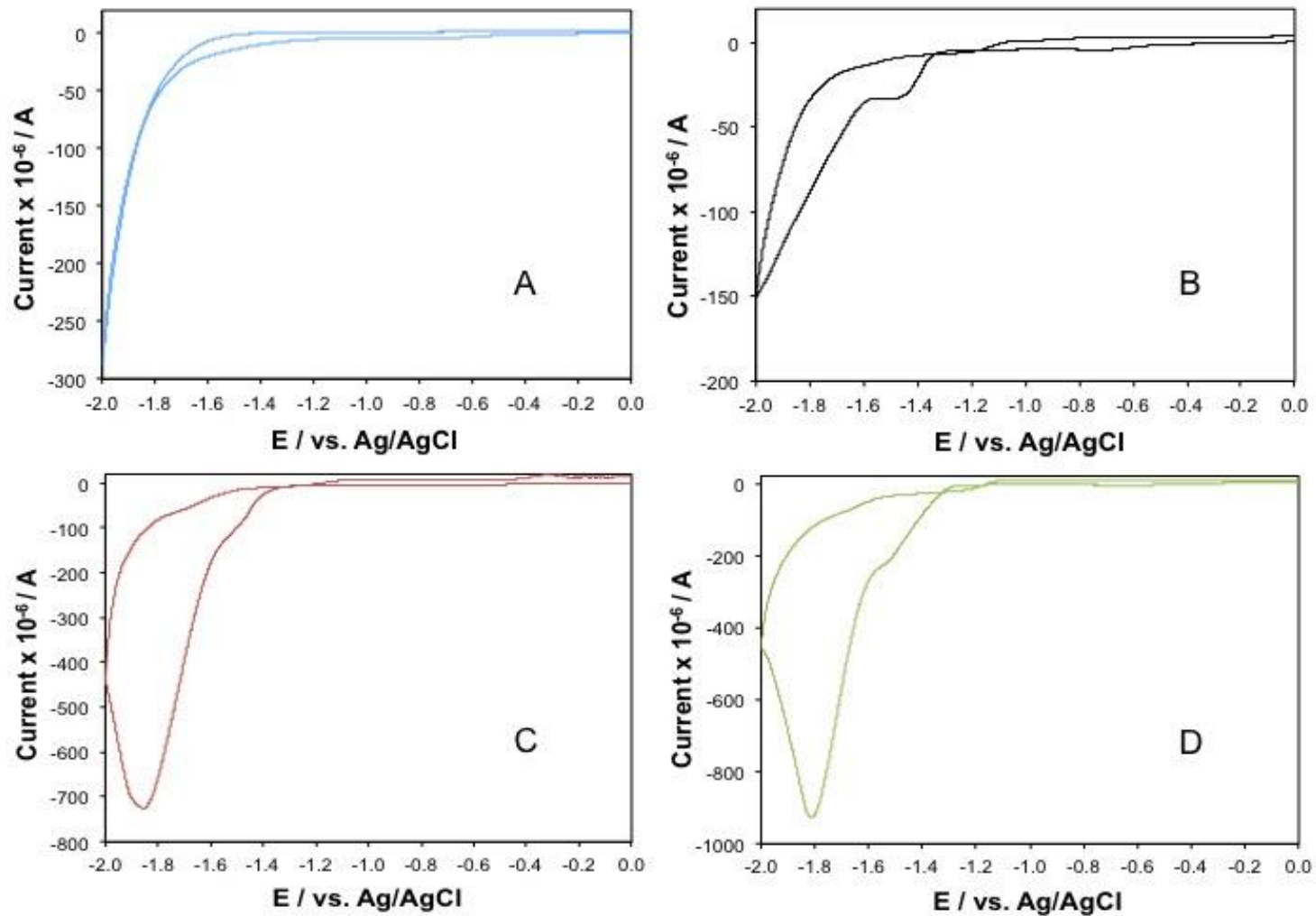


Figure 2.9 - Current response for blank GC electrode (a), solution phase 800 nm QDs (b), a bare 800 nm QD film (c) and a 800 nm QD/chitosan film (d) at a scan rate of 100 mV s^{-1} over the potential range $-2 \text{ V} \leq v \leq 0 \text{ V}$ vs. Ag/AgCl in 0.1 M PBS.

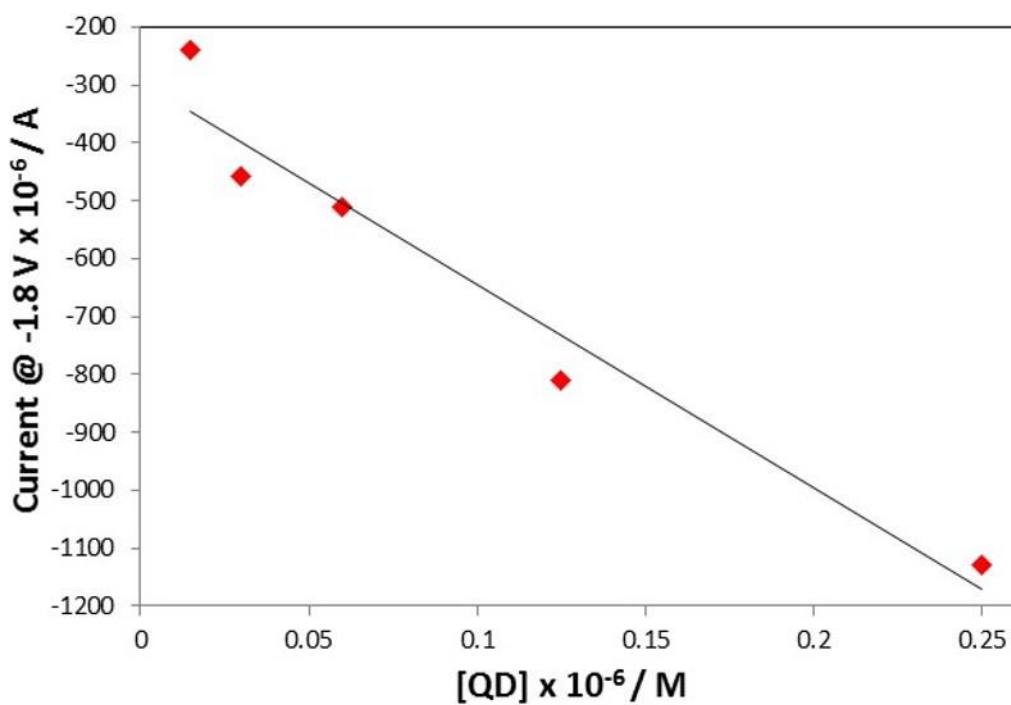


Figure 2.10 - Peak current at ~ -1.8 V vs Ag/AgCl with increasing 800 nm QD concentration.

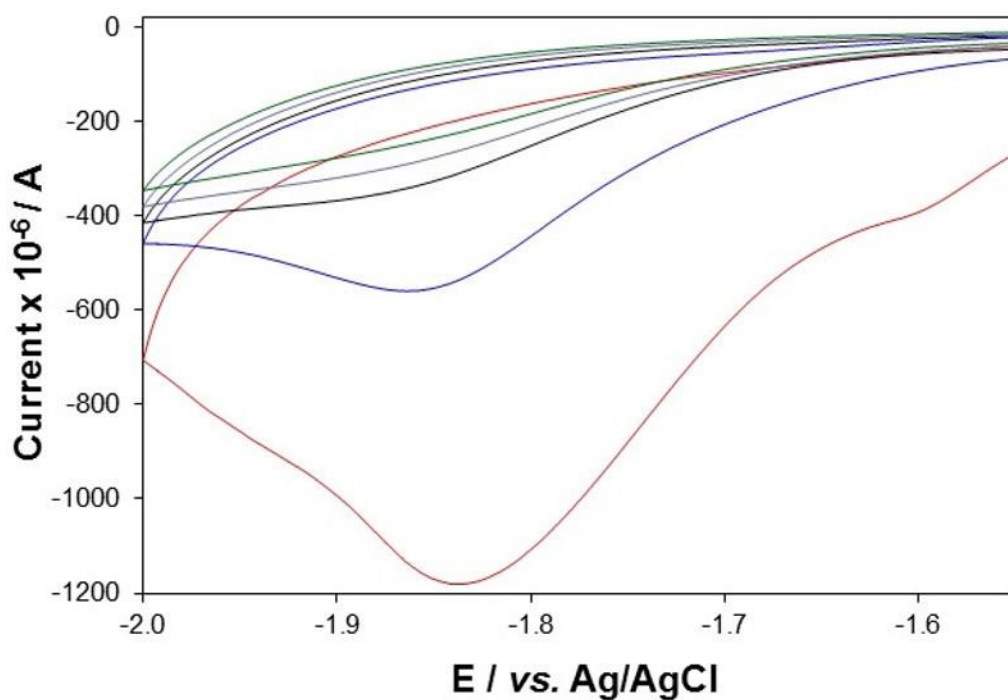


Figure 2.11 - Current response for 800 nm QD/chitosan film after 1 (red), 2 (blue), 3 (black), 4 (purple) and 5 (green) scans at a scan rate of 100 mV s^{-1} over the potential range $-2 \text{ V} \leq v \leq -1.5 \text{ V}$ vs. Ag/AgCl in 0.1 M PBS.

Figure 2.13 shows the voltammograms of 560 and 640 nm QD/chitosan films.

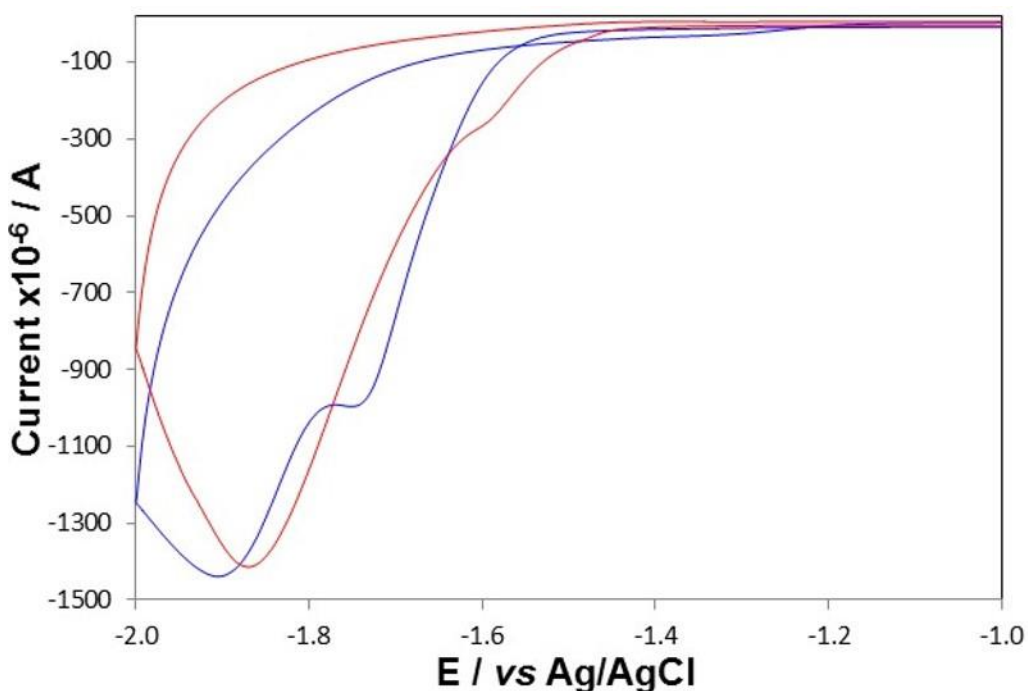


Figure 2.12 – Typical current response for 640 (red) and 560 nm (blue) QD/chitosan films at a scan rate of 100 mV s^{-1} over the potential range $-2 \text{ V} \leq v \leq -1 \text{ V}$ vs. Ag/AgCl in 0.1 M PBS.

A shift in reduction peak potentials is seen, as outlined in Table 2.4.

Table 2.4 – Comparison of QD electron injection potentials for a series of different QDs.

QD (nm)	First reduction peak / V vs. Ag/AgCl	Second reduction peak / V vs. Ag/AgCl
560	-1.70	-1.90
640	-1.55	-1.85
800	-1.50	-1.80

Combining these results confirms that the observed reduction processes are associated with electron injection into the QDs, with an increasing energy requirement for these processes as QD size decreases and the $1S(e)$ level (the lowest unoccupied molecular orbital – LUMO) becomes more energetic. Interestingly, QD composition appears to have little effect on the observed

electrochemical behaviour, particularly when compared to size effects. The 560 and 640 nm QDs comprised a CdSe/ZnS core-shell composition, whereas the 800 nm QDs were CdSeTe/ZnS. The presence of Te in these QDs is required to decrease E_g into the NIR region. It does not appear to have any significant influence on the redox behaviour of the QDs, as shown by the similar electrochemical behaviour for all investigated QDs.

The onset of the first reduction process can be used to infer the QD LUMO energy as it is related to the energy required to populate the first discrete energy level in the conduction band (the LUMO).²⁵ This gives values of -3.04, -3.19 and -3.29 eV for 560, 640 and 800 nm QDs respectively (the energy level of Ag/AgCl in a vacuum is calculated as -4.74 eV).^{26, 27} These values are more energetic than expected for QDs of this size,^{25, 27} which suggests CV may not be detecting a lower energy electron transfer event.

2.3.2.2 DPV

As a more sensitive method for electrochemical characterisation than CV, DPV was used to probe the redox behaviour of QDs. Figure 2.14 shows the anodic voltammograms for a blank electrode and a QD/chitosan composite film observed utilising DPV.

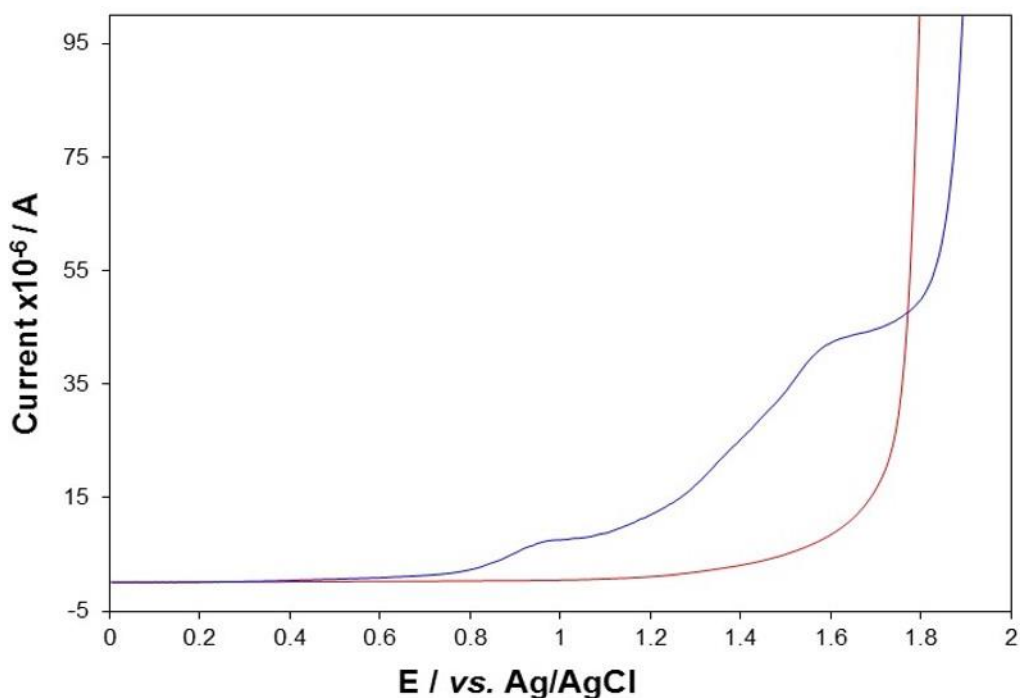
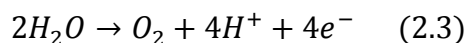


Figure 2.13 - Current response for a blank GC electrode (red) and a 800 nm QD/chitosan film (blue) over the potential range $0 \text{ V} \leq v \leq 2 \text{ V}$ vs. Ag/AgCl in 0.1 M PBS.

The profile for the blank electrode contains no peaks, with O_2 evolution through oxidation of water (equation (2.3)) resulting in the sharp increase in current at higher potentials.



Introduction of the QD film into the system yields two oxidative peaks. Onset of peak 1 occurs at 0.75 V, reaching a maximum at 0.95 V and onset of peak 2 occurs at approximately 1.40 V, reaching a maximum at 1.55 V. These peaks are likely related to the removal of an electron (hole injection) from the 1S(h) energy level of the core (the highest occupied molecular orbital – HOMO) and from an energy level lower in the valence band respectively.

The cathodic voltammograms from DPV of a blank electrode and QD/chitosan film are shown in Figure 2.15.

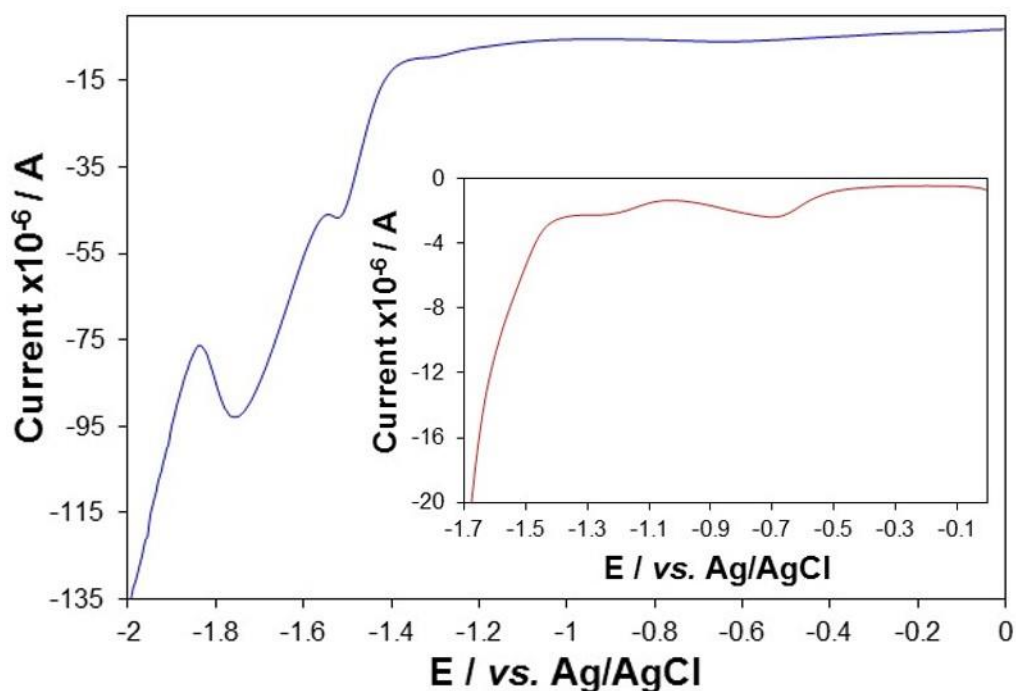
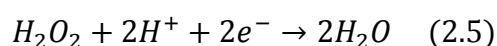
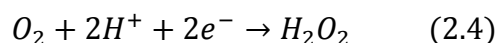


Figure 2.14 - Current response for a blank GC electrode (inset, red) and a 800 nm QD/chitosan film (blue) over the potential range $-2 \text{ V} \leq v \leq 0 \text{ V}$ vs. Ag/AgCl in 0.1 M PBS.

The cathodic profile of the blank GC electrode contained two reduction peaks at -0.65 V and -1.20 V respectively. The initial peak diminishes upon de-aeration (Figure 2.16), indicating it is related to O_2 reduction at the electrode surface. The peak at -1.20 V increases dramatically in intensity following addition of H_2O_2 to the system (Figure 2.17). This peak is linked to the 1-electron reduction of H_2O_2 to form hydroxyl radical (OH^\bullet) and OH^- , which is analogous to the Fenton reaction and has been observed at a GC electrode at a similar potential previously.²⁸ The presence of OH^\bullet as a product of H_2O_2 reduction has been confirmed by Imamura *et al.*²⁹ The appearance of this peak prior to addition of H_2O_2 suggests that O_2 reduction is occurring via the 2-electron pathway, with H_2O_2 being produced as an intermediate (equations (2.4) and (2.5)).



At approximately -1.40 V, the overpotential for water reduction results in H₂ evolution and a rapid increase in the voltammetric current (equation (2.6)).

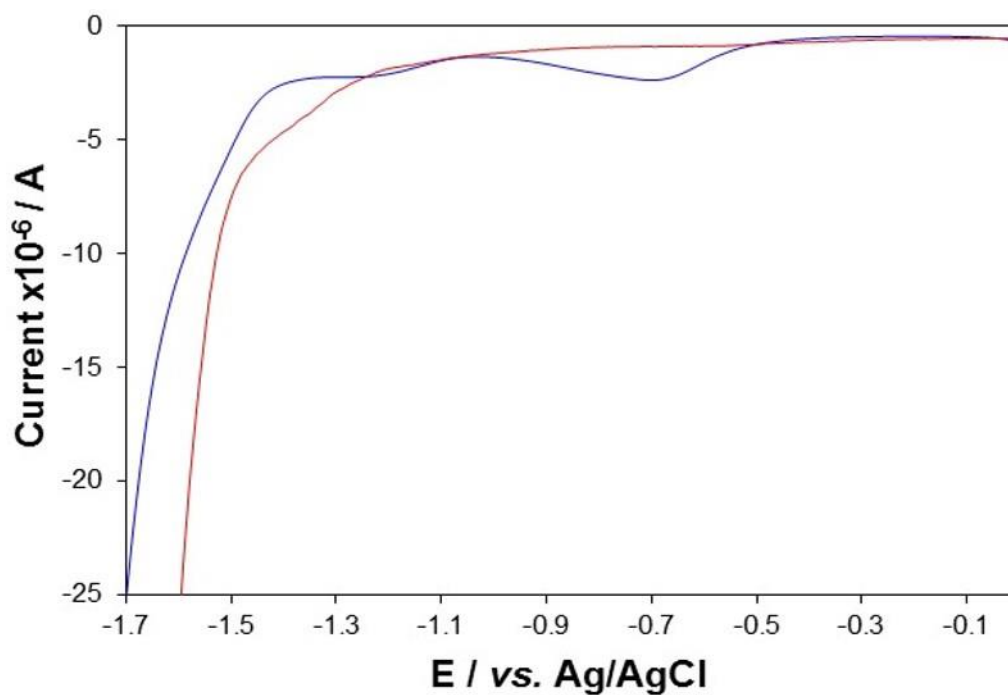
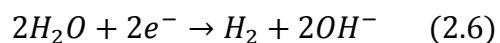


Figure 2.15 - Current response for a 800 nm QD/chitosan film in 0.1 M PBS (blue) and following de-aeration (red) over the potential range $-1.7 \text{ V} \leq v \leq 0 \text{ V}$ vs. Ag/AgCl.

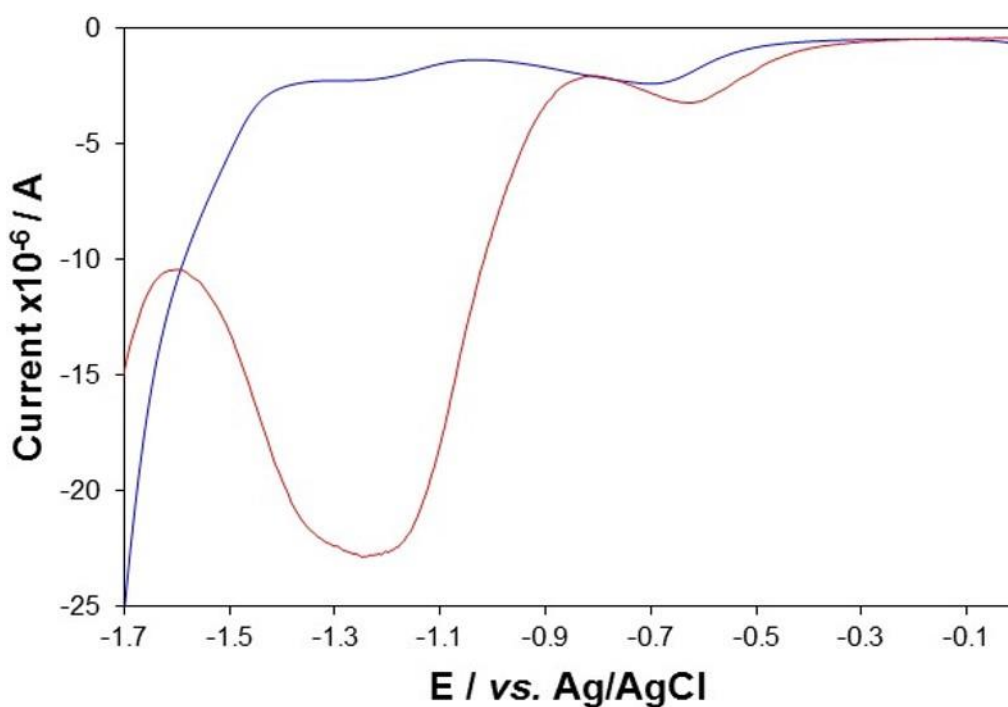


Figure 2.16 - Current response for a 800 nm QD/chitosan film in 0.1 M PBS (blue) and in 10 mM H₂O₂ (red) over the potential range $-1.7 \text{ V} \leq v \leq 0 \text{ V}$ vs. Ag/AgCl.

Modification of the GC electrode with the QD film yields two additional reduction peaks at approximately -1.45 V and -1.70 V (Figure 2.15). These are in good agreement with those seen in the voltammograms from CV (Figure 2.10) and are linked to single and multiple electron injection into the conduction band energy levels of the QDs. This was confirmed through a DPV investigation of a series of QDs (560, 640 and 800 nm), which should exhibit an increase in reduction potentials as QD size decreases (Figure 2.18)

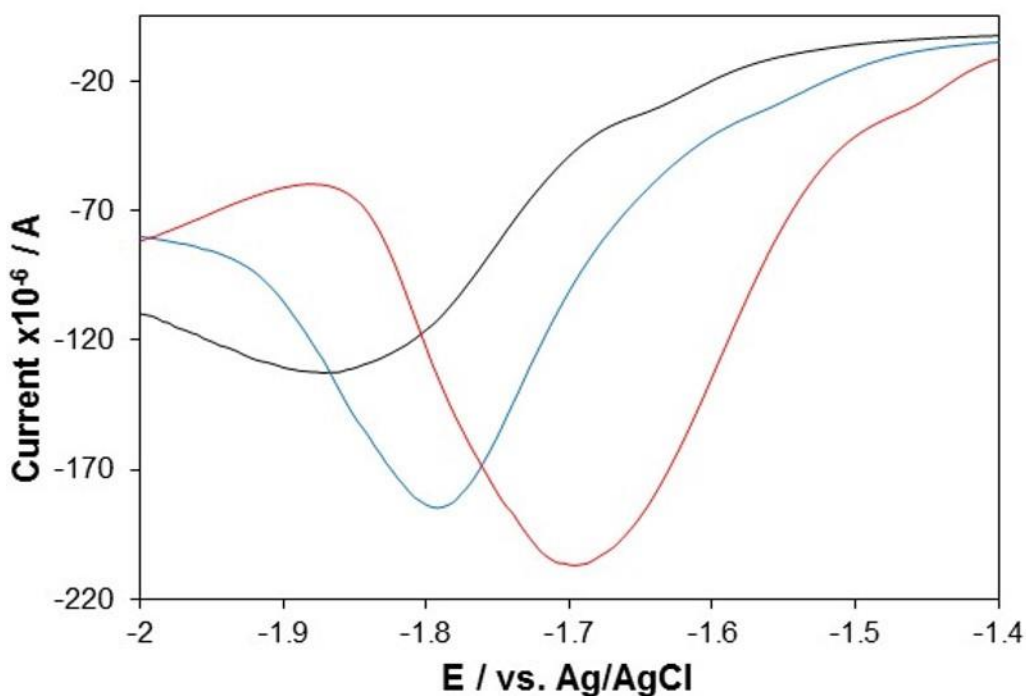


Figure 2.17 - Current response for 800 (red), 640 (blue) and 560 (black) nm QDs over the potential range $-2 \text{ V} \leq v \leq -1.3 \text{ V}$ vs. Ag/AgCl in 0.1 M PBS.

A shift in the reduction peak to -1.55 V and -1.65 V for the 640 and 560 nm QDs respectively was observed. Additionally, the peak at -1.70 V shifts by approximately 0.10 V for each decrease in QD size. These results corroborate those attained using CV, and strongly link these peaks to QD electron injection processes.

From these results, the quasi-particle gap can be calculated from the NIR QD redox potentials.³⁰ The onset of the lowest reduction and oxidation potentials that could be attributed to the NIR QDs and the resulting quasi-particle gap is outlined in Table 2.5.

Table 2.5 - Reduction and oxidation onset potentials and calculated quasi-particle gap for a series of QDs.

QD / nm	Reduction peak onset / V vs./AgCl	E_{LUMO} / eV	Oxidation peak onset / V vs./AgCl	E_{HOMO} / eV	quasi-particle gap / eV
800	-1.45	-3.29	0.75	-5.49	2.200

The estimated quasi-particle gap is significantly greater (0.63 eV) than the corresponding optical E_g . It is predicted that the quasi-particle gap is greater than the optical E_g as they are related through equation (2.7).³⁰

$$\text{Optical } E_g = \text{Quasi particle gap} - J_{e,h} \quad (2.7)$$

Where $J_{e,h}$ is the total coulomb interaction energy of the electron-hole pair.

This states that the quasi-particle gap calculated from the first cathodic and anodic peaks will include a coulombic interaction energy term (from the exciton binding energy). Using this equation and the values predicted for E_g and the quasi-particle gap, the value for $J_{e,h}$ was estimated at 0.63 eV, which is considerably greater than expected.³⁰ This indicated that the reduction or oxidation potentials used for this calculation are not representative of electron/hole injection into the 1S(e) and 1S(h) orbitals, resulting in an over-estimation of the quasi-particle gap, and HOMO and LUMO energies that are not verified and unlikely to be representative of their true values. Previous works^{25, 31, 32} have had difficulty in visualising QD reduction processes using voltammetric techniques, which could explain the discrepancies observed in this data.

2.4 Conclusions

Optical and electrochemical characterisation of NIR QDs was carried out and compared with QDs that emit in the visible region, demonstrating the size-dependent nature of these properties. Confirmation of optically-induced and ECL emission in the NIR region was achieved and used to estimate the optical E_g of these QDs. This can be used to help assess the energetics involved in future QD ECL mechanisms. ECL emission was shown to originate from the QD core, which is ideal for bioanalytical applications where surface modifications can influence the presence of surface states but not the electronic structure of the QD core.

CV and DPV were used to investigate the redox behaviour of the QDs, which was shown to be dependent upon particle size. These processes were related to electron and hole injection into quantum confined orbitals of the QDs and used to estimate their HOMO and LUMO energies. Comparison of the optical E_g with the estimated value of the quasi-particle gap indicated that additional QD redox processes were likely occurring that could not be detected using CV or DPV, a problem that has been encountered previously. An alternative method for predicting the energetics of the HOMO and LUMO was therefore required.

The data gathered in this work will be used to correlate the ECL behaviour of NIR QDs with their electronic structure and electrochemical properties. It has also confirmed that ECL emission is within the NIR region and originated from the QD core, rather than surface states.

2.5 References

1. W. Cai, D.-W. Shin, K. Chen, O. Gheysens, Q. Cao, S. X. Wang, S. S. Gambhir and X. Chen, *Nano letters*, 2006, **6**, 669-676.
2. X. Gao, Y. Cui, R. M. Levenson, L. W. Chung and S. Nie, *Nature biotechnology*, 2004, **22**, 969-976.
3. S. Kim, Y. T. Lim, E. G. Soltesz, A. M. De Grand, J. Lee, A. Nakayama, J. A. Parker, T. Mihaljevic, R. G. Laurence and D. M. Dor, *Nature biotechnology*, 2003, **22**, 93-97.
4. E. G. Soltesz, S. Kim, R. G. Laurence, A. M. DeGrand, C. P. Parungo, D. M. Dor, L. H. Cohn, M. G. Bawendi, J. V. Frangioni and T. Mihaljevic, *The Annals of thoracic surgery*, 2005, **79**, 269-277.
5. C. Woelfle and R. O. Claus, *Nanotechnology*, 2007, **18**, 025402.
6. U. Woggon, 2014.
7. L. Technologies, *Qdot 800 ITK Organic Quantum Dots*, <http://www.lifetechnologies.com/order/catalog/product/Q21771MP>, Accessed 20/08, 2014.
8. E. Z. Chong, D. R. Matthews, H. D. Summers, K. L. Njoh, R. J. Errington and P. J. Smith, *Journal of Biomedicine and Biotechnology*, 2007, **2007**, 1-7.
9. T. Pradeep, *Nano: the essentials*, Tata McGraw-Hill Education, 2007.
10. A. Barron, *Physical Methods in Chemistry and Nano Science*, http://cnx.org/content/col10699/1.20/content_info#cnx_cite_header, Accessed 30th July, 2014.
11. M. O. Manasreh, *Introduction to Nanomaterials and Devices*, 1st edn., John Wiley & Sons, Hoboken, New Jersey, 2012.
12. J. M. Elward and A. Chakraborty, *Journal of Chemical Theory and Computation*, 2013, **9**, 4351-4359.
13. G. Konstantatos and E. H. Sargent, *Colloidal Quantum Dot Optoelectronics and Photovoltaics*, Cambridge University Press, 2013.
14. L. K. Banyai, S.W., *Semiconductor Quantum Dots*, World Scientific Publishing Co., Singapore, 1993.
15. I. L. Medintz, H. T. Uyeda, E. R. Goldman and H. Mattoussi, *Nature materials*, 2005, **4**, 435-446.
16. A. J. Bard, *Electrogenerated Chemiluminescence*, Marcel Dekker, Inc., New York, 2004.
17. Z. Ding, B. M. Quinn, S. K. Haram, L. E. Pell, B. A. Korgel and A. J. Bard, *Science*, 2002, **296**, 1293-1297.
18. N. Myung, Y. Bae and A. J. Bard, *Nano Letters*, 2003, **3**, 1053-1055.
19. L. Dennany, E. J. O'Reilly, P. C. Innis, G. G. Wallace and R. J. Forster, *Electrochimica Acta*, 2008, **53**, 4599-4605.
20. L. Dennany, M. Gerlach, S. O'Carroll, T. E. Keyes, R. J. Forster and P. Bertoncello, *Journal of Materials Chemistry*, 2011, **21**, 13984-13990.
21. J. G. Vos, R. J. Forster and T. E. Keyes, *Interfacial Supramolecular Assemblies*, Wiley, 2003.
22. J. Qu, Y. Shen, X. Qu and S. Dong, *Chemical Communications*, 2004, **1**, 34-35.
23. S. K. Haram, B. M. Quinn and A. J. Bard, *Journal of the American Chemical Society*, 2001, **123**, 8860-8861.

24. S. Chen, L. A. Truax and J. M. Sommers, *Chemistry of materials*, 2000, **12**, 3864-3870.
25. Y. Wang, Z. Xie, G. Gotesman, L. Wang, B. P. Bloom, T. Z. Markus, D. Oron, R. Naaman and D. H. Waldeck, *The Journal of Physical Chemistry C*, 2012, **116**, 17464-17472.
26. B.-R. Hyun, Y.-W. Zhong, A. C. Bartnik, L. Sun, H. D. Abruna, F. W. Wise, J. D. Goodreau, J. R. Matthews, T. M. Leslie and N. F. Borrelli, *ACS Nano*, 2008, **2**, 2206-2212.
27. L. Bao, L. Sun, Z.-L. Zhang, P. Jiang, F. W. Wise, H. c. D. Abruña and D.-W. Pang, *The Journal of Physical Chemistry C*, 2011, **115**, 18822-18828.
28. J.-P. Choi and A. J. Bard, *Analytica chimica acta*, 2005, **541**, 141-148.
29. K. Imamura, Y. Tada, H. Tanaka, T. Sakiyama and K. Nakanishi, *Journal of colloid and interface science*, 2002, **250**, 409-414.
30. M. Amelia, C. Lincheneau, S. Silvi and A. Credi, *Chemical Society Reviews*, 2012, **41**, 5728-5743.
31. N. Myung, Z. Ding and A. J. Bard, *Nano Letters*, 2002, **2**, 1315-1319.
32. G. Zotti, B. Vercelli, A. Berlin, P. T. K. Chin and U. Giovanella, *Chemistry of Materials*, 2009, **21**, 2258-2271.

*Chapter 3 - Electrogenenerated chemiluminescent
behaviour of 800 nm CdSeTe/ZnS quantum dots*

3.1 Introduction

Originally, ECL investigations focused on ruthenium complexes that displayed intense, stable signals in both organic and aqueous media.¹⁻⁴ Following the discovery of ECL emission from silicon QDs,⁵ the focus of investigations shifted towards nanomaterials that displayed size-tunable emission and enhanced optical and electronic properties.⁶ The vast majority of these works focused on materials that emitted in the visible region, resulting in a good understanding of the ECL behaviour of these materials.

The ECL of visible region QDs has been studied extensively, which have been shown to produce an ECL response with a variety of co-reactants.⁷⁻¹⁰ This has allowed the development of a number of ECL biosensors that use visible region QDs as labels.¹¹⁻¹⁴ NIR QDs are of increasing interest owing to their emission wavelength that lies outside the absorption range of biological fluids and tissue. Currently, no such investigations into the behaviour of NIR QDs in different systems have been carried out, with the majority of work focused on cathodic NIR ECL with potassium persulfate co-reactant.¹⁵⁻¹⁷ Only a single example exists of anodic NIR ECL¹⁸ and there are currently no documented ECL systems that utilise NIR emitting QDs with no additional co-reactant (termed co-reactant free systems in all future work). Therefore, the ECL characteristics of these QDs have not been determined in a variety of systems, which has prevented a full understanding of their ECL behaviour. Investigation into these properties should supplement the electrochemical characterisation of these QDs and could aid in the development of a greater variety of NIR ECL biosensors.

The aim of this work was to investigate the ECL characteristics of NIR QDs in a variety of co-reactant systems and determine the likely mechanisms of their response.

3.2 Experimental

3.2.1 Apparatus

Electrochemical measurements were carried out using a CH instrument model 760D electrochemical analyser. All experiments were carried out using a conventional three-electrode assembly, consisting of a 3 mm diameter GC working electrode, Pt wire counter electrode and Ag/AgCl reference electrode. GC electrodes were cleaned by successive polishing using 1, 0.3 and 0.05 μM alumina slurry, followed by sonication in ethanol and water, respectively, for 30 mins. The electrodes were then dried under a flow of N_2 gas. CV was carried out at a scan rate of 100 mV s^{-1} and sample interval of 1 mV across a potential range outlined in each figure. Measurements involving simultaneous detection of light and current utilised a CH instrument model 760D connected to a Hamamatsu H10723-20 PMT. The input voltage to the PMT was + 5 V and the control voltage was set between 0.5 and 1.05 V depending on the required sensitivity. During electrochemical experiments, the cell was kept in a light-tight Faraday cage in a specially designed holder configuration where the working electrode was positioned directly above the PMT window. All measurements were made at room temperature.

3.2.2 Materials

Core-shell CdSeTe/ZnS QDs (Qdot® 800 ITK™ organic quantum dots, 1 μM in decane) were purchased from Invitrogen. Core-shell CdSe/ZnS QDs (Lumidot™ 560 and 640 nm QDs, 5 mg/mL in toluene), chitosan (medium molecular weight, 75-85% de-acetylated), phosphate buffered saline (PBS, pH 7.4), 2-(dimethylamino)ethanethiol (DAET), hydrogen peroxide (H_2O_2), tripropylamine (TPA), potassium persulfate ($\text{K}_2\text{S}_2\text{O}_8$) and sodium oxalate ($\text{Na}_2\text{C}_2\text{O}_4$) were all purchased from Sigma-Aldrich and used as received. All other reagents used were of analytical grade, and all solutions were prepared in milli-Q water (18 $\text{m}\Omega \text{ cm}$).

3.2.3 Methods

Preparation of water soluble CdSeTe/ZnS core-shell QDs

The method followed was similar to that developed by Woelfle and Claus.¹⁹ 0.5 mL of 0.5 M DAET in methanol was mixed with 0.25 mL of the CdSeTe/ZnS QDs in decane (1 μ M). N₂ was bubbled through the solution for 5 mins, which was then sealed and left stirring overnight at room temperature in the dark. The QDs were then precipitated with an excess of acetone followed by centrifugation at 5000 rpm for 6 mins. The filtrate was removed and the precipitate was re-dispersed in 0.25 mL of distilled water. These water-soluble QDs were centrifuged for a further 6 mins at 3000 rpm to remove any impurities and then stored in darkness at 4°C.

Preparation of CdSeTe/ZnS core-shell QD-chitosan composite films

A 0.1 % chitosan solution was prepared in 1 % acetic acid and sonicated for 5 mins. The QD/chitosan composite was prepared by mixing aliquots of the water-soluble QDs with the chitosan solution in a 1:1 (v/v) ratio and mixing for 30 s. 3 μ L of this composite was then carefully cast onto the electroactive portion of a GC electrode, with mixing of the composite for 10 s between electrodes.

Preparation of co-reactant solutions

Co-reactant solutions of TPA, Na₂C₂O₄, H₂O₂ and K₂S₂O₈ were prepared in 0.1 M PBS (pH 7.4) at the concentrations outlined in each figure. Co-reactant free experiments were carried out in 0.1 M PBS (pH 7.4) only.

3.3 Estimation of QD HOMO and LUMO energy levels

The onset of QD oxidation and reduction has previously been used to estimate the HOMO-LUMO gap,^{5, 20} also known as the quasi-particle gap. Previous work (section 2.3.2.2) has shown that the quasi-particle gap estimated in this way was not reliable, as the true oxidation and reduction potentials of the QDs could not be detected. Therefore, it was proposed that the onset potential for ECL could be used as a more accurate estimation of these potentials, as the rate-determining step for ECL generation is the oxidation or reduction of QDs. Figure 3.1 shows the anodic and cathodic ECL profiles of NIR QDs.

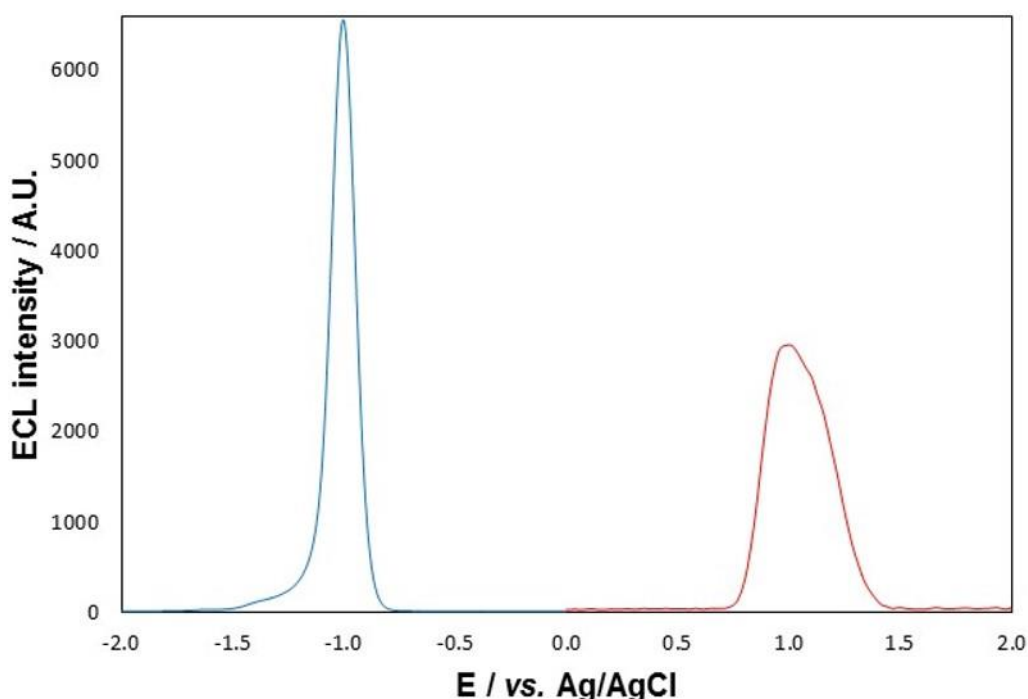


Figure 3.1 - ECL response of 800 nm QD/chitosan film in 1 mM TPA (red) and 1 mM $K_2S_2O_8$ (blue) at a scan rate of 100 mV s^{-1} over the potential range $-2 \leq v \leq 2 \text{ V vs. Ag/AgCl}$. PMT input voltage = 0.5 V.

The oxidative and reductive ECL onset potentials for the QDs and the HOMO-LUMO energy gap is shown in Table 3.1.

Table 3.1 – Reduction and oxidation ECL onset potentials and resulting HOMO-LUMO energy gap for a series of QDs.

QD / nm	Reduction ECL onset / V vs. Ag/AgCl	Oxidation ECL onset / V vs. Ag/AgCl	HOMO – LUMO energy gap / eV
800	-0.75	0.75	1.50

The estimated HOMO-LUMO energy gap of 800 nm QDs (1.50 eV) is in good agreement with the optical E_g (section 2.3.1.2) of 1.569 eV from optically-induced emission and 1.529 eV from ECL emission (section 2.3.1.3). This confirms that ECL emission is originating from the QD core. The proposed electronic structure of these NIR QDs is outlined in Figure 3.2. The HOMO and LUMO energy levels are calculated from the reduction and oxidation ECL onset potentials (the energy level of Ag/AgCl in a vacuum is calculated as -4.74 eV).^{21, 22}

HOMO energy is in excellent agreement with that obtained from DPV (section 2.3.2.2), whilst LUMO energy is 0.70 eV less energetic when using ECL onset potentials. This data suggests electron injection into the 1S(e) quantum confined orbital of the NIR QDs is taking place at a more positive potential than that observed using voltammetric techniques (sections 2.3.2.1 and 2.3.2.2). The similarity between optical E_g and the HOMO-LUMO energy gap calculated from ECL onset potentials suggests this method of electronic structure estimation is more accurate than that using CV or DPV and for that reason will be used for future data analysis.

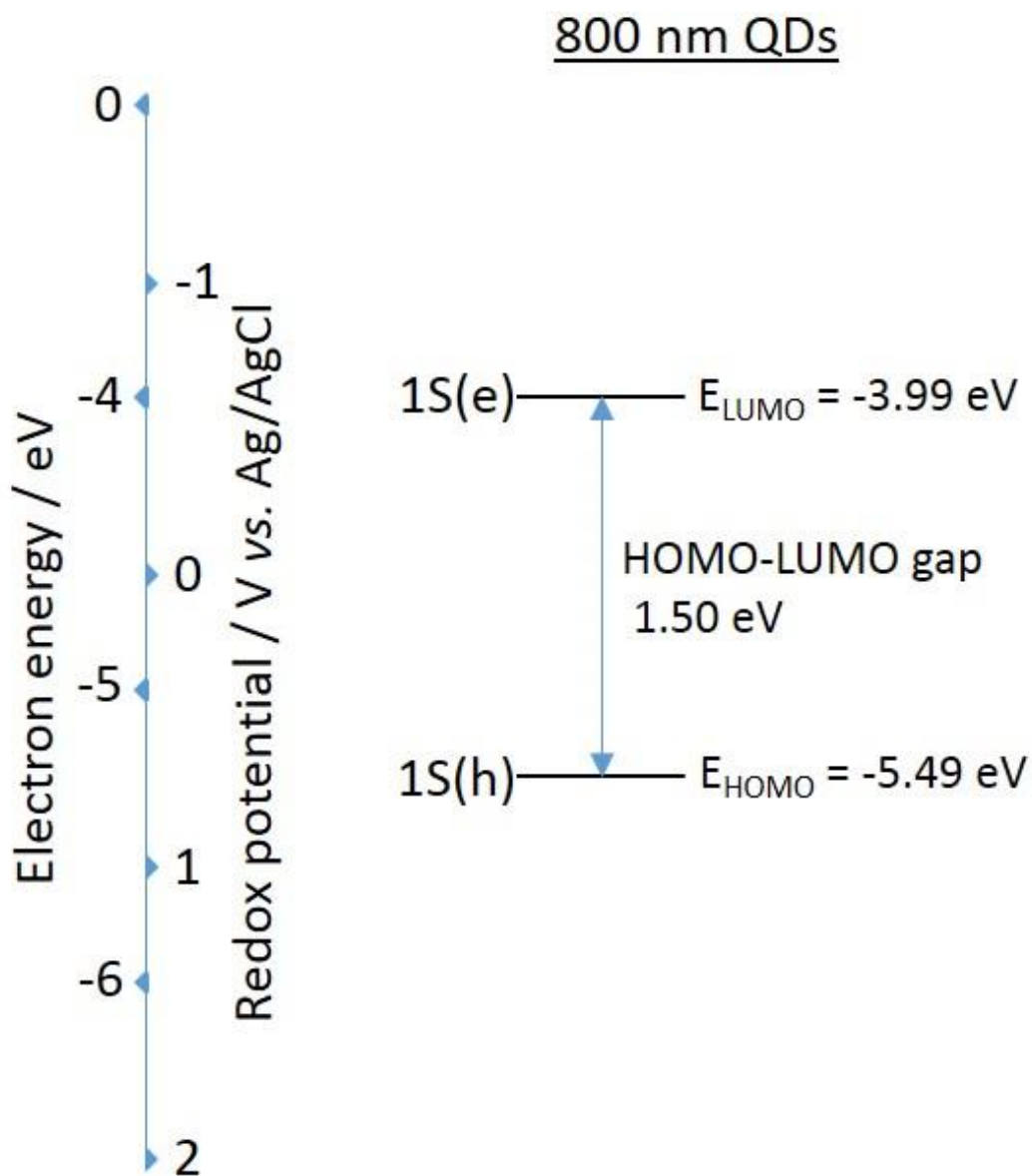


Figure 3.2 - Energy level diagram for 800 nm CdSeTe/ZnS QDs based on their reductive and oxidative ECL onset potentials and HOMO-LUMO energy gap.

3.4 ECL behaviour

3.4.1 Anodic ECL characteristics

Anodic ECL involves an oxidative-reductive system in which a hole is injected into the 1S(h) energy level of the QD through heterogeneous electron transfer with the electrode. This is followed by electron injection into the 1S(e) energy level of this charged particle via homogeneous electron transfer with a co-reactant that has sufficient reducing power. Tripropylamine (TPA) and sodium oxalate ($\text{Na}_2\text{C}_2\text{O}_4$) are typical anodic ECL co-reactants that have been studied extensively within ruthenium-containing systems.^{2, 3, 23-29} However, generation of an ECL signal between these co-reactants and NIR QDs has not yet been investigated. Figure 3.3 shows the ECL profile of NIR QDs with TPA and $\text{Na}_2\text{C}_2\text{O}_4$ co-reactants, as well as in a solution of 0.1 M PBS (co-reactant free system).

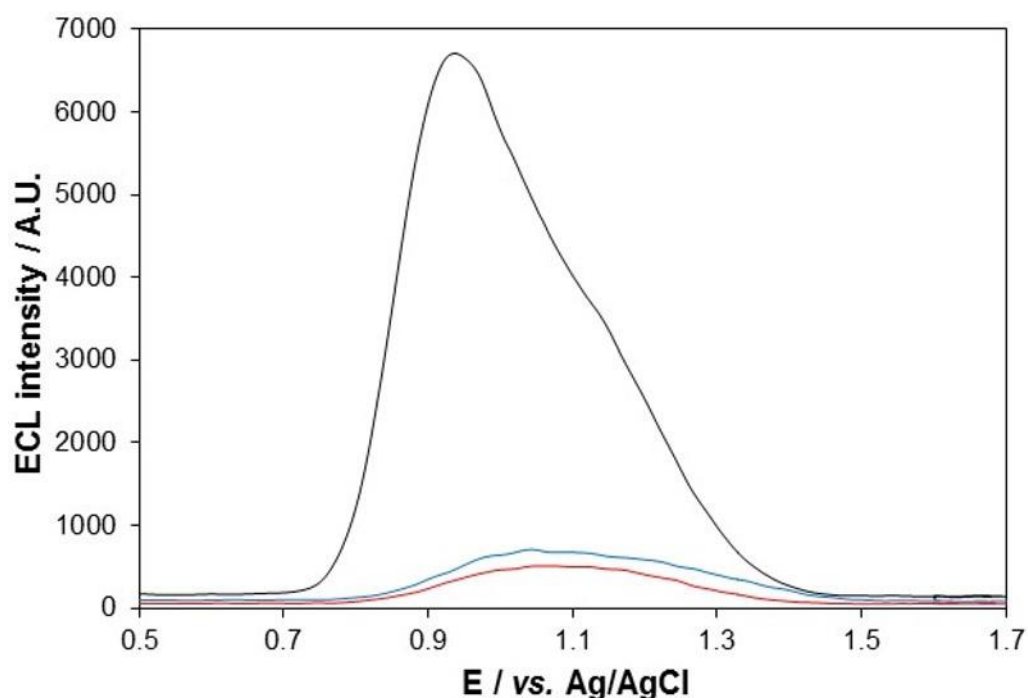


Figure 3.3 - ECL response of 800 nm QD/chitosan film in 0.1 M PBS (red) + 1mM $\text{Na}_2\text{C}_2\text{O}_4$ (blue) and + 1mM TPA (black) at a scan rate of 100 mV s^{-1} over the potential range $0.5 \leq v \leq 1.7 \text{ V vs. Ag/AgCl}$. PMT input voltage = 0.75 V.

Anodic ECL was observed in all solutions, with appearance of ECL at 0.75 V in TPA and 0.79 V in both Na₂C₂O₄ and PBS. This small shift in ECL onset is associated with the ability to directly oxidise TPA at the electrode surface, rather than requiring initial QD oxidation as with Na₂C₂O₄ and PBS. Maximum ECL intensity is at 0.93 and 1.05 V for TPA and Na₂C₂O₄/PBS respectively. ECL intensity is almost 10 times greater using TPA compared to Na₂C₂O₄, which is itself only just discernable from the background ECL response.

3.4.1.1 Elucidation of anodic ECL mechanisms

PBS co-reactant pathway

Superoxide anion, O₂^{•-}, a reactive oxygen species (ROS) formed through 1-electron reduction of O₂, has previously been shown to generate anodic ECL in PBS at indium tin oxide (ITO) electrodes,^{30,31} suggesting this as a possible route for this system. To confirm the role of O₂ in this ECL mechanism, the effect of de-aeration on the ECL response was monitored (Figure 3.4).

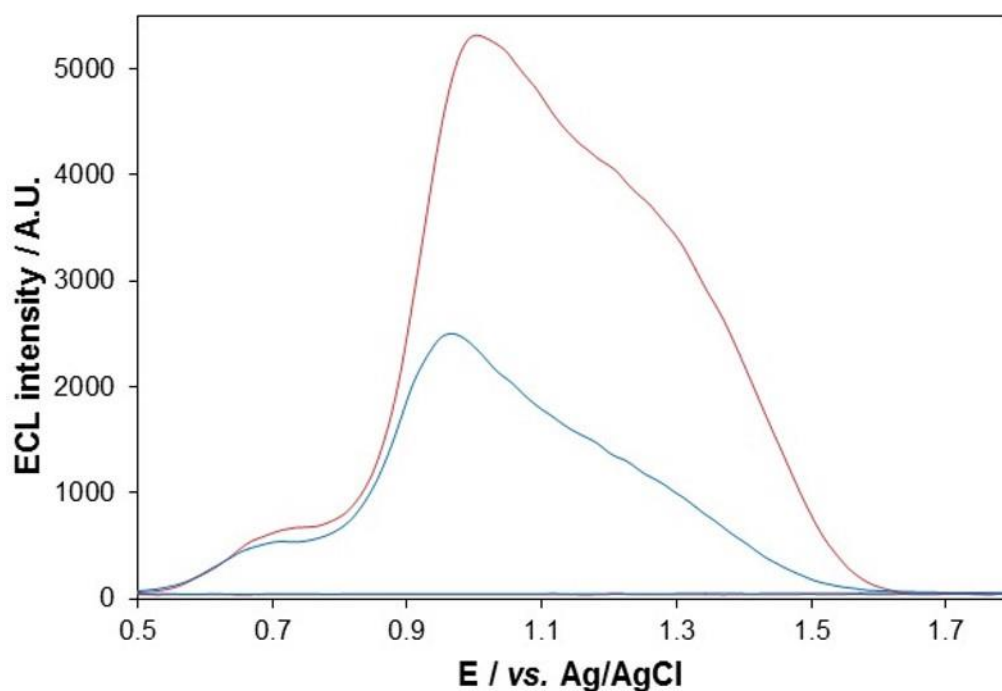


Figure 3.4 - ECL response of 800 nm QD/chitosan film in 0.1 M PBS (red) and after de-aeration for 30 mins (blue) at a scan rate of 100 mV s^{-1} over the potential range $0.5 \leq v \leq 1.8 \text{ V vs. Ag/AgCl}$. PMT input voltage = 0.70 V.

Purging with N_2 for 30 mins results in a significant decrease in ECL intensity, linking O_2 to ECL production with the NIR QDs. Complete loss of response is not observed due to confinement of O_2 within the QD/chitosan film. Superoxide dismutase (SOD), an efficient quencher of $\text{O}_2^{\cdot-}$,³² was added to PBS to confirm its role as the reducing agent in this system (Figure 3.5).

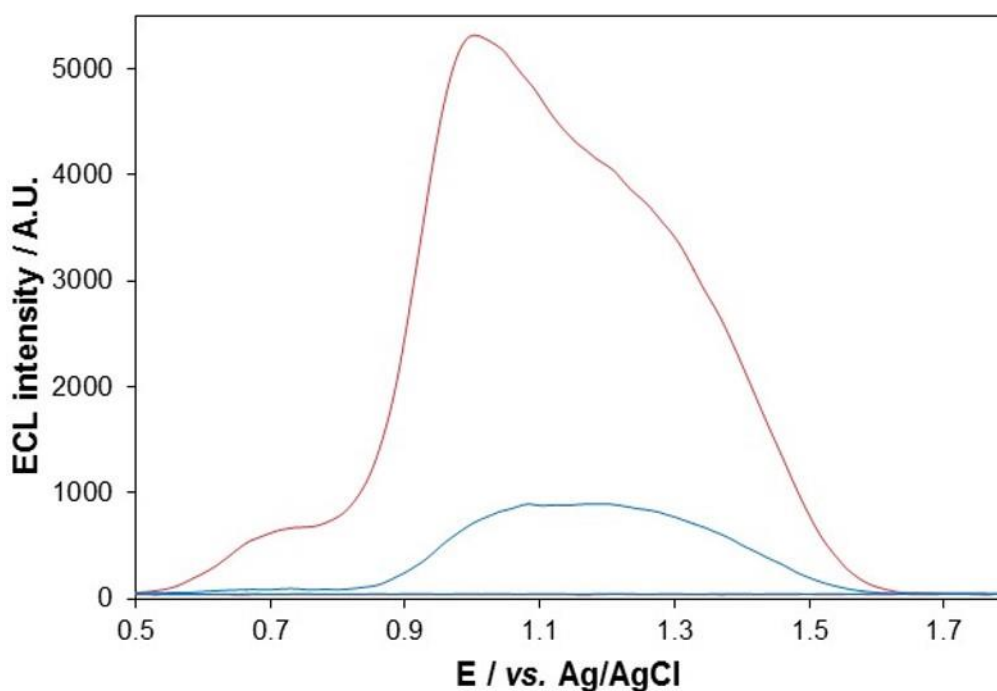
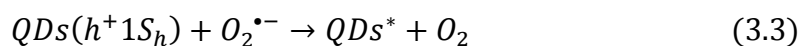
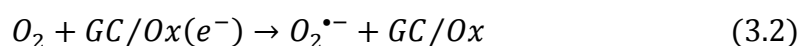
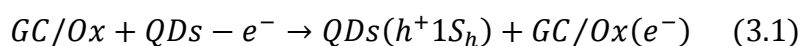


Figure 3.5 - ECL response of 800 nm QD/chitosan film in 0.1 M PBS (red) and after addition of 0.46 mg/mL SOD (blue) at a scan rate of 100 mV s^{-1} over the potential range $0.5 \leq v \leq 1.8 \text{ V vs. Ag/AgCl}$. PMT input voltage = 0.70 V.

Addition of SOD resulted in a substantial inhibition of ECL production, confirming $\text{O}_2^{\bullet-}$ as the species capable of injecting an electron into the $1\text{S}(e)$ energy level of the oxidised QDs, resulting in ECL emission. The formation of $\text{O}_2^{\bullet-}$ and mechanism of ECL generation are outlined in equations (3.1)-(3.4).



Production of $\text{O}_2^{\bullet-}$ is thought to occur via oxides on the surface of the GC electrode. Oxidation of QDs gives rise to electron injection into these surface oxides (equation (3.1)), which can then be transferred to O_2 forming $\text{O}_2^{\bullet-}$ (equation (3.2)), a process similar to that seen with ITO electrodes.³¹ $\text{O}_2^{\bullet-}$ can then inject an electron into the $1\text{S}(e)$ energy level of $\text{QDs}(h^+(1\text{S}_h))$ to form excited state QDs (equation (3.3)) that emit an ECL signal (equation (3.4)).

The energetics of this process are shown in Figure 3.6 and are based on a standard redox potential of the $O_2^{\bullet-}/O_2$ couple of -0.57 V (vs. Ag/AgCl).²²

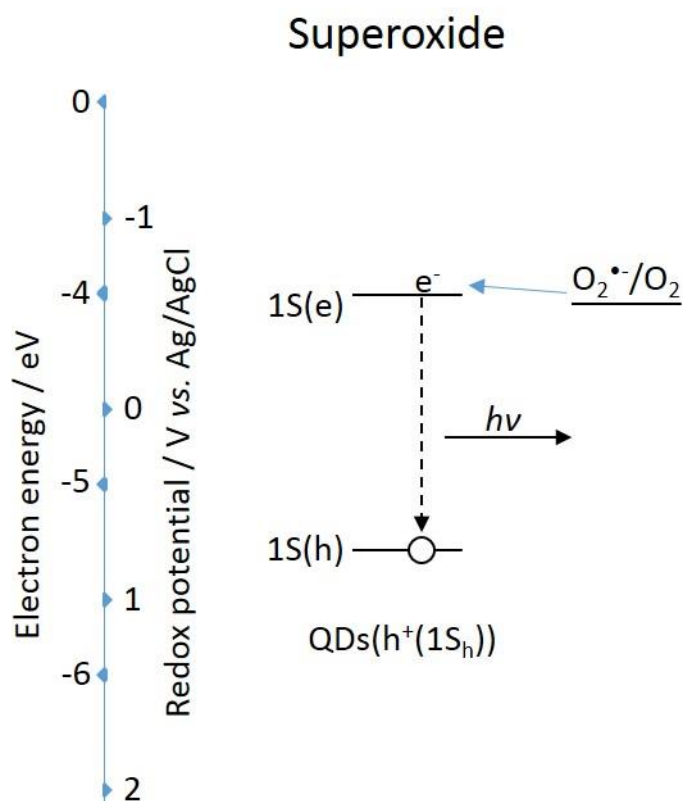
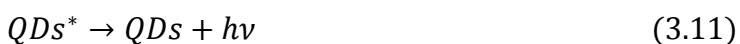
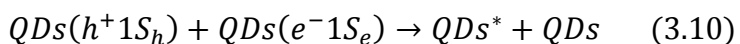
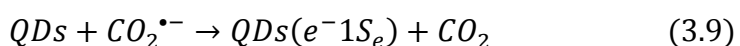
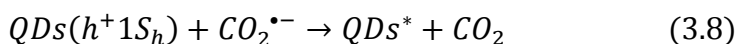
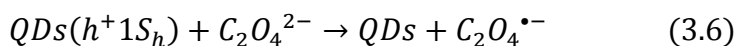


Figure 3.6 - Significant energy level interactions and resulting ECL process of 800 nm QDs with superoxide.

The very similar energetics of the QD LUMO level and $O_2^{\bullet-}/O_2$ couple suggest that electron transfer between them would not be an efficient process, however, an ECL response is observed. The slow electron transfer kinetics of this process manifests itself in a weak ECL signal that appears at a higher potential than that with TPA co-reactant. The closeness in energy between the $O_2^{\bullet-}/O_2$ couple and the QD LUMO level suggest that an ST type route may be involved in excited state formation. Alternatively, another ROS species could be taking part that is more capable of injecting an electron into the QD LUMO, however, the nature of this species is currently unknown. It must also be noted that E_{LUMO} is an estimated value and may be subject to error.

Na₂C₂O₄ co-reactant pathway

The mechanism for ECL generation with Na₂C₂O₄ involves CO₂^{•-}, a strong reducing agent formed through oxidation of C₂O₄²⁻.²⁴ The NIR QD-oxalate ECL pathway is outlined in equation (3.5)-(3.11).²⁴



Initially, QDs are oxidised through removal of an electron from the 1S(h) quantum confined orbital to produce a hole-injected QD, QDs(h⁺(1S_h)) (equation (3.5)), which is capable of oxidising oxalate into its radical anion form (equation (3.6)). This undergoes rapid decomposition to form CO₂^{•-} (equation (3.7)), a strongly reducing anion radical that injects an electron into the 1S(e) energy level of QDs(h⁺(1S_h)) to form an excited state QD (equation (3.8)), or injects an electron into an uncharged QD to create an electron-injected QD, QDs(e⁻(1S_e)) (equation (3.9)). This can then recombine with QDs(h⁺(1S_h)) to create an excited state QD (equation 3.10) that can emit light (equation (3.11)). The energetics of electron transfer in this process are shown in Figure 3.7 and are based on a standard redox potential of the CO₂^{•-}/CO₂ couple of approximately -2 V (vs. Ag/AgCl).³³

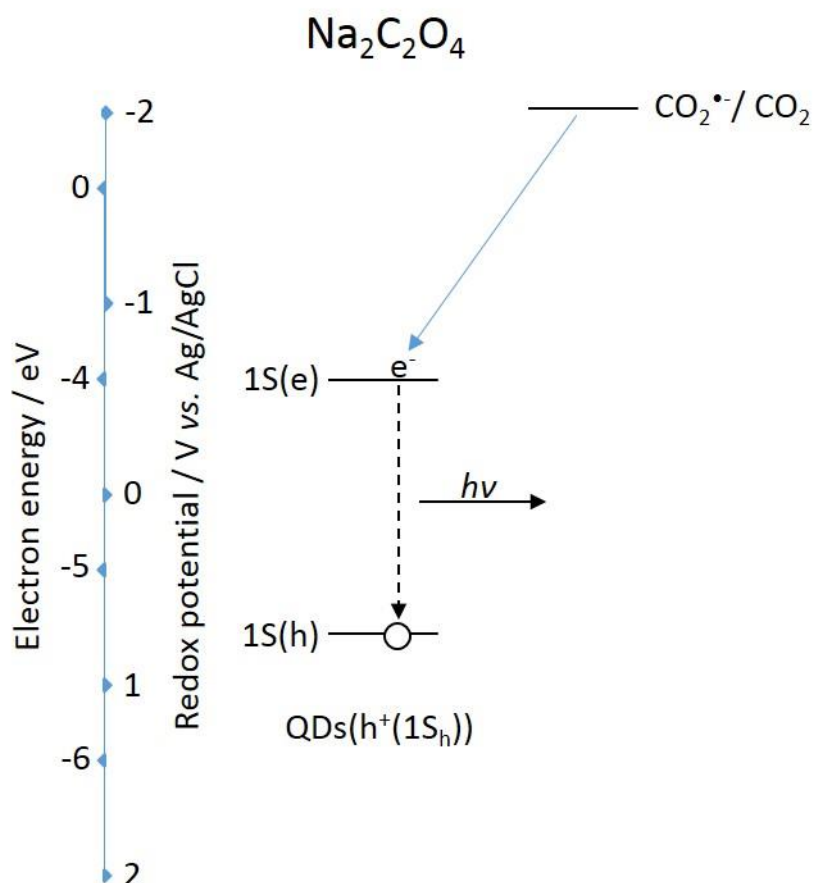


Figure 3.7 - Significant energy level interactions and resulting ECL process of 800 nm QDs with $\text{Na}_2\text{C}_2\text{O}_4$ co-reactant.

This demonstrates the strong reducing ability of $\text{CO}_2^{\bullet-}$, which can easily inject an electron into the 1S(e) orbital of $\text{QDs}(\text{h}^+(1\text{S}_\text{h}))$ for generation of the excited state species. The reducing strength of this couple is significantly greater than that of the $\text{O}_2^{\bullet-}/\text{O}_2$ couple (Figure 3.6) and so electron transfer kinetics and subsequent intensity of ECL should be greater with this system. However, their ECL intensities are very similar and this is caused by slow kinetics of direct $\text{Na}_2\text{C}_2\text{O}_4$ oxidation at the electrode surface.^{3, 34} Additionally, any $\text{CO}_2^{\bullet-}$ formed through direct oxidation of $\text{C}_2\text{O}_4^{2-}$ at the electrode surface would be unlikely to participate in the ECL process because it is a much stronger reducing agent than $\text{C}_2\text{O}_4^{2-}$, and would be rapidly oxidised to CO_2 through transfer of an electron to the electrode.^{24, 35} Therefore, the major route of $\text{C}_2\text{O}_4^{2-}$ oxidation to form $\text{CO}_2^{\bullet-}$ is through electron transfer with $\text{QDs}(\text{h}^+(1\text{S}_\text{h}))$ in the diffusion layer

surrounding the electrode surface, which produces ground state QDs as a by-product (equation (3.6)). This will cause a decrease in ECL intensity as consumption of $\text{QDs}(\text{h}^+(1\text{S}_\text{h}))$ during co-reactant oxidation will reduce the concentration of this ECL precursor at the electrode surface. Additionally, the concentration of $\text{CO}_2^{\cdot-}$ will be limited as it cannot be produced directly at the electrode surface. For these reasons, the ECL signal generated with $\text{Na}_2\text{C}_2\text{O}_4$ co-reactant has a very similar intensity to the co-reactant free system and is significantly weaker than the QD/TPA system. The lack of any additional oxidation peaks in the QD/chitosan voltammogram with $\text{Na}_2\text{C}_2\text{O}_4$ confirms direct oxidation of the co-reactant is not occurring to any appreciable extent at the electrode surface (Figure 3.8).

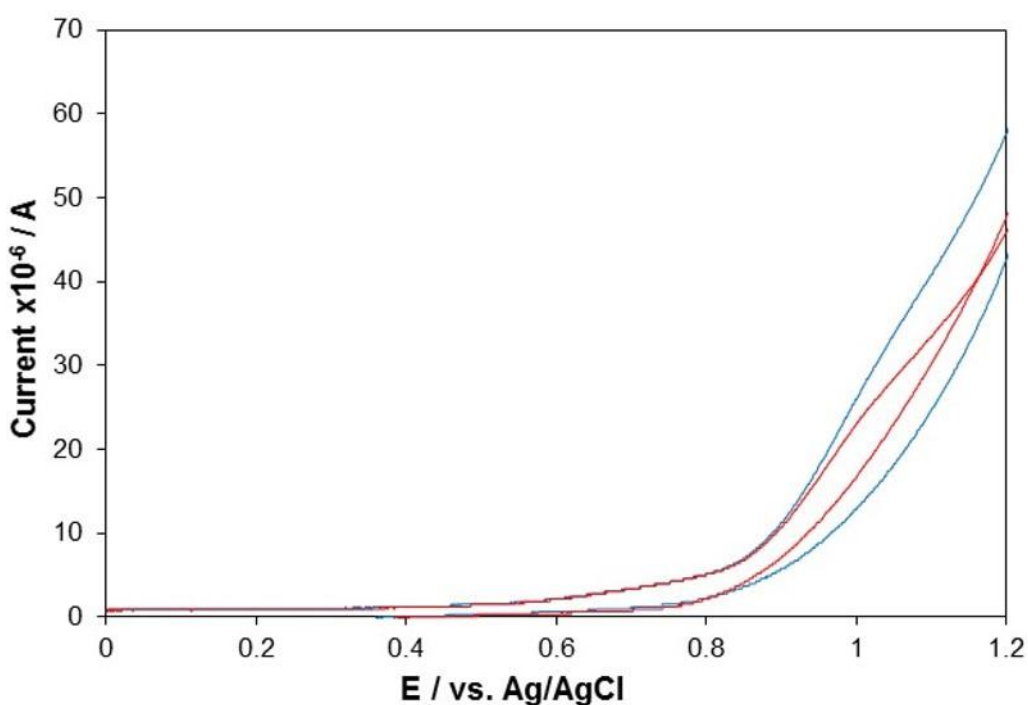
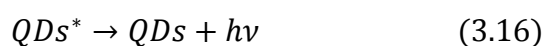
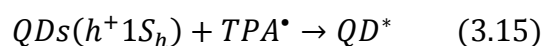
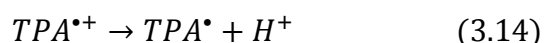
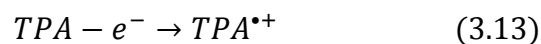
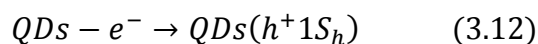


Figure 3.8 - Current response of 800 nm QD/chitosan film in 0.1 M PBS (red) and following addition of 1 mM $\text{Na}_2\text{C}_2\text{O}_4$ (blue) at a scan rate of 100 mV s^{-1} over the potential range $0 \text{ V} \leq v \leq 1.2 \text{ V vs. Ag/AgCl}$.

This explains the increase in ECL onset potential compared to the QD/TPA system (Figure 3.3), as QD oxidation must precede co-reactant oxidation, which will delay the formation of excited state QDs as $\text{CO}_2^{\cdot-}$ is being produced.

TPA co-reactant pathway

ECL generation with TPA is the consequence of the formation of TPA[•] through direct oxidation and subsequent de-protonation of TPA at the electrode surface.²⁵ The mechanism of the QD/TPA ECL system is displayed in equations (3.12)-(3.16).²⁵



QD oxidation leads to production of QDs(h⁺(1S_h)) (equation (3.12)) and direct oxidation of TPA leads to generation of the radical cation TPA^{•+} (equation (3.13)). TPA^{•+} rapidly loses a proton to form TPA[•] (equation (3.14)), a strongly reducing intermediate that can inject an electron into QDs(h⁺(1S_h)) to create an excited state QD (equation (3.15)) that can emit light (equation (3.16)). Direct oxidation of TPA at the electrode surface can be observed in a voltammogram of the QD/chitosan film in 1 mM TPA (Figure 3.9).

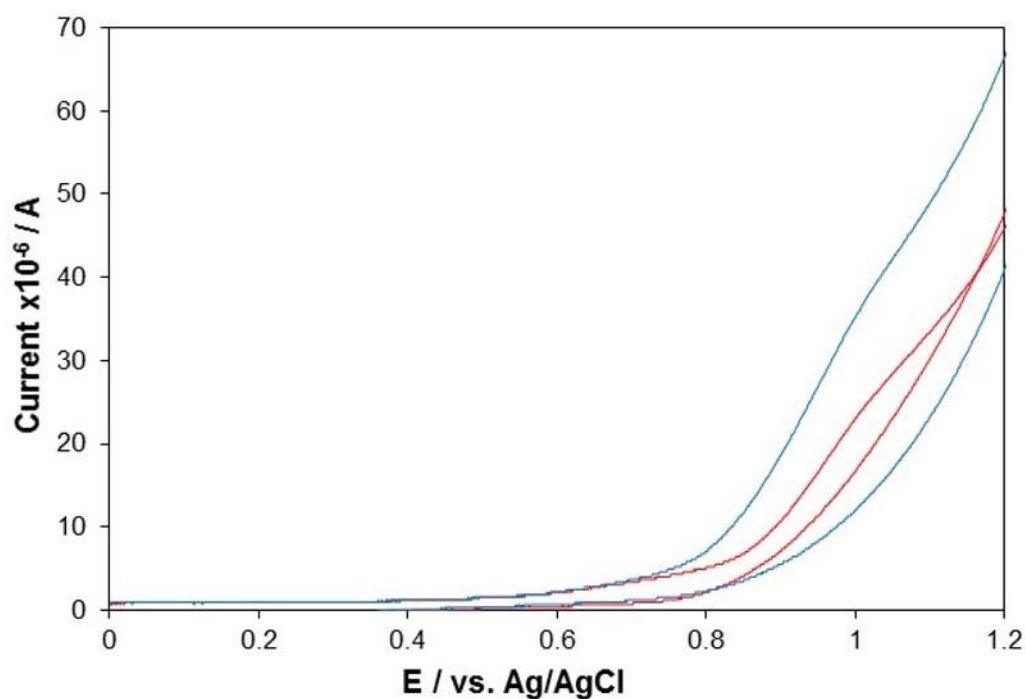


Figure 3.9 - Current response of 800 nm QD/chitosan film in 0.1 M PBS (red) and following addition of 1 mM TPA (blue) at a scan rate of 100 mV s⁻¹ over the potential range 0 V ≤ v ≤ 1.2 V vs. Ag/AgCl.

A significant increase in current is observed with onset at approximately 0.70 V, which is consistent with TPA oxidation at a modified GC electrode.³⁶ The electronic interactions that take place during formation of the excited state QDs are defined in Figure 3.10. The standard redox potential of TPA[•]/P (where P is the product of TPA[•] oxidation, namely an iminium cation) is approximately -1.70 V (vs. Ag/AgCl).²

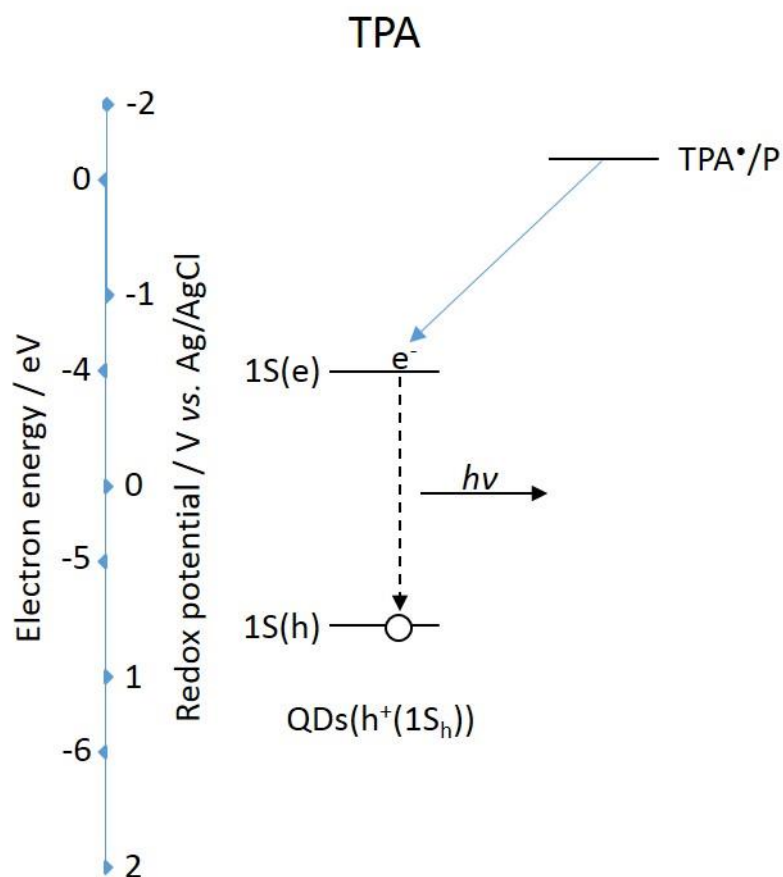


Figure 3.10 - Significant energy level interactions and resulting ECL process of 800 nm QDs with TPA co-reactant.

As with $\text{CO}_2^{\cdot-}$, TPA^{\cdot} has sufficient reducing strength to efficiently inject an electron into $1\text{S}(\text{e})$ of $\text{QDs}(\text{h}^+(1\text{S}_\text{h}))$. TPA-induced ECL is significantly more intense than the $\text{Na}_2\text{C}_2\text{O}_4$ system as electrogeneration of TPA^{\cdot} can occur directly at the electrode surface and so the concentration available for ECL reactions is greater.

3.4.2 Cathodic ECL characteristics

Cathodic ECL involves formation of ECL precursor species through reduction at the electrode surface, followed by homogenous electron transfer between these species to generate an excited state (reductive-oxidative system). For QDs, an electron is injected into the $1\text{S}(\text{e})$ energy level of their conduction band at a potential governed by their size. For efficient generation of an ECL

signal, hole injection into the 1S(h) orbital of this charged QD is then required, which is achieved through interaction with a strong oxidising agent created via reduction and decomposition of a suitable co-reactant species. Typical co-reactant species capable of forming such reactive intermediates include hydrogen peroxide (H_2O_2) and potassium persulfate ($\text{K}_2\text{S}_2\text{O}_8$).^{1, 16, 37-42} Figure 3.11 shows the QD ECL profile with H_2O_2 and $\text{K}_2\text{S}_2\text{O}_8$ co-reactants, and in PBS (co-reactant free system).

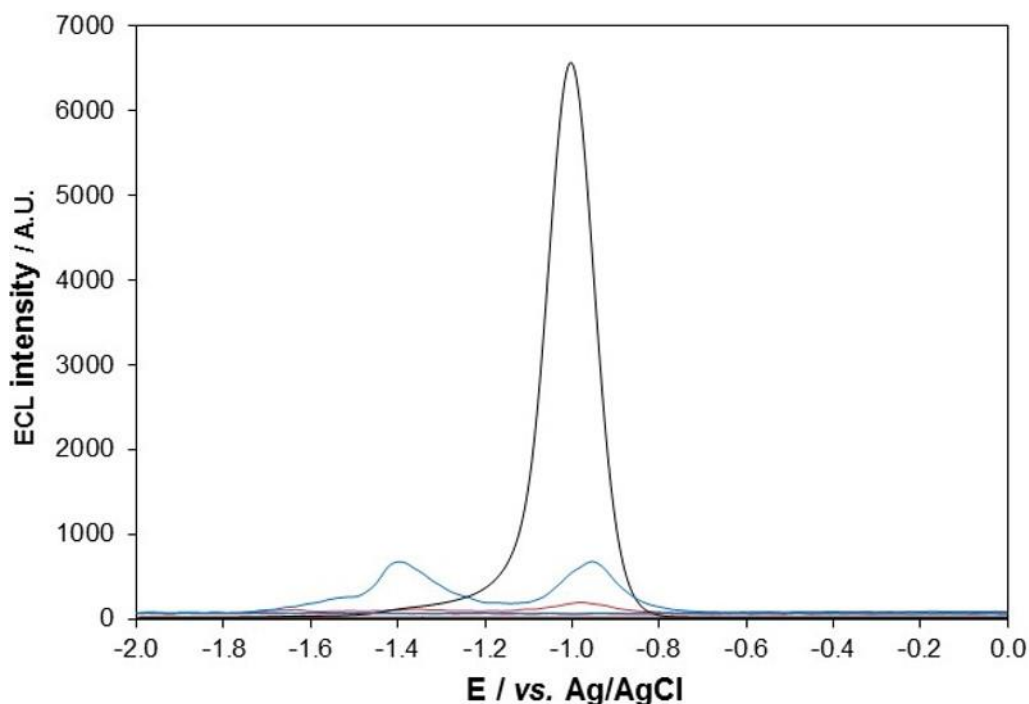


Figure 3.11 - ECL response of 800 nm QD/chitosan film in 0.1 M PBS (red), 1 mM H_2O_2 (blue) and 1 mM $\text{K}_2\text{S}_2\text{O}_8$ (black) at a scan rate of 100 mV s^{-1} over the potential range $-2 \leq v \leq 0 \text{ V vs. Ag/AgCl}$. PMT input voltage = 0.50 V.

Cathodic ECL was observed with $\text{K}_2\text{S}_2\text{O}_8$ and H_2O_2 co-reactants and with the co-reactant free system. Both H_2O_2 and 0.1 M PBS exhibit a double peak profile with onset of reductive ECL peak 1 at -0.75 V and onset of peak 2 at -1.15 V. Maximum intensity of these peaks are reached at -1.00 and -1.35 V respectively. The strongest ECL signal was obtained with $\text{K}_2\text{S}_2\text{O}_8$, which displayed a single reductive ECL peak with onset at -0.75 V and peak maximum at -1.00 V.

3.4.2.1 Elucidation of cathodic ECL mechanisms

PBS co-reactant pathway

A clearer profile of ECL emission in PBS is shown in Figure 3.12, which highlights the double peak nature of the signal.

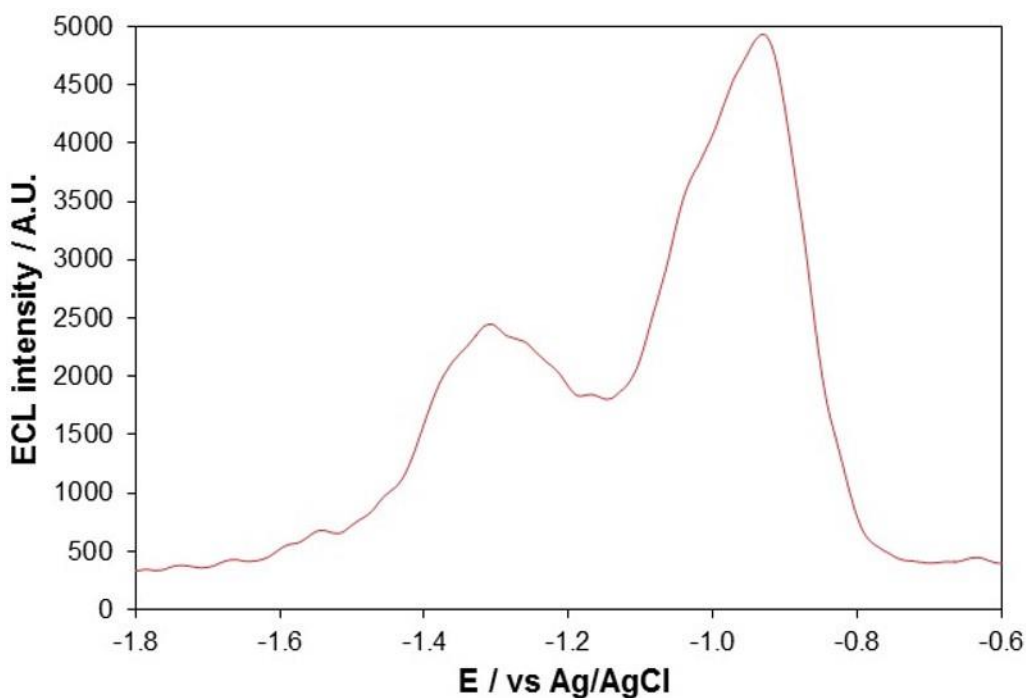


Figure 3.12 - ECL response of 800 nm QD/chitosan film in 0.1 M PBS at a scan rate of 100 mV s^{-1} over the potential range $-1.8 \leq v \leq -0.6 \text{ V vs. Ag/AgCl}$. PMT input voltage = 0.95 V.

As with the anodic PBS mechanism, ROS were expected to act as the co-reactant in this system. This was confirmed through observation of a significant loss in signal intensity following de-aeration of the sample solution (Figure 3.13). Determination of peak specific ROS acting as co-reactant was attempted through addition of thiourea, a free radical scavenger with particular activity towards hydroxyl radicals (OH^\bullet),⁴³ and SOD (Figure 3.13).

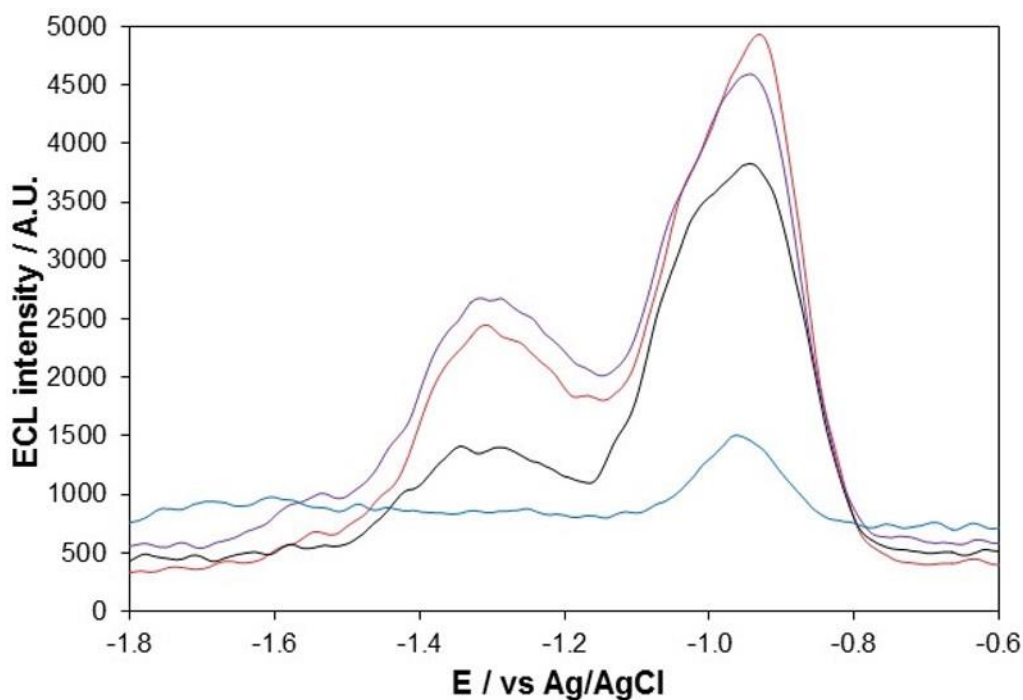
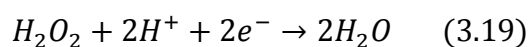
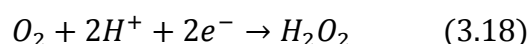
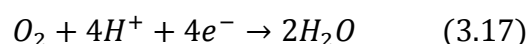


Figure 3.13 - ECL response of 800 nm QD/chitosan film in 0.1 M PBS (red), following de-aeration (blue) and following addition of 100 mM thiourea (black) and 0.46 mg/mL SOD (purple) at a scan rate of 100 mV s^{-1} over the potential range $-1.8 \leq v \leq -0.6 \text{ V vs. Ag/AgCl}$. PMT input voltage = 0.95 V.

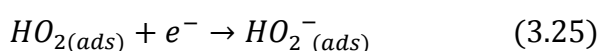
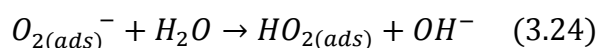
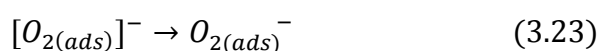
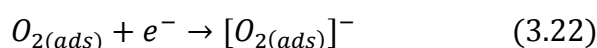
Addition of thiourea caused a small decrease in peak 1 and a significant loss of intensity of peak 2. SOD had no observable effect on either peak, demonstrating $\text{O}_2^{\cdot-}$ was not involved in the ECL mechanism of either. De-aeration caused an almost complete loss of all ECL emission confirming the participation of dissolved O_2 in the ECL pathway. This data indicated that non-radical ROS were the major electron transfer species for generation of ECL peak 1 and that radical ROS were the dominant species involved in the ECL pathway for peak 2.

ROS are created through the oxygen reduction reaction (ORR), which has three common routes (equations (3.17) – (3.20)).⁴⁴



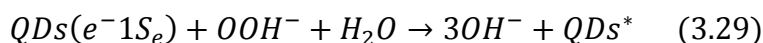
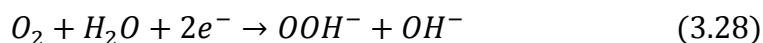


4-electron reduction to H₂O (equation (3.17)), multiple 2-electron reductions to produce H₂O via an H₂O₂ intermediate (equations (3.18) and (3.19)) or a 1-electron reduction to produce superoxide (3.20) are all possible routes of the ORR. The favoured pathway is determined predominantly by the electrode material, electrolyte and catalyst.⁴⁴ GC electrodes are known to catalyse 2-electron reductions via a complex process that comprises a number of transient intermediate species.⁴⁴ A variety of these are likely involved in the ECL pathways of peaks 1 and 2. One such non-radical ROS intermediate that could be involved in the generation of peak 1 and is well-documented as an ECL co-reactant is the perhydroxyl anion, HOO⁻,^{10, 38, 45} which is a proposed product of the carbon-catalysed ORR. Its suggested mechanism of formation on a GC electrode is shown in equations (3.21) – (3.26).^{44, 46}



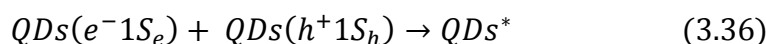
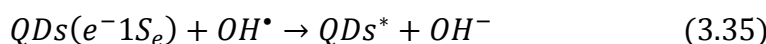
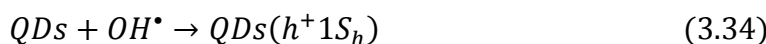
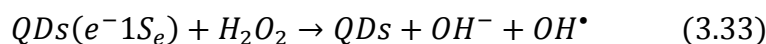
Where “ads” represents species is adsorbed on the electrode surface.

1-electron reduction of adsorbed O₂ generates adsorbed superoxide (equation (3.22)), which can then migrate to an active site on the electrode surface for reduction to form adsorbed OOH (equations (3.23) and (3,24) respectively). This species undergoes a further 1-electron reduction to produce OOH⁻ (equation (3.25)) that can then desorb from the electrode surface giving rise to solution phase OOH⁻ (equation (3.26)). This species can then interact with QDs to induce ECL as shown in equations (3.27) – (3.30).¹⁰



$QDs(e^-(1S_e))$ are formed through heterogeneous electron injection into $1S(e)$ of QDs (equation (3.17) and OOH^- through 2-electron reduction of O_2 (equations (3.21) – (3.26)). Electron transfer from the $1S(h)$ energy level of $QDs(e^-(1S_e))$ to OOH^- results in the formation of three hydroxyl anions and QDs^* (equation (3.19)). In this process, superoxide is adsorbed on the electrode surface (equations (3.22) and (3.23)) and is not involved in ECL production, preventing signal loss following addition of SOD. The non-radical nature of OOH^- ensures addition of a free-radical scavenger (thiourea) has little effect on ECL intensity.

From equation (3.18) it can be seen that H_2O_2 can be produced as an intermediate in the 2-electron reduction of O_2 , which could explain the similarity between ECL profiles with PBS and H_2O_2 co-reactants (Figure 3.11) and the presence of an ECL signal (peak 2) that is sensitive to free-radical concentration. This is because the key species for ECL production with H_2O_2 co-reactant is the hydroxyl radical, OH^\bullet .^{1, 47-49} The ECL pathway for this system is shown in equations (3.31) – (3.37).⁴⁹



Electron-injected QD intermediates are formed at the electrode surface (equation (3.31)). OH^\bullet can be formed by either direct 1-electron reduction of H_2O_2 (equation (3.31)) or through a Haber-Weiss type reaction with $\text{QDs}(e^-(1\text{S}_e))$ (equation (3.33)). This species can then inject a hole into an uncharged (QDs) or charged QD ($\text{QDs}(e^-(1\text{S}_e))$) to create $\text{QDs}(h^+(1\text{S}_h))$ and QDs^* respectively (equations (3.34) and (3.35)). This process is favourable owing to the high standard redox potential of the $\text{OH}^-/\text{OH}^\bullet$ couple (2.16 V vs. Ag/AgCl at physiological pH).²² Recombination of $\text{QDs}(e^-(1\text{S}_e))$ and $\text{QDs}(h^+(1\text{S}_h))$ can then generate additional QDs^* (equation (3.36)), although this process is thought to contribute little to the overall ECL intensity.⁵⁰

ECL emission via this pathway will be sensitive to OH^\bullet , which is confirmed experimentally through a decrease in intensity following addition of thiourea (Figure 3.13). This data attributes the major contributing source of ECL peak 2 to the presence of OH^\bullet , created through the interaction of $\text{QDs}(e^-(1\text{S}_e))$ with H_2O_2 following 2-electron reduction of dissolved O_2 . The delayed onset of peak 2 suggests the rate-determining step for ECL production is no longer QD reduction but governed by the kinetics of OH^\bullet formation, which is produced at -1.20 V (section 2.3.2.2, Figure 2.17). This is at a more negative potential than that estimated for QD reduction and explains the appearance of a double peak profile. Peak 1 is generated immediately following QD reduction through interaction with ROS such as OOH^- and peak 2 observed following 1-electron reduction of H_2O_2 to produce OH^\bullet , which can then interact with $\text{QDs}(e^-(1\text{S}_e))$. The reduced intensity of ECL peak 2 is likely caused by consumption of $\text{QDs}(e^-(1\text{S}_e))$ during generation of the first ECL signal.

To confirm the major contributing factor to the observed double peak ECL profile was the nature of the ORR and resulting ROS intermediates, a Pt electrode was modified with the same QD/chitosan film and the ECL response in PBS was monitored (Figure 3.14).

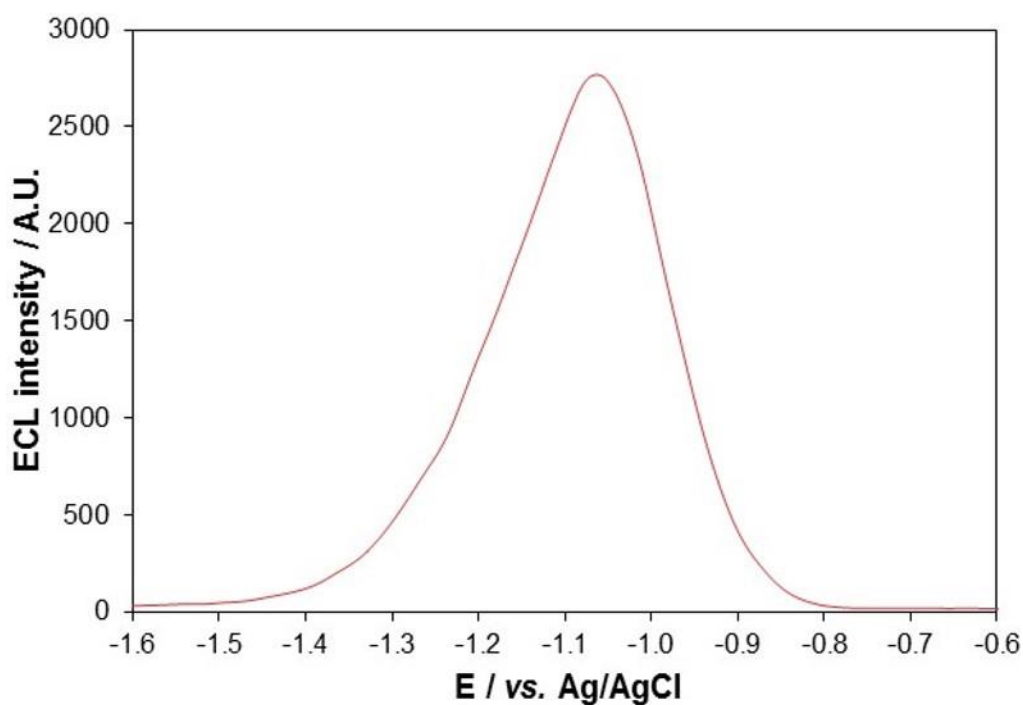


Figure 3.14 - ECL response of 800 nm QD/chitosan film on Pt electrode in 0.1 M PBS at a scan rate of 100 mV s^{-1} over the potential range $-1.6 \leq v \leq -0.6 \text{ V vs. Ag/AgCl}$. PMT input voltage = 0.65 V.

A single reductive ECL peak is observed at -1.10 V (appears at -0.75 V), which differs significantly from the double peak profile obtained with a GC electrode. The identical onset potential for ECL demonstrates that QD reduction is not influenced by electrode material. In contrast to the ORR on GC, the Pt-catalysed ORR is a major 4-electron process (equation (3.17)) that involves a number of reaction intermediates.⁴⁴ This difference in favoured route leads to alteration in ROS produced at the electrode surface that are available for electron transfer with QDs($e^-(1S_e)$). This is highlighted in Figure 3.16, which shows the effect of thiourea and SOD on the observed ECL response.

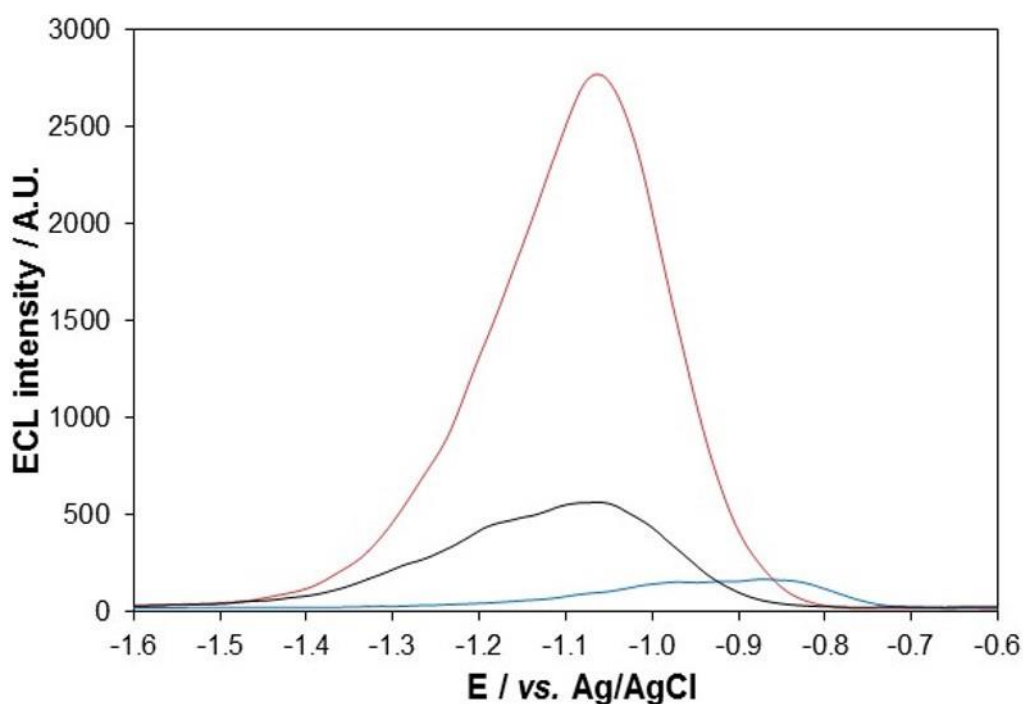
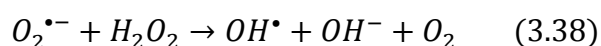


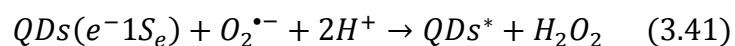
Figure 3.15 - ECL response of 800 nm QD/chitosan film on a Pt electrode in 0.1 M PBS (red), after addition of 100 mM thiourea (blue) and after addition of 0.46 mg/mL SOD (black) at a scan rate of 100 mV s⁻¹ over the potential range -1.6 ≤ v ≤ -0.6 V vs. Ag/AgCl. PMT input voltage = 0.65 V.

The presence of thiourea causes an almost complete loss of ECL signal, signifying radical ROS as the major co-reactant species with the Pt electrode. The shift in peak potential in the presence of thiourea is not entirely clear, but may be caused by ECL generation with non-radical ROS that are masked when a radical quencher is not present. In contrast with a GC electrode, one of the most prevalent of these radical species appears to be O₂^{•-}, which can be formed in the first electron transfer process with O₂ at the Pt surface.⁵¹ Addition of SOD resulted in a decrease in ECL intensity of over 80 %. It is believed that consumption of O₂^{•-} by SOD inhibits the formation of OH[•] via a Haber-Weiss type reaction (equation (3.38)).



Consequently, the ECL intensity decreases as the rate of hole injection into QDs (equations (3.33) and (3.34)) diminishes due to a lower concentration of

OH[•]. As H₂O₂ is only a minor product in the Pt-catalysed ORR,⁴⁴ O₂^{•-} could be acting as a direct co-reactant itself (equations (3.39) – (3.42)).⁵²



The competing reaction of O₂^{•-} with SOD will decrease the concentration available for QDs* formation, resulting in a drop in observed ECL intensity.

Previous incidences of a double peak profile have been documented in the literature.^{38, 48} This was reported as resulting from interaction of individual and assemblies of reduced QDs with oxidative co-reactants.⁴⁸ However, in this case it does not explain the variation in ECL profile observed with alternative co-reactants or electrode materials. It also is not clear why addition of interfering species (thiourea) would influence these peaks to a different extent.

An alternative explanation was an annihilation process leading to peak 1 and a co-reactant process leading to peak 2.³⁸ QD hole injection by ROS formed during the ORR at approximately -0.65 V (section 2.3.2.2) could result in the formation of QDs(h⁺(1S_h)), which could then recombine with QDs(e⁻(1S_e)) formed at their reduction potential (approximately -0.75 V) to generate ECL peak 1. ECL peak 2 could then be produced following formation of OH[•] (at ~-1.20 V), which could inject a hole into QDs(e⁻(1S_e)) and generate the excited state species. However, the ECL intensity of peak 1 is greater than that of peak 2, which would be very surprising if indeed it was being formed through an annihilation process as the stability of charged QD species is poor.^{9, 53} In documented cases, the signal originating from co-reactant species is more intense than that from the annihilation process,³⁸ which is not observed here. Additionally, it has been shown that hole injection into uncharged QDs results in extremely low annihilation ECL intensities, likely due to irreversible QD

oxidation processes (preventing radiative recombination and thus ECL emission).^{5, 50, 53, 54} This intensity is increased substantially if hole injection occurs into QDs($e^-(1S_e)$), which allows rapid recombination and ECL emission.⁵⁰ Again, this predicts a significantly larger intensity of ECL generated via a co-reactant route (peak 2) compared to an annihilation route (peak 1), which is not observed here. As a result, it appears most likely that both peaks are the result of a co-reactant pathway, with hole injection into QDs($e^-(1S_e)$) from distinct ROS formed at different potentials.

This data indicates that the formation of ROS through the ORR dictates the major cathodic ECL pathway with dissolved O_2 co-reactant. Alterations in the nature of these reactions leads to a change in the obtained ECL profile, whilst the kinetics of these interactions also have an impact on the spectra. It must be noted that the precise mechanism of the ORR is still not fully understood and it is likely that a variety of species are contributing to ECL generation.

H₂O₂ co-reactant pathway

Figure 3.16 shows an overlay of the double peak nature of the ECL profile with H_2O_2 co-reactant and its associated voltammogram from DPV.

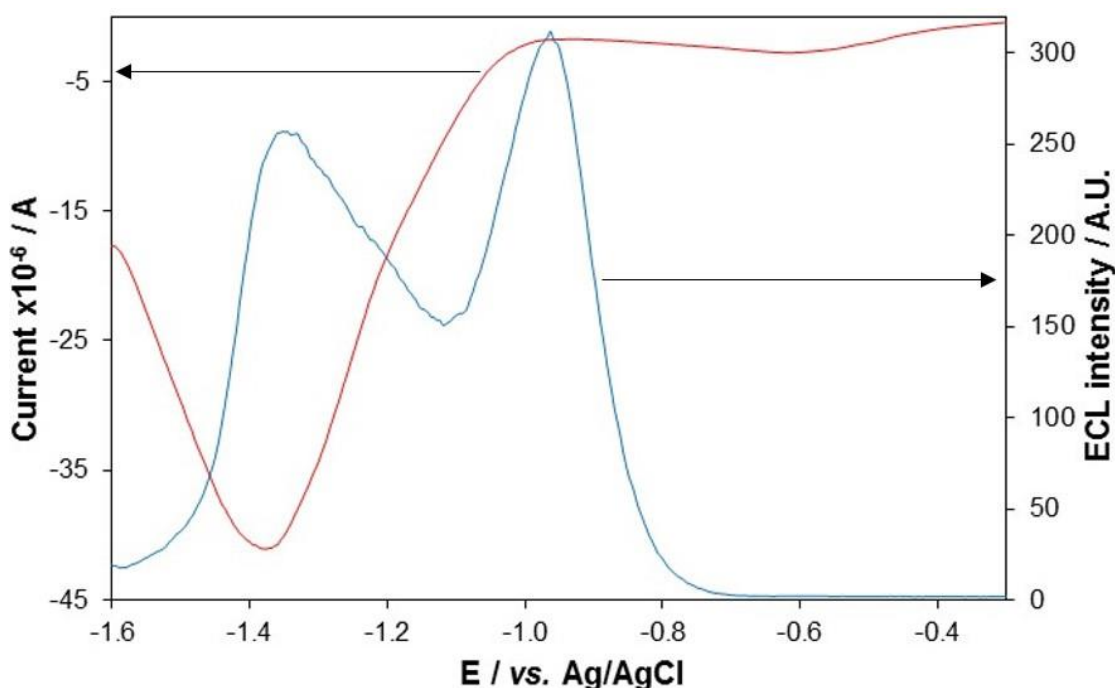


Figure 3.16 – Typical voltammogram (from DPV, red) and ECL response (blue) of 800 nm QD/chitosan film in 2 mM H₂O₂ at a scan rate of 100 mV s⁻¹ over the potential range -1.6 ≤ v ≤ -0.3 V vs. Ag/AgCl. PMT input voltage = 0.50 V.

The voltammogram exhibits a small reduction peak at -0.65 V that is related to the ORR (section 2.3.2.2). At this potential no ECL response is observed as QD reduction has not yet taken place. At approximately -0.75 V an ECL response appears, following electron transfer between ROS and QDs($e^-(1S_e)$). A large reduction peak appears in the voltammogram at -1.00 V and is attributed to 1-electron reduction of H₂O₂ to form OH[•] (section 2.3.2.2). A simultaneous ECL response appears at the same potential (peak 2), which is due to interaction of OH[•] with QDs($e^-(1S_e)$) to create the excited state species. The H₂O₂ ECL pathway is well-established and is defined in equations (3.31) – (3.37). The electronic interactions that occur to generate excited state QDs with OH[•] are shown in Figure 3.17 (the standard redox potential (vs. Ag/AgCl) for the OH[•]/OH⁻ couple is approximately 2.16 V at physiological pH).²²

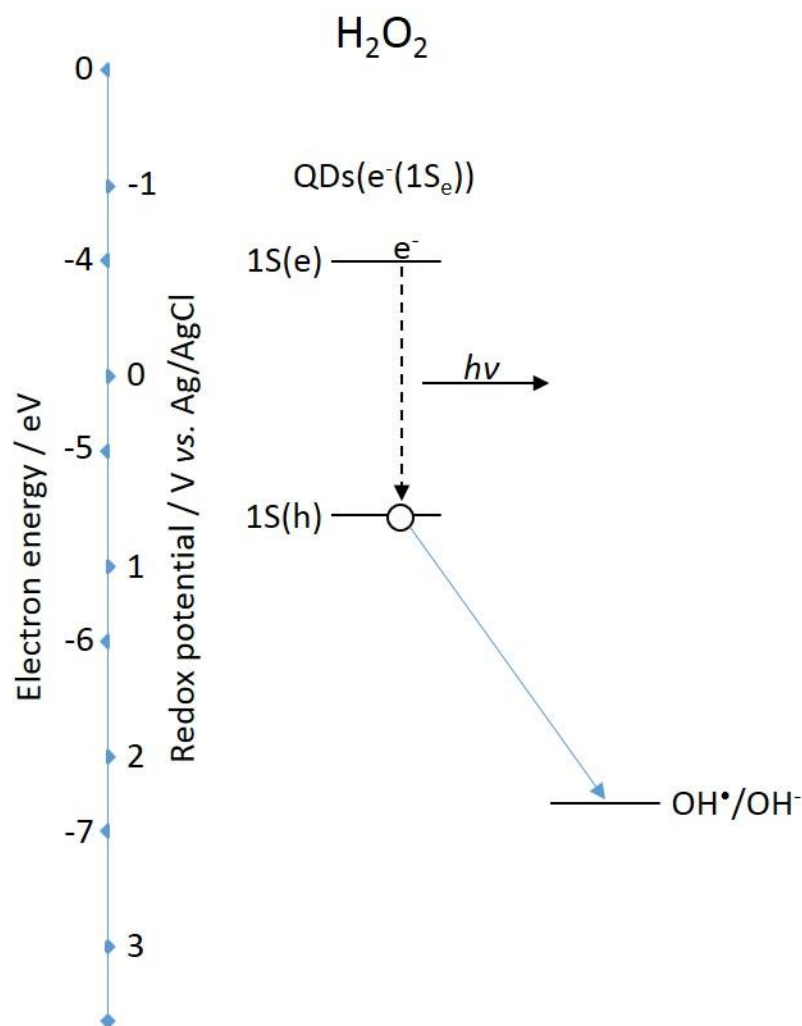


Figure 3.17 - Significant energy level interactions and resulting ECL process of 800 nm QDs with H₂O₂ co-reactant.

OH^{*} is capable of injecting a hole into 1S(h) of QDs(e⁻(1S_e)) to create QDs^{*}. This is a rapid process owing to the strong oxidising strength of OH^{*} and ECL generation is an efficient process.

Work in the previous section had proposed that peak 2 was the consequence of these same interactions, following the production of H₂O₂ at the electrode surface during the ORR. To confirm the sensitivity of this peak to H₂O₂, the ECL response of the QD/chitosan film to increasing H₂O₂ concentrations was monitored (Figure 3.18).

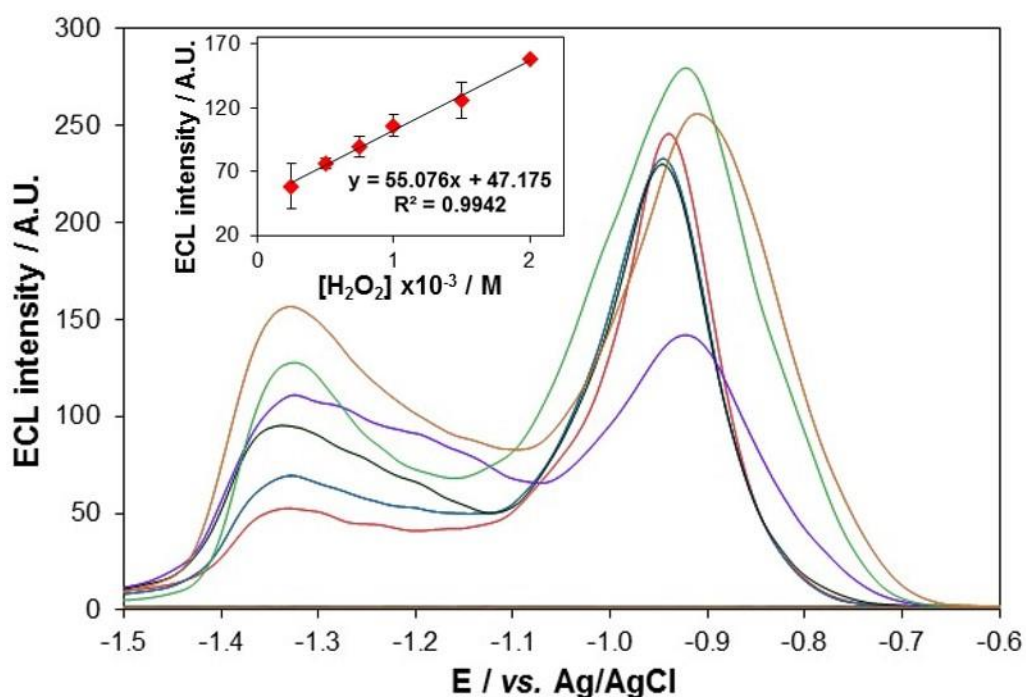


Figure 3.18 - ECL response of 800 nm QD/chitosan film in 0.25 (red), 0.5 (blue), 0.75 (black), 1 (purple), 1.5 (green) and 2 (orange) mM H₂O₂ at a scan rate of 100 mV s⁻¹ over the potential range $-1.5 \leq v \leq -0.6$ V vs. Ag/AgCl. Inset shows the linear dependence of ECL response (at -1.35 V) with respect to [H₂O₂] for the 800 nm QD/chitosan film. Error bars represent standard deviations from triplicate data points. PMT input voltage = 0.50 V.

The data shows no relationship between peak 1 and H₂O₂ concentration but a strong, reproducible linear dependence of peak 2 on H₂O₂ concentration. The sensitivity of peak 2 to H₂O₂ confirms its mechanism involves OH[•]. These results illustrate that the ECL (peak 2 at -1.35 V) of NIR QDs is sensitive to H₂O₂ concentration and can be used for its quantification. This is the first NIR ECL based detection system for H₂O₂, which is significant owing to the variety of biological processes that can be monitored by their production or consumption of this small molecule.^{55, 56}

As peak 1 did not exhibit sensitivity towards H₂O₂, investigation into the ECL pathway for its generation was carried out through examining the effect of thiourea, SOD and de-aeration on its intensity (Figure 3.19).

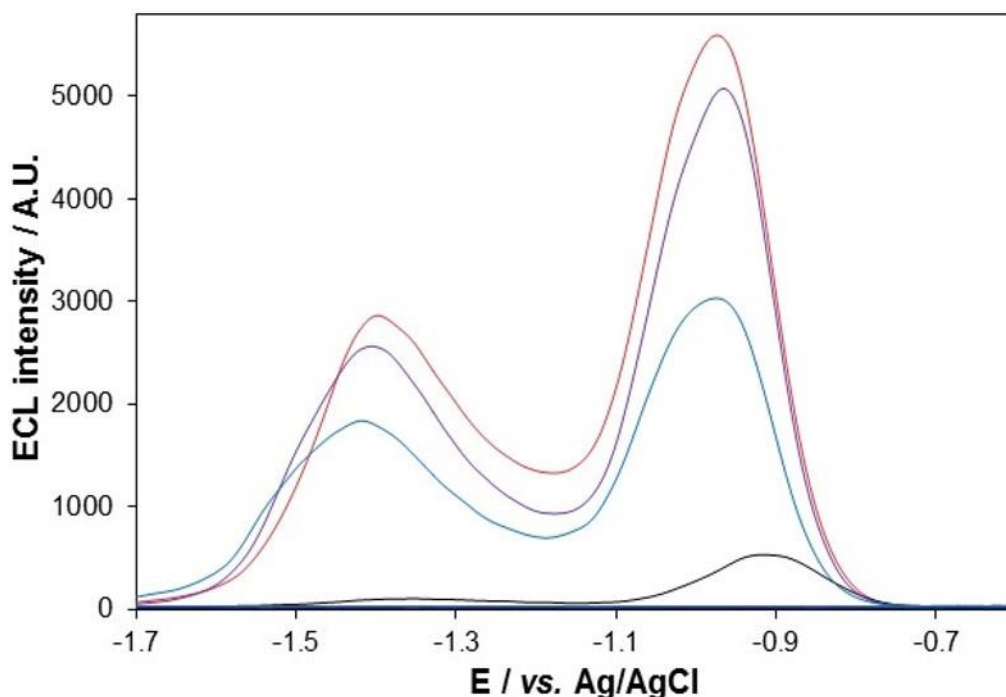


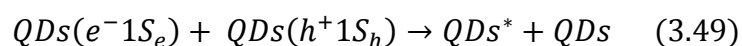
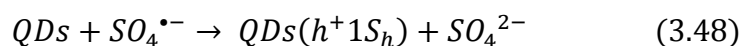
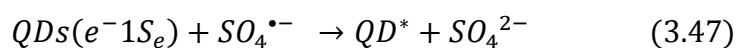
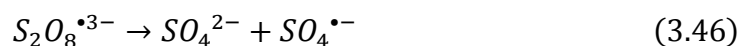
Figure 3.19 - ECL response of 800 nm QD/chitosan film in 10 mM H₂O₂ (red), after de-aeration (blue), and after addition of 100 mM thiourea (black) and 0.46 mg/mL SOD (purple) at a scan rate of 100 mV s⁻¹ over the potential range -1.7 ≤ v ≤ -0.6 V vs. Ag/AgCl. PMT input voltage = 0.70 V.

These results specify that dissolved O₂ is no longer the fundamental contributing species to ECL generation as de-aeration still permits production of a strong ECL response at both peaks. As with PBS, the addition of SOD has negligible effect on ECL intensity and O₂^{•-} is therefore not regarded as contributing to the ECL signal. The presence of thiourea results in a marked decrease in the ECL intensity of both peaks 1 and 2, stipulating the participation of radical species in the ECL pathways of both. This is in contrast with dissolved O₂ co-reactant, which did not exhibit significant radical species sensitivity for peak 1. This suggested that the ECL mechanism for generation of peak 1 with H₂O₂ co-reactant involves different ROS. The exact nature of these species is not known, but is thought to involve radical products of the ORR and degradation products of H₂O₂ that have been reduced at the electrode surface. It is possible that generation of OH[•] may be occurring through reduction of H₂O₂ by QDs(e⁻(1S_e)), via a Haber-Weiss type reaction (equation (3.33)). This would explain the sensitivity of this peak to thiourea and

its insensitivity to H₂O₂ if the process is limited by the QD concentration in the film, rather than the H₂O₂ concentration in solution.

K₂S₂O₈ co-reactant pathway

Figure 3.11 shows a single reductive peak ECL profile with K₂S₂O₈ co-reactant. This differs from that with H₂O₂ or dissolved O₂ as ROS are no longer the major contributing species to generation of the ECL signal. Instead, reduction and decomposition of S₂O₈²⁻ produces the sulfate radical anion, SO₄^{•-},⁵⁷ a potent oxidising agent capable of rapid, efficient hole injection into the 1S(h) orbital of the QDs. The greater reactivity of this species compared to ROS (e.g. OH[•], OOH[•]) prevents the formation of a double peak as these species cannot compete with the rate of electron transfer between SO₄^{•-} and QDs. The preceding electron transfer reactions leading to ECL emission with this system are shown in equations (3.44) - (3.50).¹⁵



Direct reduction of QDs and S₂O₈²⁻ at the electrode creates QDs(e⁻(1S_e)) and S₂O₈^{•3-} (equations (3.44) and (3.45)), which rapidly decomposes to form SO₄^{•-} (equation (3.46)). This can then abstract an electron from the HOMO of QDs(e⁻(1S_e)) to generate excited state QDs (equation (3.47)). Oxidation of an uncharged QD by SO₄^{•-} can also produce QDs(h⁺(1S_h)) (equation (3.48)), which recombines with QDs(e⁻(1S_e)) to form QDs* (equation (3.49)). ECL emission via this annihilation route is expected to contribute minimally to the observed response.⁵⁰ The electronic interactions between QDs(e⁻(1S_e)) and

$\text{SO}_4^{\bullet-}$ are outlined in Figure 3.20. The standard redox potential (vs. Ag/AgCl) for the $\text{SO}_4^{\bullet-}/\text{SO}_4^{2-}$ couple is approximately 3.16 V.⁵⁸

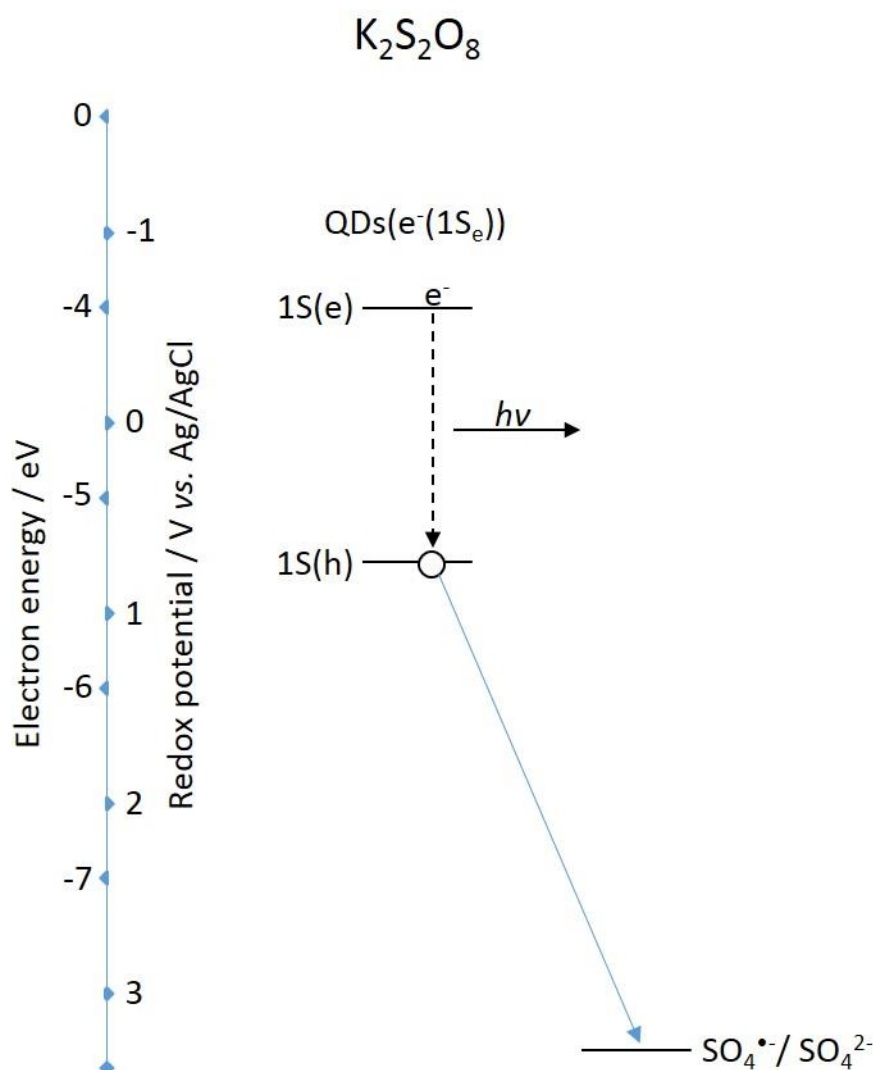


Figure 3.20 - Significant energy level interactions and resulting ECL process of 800 nm QDs with $\text{K}_2\text{S}_2\text{O}_8$ co-reactant.

$\text{SO}_4^{\bullet-}$ is easily capable of hole injection into the $1S(h)$ quantum confined orbital of the NIR QDs. The strong oxidising strength of $\text{SO}_4^{\bullet-}$ ensures rapid homogenous electron transfer kinetics with $\text{QDs}(e^-(1S_e))$, manifesting itself in generation of an intense ECL signal, which is substantially greater than that attained with ROS.

A voltammogram of the QD/chitosan film in $K_2S_2O_8$ (Figure 3.21) is dominated by a large, irreversible reduction peak at -1.15 V (onset at -0.35 V), which is associated with direct one-electron reduction of $S_2O_8^{2-}$.

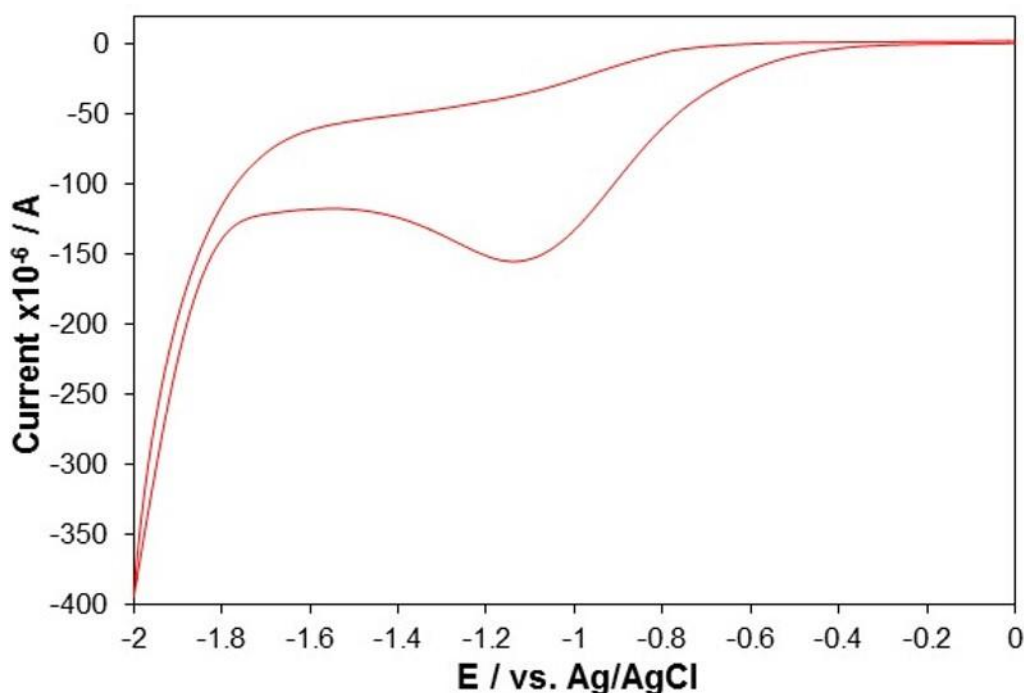


Figure 3.21 - Current response of 800 nm QD/chitosan film in 50 mM $K_2S_2O_8$ over the potential range $-2 \text{ V} \leq v \leq 0 \text{ V}$ vs. Ag/AgCl.

A delayed ECL onset potential (-0.75 V (Figure 3.11)) compared to this reduction process confirms QD reduction as the rate-determining step for light emission with this pathway. This is because QD ECL precursors cannot be formed until the Fermi level of the electrode reaches a potential at which efficient electron injection into the $1S(e)$ energy level is possible, which exists at a potential negative of that required for $S_2O_8^{2-}$ reduction.

3.5 Conclusions

This work has detected the first anodic ECL emission from NIR QDs with a co-reactant free system. This is achieved through electron transfer between electrogenerated O_2^- and $QDs(h^+(1S_h))$ to form excited state QDs. The potential of such a co-reactant free system is great as signal production can

be attained in any aqueous solution without disruption through addition of a co-reactant. This opens up opportunities to develop novel, co-reactant free biosensors with NIR ECL emission.

A greater than 10-fold enhancement in this ECL signal was then accomplished through the addition of TPA. Its oxidation generated the strong reducing agent $\text{TPA}^{\cdot-}$, which could efficiently inject electrons into $1\text{S}(e)$ of $\text{QDs}(h^+(1\text{S}_h))$, increasing the ECL signal. Enhancement in this manner should allow improved ECL sensitivity, which is ideal for the detection of low concentration analytes, routinely required for biosensing applications. Addition of an alternative anodic ECL co-reactant, $\text{Na}_2\text{C}_2\text{O}_4$, provided no significant enhancement in ECL intensity, which could be explained by consumption of the ECL precursor, $\text{QDs}(h^+(1\text{S}_h))$, during $\text{C}_2\text{O}_4^{2-}$ oxidation. Therefore, analysis of the data signified that the mechanism of ECL precursor formation had a significant effect on ECL intensity. Direct oxidation of both at the electrode surface permits substantial improvements in intensity. It highlighted the most suitable co-reactant for sensitive anodic ECL detection was TPA, which is useful knowledge for any future development of anodic ECL biosensors.

NIR QDs also demonstrated strong ECL signals in the cathodic region with and without additional co-reactants. This work has established the first cathodic co-reactant free system with NIR emission, which can be enhanced by the addition of H_2O_2 and $\text{K}_2\text{S}_2\text{O}_8$. A double peak profile was apparent in both PBS and H_2O_2 . The appearance of peak 1 was largely dependent upon ROS products of the ORR. Peak 2 ECL was reliant upon H_2O_2 reduction to generate $\text{OH}^{\cdot-}$, which could then interact with reduced QDs to create the excited state. This peak proved to be sensitive to H_2O_2 , which permitted its quantification and was the first NIR ECL biosensor of this substrate. It was concluded that the reaction pathway and ROS intermediates created during the ORR had a significant impact on the observed ECL profile of these large, NIR emitting QDs.

$K_2S_2O_8$ resulted in the largest enhancement in ECL intensity due to the powerful oxidising nature of its electrogenerated precursor, $SO_4^{\cdot-}$. This species permitted rapid hole injection into the 1S(h) energy level of the QDs immediately following their reduction, which ensured an intense ECL peak. The energetics of this process permitted generation of an intense ECL signal, which masked the formation of any further peaks in the ECL profile.

This work confirmed that ECL emission originated from the QD core through estimation of the HOMO-LUMO energy gap from ECL onset potentials. This data was used to predict the electronic structure of 800 nm CdSeTe/ZnS QDs; this could then be used to correlate excited state formation in the ECL process with different co-reactant species.

Overall, this data has established that NIR emitting QDs can generate an ECL signal with and without a variety of co-reactants in the cathodic and anodic regions. This highlighted their versatility and flexibility for incorporation into ECL systems and provides a basis from which to optimise the sensitivity and stability of this response in the following chapter.

3.6 References

1. J.-P. Choi and A. J. Bard, *Analytica chimica acta*, 2005, **541**, 141-148.
2. W. Miao, J.-P. Choi and A. J. Bard, *Journal of the American Chemical Society*, 2002, **124**, 14478-14485.
3. F. Kanoufi and A. J. Bard, *The Journal of Physical Chemistry B*, 1999, **103**, 10469-10480.
4. P. McCord and A. J. Bard, *Journal of electroanalytical chemistry and interfacial electrochemistry*, 1991, **318**, 91-99.
5. Z. Ding, B. M. Quinn, S. K. Haram, L. E. Pell, B. A. Korgel and A. J. Bard, *Science*, 2002, **296**, 1293-1297.
6. H. Qi, Y. Peng, Q. Gao and C. Zhang, *Sensors*, 2009, **9**, 674-695.
7. S. Wang, E. Harris, J. Shi, A. Chen, S. Parajuli, X. Jing and W. Miao, *Physical Chemistry Chemical Physics*, 2010, **12**, 10073-10080.
8. P.-Z. Liu, X.-W. Hu, C.-J. Mao, H.-L. Niu, J.-M. Song, B.-K. Jin and S.-Y. Zhang, *Electrochimica Acta*, 2013, **113**, 176-180.
9. Y. Wang, J. Lu, L. Tang, H. Chang and J. Li, *Analytical chemistry*, 2009, **81**, 9710-9715.
10. Z. Wang, H. Song, H. Zhao and Y. Lv, *Luminescence*, 2013, **28**, 259-264.
11. P. Yan, Q. Tang, A. Deng and J. Li, *Sensors and Actuators B: Chemical*, 2014, **191**, 508-515.
12. S. Li, J. Luo, X. Yang, Y. Wan and C. Liu, *Sensors and Actuators B: Chemical*, 2014, **197**, 43-49.
13. S. Deng, J. Lei, Y. Huang, Y. Cheng and H. Ju, *Analytical chemistry*, 2013, **85**, 5390-5396.
14. W. Fei, F. Chen, L. Sun, Q. Li, J. Yang and Y. Wu, *Microchimica Acta*, 2014, **181**, 419-425.
15. G.-X. Liang, L.-L. Li, H.-Y. Liu, J.-R. Zhang, C. Burda and J.-J. Zhu, *Chemical Communications*, 2010, **46**, 2974-2976.
16. R. Cui, Y.-P. Gu, L. Bao, J.-Y. Zhao, B.-P. Qi, Z.-L. Zhang, Z.-X. Xie and D.-W. Pang, *Analytical chemistry*, 2012, **84**, 8932-8935.
17. J. Wang, H. Han, X. Jiang, L. Huang, L. Chen and N. Li, *Analytical chemistry*, 2012, **84**, 4893-4899.
18. G. Liang, S. Liu, G. Zou and X. Zhang, *Analytical chemistry*, 2012, **84**, 10645-10649.
19. C. Woelfle and R. O. Claus, *Nanotechnology*, 2007, **18**, 025402.
20. Y. Wang, Z. Xie, G. Gotesman, L. Wang, B. P. Bloom, T. Z. Markus, D. Oron, R. Naaman and D. H. Waldeck, *The Journal of Physical Chemistry C*, 2012, **116**, 17464-17472.
21. B.-R. Hyun, Y.-W. Zhong, A. C. Bartnik, L. Sun, H. D. Abruna, F. W. Wise, J. D. Goodreau, J. R. Matthews, T. M. Leslie and N. F. Borrelli, *ACS Nano*, 2008, **2**, 2206-2212.
22. L. Bao, L. Sun, Z.-L. Zhang, P. Jiang, F. W. Wise, H. c. D. Abruña and D.-W. Pang, *The Journal of Physical Chemistry C*, 2011, **115**, 18822-18828.
23. D. R. Skotty and T. A. Nieman, *Journal of Chromatography B: Biomedical Sciences and Applications*, 1995, **665**, 27-36.

24. I. Rubinstein and A. J. Bard, *Journal of the American Chemical Society*, 1981, **103**, 512-516.
25. Y. Zu and A. J. Bard, *Analytical chemistry*, 2000, **72**, 3223-3232.
26. M. M. Collinson, J. Taussig and S. A. Martin, *Chemistry of materials*, 1999, **11**, 2594-2599.
27. Y. Kim and J. Kim, *Analytical chemistry*, 2014, **86**, 1654-1660.
28. M.-C. Lu and C.-W. Whang, *Analytica chimica acta*, 2004, **522**, 25-33.
29. Y. Zu and A. J. Bard, *Analytical chemistry*, 2001, **73**, 3960-3964.
30. X. Liu, H. Jiang, J. Lei and H. Ju, *Analytical chemistry*, 2007, **79**, 8055-8060.
31. T. Hu, T. Li, L. Yuan, S. Liu and Z. Wang, *Nanoscale*, 2012, **4**, 5447-5453.
32. S. Marklund and G. Marklund, *European Journal of Biochemistry*, 1974, **47**, 469-474.
33. W. H. Koppenol and J. D. Rush, *Journal of Physical Chemistry*, 1987, **91**, 4429-4430.
34. I. Rubinstein, C. R. Martin and A. J. Bard, *Analytical chemistry*, 1983, **55**, 1580-1582.
35. M.-M. Chang, T. Saji and A. J. Bard, *Journal of the American Chemical Society*, 1977, **99**, 5399-5403.
36. H. Wang, X. Zhang, Z. Tan, W. Yao and L. Wang, *Electrochemistry Communications*, 2008, **10**, 170-174.
37. X. Hu, H. Han, L. Hua and Z. Sheng, *Biosensors and Bioelectronics*, 2010, **25**, 1843-1846.
38. G.-F. Jie, B. Liu, J.-J. Miao and J.-J. Zhu, *Talanta*, 2007, **71**, 1476-1480.
39. W. Li, R. Yuan, Y. Chai, L. Zhou, S. Chen and N. Li, *Journal of biochemical and biophysical methods*, 2008, **70**, 830-837.
40. D. Yuan, S. Chen, R. Yuan, J. Zhang and W. Zhang, *Analyst*, 2013, **138**, 6001-6006.
41. Z. Chen, K. M.-C. Wong, E. C.-H. Kwok, N. Zhu, Y. Zu and V. W.-W. Yam, *Inorganic chemistry*, 2011, **50**, 2125-2132.
42. X. Tong, P. Sheng, Z. Yan, T. Tran T, X. Wang, J. Cai and Q. Cai, *Sensors and Actuators B: Chemical*, 2014, **198**, 41-48.
43. M. Wasil, B. Halliwell, M. Grootveld, C. P. Moorhouse, D. C. Hutchison and H. Baum, *Biochemical Journal*, 1987, **243**, 867-870.
44. C. Song and J. Zhang, *PEM fuel cell electrocatalysts and catalyst layers*, Springer, Editon edn., 2008, pp. 89-134.
45. H. Han, Z. Sheng and J. Liang, *Analytica chimica acta*, 2007, **596**, 73-78.
46. E. Yeager, *Journal of Molecular Catalysis*, 1986, **38**, 5-25.
47. H. Jiang and H. Ju, *Analytical chemistry*, 2007, **79**, 6690-6696.
48. G. Zou and H. Ju, *Analytical chemistry*, 2004, **76**, 6871-6876.
49. L. Dennany, M. Gerlach, S. O'Carroll, T. E. Keyes, R. J. Forster and P. Bertoncello, *Journal of Materials Chemistry*, 2011, **21**, 13984-13990.
50. S. K. Poznyak, D. V. Talapin, E. V. Shevchenko and H. Weller, *Nano Letters*, 2004, **4**, 693-698.
51. M.-h. Shao, P. Liu and R. R. Adzic, *Journal of the American Chemical Society*, 2006, **128**, 7408-7409.
52. J. A. Imlay, *Annual review of biochemistry*, 2008, **77**, 755.

53. P. Guyot-Sionnest and C. Wang, *The Journal of Physical Chemistry B*, 2003, **107**, 7355-7359.
54. C. Wang, M. Shim and P. Guyot-Sionnest, *Science*, 2001, **291**, 2390-2392.
55. S. Singh, A. Chaubey and B. D. Malhotra, *Analytica Chimica Acta*, 2004, **502**, 229-234.
56. X.-L. Luo, J.-J. Xu, Y. Du and H.-Y. Chen, *Analytical Biochemistry*, 2004, **334**, 284-289.
57. W. Miao, *Chemical Reviews*, 2008, **108**, 2506-2553.
58. B. Pettinger, H. R. Schöppel and H. Gerischer, *Berichte der Bunsengesellschaft für physikalische Chemie*, 1976, **80**, 849-855.

*Chapter 4 - Optimisation of electrogenerated
chemiluminescent performance of 800 nm CdSeTe/ZnS
quantum dots*

4.1 Introduction

The potential benefits of NIR emitting species in biosensing and imaging applications have been well documented because of their improved penetrability through biological samples and reduced tissue autofluorescence.^{1,2} This can provide more detailed and better defined images for deep tissue imaging. For biosensing, it opens up opportunities for development of systems with detection directly from whole blood samples, negating the requirement for time-consuming and expensive sample preparation procedures.

NIR emitting QDs are beginning to emerge as leaders in this field as a result of their excellent optical properties, large surface-to-volume ratio and surface modification opportunities.³ They have successfully been used within *in vivo* imaging studies,⁴⁻⁸ however, there has been limited work on their application within ECL biosensing platforms.^{9, 10} The research reviewed in chapter 3 demonstrated the flexibility of NIR QDs, which can generate an ECL signal with a variety of co-reactant systems. Therefore, the next stage of development was the optimisation of these conditions to obtain the most sensitive, responsive and stable ECL signal. This has not been done previously with NIR QDs and there is thus a clear requirement for such investigations.

The aim of this work was to determine the conditions under which optimal ECL performance was achieved using water-soluble NIR emitting QDs. A selection of criteria were selected for investigation and focused on the co-reactant, film composition, buffer and other electrochemical parameters.

4.2 Experimental

4.2.1 Apparatus

Electrochemical measurements were carried out using a CH instrument model 760D electrochemical analyser. All experiments were carried out using a conventional three-electrode assembly, consisting of a 3 mm diameter GC working electrode (unless otherwise stated), Pt wire counter electrode and Ag/AgCl reference electrode. Working electrodes were cleaned by successive polishing using 1, 0.3 and 0.05 μM alumina slurry, followed by sonication in ethanol and water, respectively, for 30 mins. The electrodes were then dried under a flow of N_2 gas. CV was carried out at a scan rate of 100 mV s^{-1} and sample interval of 1 mV across a potential range outlined in each figure. Measurements involving simultaneous detection of light and current utilised a CH instrument model 760D connected to a Hamamatsu H10723-20 PMT. The input voltage to the PMT was + 5 V and the control voltage was set between 0.5 and 1.05 V depending on the required sensitivity. The scan rate was 100 mV s^{-1} (unless otherwise stated). During electrochemical experiments, the cell was kept in a light-tight Faraday cage in a specially designed holder configuration where the working electrode was positioned directly above the PMT window. All measurements were made at room temperature.

4.2.2 Materials

Core-shell CdSeTe/ZnS QDs (Qdot® 800 ITK™ organic quantum dots, 1 μM in decane) were purchased from Invitrogen. 2-(dimethylamino)ethanethiol (DAET), Nafion® 117 solution, chitosan (medium molecular weight, 75-85% deacetylated), phosphate buffered saline (PBS, pH 7.4), potassium persulfate ($\text{K}_2\text{S}_2\text{O}_8$), hydrogen peroxide (H_2O_2), tripropylamine (TPA), sodium oxalate ($\text{Na}_2\text{C}_2\text{O}_4$), tris acetate-EDTA buffer (TAE), 4-Morpholineethanesulfonic acid hydrate (MES), sodium bicarbonate, sulfuric acid (H_2SO_4) and sodium hydroxide (NaOH) were all purchased from Sigma-Aldrich and used as

received. All other reagents used were of analytical grade, and all solutions were prepared in milli-Q water (18 mΩ cm).

4.2.3 Methods

Preparation of water soluble CdSeTe/ZnS core-shell QDs

The method followed was similar to that developed by Woelfle and Claus.¹¹ 0.5 mL of 0.5 M DAET in methanol was mixed with 0.25 mL of the CdSeTe/ZnS QDs in decane (1 μM). N₂ was bubbled through the solution for 5 mins, which was then sealed and left stirring overnight in the dark at room temperature. The QDs were then precipitated with an excess of acetone followed by centrifugation at 5000 rpm for 6 mins. The filtrate was removed and the precipitate was re-dispersed in 0.25 mL of distilled water. These water-soluble QDs were centrifuged for a further 6 mins at 3000 rpm to remove any impurities and then stored in darkness at 4°C.

Preparation of CdSeTe/ZnS core-shell QD-polymer composite films

A 0.1 % chitosan solution was prepared in 1 % acetic acid and sonicated for 5 mins. The QD/chitosan composite was prepared by mixing aliquots of the water-soluble QDs with the chitosan solution in a 1:1 (v/v) ratio and mixing for 30 s. 3 μL of this composite was then carefully cast onto the electroactive portion of a GC electrode, with mixing of the composite for 10 s between electrodes. The film was allowed to dry for 1 h at 4°C. A film of bare QDs was prepared in the same manner, with water used instead of chitosan. A film of bare QDs and QD-nafion was prepared in the same manner, with water and 0.1 % Nafion 117 in MeOH/H₂O (4/1) used instead of chitosan respectively. The polymer concentration was altered by changing the concentration of its stock solution pre-dilution with the QDs.

QD concentration in the film was altered by mixing the water-soluble QDs with a suitable volume of water prior to mixing in a 1:1 (v/v) ratio with chitosan.

Preparation of co-reactant solutions

Co-reactant solutions of TPA, $\text{Na}_2\text{C}_2\text{O}_4$, H_2O_2 and $\text{K}_2\text{S}_2\text{O}_8$ were prepared in 0.1 M PBS (pH 7.4) at the concentrations outlined in each figure. Co-reactant free experiments were carried out in 0.1 M PBS (pH 7.4) only.

Preparation of buffer solutions

All buffers were prepared as 0.1 M solutions in distilled water (pH 7.4) following manufacturer guidelines. Buffer pH was altered through drop-wise addition of concentrated $\text{H}_2\text{SO}_4/\text{NaOH}$.

4.3 Optimisation of ECL performance

4.3.1 Film composition

ECL is regularly obtained from QD thin films that have been deposited onto an electrode surface.¹²⁻¹⁴ The benefit of this is QDs are pre-concentrated directly on the electrode surface and are therefore very close or within the ECL active zone. This results in stronger ECL signals than with solution phase QDs, where solubility problems and a lower concentration of QDs at the electrode surface can limit ECL intensity.¹⁵ Additionally, incorporation into a polymer film was required to minimise leaching into solution, a problem associated with a film of bare QDs due to their water solubility.¹⁶ As a result, NIR QDs were incorporated into a polymer film and deposited onto the electrode surface to maximise their ECL response and stability. Optimisation of film composition was therefore required.

4.3.1.1 Polymer type

The intended use of NIR QDs is within biosensors and as such the polymer had to be non-toxic and biocompatible, as well as cheap, readily available and electrically conductive without being an ECL emitter itself. Nafion and chitosan are both polymers that meet this criteria and have been used as film components in previous electrochemical systems.^{17, 18} Figure 4.1 shows the ECL response of these 800 nm QD/polymer films and a film of bare QDs.

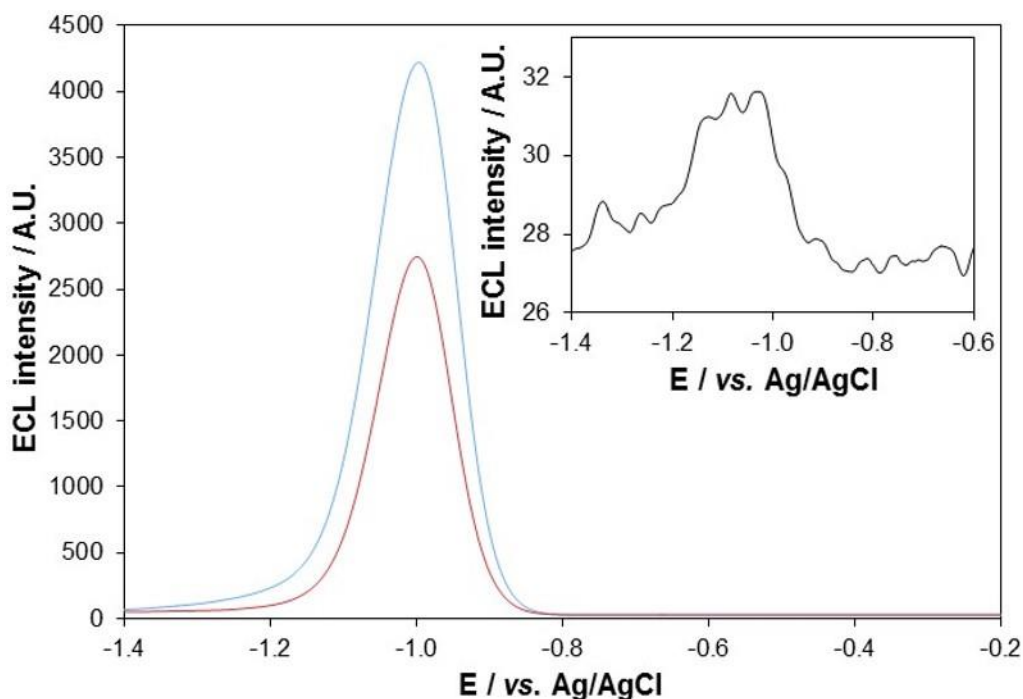


Figure 4.1 – Typical ECL response of 800 nm QD/chitosan film (red), bare 800 nm QDs (blue) and 800 nm QD/Nafion film (inset, black) with 0.1 mM $K_2S_2O_8$ at a scan rate of 100 mV s^{-1} over the potential range $-1.4 \leq v \leq -0.2 \text{ V vs. Ag/AgCl}$. PMT input voltage = 0.45 V.

ECL appears at approximately -0.75 V (-0.85 V with Nafion) and is centered at -1.00 V. The most intense signal is achieved with the bare QD film, which is 1.5 times more intense than the QD/chitosan film. The ECL signal from the QD/nafion film was very weak, approximately 130 and 85 times weaker than bare QDs and QD/chitosan film respectively. It has previously been reported that Nafion enhances the ECL signal of CdSe/ZnS QDs and other emitters through pre-concentration of QDs in the film.^{16, 19} However, with these QDs, which are passivated with the same ligand (DAET), the signal is significantly smaller and barely distinguishable from the background. Nafion is an inert cationic ion-exchange polymer that is ideal for immobilising positively charged species, such as these DAET-modified NIR QDs. Previous investigations have shown that Nafion is effective at excluding negatively charged species (such as $K_2S_2O_8$, the co-reactant used in Figure 4.1) due to its permselective properties.¹⁶ However, even with an alternative co-reactant (H_2O_2) that has been shown to exhibit an intense ECL response with visible-region QDs,¹⁶ the ECL signal remains very weak (Figure 4.2).

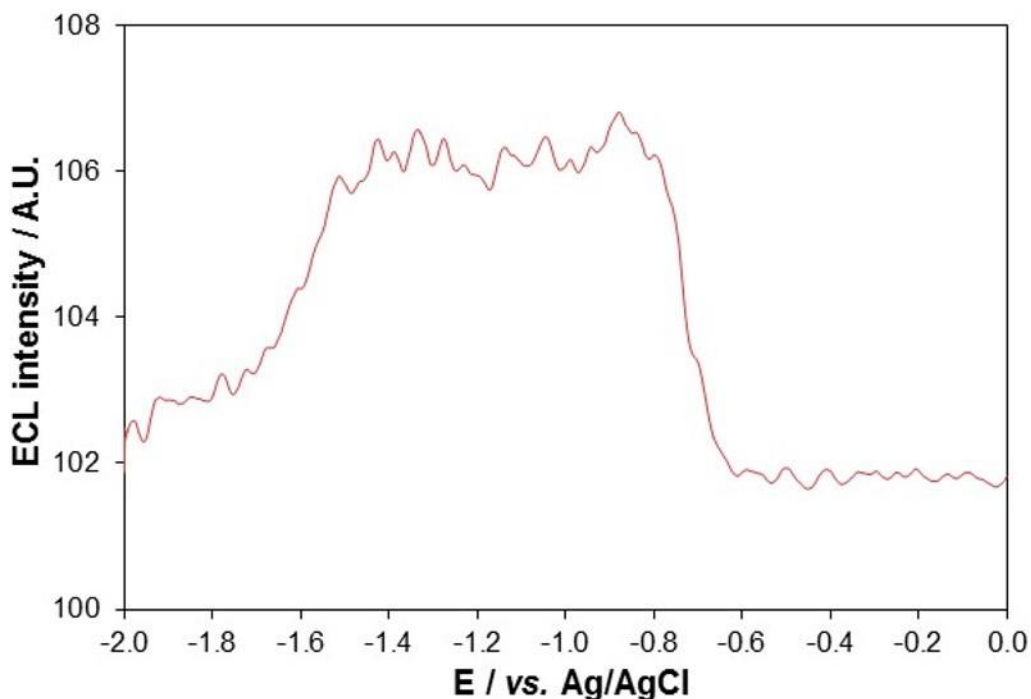


Figure 4.2 - Typical ECL response of 800 nm QD/Nafion film in 1 mM H₂O₂ at a scan rate of 100 mV s⁻¹ over the potential range $-2 \leq v \leq 0$ V vs. Ag/AgCl. PMT input voltage = 0.45 V.

This suggests that something other than co-reactant permeability is inhibiting the ECL response. Pre-concentration of QDs within Nafion may actually decrease the contact area between them and the electrode, inhibiting efficient electron transfer and limiting the concentration of electrogenerated QD precursors. Interactions between positively charged QDs and Nafion could also affect their contact with the electrode surface, further limiting the generation of QDs($e^-(1S_e)$).

Chitosan is a naturally occurring, linear polysaccharide that is positively charged in neutral and acidic conditions owing to the amino group in its backbone.²⁰ It is ideal for use in biological systems due to its biocompatibility and non-toxicity.²¹ The decrease in ECL intensity of the QD/chitosan film compared to bare QDs is caused by a variety of contributing factors. Firstly, the number of QDs in direct contact with the electrode surface will fall as they are now confined within a film, so the concentration of electrogenerated QDs($e^-(1S_e)$)

($1S_e$) will decrease. Secondly, the application of a chitosan film onto the electrode surface will affect electrical conductivity. In its parent form, chitosan has a very low electrical conductivity due to strong bonding of its hydrogen atoms that cannot move under the action of an electric field. Incorporation of electrolyte into the film following immersion in solution permits conduction, however, the rate of electron transfer will be influenced by this change in environment, which will affect the production of ECL precursor species. Thirdly, the presence of a polymer film may hinder the diffusion and interaction of electrogenerated precursor species, which must interact with one another to form an activated complex before electron transfer (and the subsequent formation of QDs*) can occur. Finally, the presence of a polymer film on the electrode surface can effectively block certain sites on the electrode surface, decreasing the area available for heterogeneous electron transfer reactions. A film of bare QDs is in direct contact with both the electrode surface and co-reactant solution and so formation of precursor species can occur more readily and their subsequent interaction to generate QDs* occurs more rapidly. An increase in the rate of electron transfer between precursor species means the electron transfer process itself is more likely to occur (from the Frank-Condon principle, which states that the most instantaneous electron transfer is the most probable (see section 1.1.2)) and therefore the likelihood of generating an excited state increases.

However, reproducibility of the ECL response with bare QDs is very poor. This is because they 'fall off' the electrode surface when not confined and protected within a film due to their water-solubility. The response variability of these different QD films is shown in Figure 4.3.

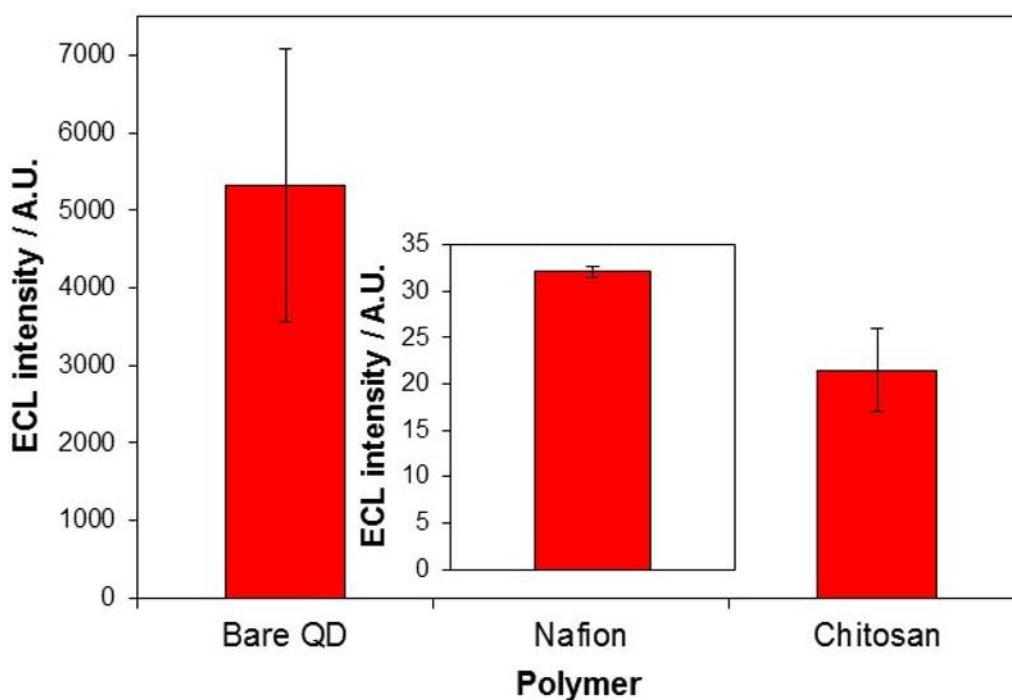


Figure 4.3 - Average ECL response of bare 800 nm QDs, 800 nm QD/Nafion film (inset) and 800 nm QD/chitosan film with 0.1 mM $K_2S_2O_8$ at a scan rate of 100 mV s^{-1} at -1 V vs. Ag/AgCl. Error bars represent standard deviations from triplicate data set. PMT input voltage = 0.45 V.

This data shows greater response stability following incorporation of the QDs into a polymer film. As reproducibility is absolutely critical in the development of any biosensing system, a compromise must be made at the expense of optimal sensitivity. As the 800 nm QD/chitosan film generated the best combination of sensitivity and reproducibility, it was used for all future work.

4.3.1.2 Polymer concentration

The concentration of chitosan in the QD/chitosan film was investigated to determine the optimal concentration for ECL generation. Typically, 0-1% chitosan solutions are used with electrochemical analysis.^{22, 23} It has previously been shown (Figure 4.1) that QD/chitosan films suffer from poorer sensitivity than bare QDs. Therefore, the lower end of this concentration range was investigated. Figure 4.4 shows the effect of chitosan concentration on the observed ECL signal.

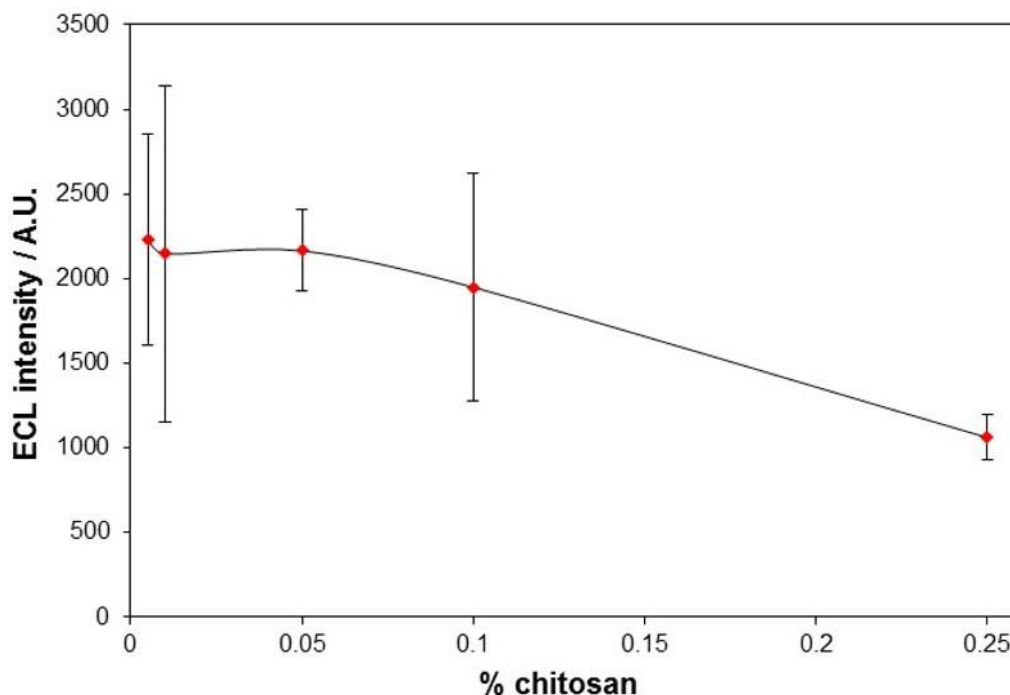


Figure 4.4 – Average ECL response of 800 nm QDs in a 0.005, 0.01, 0.05, 0.1 and 0.25 % chitosan film with 0.05 mM $K_2S_2O_8$ at a scan rate of 100 mV s^{-1} at -1 V vs. $Ag/AgCl$. Error bars represent standard deviations from triplicate data set. PMT input voltage = 0.50 V .

For 0.005, 0.01 and 0.05 % chitosan, the average ECL intensity remains fairly constant, whilst at higher chitosan concentrations the ECL signal decreases. This decrease is a result of increasingly inhibited electron transfer and diffusion of precursor species through the polymer as it becomes more concentrated. Fewer excited state QDs will be formed and the ECL intensity decreases. At 0.005 and 0.01% chitosan, the response variability is large as QD protection within the film is minimal. Leaching of the QDs into the surrounding solution was a problem at these concentrations, which could be seen with the naked eye upon insertion of the modified electrode into solution. A film containing 0.05% chitosan did not diminish the ECL intensity by an appreciable extent and improved QD protection, reducing response variability. This chitosan concentration was therefore selected for future film preparations.

4.3.1.3 QD concentration

QD concentration within the polymer film was investigated across the range 0.0145-0.232 μM . The upper limit of this range was determined by the concentration of the stock solution. This must be diluted in chitosan in order to construct the film. The concentration of the QD stock solution after ligand exchange was determined using optical absorption from a series of standards. The calibration graph is shown in Figure 4.5. From this calibration graph, the concentration of the ligand exchanged QD stock was calculated at 0.464 μM . Figure 4.6 shows the effect of QD concentration on the observed ECL intensity.

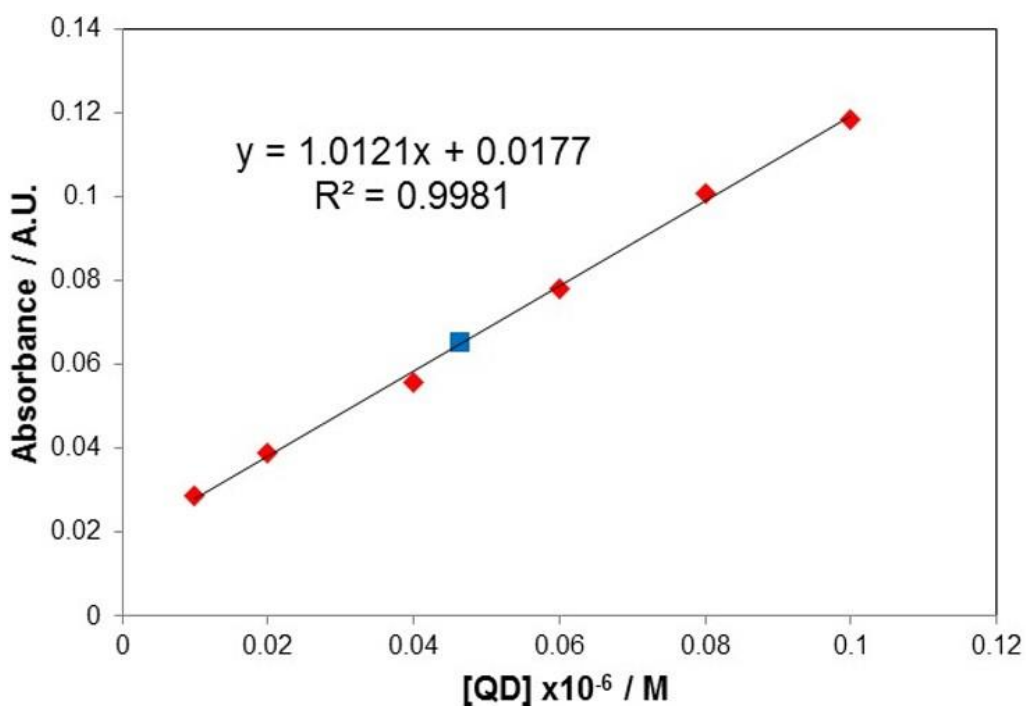


Figure 4.5 - Optical absorbance (at 450 nm) of 800 nm QD standards (red) and 800 nm ligand exchanged QD stock solution (blue).

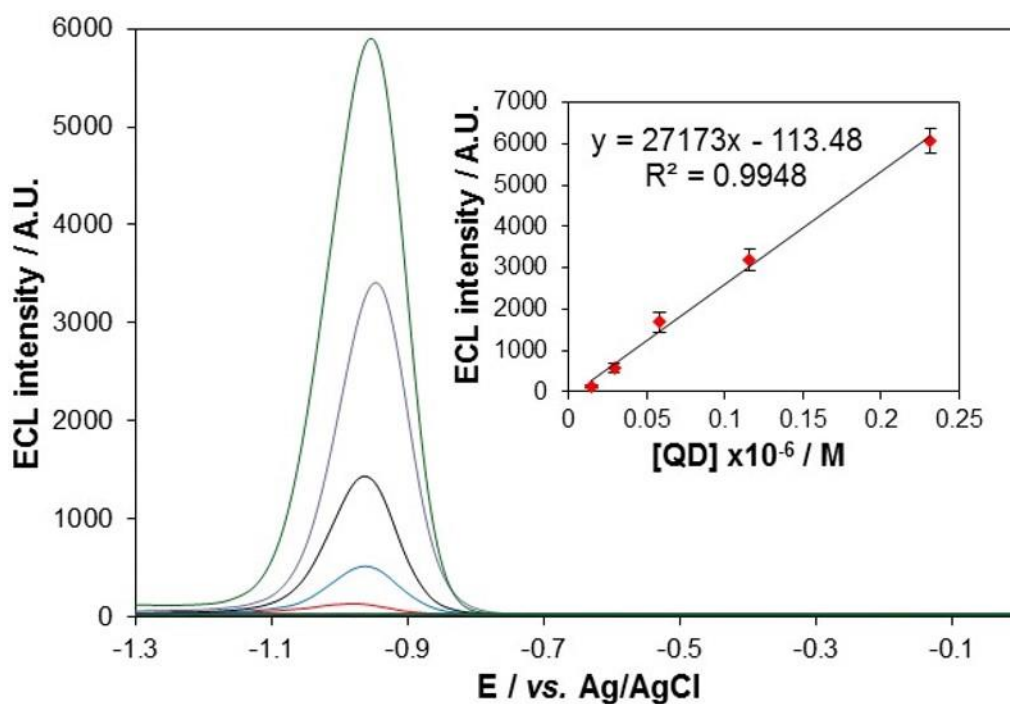


Figure 4.6 - Typical ECL response of 0.0145 (red), 0.029 (blue), 0.058 (black), 0.116 (purple) and 0.232 (green) μM 800 nm QDs in a 0.05 % chitosan film with 0.01 mM $\text{K}_2\text{S}_2\text{O}_8$ at a scan rate of 100 mV s^{-1} over the potential range $-1.3 \leq v \leq 0 \text{ V vs. Ag/AgCl}$. Inset shows linear dependence of this ECL response on [QD], in 0.01 mM $\text{K}_2\text{S}_2\text{O}_8$ at -1 V vs. Ag/AgCl . Error bars represent standard deviations from triplicate data set. PMT input voltage = 0.60 V.

This shows a linear dependence of ECL intensity on QD concentration across the investigated range. As the concentration of QDs in the film increases, the number available for electron injection also increases. This is confirmed by examining the reduction peak at -1.80 V , which has previously been related to direct reduction of the QDs (section 2.3.2.1 and 2.3.2.2). Figure 4.7 shows the effect of increasing QD concentration on the peak current at -1.80 V .

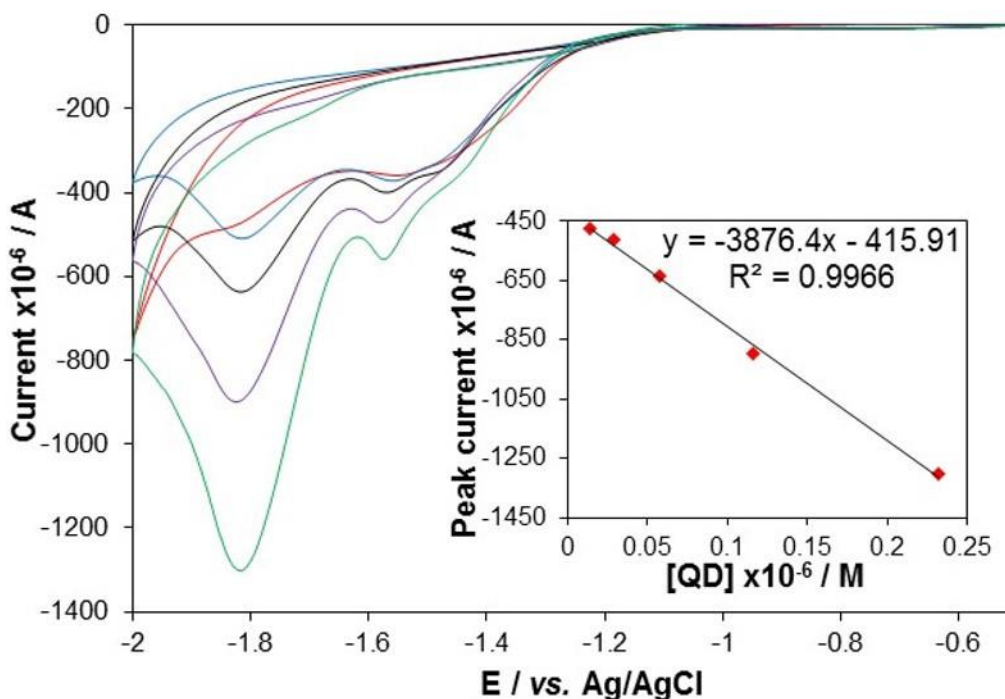


Figure 4.7 - Current response of 0.0145 (blue), 0.029 (red), 0.058 (black), 0.116 (purple) and 0.232 (green) μM 800 nm QDs in a chitosan film in 0.01 mM $\text{K}_2\text{S}_2\text{O}_8$ at a scan rate of 100 mV s^{-1} over the potential range $-2 \leq v \leq -0.5 \text{ V vs. Ag/AgCl}$. Inset shows the linear dependence of the peak current at $\sim -1.8 \text{ V vs. Ag/AgCl}$ on [QD] at a scan rate of 100 mV s^{-1} .

A linear relationship exists between peak current at -1.80 V and QD concentration, demonstrating an increase in the number of QDs available for electron injection at the electrode surface. A greater concentration of QDs (e^- (1S_e)) increases the probability of a successful electron transfer reaction taking place. Provided this is with a suitably strong reducing agent, a greater number of excited state QDs will form. This leads to an increase in QD/chitosan film ECL intensity.

Previous work has shown that high concentrations of QDs can actually lead to a reduction in ECL intensity.²⁴ This is caused by self-quenching of the emitted light due to extensive overlap of the absorption and emission profiles of QDs. This is not observed with these QDs, which could be due to their limited concentration in this procedure and may still occur at concentrations above that examined. These results show the maximum QD concentration should be

used, which is governed by the concentration of the stock solution. Therefore, 0.232 μM QDs was selected as the optimal concentration.

4.3.1.4 QD/chitosan film volume

Thin film drop-casting was used as the technique for electrode modification with QDs. This technique is routinely used in electrochemistry as a method of immobilising species on the electrode surface due to its simplicity and effectiveness.²⁵⁻²⁷ Drop-cast volume determines film thickness and the number of QDs present on the electrode surface, and so was examined in order to establish its effect on ECL intensity (Figure 4.8).

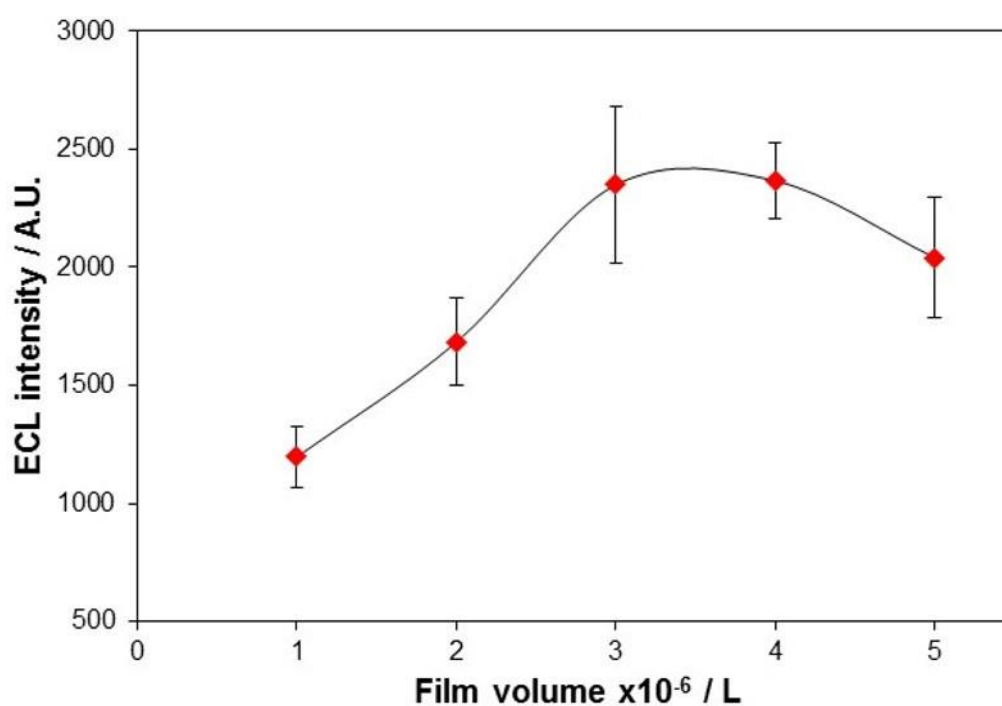


Figure 4.8 - Average ECL response of increasing volumes of 800 nm QD/chitosan film with 0.1 mM $\text{K}_2\text{S}_2\text{O}_8$ at a scan rate of 100 mV s^{-1} at $\sim -1 \text{ V}$ vs. Ag/AgCl. Error bars represent standard deviations from triplicate data set. PMT input voltage = 0.50 V.

This shows an increase in ECL intensity from 1 to 3 μL , which begins to decrease when volumes above 4 μL are drop-cast onto the electrode surface. The initial increase in intensity is related to a rise in the number of QDs in the

polymer film. This permits formation of a higher concentration of QDs($e^-(1S_e)$) at the electrode surface that can take part in ECL emitting reactions. Figure 4.9 shows the voltammograms for each of these drop-cast volumes, confirming that an increase in film volume is accompanied by a consistent increase in the number of QDs present.

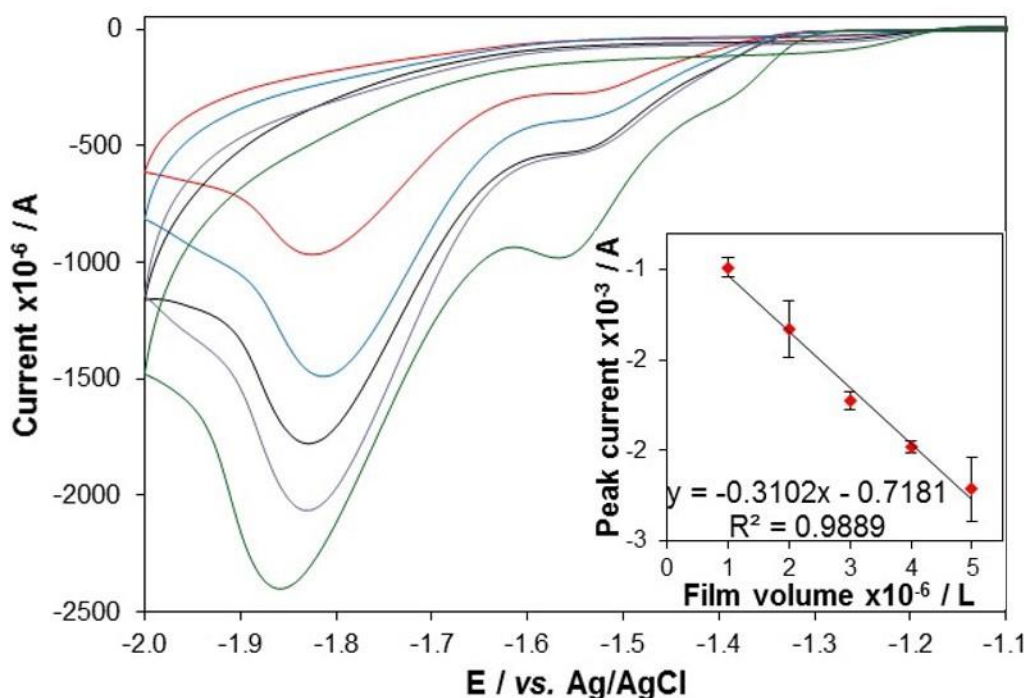


Figure 4.9 - Typical current response of 800 nm QD/chitosan film with a drop-cast volume of 1 (red), 2 (blue), 3 (black), 4 (purple) and 5 (green) μL in 0.1 mM $\text{K}_2\text{S}_2\text{O}_8$ at a scan rate of 100 mV s^{-1} over the potential range $-2 \leq v \leq -1.1 \text{ V vs. Ag/AgCl}$. Inset shows the linear dependence of the peak current at $\sim -1.8 \text{ V vs. Ag/AgCl}$ on film volume at a scan rate of 100 mV s^{-1} . Error bar represent standard deviations from triplicate data set.

Peak current at -1.80 V has been related to QD concentration (Figure 4.7). Figure 4.9 shows an increase in this peak current as film volume increases, indicating an increase in the number of QDs within the film available for heterogeneous electron transfer. This peak current gradually shifts by approximately 50 mV towards -1.85 V as the film volume increases, which shows electron transfer kinetics decrease as the film becomes thicker. These competing processes, namely an increase in ECL intensity associated with a higher QD concentration, along with inhibition of ECL intensity due to slower

electron transfer, results in an increase in intensity from 1 - 3 μL drop-cast volume, followed by a plateau and subsequent decline in intensity from 3 - 5 μL . At these larger volumes, the number of QDs in the film continues to increase (Figure 4.9), however, the decrease in film conductivity and electron transfer kinetics associated with a thicker film^{28, 29} begins to dominate within the system, causing a reduction in observed ECL intensity. Diffusion of co-reactant molecules to the electrode surface will also be affected due to slower diffusion through a thicker film.³⁰ This will influence the rate at which ECL precursor species are formed and the resulting ECL intensity. These results show that a QD/chitosan drop-cast volume of 3 μL generated the optimal ECL response.

Overall, these results have shown that film composition plays an important role in NIR QD ECL performance. Optimum film composition has been established, with the final parameters outlined in Table 4.1.

Table 4.1 – Optimum film composition for generation of ECL response from 800 nm QDs.

Parameter	Optimum
Polymer	Chitosan
Polymer concentration	0.05%
QD concentration	0.232 \pm 0.017 μM
Dropcast volume	3 \pm 0.03 μL

4.3.2 Co-reactant

4.3.2.1 Co-reactant selection

In order to develop a highly sensitive ECL system, a number of co-reactants were examined to ensure maximum performance for these NIR QDs. As biomedical diagnostics continually drives towards improved biosensor sensitivities, this is a key parameter in the development of any sensing system.

Work described in chapter 3 illustrated that a NIR QD ECL response can be generated in the presence of commonly used cathodic ($K_2S_2O_8$ and H_2O_2) and anodic (TPA and $Na_2C_2O_4$) region co-reactants, which were shown to enhance ECL intensities compared to co-reactant free systems. Therefore, these co-reactants were selected for investigation with the aim of determining which system provided optimal ECL performance. A comparison of the ECL response from these co-reactants is shown in Figure 4.10.

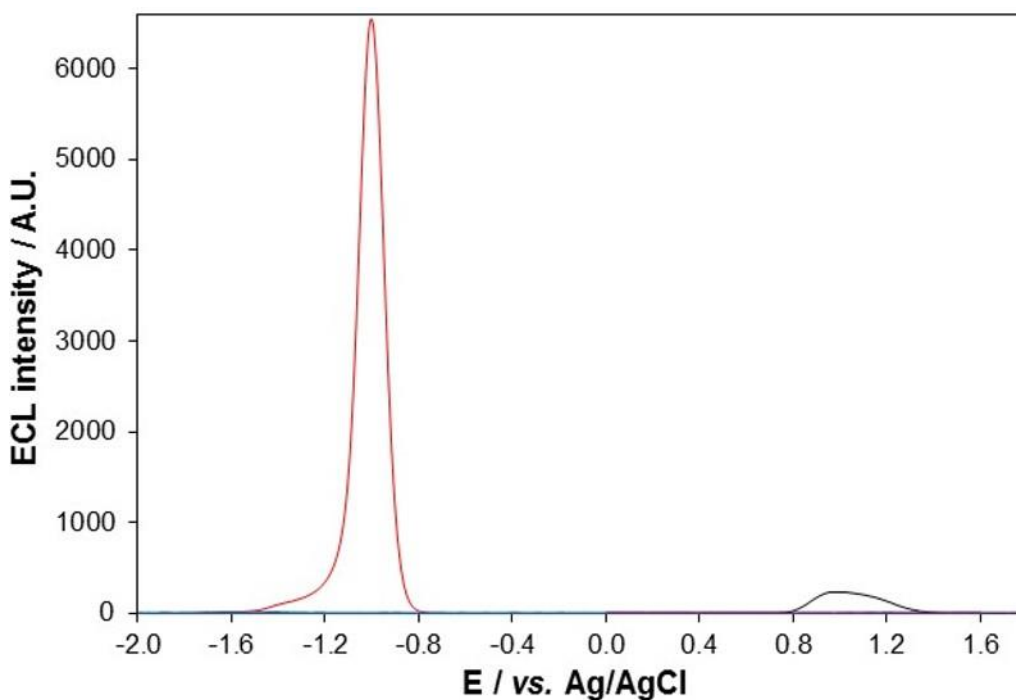


Figure 4.10 - ECL response of 800 nm QD/chitosan film with 1 mM $K_2S_2O_8$ (red), 1 mM H_2O_2 (blue), 1 mM TPA (black) and 1 mM $Na_2C_2O_4$ (purple) at a scan rate of 100 mV s^{-1} over the potential range $-2 \leq v \leq 1.8 \text{ V vs. Ag/AgCl}$. PMT input voltage = 0.50 V.

It is clearly evident from Figure 4.10 that $K_2S_2O_8$ generates the most intense ECL response from NIR QDs that have been confined to the electrode surface. This is followed by TPA, H_2O_2 and $Na_2C_2O_4$. Table 4.2 shows the maximum ECL intensity attained with each co-reactant.

Table 4.2 – Maximum ECL intensity of 800 nm QD/chitosan film in a selection of co-reactant systems. PMT input voltage = 0.50 V.

Co-reactant	Maximum ECL intensity / A.U.
$K_2S_2O_8$	6550
H_2O_2	14
TPA	230
$Na_2C_2O_4$	6

This data illustrates that maximum ECL intensity was obtained with $K_2S_2O_8$, which was over 450 times greater than with alternative cathodic co-reactant, H_2O_2 . It was 30 times greater than with TPA and over 1100 times greater than with $Na_2C_2O_4$. With anodic co-reactants, maximum ECL intensity was 40 times greater in TPA compared to $Na_2C_2O_4$. Figure 4.11 shows a clearer image of the ECL response with H_2O_2 , TPA and $Na_2C_2O_4$ using more sensitive PMT settings, confirming the trend in sensitivity is $TPA > H_2O_2 > Na_2C_2O_4$.

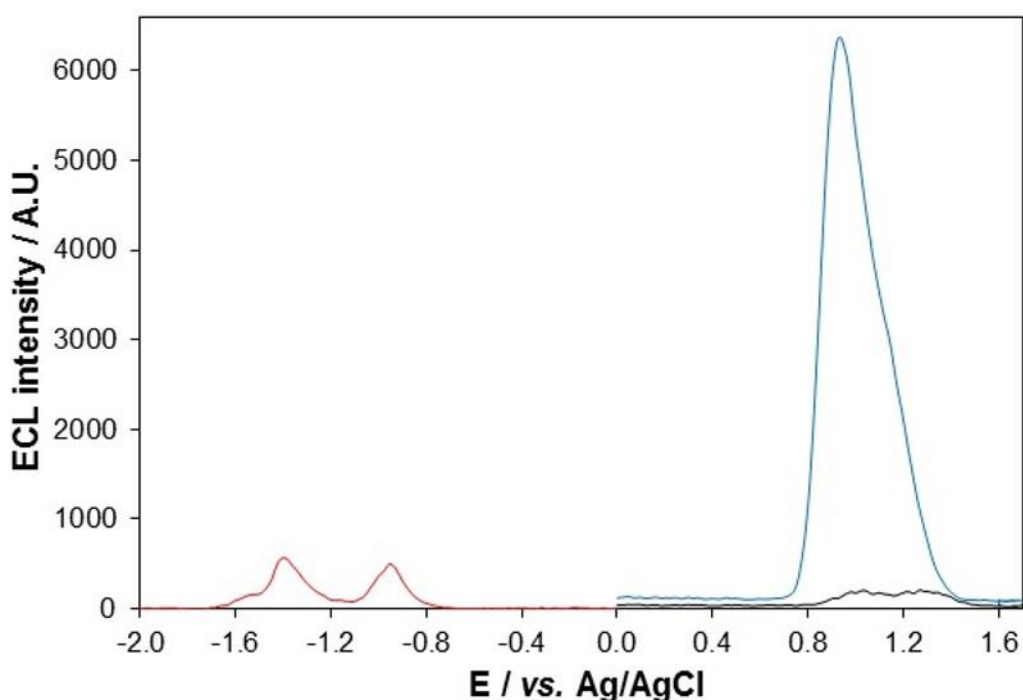


Figure 4.11 - ECL response of 800 nm QD/chitosan film with 1 mM H_2O_2 (red), 1 mM TPA (blue) and 1 mM $Na_2C_2O_4$ (black) at a scan rate of 100 mV s^{-1} over the potential range $-2 \leq v \leq 1.8 \text{ V vs. Ag/AgCl}$. PMT input voltage = 0.75 V.

For cathodic ECL, one of the key reactions in the formation of excited state QDs is the injection of a hole into the $1S_h$ orbital of a negatively charged QD.³¹ This occurs through interaction with a suitably strong reducing agent – $SO_4^{\cdot-}$ and OH^{\cdot} for $K_2S_2O_8$ and H_2O_2 co-reactants respectively (section 3.3.1.1). Rapid band-edge recombination of this excited state QD dominates over any oxidation processes, protecting destruction of the QDs following hole injection and allowing efficient ECL production.³¹ The rate of this intermolecular electron transfer between a negatively charged QD and the oxidising agent is a major factor in the generated ECL intensity.³² Therefore, the strength of the oxidising agent has a critical impact on the observed ECL intensity. The standard redox potential (vs. Ag/AgCl) for the $SO_4^{\cdot-}/SO_4^{2-}$ couple is approximately 3.16 V,³³ whereas for the OH^{\cdot}/OH^- couple it is 2.16 V (vs. Ag/AgCl) at physiological pH.¹³ Figure 4.12 shows a comparison of the energetics of these species with the QD HOMO and LUMO levels (section 3.3), and their interactions during the ECL process.

Both oxidising species are capable of hole injection into the $1S(h)$ quantum confined orbital of the NIR QDs. This can be seen in both Figure 4.12 as well as the fact that an ECL response is observed with both co-reactants. The greater oxidising strength of $SO_4^{\cdot-}$ compared to OH^{\cdot} results in more efficient generation of QD excited states. This manifests itself as an increase in ECL intensity with the $K_2S_2O_8$ system. It must be noted that the double peak nature of the ECL profile in H_2O_2 will likely influence the ECL intensity of the H_2O_2 sensitive peak (peak 2, section 3.3.1.1). This is because the concentration of QDs($e^-(1S_e)$) for interaction with OH^{\cdot} will have been diminished following consumption during generation of peak 1.

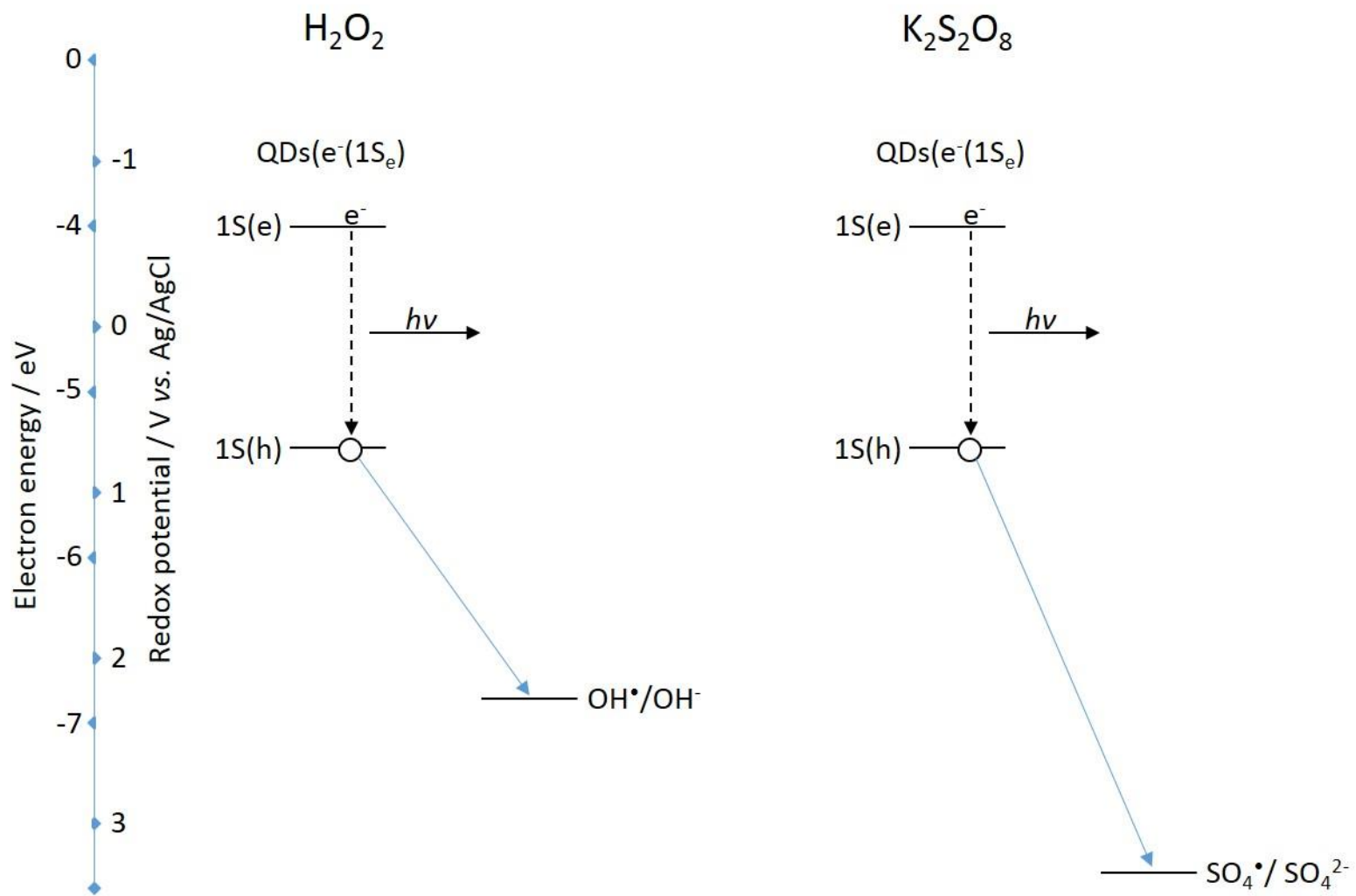


Figure 4.12 - Significant energy level interactions and resulting ECL process of 800 nm QDs with H_2O_2 and $\text{K}_2\text{S}_2\text{O}_8$ co-reactants.

For anodic ECL, one factor affecting intensity is the ability of the electrogenerated co-reactant species to inject an electron into the $1S(e)$ energy level of oxidised QDs. Figure 4.13 shows a comparison of the energetics of these co-reactant species (TPA $^{\bullet}$ and CO $_2^{\bullet-}$ (section 3.3.1.1)) with the QD HOMO and LUMO levels (section 3.4) and their interactions during the ECL process. The standard redox potential of TPA $^{\bullet}$ /P, where P is the products of TPA $^{\bullet}$ oxidation, is approximately -1.70 V (vs. Ag/AgCl)³⁴ and that of CO $_2^{\bullet-}$ /CO $_2$ is approximately -2.00 V (vs. Ag/AgCl).³⁵

The stronger reducing power of CO $_2^{\bullet-}$ compared to TPA $^{\bullet}$ does not result in a more intense ECL signal (Table 4.2), as would be expected due to faster homogenous electron transfer with QDs($h^+(1S_h)$). This means another factor is affecting excited state formation in this system. This has been discussed in section 3.3.1.1 and is related to consumption of QDs($h^+(1S_h)$) during electrogeneration of CO $_2^{\bullet-}$. The result is that ECL intensity of the QD/TPA system is significantly greater, as electrogeneration of TPA $^{\bullet}$ can occur directly at the electrode surface, even though homogeneous electron transfer kinetics in this system are likely slower.

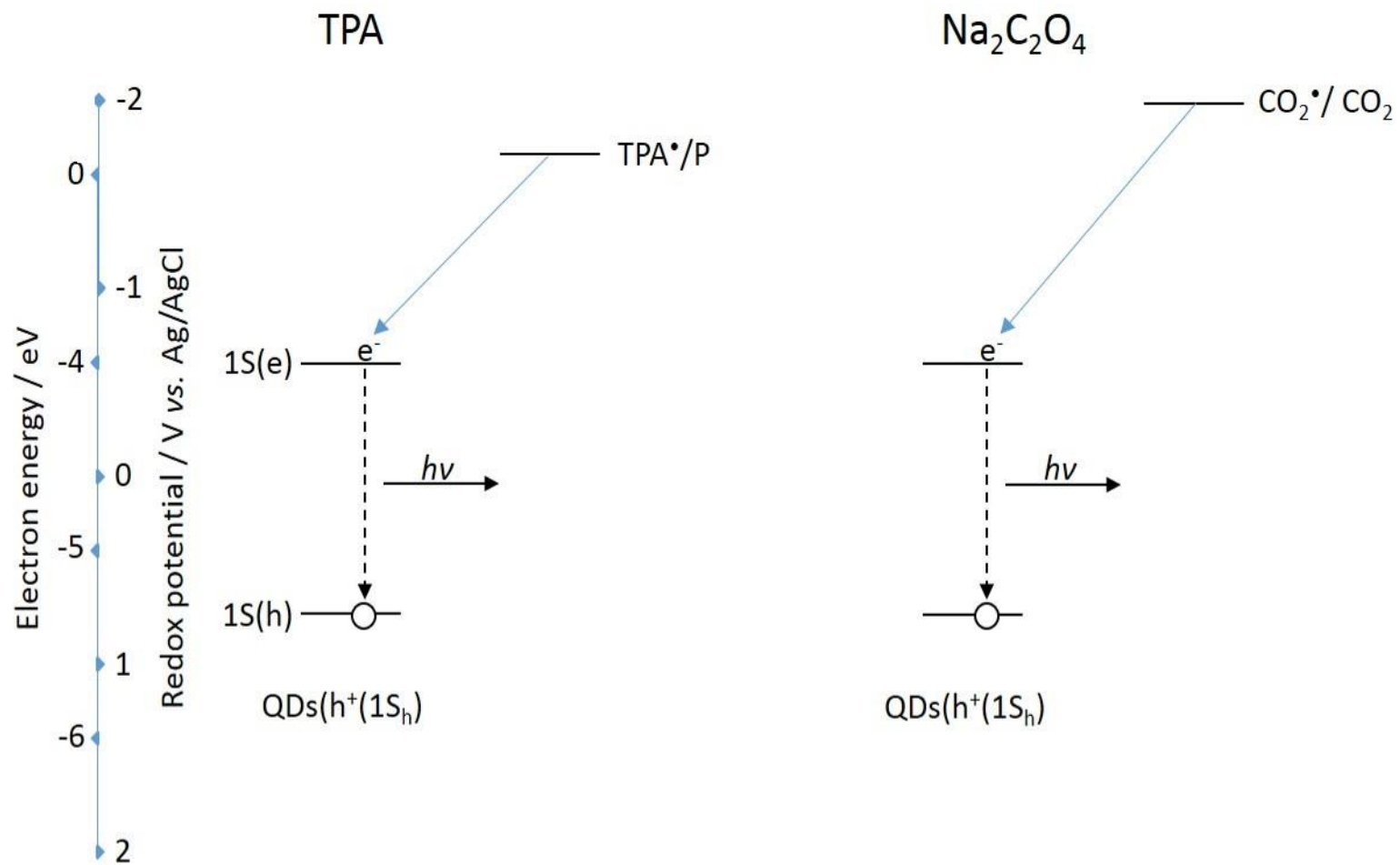


Figure 4.13 - Significant energy level interactions and resulting ECL process of 800 nm QDs with TPA and Na₂C₂O₄ co-reactants.

These results clearly show that maximum NIR QD ECL sensitivity is achieved in the cathodic region with $K_2S_2O_8$ co-reactant. Development of NIR QD ECL systems that require maximum sensitivity should therefore focus on cathodic ECL with this co-reactant. The data has also shown that H_2O_2 and TPA are suitable co-reactants, however, a limited response with $Na_2C_2O_4$ suggests it is unsuitable for use in this system.

Co-reactant free systems

As co-reactant free systems have been shown to generate a NIR QD ECL response (sections 3.3.1.1 and 3.3.2.1), the relative intensity of these systems was compared to determine which region exhibited maximum ECL performance (Figure 4.14).

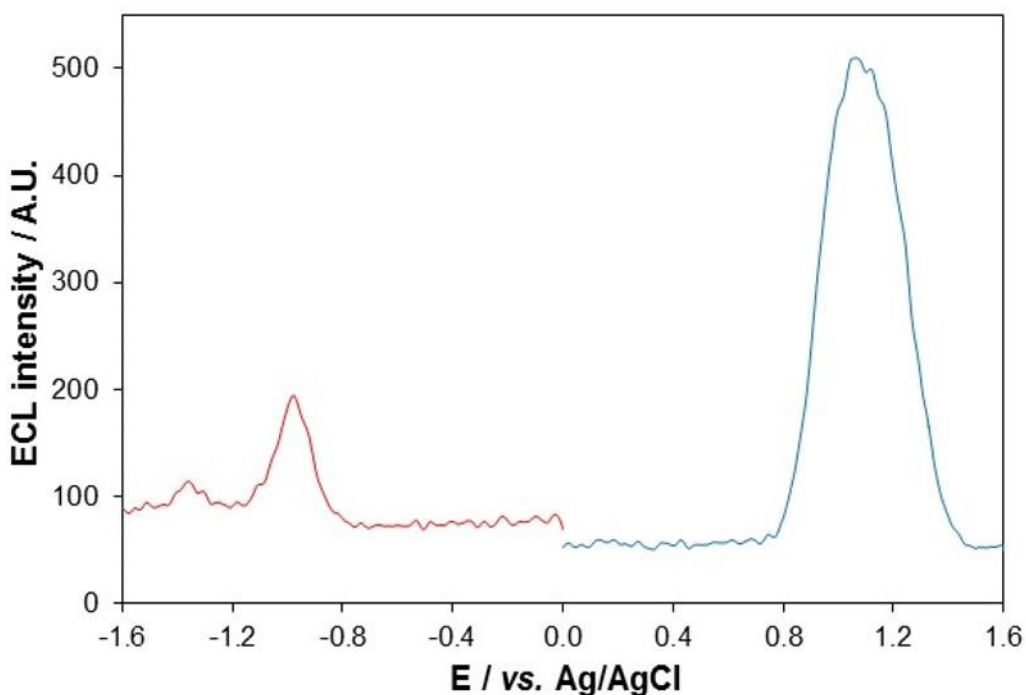


Figure 4.14 - ECL response of 800 nm QD/chitosan film in 0.1 M PBS at a scan rate of 100 mV s^{-1} over the potential range $-1.6 \leq v \leq 0 \text{ V}$ (red) and $0 \leq v \leq 1.6 \text{ V}$ (blue) vs. Ag/AgCl. PMT input voltage = 0.75 V.

This shows an anodic ECL intensity approximately 5 times greater than the responsive cathodic ECL peak (at -1.35 V). This is because the reductive ECL

pathway (section 3.3.2.1) involves OH^\bullet , which is formed from H_2O_2 , a 2-electron intermediate of the ORR. Its concentration at the electrode surface will therefore be low as its formation is reliant upon a number of preceding reactions. In the anodic region, superoxide has been shown to be capable of injecting an electron into $1\text{S}(\text{e})$ (section 3.3.1.1). The energetics of this process are discussed in section 3.3.1.1, Figure 3.6. ECL intensity may also be affected by the relative stability of superoxide compared to OH^\bullet , 99% of which has been shown to interact with CO_2 , O_2 , another OH^\bullet or H_2O_2 within 5 μs of its formation.³⁶ The half-life of $\text{O}_2^{\bullet-}$ is in the order of μs ,³⁷ which compares to a half-life in the ns range for OH^\bullet .³⁸ Therefore, the concentration of $\text{O}_2^{\bullet-}$ available for electron transfer with QDs should be much greater than the concentration of OH^\bullet , which explains the superior ECL intensity with $\text{O}_2^{\bullet-}$ co-reactant.

4.3.2.2 Co-reactant concentration

The next step of optimisation focused on determining the concentration of $\text{K}_2\text{S}_2\text{O}_8$ that produced the most intense ECL signal with NIR QDs. The results are shown in Figure 4.15.

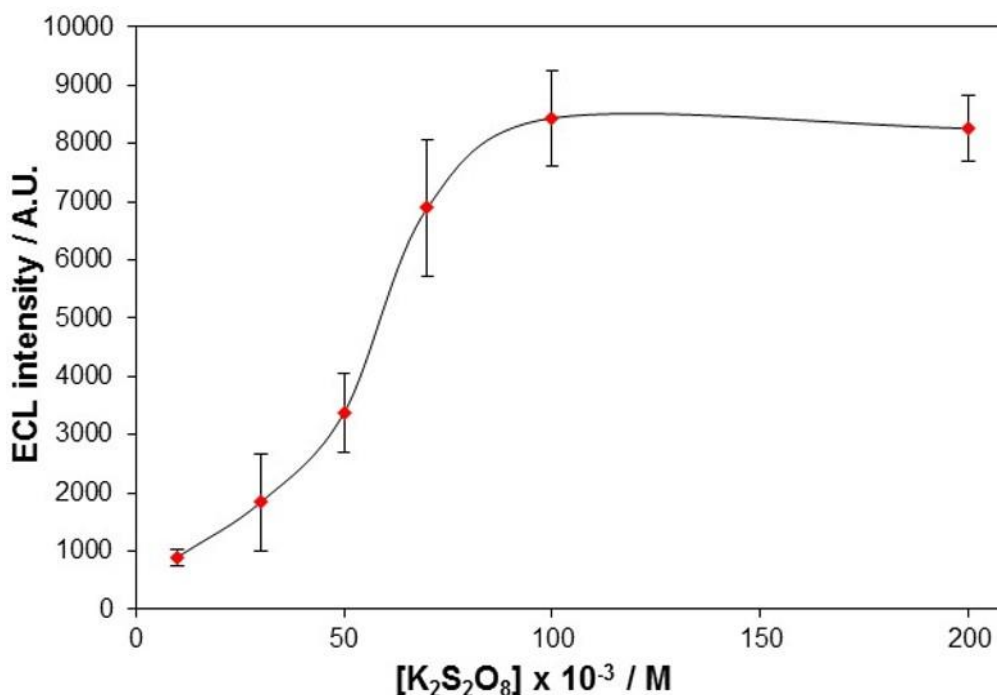
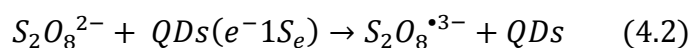
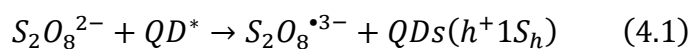


Figure 4.15 - ECL response of 800 nm QD/chitosan film with increasing concentrations of K₂S₂O₈ at a scan rate of 100 mV s⁻¹ at ~ -1.3. V vs. Ag/AgCl. Error bars represent standard deviations from triplicate data set. PMT input voltage = 1.00 V.

The data shows an increasing ECL intensity up to 100 mM K₂S₂O₈, above which the response begins to plateau. This is related to an increase in persulfate ion (S₂O₈²⁻) concentration that can then be reduced and decomposed to SO₄^{•-} for electron transfer with QDs(e⁻(1S_e)). A plateauing of ECL intensity is observed at high K₂S₂O₈ concentrations because S₂O₈²⁻ can act as an excited state quencher (equation (4.1)) and consume QDs(e⁻(1S_e)) (equation (4.2)).³⁹



The quenching process occurring in equation (4.1) will inhibit the ECL response through oxidation of excited state QDs. Consumption of QDs(e⁻(1S_e)) (equation (4.2)) will limit the formation of QDs*. These processes prevent a linear relationship between ECL intensity and K₂S₂O₈ concentration, as the signal is both generated and quenched by the same co-reactant

species. The data indicates maximum ECL intensity was achieved with 100 mM $K_2S_2O_8$.

4.3.3 Buffer

The main purpose of a buffer in this system is to maintain the pH at the electrode surface where redox reactions are occurring.⁴⁰ The type of buffer⁴¹ and pH^{24, 42} are known to influence ECL and so optimisation of these parameters was carried out.

4.3.3.1 Buffer selection

A number of buffers are routinely used in electrochemical bioassays and a selection were investigated to determine their influence on the ECL response. Each of these had a pK_a (Table 4.3) and useful pH range around physiological pH in order to maximise biocompatibility.

Table 4.3 - pK_a values of selected buffers.

<i>Buffer</i>	<i>pK_a (at 25°C)</i>
PBS	7.21
MES	6.10
TAE	8.07
Bicarbonate	6.10

PBS was chosen as it is one of the most commonly used buffers and is routinely used in electrochemistry.^{34, 43-45} MES was chosen as it is often used in biological assays, particularly for conjugation of biomolecules.^{46, 47} TAE is a commonly utilised, biocompatible buffer, often used with DNA.^{48, 49} The bicarbonate buffering system is essential in the maintenance of blood pH and is also a good buffer for use with antibodies.^{50, 51} Figure 4.16 shows the ECL response of a QD/chitosan film in these different buffers.

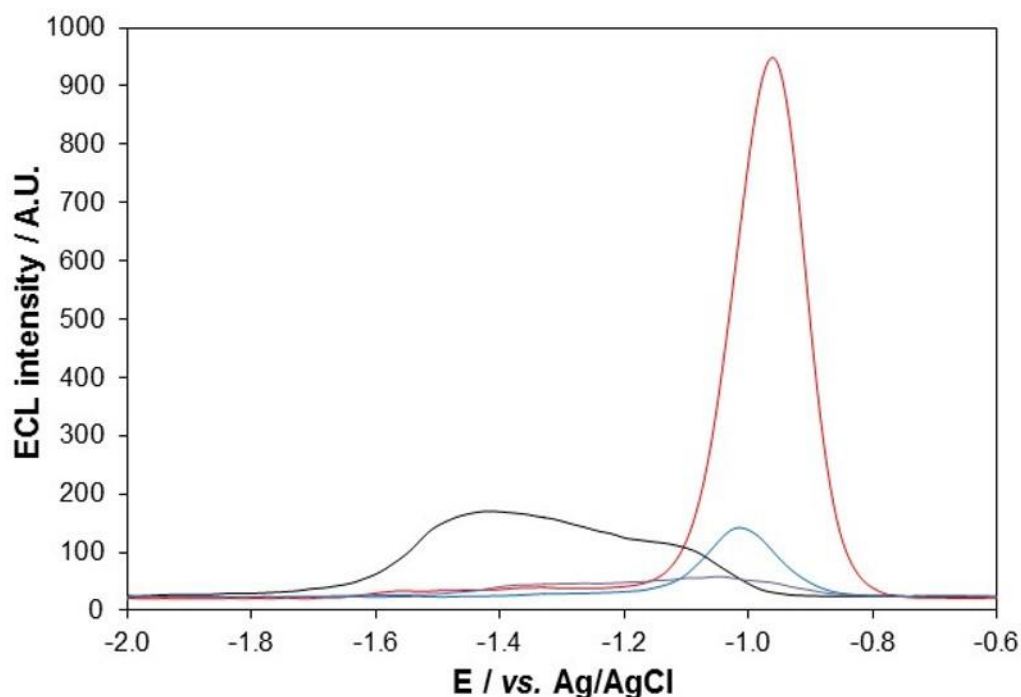


Figure 4.16 - ECL response of 800 nm QD/chitosan film with 0.01 mM $K_2S_2O_8$ in 0.1 M PBS (red), 0.1 M MES (blue), 0.1 M TAE (black) and 0.1 M bicarbonate (purple) buffer at a scan rate of 100 mV s^{-1} over the potential range $-2 \leq v \leq -0.6 \text{ V vs. Ag/AgCl}$. PMT input voltage = 0.50 V.

ECL in PBS, MES and bicarbonate appears and reaches a maximum at approximately -0.75 V and -1.00 V respectively. With TAE, this shifts to -0.90 V and -1.40 V. Increase in reduction potential associated with TAE denotes inhibited QD reduction, which may be due to the formation of a passivation layer around the positively charged QDs by EDTA, a well-established cation-binding hexadentate ligand.⁵² This will inhibit QD electron injection due to less efficient electron transfer through a thicker passivation layer, influencing both the appearance and intensity of ECL. Maximum ECL intensities are outlined in Table 4.4.

Table 4.4 – Maximum ECL intensity of 800 nm QD/chitosan film in different buffer systems containing 0.01 mM K₂S₂O₈. PMT input voltage = 0.50 V.

Buffer	Maximum ECL intensity / A.U.
PBS	949
MES	142
TAE	170
Bicarbonate	58

The ECL system in PBS buffer displayed the strongest ECL signal, which is approximately 6 times greater than MES and TAE and 16 times greater than bicarbonate.

The difference in ECL intensity could be caused by the different reactivities of buffering species towards electrogenerated precursors (QDs(e⁻(1S_e)) and SO₄^{•-}, in this case). As a strong oxidising agent, SO₄^{•-} is able to react with organic substrates to form radical cation species.⁵³ As a strong electrophile, it can also undergo a variety of other reactions involving organic compounds. It is particularly reactive towards carboxylate ions.^{53, 54} MES, TAE and bicarbonate all contain organic moieties that have the potential to interact with SO₄^{•-}, whereas PBS does not. This consumption of SO₄^{•-} by reactions not involved in ECL generation could explain the decrease in ECL intensity associated with these buffers.

4.3.3.2 Buffer pH

Buffer pH is known to influence ECL intensity as it can influence the rate and occurrence of redox processes.⁵⁵⁻⁵⁷ This will effect electrogeneration of ECL precursor species and so its impact on ECL performance was assessed (Figure 4.17 and Table 4.5).

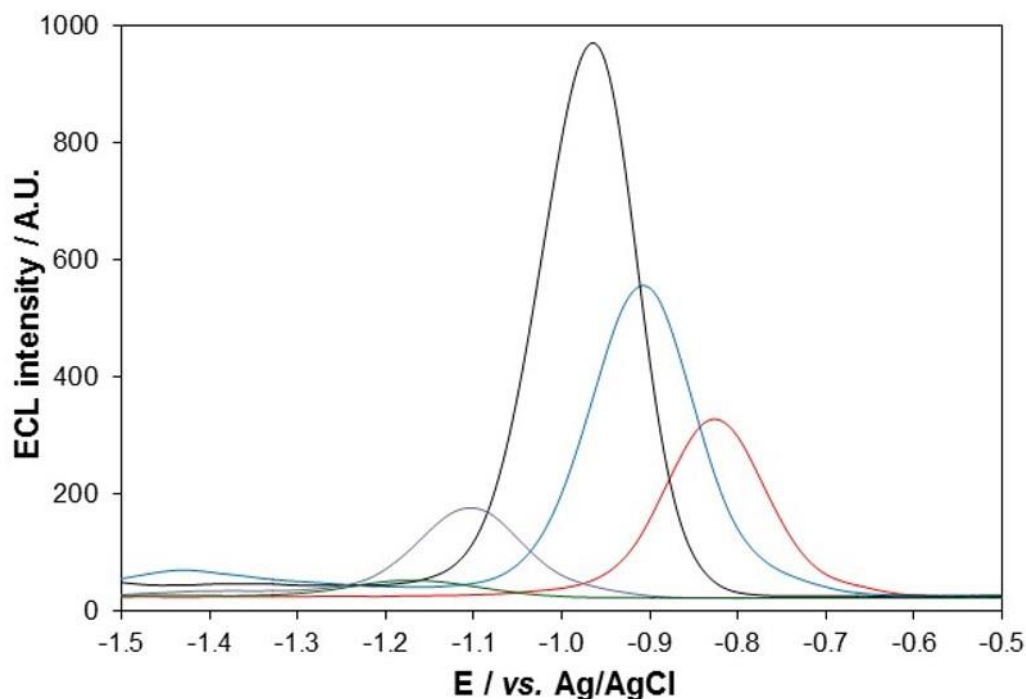


Figure 4.17 - ECL response of 800 nm QD/chitosan film with 0.01 mM $K_2S_2O_8$ in 0.1 M PBS at pH 1 (red), 4.5 (blue), 7.4 (black), 10 (purple) and 12 (green) at a scan rate of 100 mV s^{-1} over the potential range $-1.3 \leq v \leq -0.5 \text{ V vs. Ag/AgCl}$. PMT input voltage = 0.60 V.

Table 4.5 - ECL onset and peak potentials (vs. Ag/AgCl) of 800 nm QD/chitosan film in 0.01 mM $K_2S_2O_8$ in 0.1 M PBS at different pH values.

pH	Onset potential / V (vs. Ag/AgCl)	Peak potential / V (vs. Ag/AgCl)
1	-0.60	-0.85
4.5	-0.60	-0.90
7.4	-0.75	-1.00
10	-0.85	-1.10
12	-0.95	-1.15

Below pH 4.5, appearance of an ECL signal remains constant at -0.60 V, showing this is the minimum ECL onset potential possible with this specific system. A study of the pH stability of thiolate ligands on CdSe QDs indicated that in acidic conditions, extensive dissociation of the ligand from the QD can occur.⁵⁸ This may explain the decrease in ECL onset potential if the DAET

passivating ligand is dissociating from the QD surface. This could expose surface states and allow ECL emission from these rather than the core. An examination of the ECL emission profile in acidic conditions should therefore be carried out. The trend of increasing ECL onset potential with increasing pH appears to be dependent on QD reduction (that is known to be the rate-determining step for ECL production with $K_2S_2O_8$ co-reactant (section 3.3.2.1)) as it is not affected by alternative co-reactants or the incorporation of QDs within the chitosan film. This suggests that pH affects the passivation layer surrounding the QDs, dictating the ease of electron injection and thus the onset of an ECL signal. The exact nature of these changes are currently not known but may involve de-protonation of the passivating ligand in basic conditions or its dissociation in acidic conditions, as discussed previously.

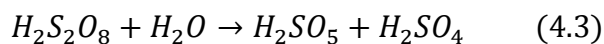
The potential of maximum ECL intensity increases across the range from pH 1 to 12, with peak shape remaining constant at all values. ECL intensity increases from pH 1, reaching a maximum at 7.4 and then drops sharply in basic conditions reaching close to zero at pH 12. Table 4.6 highlights these intensities.

Table 4.6 – Maximum ECL intensity of 800 nm QD/chitosan film in 0.01 mM $K_2S_2O_8$ in 0.1 M PBS at different pH values. PMT input voltage = 0.60 V.

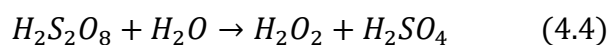
pH	Maximum ECL intensity / A.U.
1	328
4.5	556
7.4	971
10	176
12	52

The relationship between ECL intensity and pH can be explained by a combination of the electron transfer kinetics and the behaviour of $S_2O_8^{2-}$ across the investigated pH range. The increasing potential for ECL production signifies a decrease in electron transfer kinetics with increasing pH, which will

adversely affect ECL intensity. However, under strongly acidic conditions, $S_2O_8^{2-}$ exists as $H_2S_2O_8$ and can react with H_2O to produce peroxymonopersulfate anions (equation (4.3)).⁵⁷ This decreases the concentration of $S_2O_8^{2-}$ available for reduction to form $SO_4^{\cdot-}$, inhibiting ECL intensity.



This is observed in Figure 4.18 as intensity at pH 1 is weaker than at pH 4.5 and 7.4. Under more weakly acidic conditions, hydrolysis of $S_2O_8^{2-}$ can result in the formation of H_2O_2 (equation (4.4)).⁵⁷



This will reduce the concentration of $SO_4^{\cdot-}$ being produced at the electrode surface, as there are less $S_2O_8^{2-}$ ions available for reduction. However, as a co-reactant itself, H_2O_2 should generate a small ECL response. This can be seen in Figure 4.18, which shows the ECL response at pH 4.5.

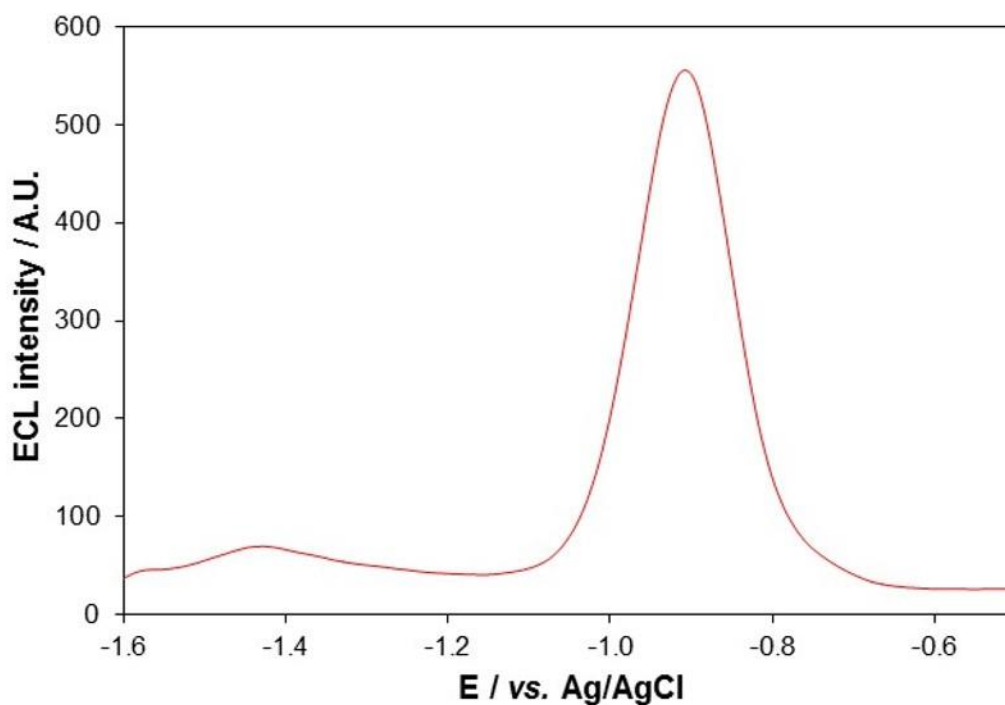
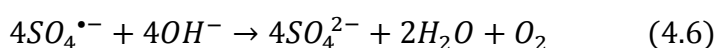
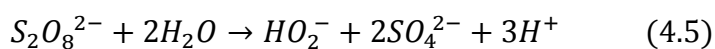


Figure 4.18 - ECL response of 800 nm QD/chitosan film in 0.01 mM $K_2S_2O_8$ at pH 4.5 at a scan rate of 100 mV s^{-1} over the potential range $-1.6 \leq v \leq -0.5 \text{ V vs. Ag/AgCl}$. PMT input voltage = 0.60 V.

A very weak ECL signal is observed at approximately -1.40 V, which is consistent with ECL generation from this QD/chitosan film with H_2O_2 co-reactant (section 3.3.1.1).

Under basic conditions, a sharp decline in ECL intensity is observed (Figure 4.17). This is caused by base-catalysed hydrolysis of $S_2O_8^{2-}$ (equation (4.5))⁵⁹ and the reaction of $SO_4^{\bullet-}$ with OH^- (equation (4.6)).⁶⁰



These reactions indicate that under basic conditions the concentration of $S_2O_8^{2-}$ available for reduction at the electrode surface will decline. Any $SO_4^{\bullet-}$ formed can then react with OH^- , further reducing the concentration available for hole injection into reduced QDs. The final result is a significant decrease in ECL intensity observed in basic conditions. $SO_4^{\bullet-}$ is a relatively weak hydrogen

acceptor and is therefore more stable in acidic conditions.⁵³ Combined with the faster electron transfer kinetics at lower pH, this explains the increase in ECL intensity in acidic compared to basic conditions.

Another factor that may inhibit ECL intensity in basic conditions is the porosity of the chitosan film. The amino group on chitosan has a pK_a of 6.5 and is therefore protonated in acidic and neutral conditions.⁶¹ Protonation results in an increase in film porosity because of repulsion between neighbouring positive charges ($-^+NH_3$ groups). At higher pH, the inferior film porosity could hinder diffusion of co-reactant molecules to the electrode surface and contribute to the decreased ECL intensity observed under basic conditions.

At pH 7.4, the concentration of $S_2O_8^{2-}$ should not be inhibited pre-reduction by either acid or base-catalysed hydrolysis (equations (4.3)-(4.5)) and the stability of $SO_4^{\cdot-}$ should not be affected to a great degree by the presence of OH^- (equation (4.6)). As a result, the most intense ECL response is observed at this pH.

4.3.4 Electrochemical System

4.3.4.1 Electrode material

Electrode material is known to influence the ECL behaviour of a system.^{62, 63} The most common materials are GC, Pt and Au and the ECL profiles of NIR QDs on these materials are shown in Figure 4.19.

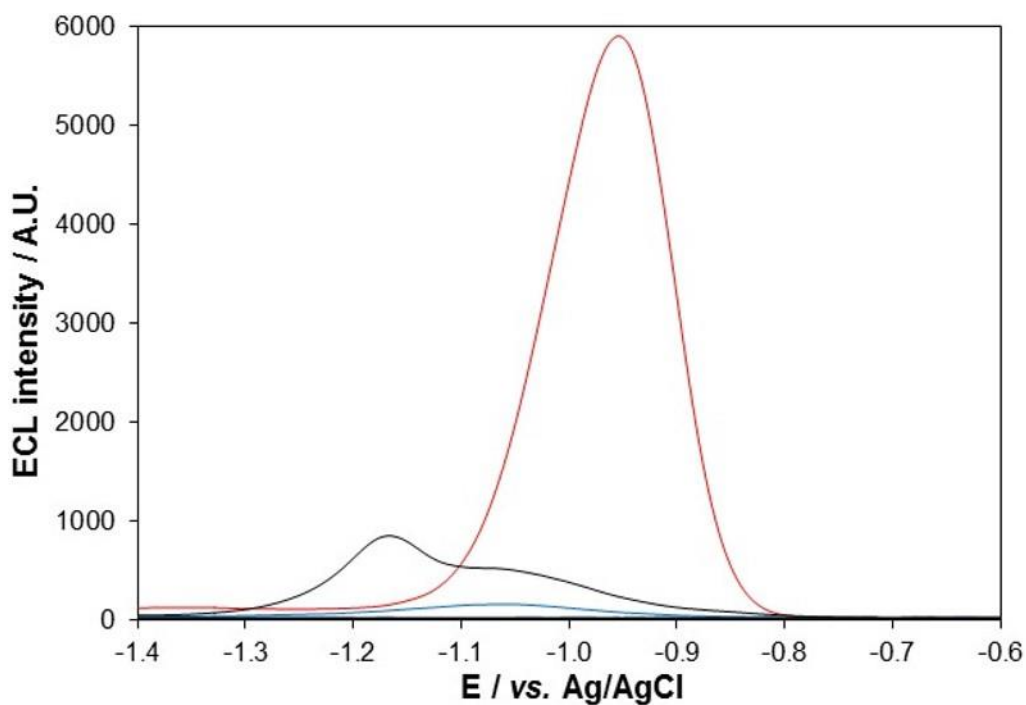


Figure 4.19 - ECL response of 800 nm QD/chitosan film on GC (red), Pt (blue) and Au (black) electrode in 0.01 mM $K_2S_2O_8$ at a scan rate of 100 mV s^{-1} over the potential range $-1.4 \leq v \leq -0.6 \text{ V vs. Ag/AgCl}$. PMT input voltage = 0.60 V.

With all electrode materials, ECL production is observed commencing at -0.75 V. However, maximum ECL intensity is reached at a potential governed by the specific electrode material. This follows the trend $GC < Pt < Au$. Unaltered appearance of ECL at -0.75 V indicates QD reduction and ECL initiation are not influenced by electrode material. Figure 4.20 shows the average ECL response for 3 repeats with each material.

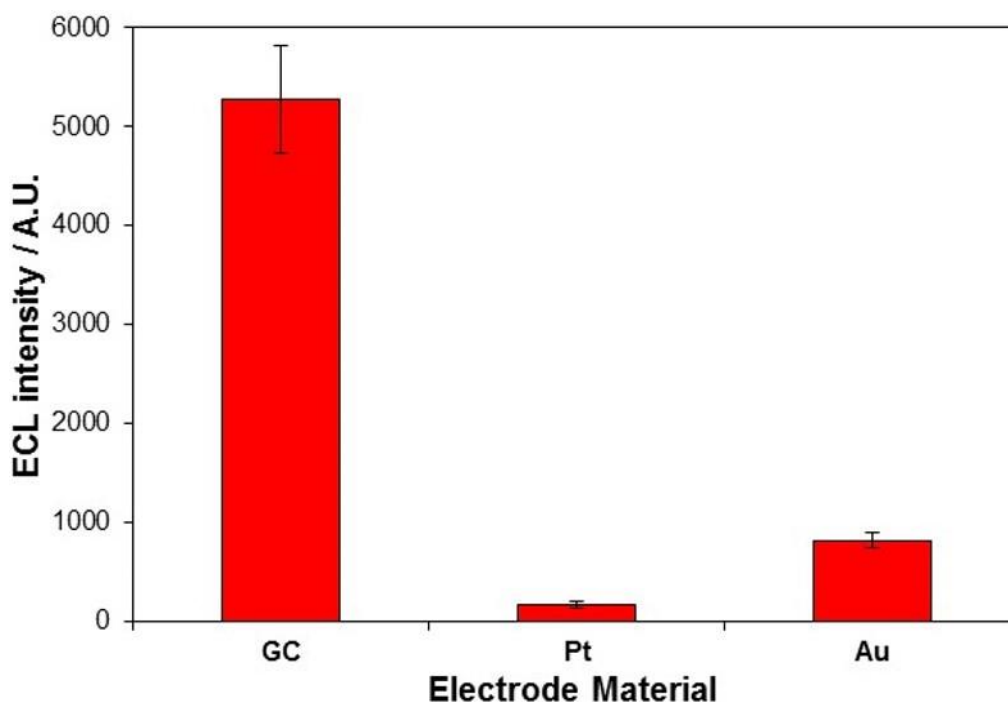


Figure 4.20 - Average ECL response of 800 nm QD/chitosan film on GC, Pt and Au electrode with 0.01 mM $K_2S_2O_8$ at a scan rate of 100 mV s^{-1} . Error bars represent standard deviations from triplicate data set. PMT input voltage = 0.60 V.

A QD/chitosan film on GC electrode produced the most intense ECL signal, over 30 times stronger than on Pt and 6 times stronger than on Au. As ECL initiation is constant for all materials, it is likely that variation in the concentration of precursor species and their subsequent interaction that influences the observed ECL intensity. This can be caused by competition between QD/co-reactants and other species in solution for active/adsorption sites on the electrode surface. Fewer available active sites for QD/co-reactant reduction will result in a decreased concentration of precursor species and a drop in ECL intensity. Pt electrodes are known to stabilise hydrogen atoms by adsorption (Pt hydride formation),⁶⁴ which will decrease the number of active sites on its surface and could explain the decrease in observed ECL intensity. Carbon based electrode materials do not suffer from this formation of hydrides upon cathodic scanning⁶⁴ and the number of active sites available for interaction with QDs or co-reactants is therefore greater. A greater concentration of ECL precursor species can be generated and the ECL intensity increases. At Pt and Au electrodes, further reduction in ECL intensity

may be attributable to the evolution of H₂ at potentials more positive than that for ECL generation. Figure 4.21 shows the voltammograms for each electrode material up to the completion of the ECL process.

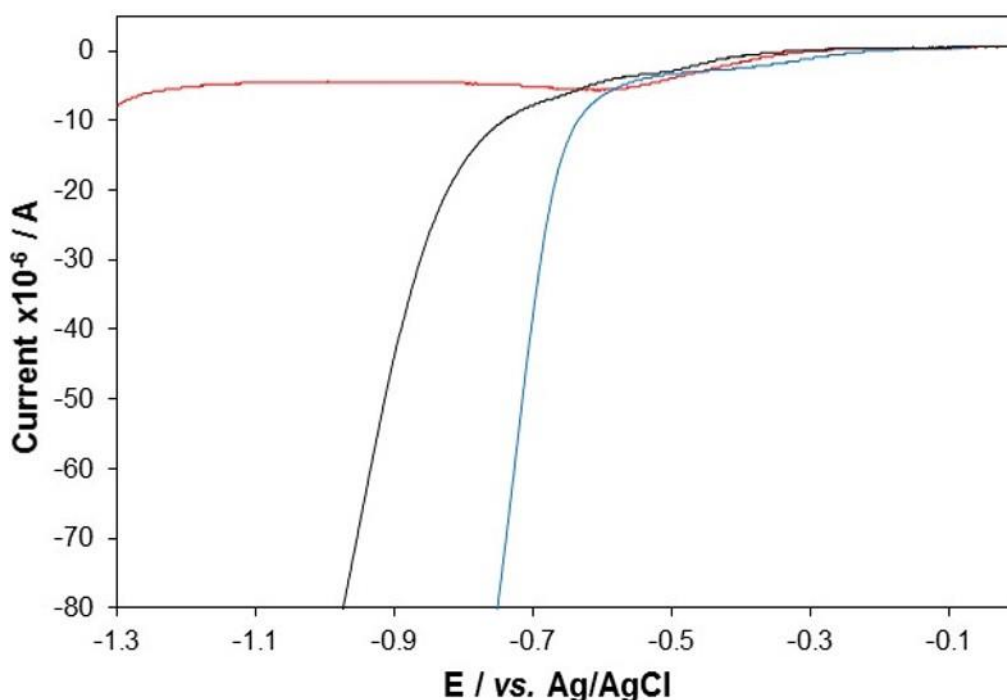


Figure 4.21 - Current response of 800 nm QD/chitosan film on a GC (red), Pt (blue) and Au (black) electrode with 0.01 mM K₂S₂O₈ at a scan rate of 100 mV s⁻¹ over the potential range -1.3 ≤ v ≤ 0 V vs. Ag/AgCl. Reverse scans are not shown for clarity.

This shows a reduction process, attributed to H⁺ reduction and H₂ evolution,^{65, 66} which appears at -0.50 and -0.70 for Pt and Au respectively. No such process is observed with the GC electrode. H₂ evolution from the Pt and Au electrodes at a potential more positive than that for ECL generation will likely interfere with the ECL process and result in the decreased ECL intensity observed in Figure 4.20.

These results have shown that selection of electrode material is critical for optimisation of ECL performance. Variations in electrode-species interactions and the redox behaviour at these different electrode materials can have a profound influence on the ECL intensity. This was observed in these

investigations, which demonstrated that maximum ECL intensity with these NIR QDs is obtained at a GC electrode.

4.3.4.2 Scan rate

Scan rate has previously been shown to affect the ECL response of certain systems.^{24, 67} It is thought this is associated with decomposition of electrogenerated species, especially at slower scan rates,⁶⁸ and production of a higher concentration of these species at higher scan rates.²⁴ Its effect on this specific system is shown in Figure 4.22.

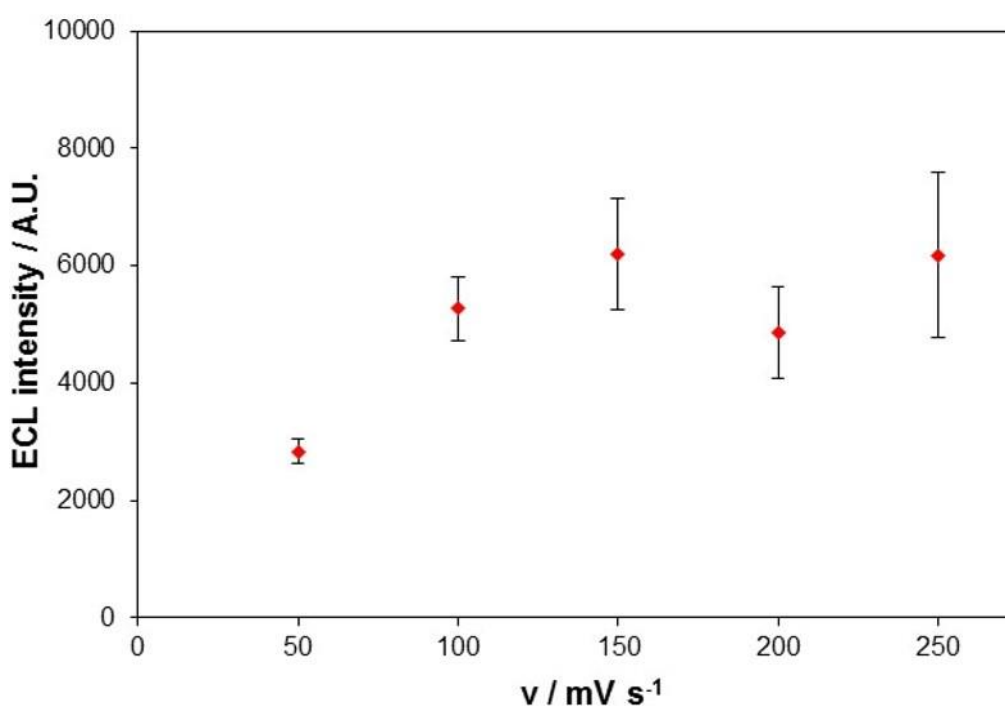


Figure 4.22 - Average ECL response of 800 nm QD/chitosan film with 0.01 mM $\text{K}_2\text{S}_2\text{O}_8$ at different scan rates. Error bars represent standard deviation from triplicate data set.

An increase in ECL intensity is seen from 50 to 100 mV s^{-1} , above which the signal remains relatively constant illustrating the ECL response of this system is not scan rate dependent in the range 100-250 mV s^{-1} . At 50 mV s^{-1} ECL intensity drops, as the experimental time scale permits decomposition of electrogenerated ECL precursors prior to emission. A scan rate of 100 mV s^{-1}

was chosen as it is regularly used with ECL techniques.^{28, 69, 70}

4.4 Conclusions

This research has successfully optimised the film composition, co-reactant, buffer and electrochemical setup of an ECL system that incorporates NIR QDs into its design. Significantly, this is the first detailed investigation into the optimal conditions for generation of ECL from NIR QDs, which are likely to play a key role in future development of ECL biosensors.³ These conditions are outlined in Table 4.7.

Table 4.7 – Outline of optimal conditions achieved in this work.

Parameter	Optimal conditions
Polymer	Chitosan
Polymer concentration	0.05%
QD concentration	0.232±0.017 μM
QD/polymer film volume	3±0.03 μL
Co-reactant	$\text{K}_2\text{S}_2\text{O}_8$
Co-reactant concentration	100 mM
Buffer	PBS
Buffer pH	7.4
Electrode material	GC
Scan rate	100 mV s^{-1}

In the future, this research will aid in the selection of suitable parameters for achieving optimal biosensor response from these NIR QDs. Three parameters are of particular significance. Firstly, the far superior sensitivity of $\text{K}_2\text{S}_2\text{O}_8$ co-reactant ECL compared to other common co-reactants indicates that this should be used preferentially to obtain the most intense response. However, the detection of both cathodic and anodic ECL responses demonstrates the versatility of these NIR QDs, which should allow their use in a wide variety of sensing systems. Secondly, optimal performance at physiological pH is very encouraging as future work is likely to focus on biological detection directly

from whole blood samples, so biocompatibility is essential. Finally, the considerable improvement in response with GC electrodes compared to Pt and Au is important because a number of biosensor systems utilise Au electrodes due to their ease of functionalisation via thiolated molecules.^{45, 71-74} This work has shown that a significant improvement in NIR QD biosensor sensitivity would be achieved through the use of GC as the electrode material of choice.

Overall, these investigations have outlined the best electrochemical system for generation of an intense NIR QD ECL response. This provides the framework for further NIR QD ECL biosensor development.

4.5 References

1. J. V. Frangioni, *Current opinion in chemical biology*, 2003, **7**, 626-634.
2. J. Wang and H. Han, *Reviews in Analytical Chemistry*, 2013, **32**, 91-101.
3. L. Chen and H. Han, *Microchimica Acta*, 2014, 1-11.
4. W. Cai, D.-W. Shin, K. Chen, O. Gheysens, Q. Cao, S. X. Wang, S. S. Gambhir and X. Chen, *Nano letters*, 2006, **6**, 669-676.
5. Y. Hama, Y. Koyama, Y. Urano, P. L. Choyke and H. Kobayashi, *Breast cancer research and treatment*, 2007, **103**, 23-28.
6. D. Fatehi, T. N. Baral and A. Abulrob, *Journal of nanoscience and nanotechnology*, 2014, **14**, 5355-5362.
7. K. Yang, C. Zhao, Y.-A. Cao, H. Tang, Y.-L. Bai, H. Huang, C.-R. Zhao, R. Chen and D. Zhao, *Oncology reports*, 2012, **27**, 1925.
8. N. Y. Morgan, S. English, W. Chen, V. Chernomordik, A. Russo, P. D. Smith and A. Gandjbakhche, *Academic radiology*, 2005, **12**, 313-323.
9. J. Wang, H. Han, X. Jiang, L. Huang, L. Chen and N. Li, *Analytical chemistry*, 2012, **84**, 4893-4899.
10. G. Liang, S. Liu, G. Zou and X. Zhang, *Analytical chemistry*, 2012, **84**, 10645-10649.
11. C. Woelfle and R. O. Claus, *Nanotechnology*, 2007, **18**, 025402.
12. J. Wang, Y. Shan, W.-W. Zhao, J.-J. Xu and H.-Y. Chen, *Analytical chemistry*, 2011, **83**, 4004-4011.
13. L. Bao, L. Sun, Z.-L. Zhang, P. Jiang, F. W. Wise, H. c. D. Abruña and D.-W. Pang, *The Journal of Physical Chemistry C*, 2011, **115**, 18822-18828.
14. F. Sun, F. Chen, W. Fei, L. Sun and Y. Wu, *Sensors and Actuators B: Chemical*, 2012, **166**, 702-707.
15. X. Peng and D. M. P. Mingos, *Semiconductor nanocrystals and silicate nanoparticles*, Springer, 2005.
16. L. Dennany, M. Gerlach, S. O'Carroll, T. E. Keyes, R. J. Forster and P. Bertoncello, *Journal of Materials Chemistry*, 2011, **21**, 13984-13990.
17. Q. Liu, X. Lu, J. Li, X. Yao and J. Li, *Biosensors and Bioelectronics*, 2007, **22**, 3203-3209.
18. Q. Li, J. Y. Zheng, Y. Yan, Y. S. Zhao and J. Yao, *Advanced Materials*, 2012, **24**, 4745-4749.
19. H. N. Choi, S.-H. Cho and W.-Y. Lee, *Analytical chemistry*, 2003, **75**, 4250-4256.
20. M. George and T. E. Abraham, *Journal of controlled release*, 2006, **114**, 1-14.
21. Z. Li, Y. Du, Z. Zhang and D. Pang, *Reactive and Functional Polymers*, 2003, **55**, 35-43.
22. X. Hun and Z. Zhang, *Sensors and Actuators B: Chemical*, 2008, **131**, 403-410.
23. L. Zhang and X. Zheng, *Analytica chimica acta*, 2006, **570**, 207-213.
24. H. Han, Z. Sheng and J. Liang, *Analytica chimica acta*, 2007, **596**, 73-78.
25. Y. Wang, Z. Xie, G. Gotesman, L. Wang, B. P. Bloom, T. Z. Markus, D. Oron, R. Naaman and D. H. Waldeck, *The Journal of Physical Chemistry C*, 2012, **116**, 17464-17472.

26. S. Roy, N. Soin, R. Bajpai, D. S. Misra, J. A. McLaughlin and S. S. Roy, *Journal of Materials Chemistry*, 2011, **21**, 14725-14731.
27. A. S. Cuharuc, L. L. Kulyuk, R. I. Lascova, A. A. Mitioğlu and A. I. Dikumar, *Surface Engineering and Applied Electrochemistry*, 2012, **48**, 193-211.
28. H. Jiang and H. Ju, *Analytical chemistry*, 2007, **79**, 6690-6696.
29. Y. Bae, D. C. Lee, E. V. Rhogojina, D. C. Jurbergs, B. A. Korgel and A. J. Bard, *Nanotechnology*, 2006, **17**, 3791.
30. H. N. Choi, S. H. Yoon, Y. K. Lyu and W. Y. Lee, *Electroanalysis*, 2007, **19**, 459-465.
31. S. K. Poznyak, D. V. Talapin, E. V. Shevchenko and H. Weller, *Nano Letters*, 2004, **4**, 693-698.
32. A. J. Bard, *Electrogenerated Chemiluminescence*, Marcel Dekker, Inc., New York, 2004.
33. B. Pettinger, H. R. Schöppel and H. Gerischer, *Berichte der Bunsengesellschaft für physikalische Chemie*, 1976, **80**, 849-855.
34. W. Miao, J.-P. Choi and A. J. Bard, *Journal of the American Chemical Society*, 2002, **124**, 14478-14485.
35. W. H. Koppenol and J. D. Rush, *Journal of Physical Chemistry*, 1987, **91**, 4429-4430.
36. K. Imamura, Y. Tada, H. Tanaka, T. Sakiyama and K. Nakanishi, *Journal of colloid and interface science*, 2002, **250**, 409-414.
37. M. Nikinmaa, *An Introduction to Aquatic Toxicology*, Elsevier Science, Waltham, MA, 2014.
38. H. Sies, *European Journal of Biochemistry Reviews*, 1994, **1993**, 101-107.
39. H. S. White and A. J. Bard, *Journal of the American Chemical Society*, 1982, **104**, 6891-6895.
40. D. R. Crow, *Principles and applications of electrochemistry*, CRC Press, 1994.
41. A. W. Knight, *Trends in Analytical Chemistry*, 1999, **18**, 47-62.
42. Y. Wang, J. Lu, L. Tang, H. Chang and J. Li, *Analytical chemistry*, 2009, **81**, 9710-9715.
43. G. Zou and H. Ju, *Analytical chemistry*, 2004, **76**, 6871-6876.
44. X. Hu, H. Han, L. Hua and Z. Sheng, *Biosensors and Bioelectronics*, 2010, **25**, 1843-1846.
45. Q. Liu, M. Han, J. Bao, X. Jiang and Z. Dai, *Analyst*, 2011, **136**, 5197-5203.
46. S. Wang, J. Milam, A. C. Ohlin, V. H. Rambaran, E. Clark, W. Ward, L. Seymour, W. H. Casey, A. A. Holder and W. Miao, *Analytical chemistry*, 2009, **81**, 4068-4075.
47. D. Du, Z. Zou, Y. Shin, J. Wang, H. Wu, M. H. Engelhard, J. Liu, I. A. Aksay and Y. Lin, *Analytical chemistry*, 2010, **82**, 2989-2995.
48. Y. Chen, J. Xu, J. Su, Y. Xiang, R. Yuan and Y. Chai, *Analytical chemistry*, 2012, **84**, 7750-7755.
49. M.-K. So, A. M. Loening, S. S. Gambhir and J. Rao, *Nature protocols*, 2006, **1**, 1160-1164.
50. X. Zhou, D. Xing, D. Zhu and L. Jia, *Analytical chemistry*, 2008, **81**, 255-261.
51. J. Choi, N. S. Wang and V. Reipa, *Bioconjugate chemistry*, 2008, **19**, 680-685.

52. W. Masterton, C. Hurley and E. Neth, *Chemistry: principles and reactions*, Cengage Learning, 2011.
53. Z. V. Todres, *Ion-radical organic chemistry: principles and applications*, CRC Press, 2008.
54. M. J. Davies, B. C. Gilbert, C. B. Thomas and J. Young, *Journal of the Chemical Society-Perkin Transactions 2*, 1985, 1199-1204.
55. P. Pastore, D. Badocco and F. Zanon, *Electrochimica acta*, 2006, **51**, 5394-5401.
56. C. Liang, Z.-S. Wang and C. J. Bruell, *Chemosphere*, 2007, **66**, 106-113.
57. I. M. Kolthoff and I. K. Miller, *Journal of the American Chemical Society*, 1951, **73**, 3055-3059.
58. J. Aldana, N. Lavelle, Y. Wang and X. Peng, *Journal of the American Chemical Society*, 2005, **127**, 2496-2504.
59. O. S. Furman, A. L. Teel and R. J. Watts, *Environmental science & technology*, 2010, **44**, 6423-6428.
60. K. Yamashita, S. Yamazaki-Nishida, Y. Harima and A. Segawa, *Analytical chemistry*, 1991, **63**, 872-876.
61. P. Sorlier, A. Denuzière, C. Viton and A. Domard, *Biomacromolecules*, 2001, **2**, 765-772.
62. W. Miao and A. J. Bard, *Analytical chemistry*, 2004, **76**, 5379-5386.
63. J. E. Vitt, D. C. Johnson and R. C. Engstrom, *Journal of The Electrochemical Society*, 1991, **138**, 1637-1643.
64. A. M. Couper, D. Pletcher and F. C. Walsh, *Chemical Reviews*, 1990, **90**, 837-865.
65. F. Scholz, *Electroanalytical methods: guide to experiments and applications*, Springer, 2009.
66. G. J. Brug, M. Sluyters-Rehbach, J. H. Sluyters and A. Hemelin, *Journal of electroanalytical chemistry and interfacial electrochemistry*, 1984, **181**, 245-266.
67. Z. Guo and S. Dong, *Analytical chemistry*, 2004, **76**, 2683-2688.
68. N. Myung, Z. Ding and A. J. Bard, *Nano Letters*, 2002, **2**, 1315-1319.
69. X.-F. Wang, J.-J. Xu and H.-Y. Chen, *The Journal of Physical Chemistry C*, 2008, **112**, 17581-17585.
70. X.-F. Wang, J.-J. Xu and H.-Y. Chen, *The Journal of Physical Chemistry C*, 2008, **112**, 7151-7157.
71. L. L. Li, K. P. Liu, G. H. Yang, C. M. Wang, J. R. Zhang and J. J. Zhu, *Advanced Functional Materials*, 2011, **21**, 869-878.
72. H. Huang, G. Jie, R. Cui and J.-J. Zhu, *Electrochemistry Communications*, 2009, **11**, 816-818.
73. G. Jie, L. Wang, J. Yuan and S. Zhang, *Analytical chemistry*, 2011, **83**, 3873-3880.
74. H. Huang, Y. Tan, J. Shi, G. Liang and J.-J. Zhu, *Nanoscale*, 2010, **2**, 606-612.

*Chapter 5 - Electrogenenerated chemiluminescence of 800
nm CdSeTe/ZnS quantum dots in whole blood*

5.1 Introduction

It has been shown that NIR QDs can generate a strong ECL signal in both the cathodic and anodic regions and their performance has been optimised to achieve maximum sensitivity (Chapters 3 and 4). So far, the study of NIR emitters for biosensing applications has focused on work under ideal conditions in buffer, which whilst achieving optimal performance does not take advantage of the key property of these materials, namely their emission in the NIR region. As a result, there is a clear requirement for investigations into the behaviour of these NIR emitters under conditions in which their unique properties over visible region emitters are truly scrutinised.

The potential significance of incorporating NIR QDs into biosensing systems, and the driving force behind research in this area, is the improved penetrative ability of light at this wavelength through whole blood and minimisation of tissue autofluorescence.^{1, 2} The absorption spectrum of whole blood predominately follows that of haemoglobin, which can exist in its oxygenated or de-oxygenated form.³ As the majority of clinical blood samples are venous in origin, the absorption spectrum of de-oxygenated haemoglobin is key. Roggan *et al.* carried out optical studies on whole blood, which showed an absorption minimum at 805 nm for fully de-oxygenated whole blood with maximas at 420 and 540 nm.^{4, 5} This confirms that ECL emission in the NIR region should suffer significantly less quenching from whole blood compared to emission in the visible region. For this reason, NIR QDs are promising materials for incorporation into ECL biosensors with detection directly from whole blood. Investigations into the ECL behaviour and performance of these QDs in whole blood has not been carried out previously. As such, there is a requirement for examination of these properties to confirm the suitability of NIR QDs for use with biological samples.

The main focus of this work was to establish the electrochemical properties and ECL performance of NIR QDs in whole blood. Comparison of this ECL

signal with visible region emitters and determination of its responsiveness to clinically relevant analytes, essential for all biosensing applications, were key objectives of this chapter.

5.2 Experimental

5.2.1 Apparatus

Electrochemical measurements were carried out using a CH instrument model 760D electrochemical analyser. All experiments were carried out using a conventional three-electrode assembly, consisting of a 3 mm diameter GC working electrode, Pt wire counter electrode and Ag/AgCl reference electrode. GC electrodes were cleaned by successive polishing using 1, 0.3 and 0.05 μM alumina slurry, followed by sonication in ethanol and water, respectively, for 30 mins. The electrodes were then dried under a flow of N_2 gas. CV was carried out at a scan rate of 100 mV s^{-1} and sample interval of 1 mV across a potential range outlined in each figure. For DPV, the increment potential was 4 mV, amplitude 50 mV, pulse width 50 ms, sample width 16.7 ms and pulse period 0.5 s across a potential range outlined in each figure. Measurements involving simultaneous detection of light and current utilised a CH instrument model 760D connected to a Hamamatsu H10723-20 PMT. The input voltage to the PMT was + 5 V and the control voltage was set between 0.5 and 1.05 V depending on the required sensitivity. The scan rate was 100 mV s^{-1} . During electrochemical experiments, the cell was kept in a light-tight Faraday cage in a specially designed holder configuration where the working electrode was positioned directly above the PMT window. All measurements were made at room temperature.

5.2.2 Materials

Core-shell CdSeTe/ZnS QDs (Qdot® 800 ITK™ organic quantum dots, 1 μM in decane) were purchased from Invitrogen. Core-shell CdSe/ZnS QDs (Lumidot™ 560 and 640 nm QDs, 5 mg/mL in toluene), chitosan (medium molecular weight, 75-85% de-acetylated), phosphate buffered saline (PBS, pH 7.4), potassium persulfate ($\text{K}_2\text{S}_2\text{O}_8$), tripropylamine (TPA), dopamine hydrochloride, DL-homocysteine and 2-(dimethylamino)ethanethiol (DAET) were all purchased from Sigma-Aldrich and used as received. All other

reagents used were of analytical grade, and all solutions were prepared in milli-Q water (18 mΩ cm).

Bovine whole blood was obtained from Wishaw Abattoir Ltd (185 Caledonian Road, Wishaw, Lanarkshire, ML2 0HT) and stored in aliquots at -20 °C. Aliquots were defrosted at room temperature on the day of analysis and used immediately.

5.2.3 Methods

Preparation of water soluble CdSeTe/ZnS core-shell QDs

The method followed was similar to that developed by Woelfle and Claus⁶. 0.5 mL of 0.5 M DAET in methanol was mixed with 0.25 mL of the CdSeTe/ZnS QDs in decane (1 μM). N₂ was bubbled through the solution for 5 mins, which was then sealed and left stirring overnight in the dark at room temperature. The QDs were then precipitated with an excess of acetone followed by centrifugation at 5000 rpm for 6 mins. The filtrate was removed and the precipitate was re-dispersed in 0.25 mL of distilled water. These water-soluble QDs were centrifuged for a further 6 mins at 3000 rpm to remove any impurities and then stored in darkness at 4°C.

Preparation of CdSeTe/ZnS core-shell QD-chitosan composite film

A 0.1 % chitosan solution was prepared in 1 % acetic acid and sonicated for 5 mins. The QD/chitosan composite was prepared by mixing aliquots of the water-soluble QDs with the chitosan solution in a 1:1 (v/v) ratio and mixing for 30 s. 3 μL of this composite was then carefully cast onto the electroactive portion of a GC electrode, with mixing of the composite for 10 s between electrodes. The film was allowed to dry for 1 h at 4°C. A film of bare QDs was prepared in the same manner, with water used instead of chitosan.

QD concentration in the film was altered by mixing the water-soluble QDs with a suitable volume of water prior to mixing in a 1:1 (v/v) ratio with chitosan.

Whole blood samples

Blank blood samples were diluted with 0.1 M PBS in a 9:1 (v/v) ratio. Whole blood samples containing $K_2S_2O_8$ were diluted with 10 mM $K_2S_2O_8$ in a 9:1 (v/v) ratio to obtain a working concentration of 1 mM $K_2S_2O_8$. Whole blood samples containing TPA were diluted with 200 mM TPA in a 9:1 (v/v) ratio to obtain a working concentration of 20 mM TPA.

Preparation of Homocysteine (Hcy) samples

A 10 mM stock solution of Hcy was prepared in 1 mM $K_2S_2O_8$ in 0.1 M PBS and diluted to the required concentration in 1 mM $K_2S_2O_8$ in 0.1 M PBS. For blood samples containing Hcy, 10, 20, 30, 40, 50 and 60 mM stock solutions of Hcy were prepared in 10mM $K_2S_2O_8$ in 0.1 M PBS and diluted 1:9 (v/v) in whole blood to obtain final Hcy working concentrations of 1, 2, 3, 4, 5 and 6 mM and a final working concentration of 1 mM $K_2S_2O_8$.

Preparation of dopamine samples

A 1 mM stock solution of dopamine was prepared in 0.1 M PBS and diluted to the required concentration in 0.1 M PBS. For blood samples containing dopamine, 0.375, 0.75, 1.5, 2, 3 and 4.5 mM stock solutions of dopamine were prepared in 0.1 M PBS and diluted 1:9 (v/v) in whole blood to obtain final dopamine working concentrations of 37.5, 75, 150, 200, 300 and 450 μ M.

5.3 Electrochemical characterisation

5.3.1 CV and DPV

The electrochemical behaviour of NIR QDs in whole blood was investigated through CV and DPV. Figure 5.1 shows the cathodic voltammograms from CV of a blank electrode and a QD/chitosan film in whole blood.

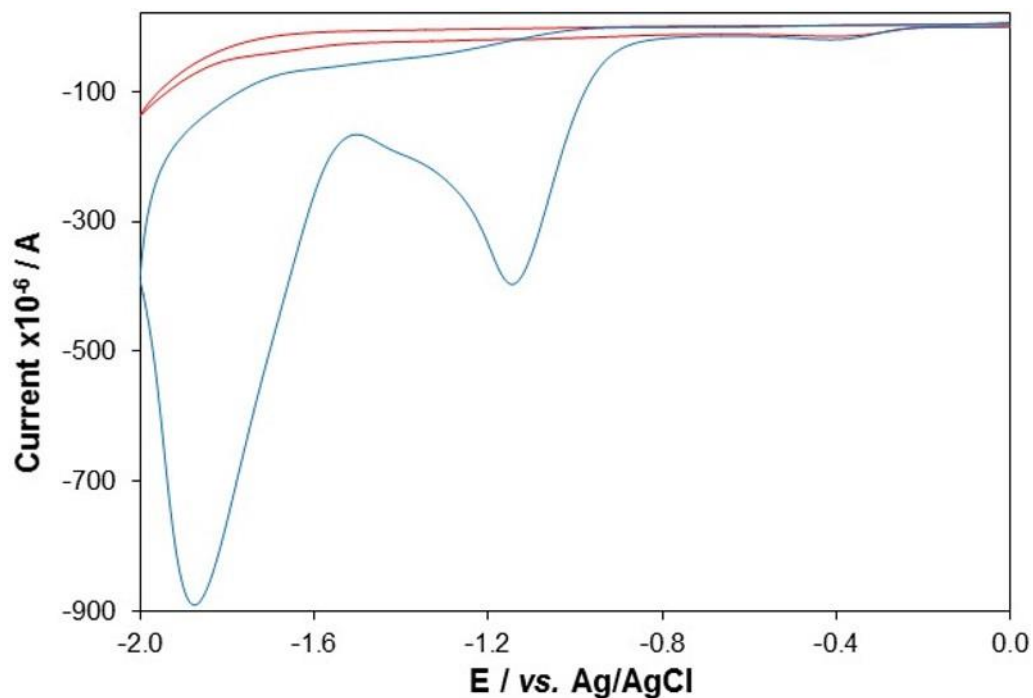


Figure 5.1 - Current response of blank GC electrode (red) and 800 nm QD/chitosan film (blue) in whole blood at a scan rate of 100 mV s⁻¹ over the potential range $-2 \leq v \leq 0$ V vs. Ag/AgCl.

The blank GC electrode exhibits a single, small irreversible reduction peak at -0.40 V, consistent with reduction of dissolved O₂ (section 2.3.2.1). The QD/chitosan film voltammogram also contains this peak, with two further reduction processes at -1.15 and -1.85 V. The peak at -1.15 V has not been seen previously (in buffered aqueous solutions), which suggests that it is related to both the QDs and a species in solution. Whole blood contains a variety of species including proteins, carbohydrates and hormones that are

potentially redox active and could interact with the positively charged QDs.⁷ Figure 5.2 shows the response of this peak as QD concentration is increased.

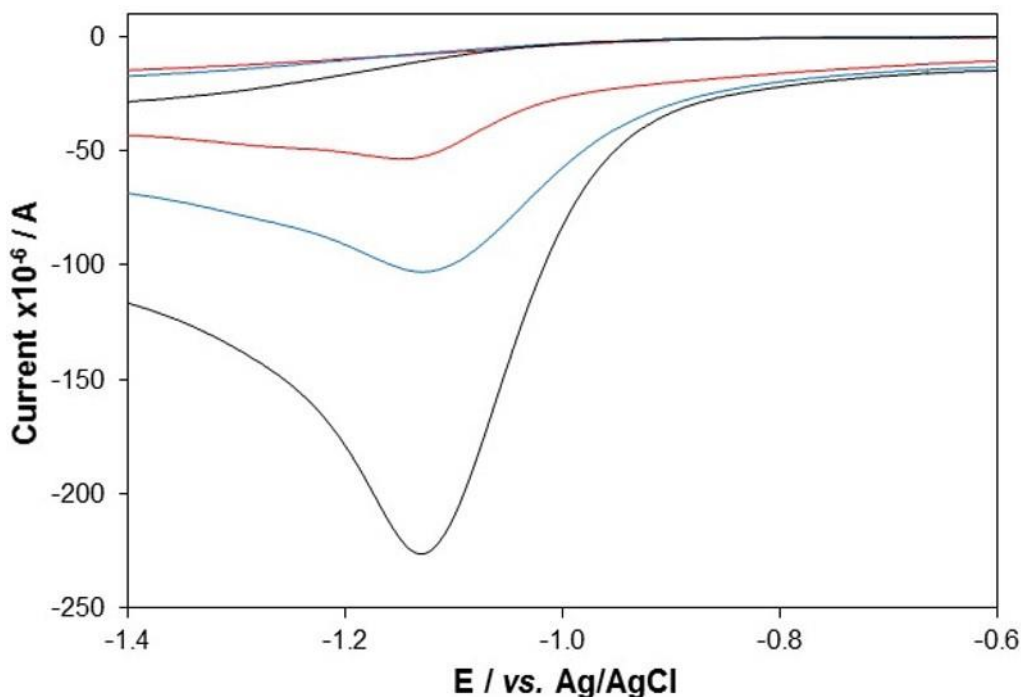


Figure 5.2 - Current response of 0.029 (red), 0.058 (blue) and 0.116 (black) μM 800 nm QD/chitosan film in whole blood at a scan rate of 100 mV s^{-1} over the potential range $-1.4 \leq v \leq -0.6 \text{ V vs. Ag/AgCl}$.

This shows an increase in peak current at -1.15 V as QD concentration rises, confirming this peak is directly related to a reduction process involving the QDs. The occurrence of this peak only in the presence of a QD/chitosan film in whole blood suggests the process is dependent upon interaction between a species in solution and the QDs. This may be reduction of a QD-bioconjugate that forms following immersion of the QD/chitosan film in whole blood. The peak at -1.85 V is consistent with that in buffered aqueous solutions (section 2.3.2.1) and is therefore related to a secondary reduction process of the QDs. The slight shift in peak potential is related to the poorer electrochemical environment of whole blood compared to a buffered solution, which will impact electron transfer.

The voltammograms from DPV are shown in Figure 5.3 and correlate well with those attained with CV. A single peak with a blank GC electrode at -0.35 V and two additional reduction peaks at -1.00 and -1.75 V after QD/chitosan electrode immobilisation are observed.

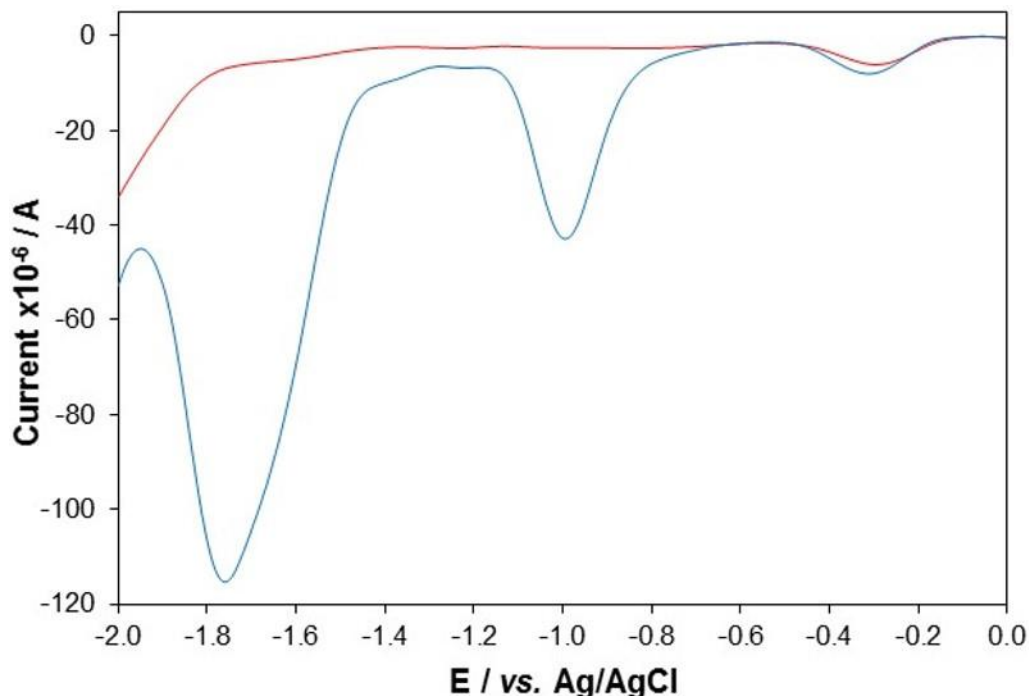


Figure 5.3 - Current response of blank GC electrode (red) and 800 nm QD/chitosan film (blue) in whole blood at a scan rate of 100 mV s⁻¹ over the potential range -2 ≤ v ≤ 0 V vs. Ag/AgCl.

These reduction peaks correspond to the same processes discussed for the CV voltammograms. A shift of approximately 100 mV towards more positive potentials is apparent for each of the three peaks compared with the voltammetric profiles obtained from CV. A shift in peak potential between voltammograms from CV and DPV has been seen before, tending not to occur only when very slow DPV scan rates are used (<1 mV s⁻¹).⁸

The whole blood electrochemical behaviour of NIR QDs (from CV) in the anodic region is outlined in Figure 5.4.

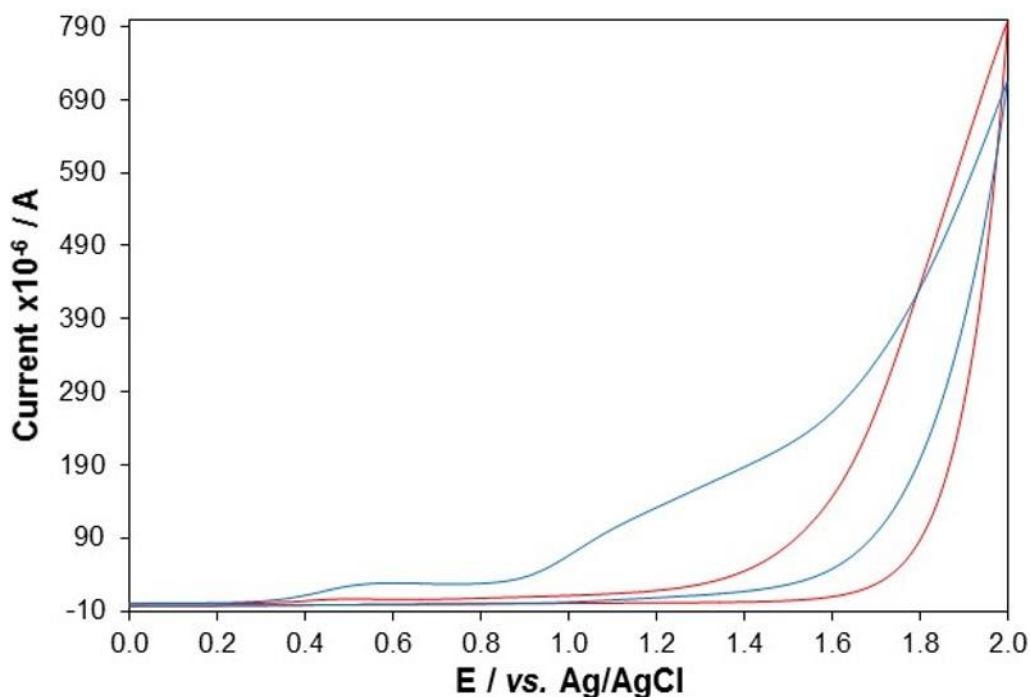


Figure 5.4 - Current response of blank GC electrode (red) and 800 nm QD/chitosan film (blue) in whole blood at a scan rate of 100 mV s^{-1} over the potential range $0 \leq v \leq 2 \text{ V}$ vs. Ag/AgCl.

The blank GC electrode voltammogram exhibits a single, irreversible oxidation peak at 0.55 V. This peak is not present with a blank GC in PBS (section 2.3.2.1) and so is related to oxidation of a whole blood species. Albumin is one of the most abundant proteins in blood, having a concentration of approximately 40 mg/mL.⁹ It can exist in its oxidised or reduced form, with oxidation occurring via a free thiol group on the amino acid cysteine-34.¹⁰ The oxidation of cysteine has been reported on a bare GC electrode at a potential very similar to that seen here (0.50 V),¹¹ indicating this peak is likely caused by oxidation of albumin in the whole blood sample. This is further confirmed as an increase in peak current of this process was also observed following nanomaterial modification of the GC electrode,¹¹ as is seen in Figure 5.4 following modification with the QD/chitosan film.

In the presence of a QD/chitosan film, a poorly defined oxidation peak at approximately 1.20 V is apparent. Peak current at this potential is dependent upon QD concentration and is therefore related to an oxidation process

involving the QDs. The anodic voltammograms (from DPV) of a blank GC electrode and QD/chitosan modified electrode are shown in Figure 5.5

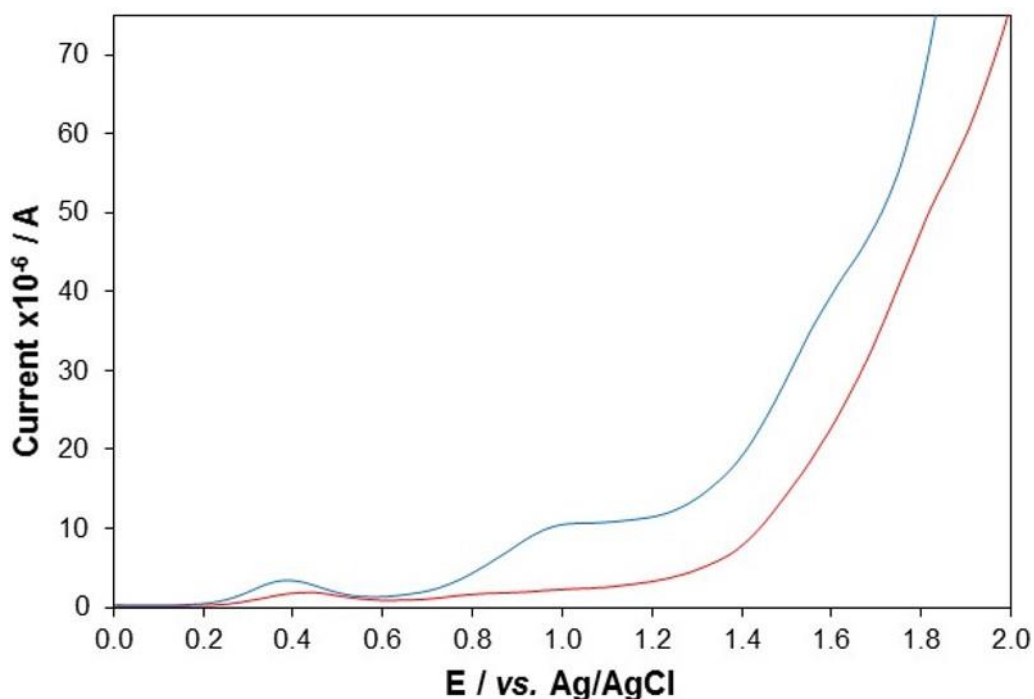


Figure 5.5 - Current response of blank GC electrode (red) and 800 nm QD/chitosan film (blue) in whole blood at a scan rate of 100 mV s^{-1} over the potential range $0 \leq v \leq 2 \text{ V vs. Ag/AgCl}$.

The bare GC electrode exhibits an oxidation peak at 0.45 V, consistent with oxidation of albumin as seen in the voltammograms from CV. The improved sensitivity and slower scan rates associated with DPV allow observation of two defined oxidation peaks not seen in the voltammetric profiles from CV. These centre at 1.00 V and 1.55 V respectively and are seen following electrode immobilisation of the QD/chitosan film, in both whole blood (Figure 5.5) and PBS (section 2.3.2.2). These processes are associated with hole injection into different energy levels of the QDs electronic structure.

This data indicates that the anodic electrochemical behaviour of NIR QDs in whole blood is similar to that in PBS as no additional oxidation peaks related to QD processes were observed. In the cathodic region, an additional peak at -1.15 V is detected that is dependent upon the presence of both QDs and an

unknown whole blood species (Figure 5.2). This signifies the reduction characteristics of NIR QDs are affected in whole blood, which could influence their ECL performance.

5.4 NIR QD ECL in whole blood

Research in chapters 3 and 4 has shown intense ECL signals can be obtained using NIR QDs in buffered solutions. The detection of NIR QD ECL has never been achieved or examined directly from whole blood. Investigation into this process was required to confirm a detectable signal was produced and that this signal was sensitive to changes in the system.

5.4.1 Detection of a cathodic ECL response

5.4.1.1 Co-reactant free system

The occurrence of a cathodic ECL response from NIR QDs in whole blood with no additional co-reactants was investigated for comparison with the same system in buffer (section 3.4.2.1). This was to determine whether any alteration in ECL behaviour was occurring through interaction with whole blood species. The detected response of the QDs in whole blood is shown in Figure 5.6.

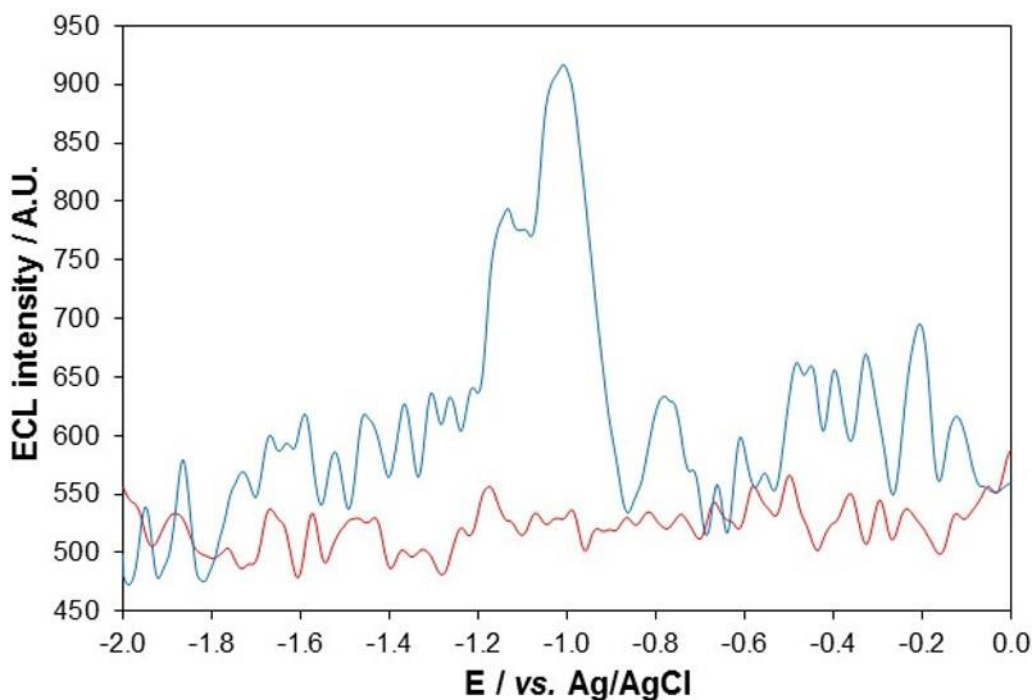


Figure 5.6 - ECL response of blank GC electrode (red) and 800 nm QD/chitosan film (blue) in whole blood at a scan rate of 100 mV s^{-1} over the potential range $-2 \leq v \leq 0 \text{ V}$ vs. Ag/AgCl. PMT input voltage = 1.05 V.

No ECL signal is observed in the absence of QDs indicating there are no ECL active emitters in the whole blood sample. Immobilisation of the QD/chitosan film on the electrode surface generates a small reductive ECL peak upon potential scanning at -1.00 V. This compares to ECL peaks at -1.00 and -1.35 V when the same films are run in PBS (section 3.4.2.1). The appearance of a peak at -1.00 V in both whole blood and PBS suggests the same ECL processes are occurring and that whole blood constituents are not affecting the mechanism of ECL production at this potential. From section 3.4.2.1, the ECL mechanism at this potential predominantly involves the interaction between reduced QDs and non-radical products of the ORR. A loss of signal intensity in whole blood is likely due to reactions of these non-radical species with molecules in blood, such as the consumption of OH^- by H_2CO_3 to form HCO_3^- , which is an essential reaction for maintenance of blood pH.¹² A minimal degree of light absorption by whole blood will also occur as its absorbance in the NIR region is not zero.⁵

The loss of ECL signal at -1.35 V in whole blood indicates that OH^\bullet (section 3.4.2.1) is not present at sufficient concentrations to elicit a detectable ECL response. This is most probably caused by quenching of the radical by a species in whole blood. As OH^\bullet formation is dependent upon O_2 , followed by H_2O_2 reduction, its concentration in solution will already be very low, so any quenching results in complete loss of ECL response. As expected, the lifetime of radical species, and therefore the concentration available for QD hole injection, appears to decrease in blood due to the presence of naturally-occurring free radical scavengers, such as uric acid and glutathione.^{13, 14}

However, the detection of a weak ECL response directly from whole blood, even without an additional co-reactant and with radical quenching taking place, was a significant discovery and instills considerable confidence in the ability of NIR QDs to generate a detectable ECL signal from within a whole blood sample.

5.4.1.2 $\text{K}_2\text{S}_2\text{O}_8$ system

Enhancement of this ECL signal was attempted through addition of $\text{K}_2\text{S}_2\text{O}_8$ co-reactant to the whole blood sample. $\text{K}_2\text{S}_2\text{O}_8$ was selected as it provides maximum ECL sensitivity with these QDs (section 4.3.2.1). The ECL response from this system is shown in Figure 5.7.

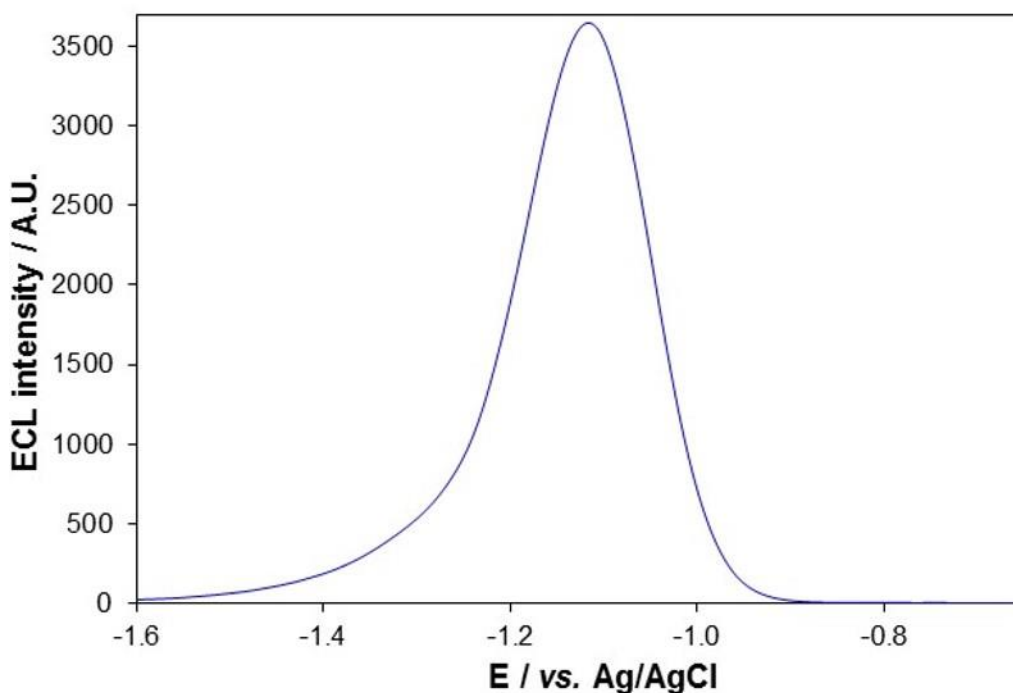


Figure 5.7 - ECL response of 800 nm QD/chitosan film in 1 mM $K_2S_2O_8$ in whole blood at a scan rate of 100 mV s^{-1} over the potential range $-1.6 \leq v \leq -0.6 \text{ V vs. Ag/AgCl}$. PMT input voltage = 0.50 V.

An intense ECL signal is observed at -1.05 V. This is at a very similar potential to that seen in the $K_2S_2O_8$ – PBS system and so is the product of excited state QD formation through QDs($e^-(1S_e)$) hole injection by $SO_4^{\cdot-}$ (section 3.4.2.1). The small shift in peak potential compared to PBS is caused by slower electron transfer in whole blood. Although radical quenching will be taking place, there is still a sufficient concentration of $SO_4^{\cdot-}$ within the ECL active zone to allow production of an intense ECL signal with the QDs. The rapid electron transfer kinetics of this system, a consequence of the high standard reduction potential of the $SO_4^{\cdot-}/SO_4^{2-}$ couple (section 4.3.2.1), will help minimise any interference from free radical scavengers in whole blood. Determination of the responsiveness of this ECL signal to changes in $SO_4^{\cdot-}$ concentration was examined through spiking of blood samples with an increasing concentration of $K_2S_2O_8$ (Figure 5.8).

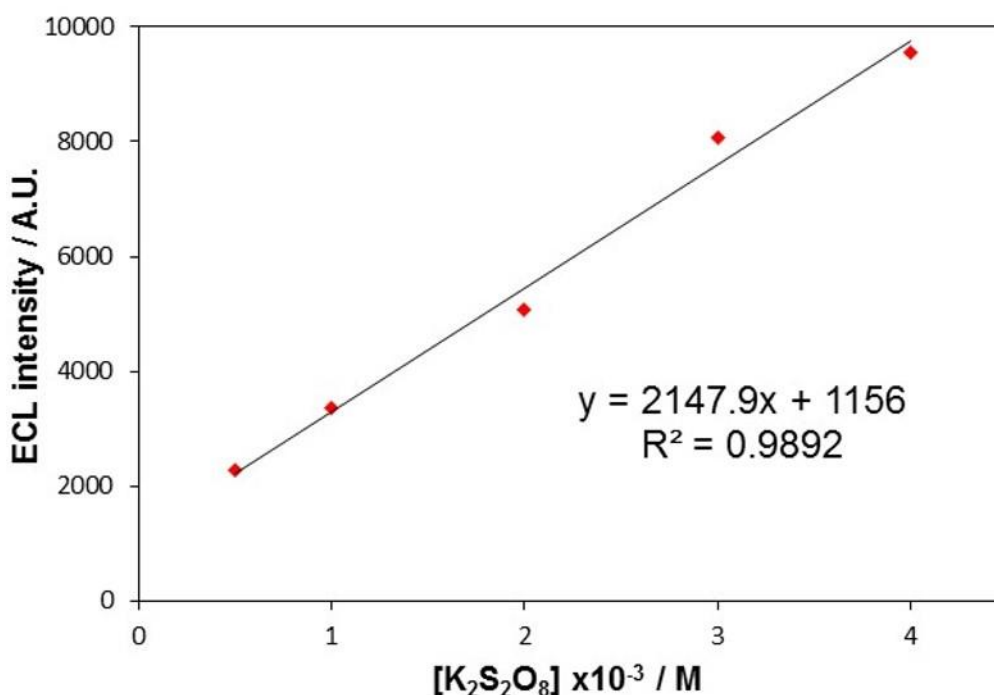


Figure 5.8 – The linear dependence of 800 nm QD/chitosan film ECL on [K₂S₂O₈] in whole blood. PMT input voltage = 0.50 V.

This shows a linear dependence of the ECL response on K₂S₂O₈ concentration in whole blood, demonstrating its sensitivity to changes in system environment.

This data shows successful enhancement of NIR QD ECL in whole blood through addition of a suitable co-reactant (K₂S₂O₈). A strong QD ECL emission in the NIR region can be produced directly in whole blood samples and it is responsive to a small, reactive molecule (SO₄²⁻). This was a very promising result as it highlighted the ability of NIR QDs to detect a species in blood that was very likely involved in a number of competing reactions with alternative molecules in the system (for example, free radical scavengers and other organic compounds). Detection from whole blood will always be affected by these competing reactions due to the presence of naturally-occurring interferences, and so the ability of NIR QDs to detect this molecule in blood provided great confidence in their biosensing ability in such conditions.

5.4.2 Detection of an anodic ECL response

5.4.2.1 Co-reactant free system

The co-reactant free system with NIR QDs is known to produce a signal through interaction between QDs($h^+(1S_h)$) and superoxide (section 3.4.1.1). The ECL profile of QD/chitosan film in whole blood is shown in Figure 5.9.

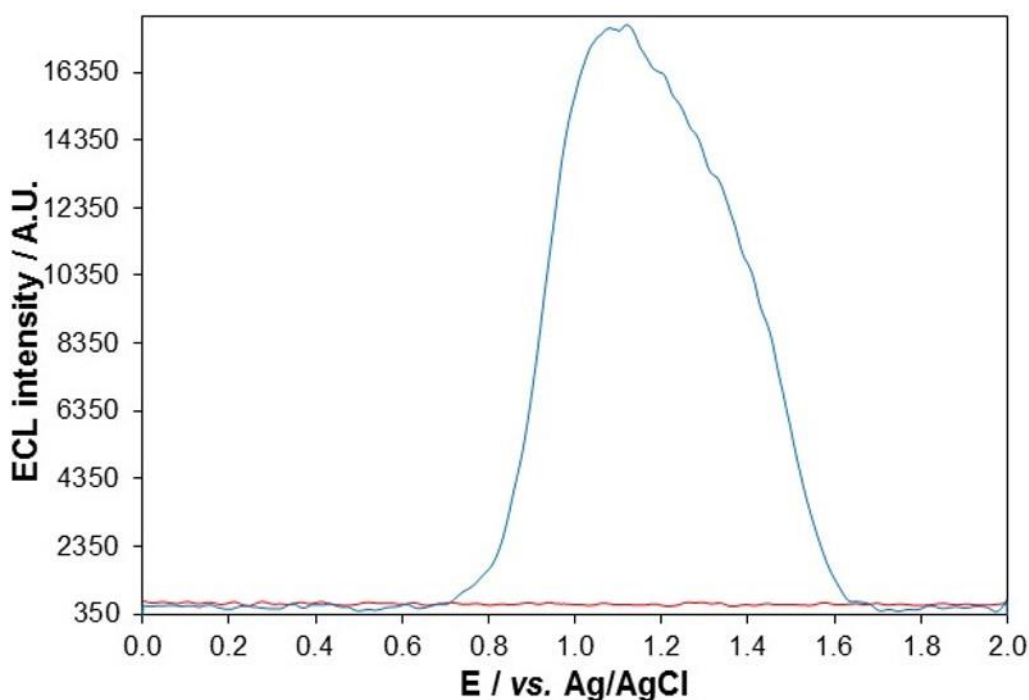


Figure 5.9 - ECL response of blank GC electrode (red) and 800 nm QD/chitosan film (blue) in whole blood at a scan rate of 100 mV s^{-1} over the potential range $0 \leq v \leq 2 \text{ V vs. Ag/AgCl}$. PMT input voltage = 1.05 V.

An intense oxidative ECL signal at 1.10 V is seen after electrode modification with a QD/chitosan film, indicating the response is a result of emission from the QDs. The similarity of anodic ECL profiles in PBS and whole blood suggest that the same electron transfer processes are taking place, which involves interaction between $\text{O}_2^{\cdot -}$ and oxidised QDs formed during the potential scan. It appears no significant quenching of ECL precursors by a species in whole blood is taking place as an intense ECL response is detected. The significantly

larger signal observed in the anodic co-reactant free system compared to the cathodic system suggests a greater stability of $O_2^{\cdot-}$ compared to OH^{\cdot} in whole blood. The half-life of $O_2^{\cdot-}$ is in the order of μs ,¹⁵ compared to a ns range half-life for OH^{\cdot} .¹⁶ Therefore, the availability of $O_2^{\cdot-}$ for ECL reactions is likely to be much greater than for OH^{\cdot} , which helps explain the difference in ECL intensities with these co-reactant species.

This data has shown that intense anodic NIR QD ECL can be produced in whole blood without the need for any additional co-reactants, which can permit development of novel co-reactant free systems with direct blood analysis.

5.4.2.2 TPA system

Enhancement was seen in ECL intensity following addition of TPA as a reductive co-reactant in PBS (section 3.4.1.1). The same procedure was carried out in whole blood to determine its effect on ECL performance (Figure 5.10).

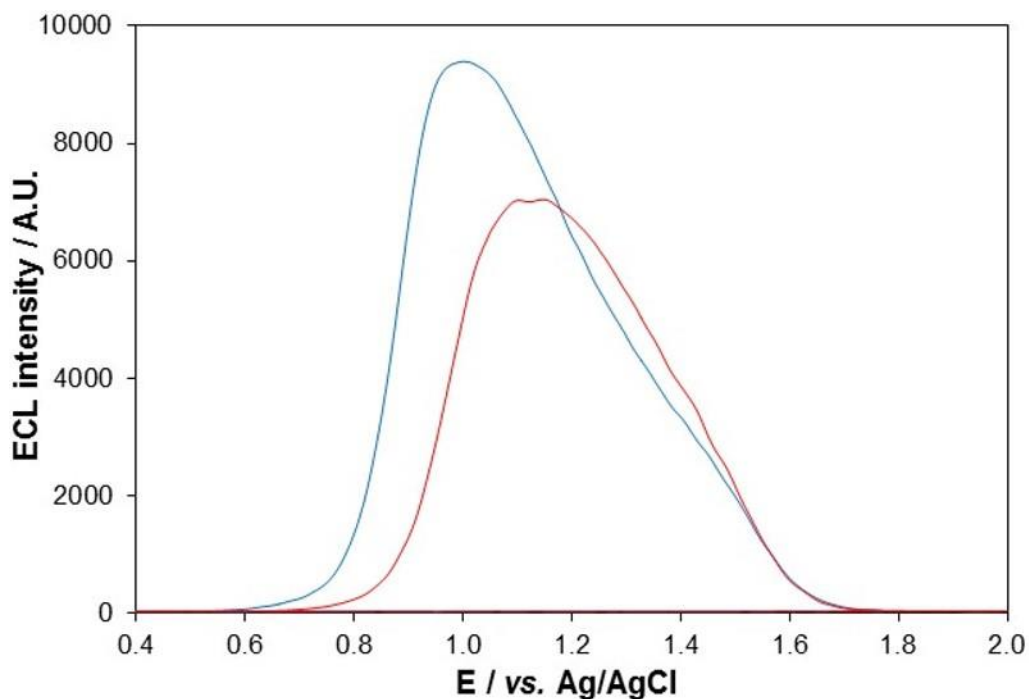


Figure 5.10 - ECL response of 800 nm QD/chitosan film in whole blood (red) and in 100 mM TPA in whole blood (blue) at a scan rate of 100 mV s⁻¹ over the potential range 0.4 ≤ v ≤ 2 V vs. Ag/AgCl. PMT input voltage = 0.75 V.

A shift in oxidation potential from 1.10 to 1.00 V is seen following addition of TPA indicating different mechanisms for ECL production are occurring (involve O₂^{•-} and TPA[•] respectively (section 3.4.1.1)) and are doing so with different electron transfer kinetics (section 4.3.2.1). Enhancement in ECL intensity is observed, however, it is not as great as that seen in PBS (section 3.4.1) demonstrating inhibition of TPA oxidation and/or quenching of TPA[•] is taking place in blood. From this data it appears that an alternative anodic co-reactant may be better suited for signal enhancement in whole blood, such as 2-(dibutylamino)ethanol, which requires further investigation in the future.

5.4.3 NIR vs visible region ECL - Light penetration through whole blood

The key advantage of these QDs over visible region QD ECL emitters is their NIR emission. Results from section 5.4.2 have shown that a strong ECL signal can be generated and detected directly from whole blood using these NIR

QDs. However, investigations have yet to be carried out to determine whether this response is superior to that generated from visible region QDs.

A comparison of the detectable ECL response from 800, 640 and 560 nm QDs was carried out to investigate the penetrability of this light signal through whole blood. In the cathodic region, $K_2S_2O_8$ was used as co-reactant as it generated the strongest ECL emission. In the anodic region, strong emission from the co-reactant free system in whole blood meant this method was used for comparison. However, it was discovered that 560 and 640 nm QDs could not produce a detectable ECL signal with this system, as the redox potential of the $O_2^{\cdot-}/O_2$ couple must not be sufficient to inject an electron into the LUMO levels of these QDs (which will be higher than the LUMO level of 800 nm QDs owing to their smaller size and larger E_g). Therefore, TPA was used in this comparison as all investigated QDs had the ability to generate an ECL signal with this co-reactant. Figure 5.11 shows the result of these comparisons and Table 5.1 the maximum ECL intensities and potentials at which they occur.

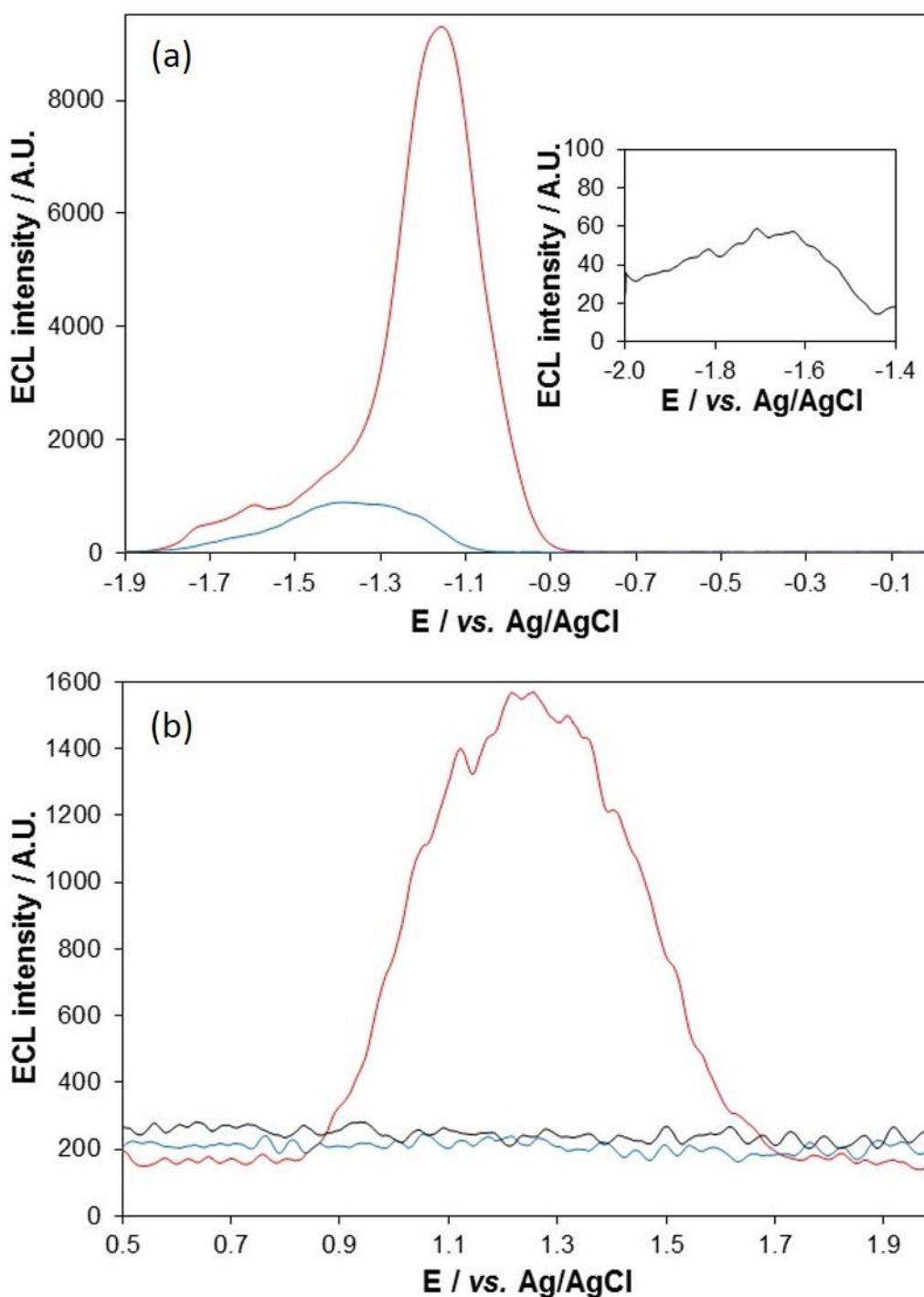


Figure 5.11 - (a) ECL response of 800 nm (red), 640 nm (blue) and 560 nm (inset, black) QD/chitosan film in 1 mM $K_2S_2O_8$ in whole blood at a scan rate of 100 mV s^{-1} over the potential range $-1.9 \leq v \leq 0 \text{ V vs. Ag/AgCl}$. (b) ECL response of 800 nm (red), 640 nm (blue) and 560 nm (black) QD/chitosan film in 20mM TPA in whole blood at a scan rate of 100 mV s^{-1} over the potential range $0.5 \leq v \leq 2 \text{ V vs. Ag/AgCl}$. PMT input voltage = 0.75 V.

Table 5.1 – E_{pc} / E_{po} and ECL intensities of 800, 640 and 560 nm QDs in whole blood + 1 mM $K_2S_2O_8$ (cathodic) or 20 mM TPA (anodic). PMT input voltage = 0.75 V.

QD emission λ / nm	E_{pc} / V vs. Ag/AgCl	ECL intensity / A.U.
800	-1.15	9299
640	-1.35	897
560	-1.65	58
QD emission λ / nm	E_{po} / V vs. Ag/AgCl	ECL intensity / A.U.
800	1.20	1569
640	n/a	n/a
560	n/a	n/a

In the cathodic region, the potential of maximum ECL intensity follows the expected trend of decreasing potential as QD size decreases (and therefore energy of the LUMO increases). An ECL signal is seen with all QDs, however, the detected response from 800 nm QDs is significantly more intense than that for the 640 or 560 nm QDs (10 and 160 times more intense respectively) for the same QD concentration. The detected response from the 640 nm QDs is 15 times more intense than that from the 560 nm QDs. These results indicate that as the wavelength of emitted light increases, the penetrability of this light through whole blood also increases. This is in line with the optical absorption of whole blood, which decreases with increasing wavelength, reaching a minimum at approximately 800 nm.⁵

In the anodic region, only NIR QDs produced a detectable ECL signal, which indicated that light generated by 640 and 560 nm QDs in TPA/whole blood did not have sufficient intensity and penetrability to reach the detector. With 800 nm QDs, a strong oxidative ECL peak at 1.20 V was observed, which provided further confirmation that these QDs are ideal for use as ECL emitters directly from whole blood.

This data has shown that NIR QD ECL has significantly improved penetrability through whole blood samples when compared to QDs with emission in the visible region. This is the first time such a comparison has been made and exemplifies the excellent optical properties associated with NIR QDs for use with direct blood analysis.

Overall, the results from this section have shown that NIR QDs can be used to generate anodic ECL in whole blood without the requirement for an additional co-reactant. The significance of this lies in the fact that an extremely simple system can be used for generation of an intense ECL response from whole blood. This is very attractive for development of biosensors (particularly point-of-care devices) as it minimises cost, sample preparation and any disruption to a biological system that may occur following co-reactant addition. It appears that only QDs with a sufficiently low LUMO energy can generate an anodic ECL response with $O_2^{\cdot-}$. Therefore, these NIR QDs are unique in their ability to both generate a strong anodic ECL response with this species and do so at such a wavelength that interference directly from whole blood is minimal.

This data has also shown that cathodic NIR QD ECL in whole blood is sensitive to addition of a small, reactive molecule, producing a strong enhancement in ECL intensity. The intense signal obtained with NIR QD - $K_2S_2O_8$ system in whole blood suggests that direct detection of low concentration analytes in blood could be possible using this system. This provided the groundwork for development of the first NIR QD ECL biosensors with direct whole blood analysis.

5.5 Development of whole blood ECL biosensors

Strong cathodic and anodic ECL signals in whole blood were observed using NIR ECL emitters and it was therefore proposed that they could be used for the detection of clinically relevant analytes in these conditions.

5.5.1 A cathodic ECL system

5.5.1.1 QD concentration

In order to confirm the viability of this NIR ECL system in whole blood, the response to changes in QD concentration was examined. Sensitivity to changes in ECL emitter concentration is crucial in the vast majority of biosensors, particularly those that operate through a sandwich-type immunoassay setup. Therefore, the usefulness of this system for incorporation into novel biosensors is dependent upon a detectable response to alterations in QD concentration. Figure 5.12 highlights the systems response to increasing QD concentration.

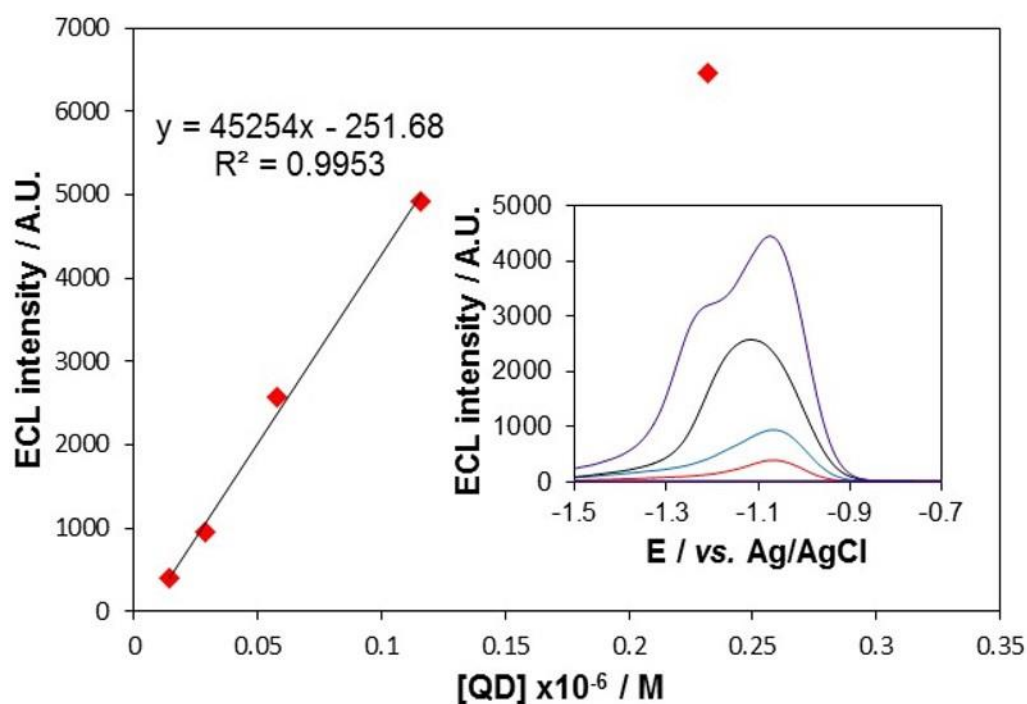


Figure 5.12 - Maximum ECL response of 0.0145, 0.029, 0.058, 0.116 and 0.232 μM 800 nm QD/chitosan film in 1 mM $\text{K}_2\text{S}_2\text{O}_8$ in whole blood at -1.15 V vs. Ag/AgCl. Inset shows ECL response of 0.0145 (red), 0.029 (blue), 0.058 (black) and 0.116 (purple) μM 800 nm QD/chitosan film in 1 mM $\text{K}_2\text{S}_2\text{O}_8$ in whole blood at a scan rate of 100 mV s^{-1} over the potential range $-1.5 \leq v \leq -0.7 \text{ V vs. Ag/AgCl}$. PMT input voltage = 0.50 V.

This shows a linear increase in ECL intensity from 0.0145 to 0.116 μM , above which the signal deviates negatively from linearity. This indicated that quenching of the ECL response is beginning to occur at these higher concentrations, however, maximum sensitivity is achieved using the highest concentration (0.232 μM). The system is responding to an increase in QD concentration in whole blood, which bodes well for future development into more sophisticated immunoassays.

5.5.1.2 Response variability

The inter-sample response variability was investigated in order to determine the effect of different whole blood samples on the ECL response (Figure 5.13).

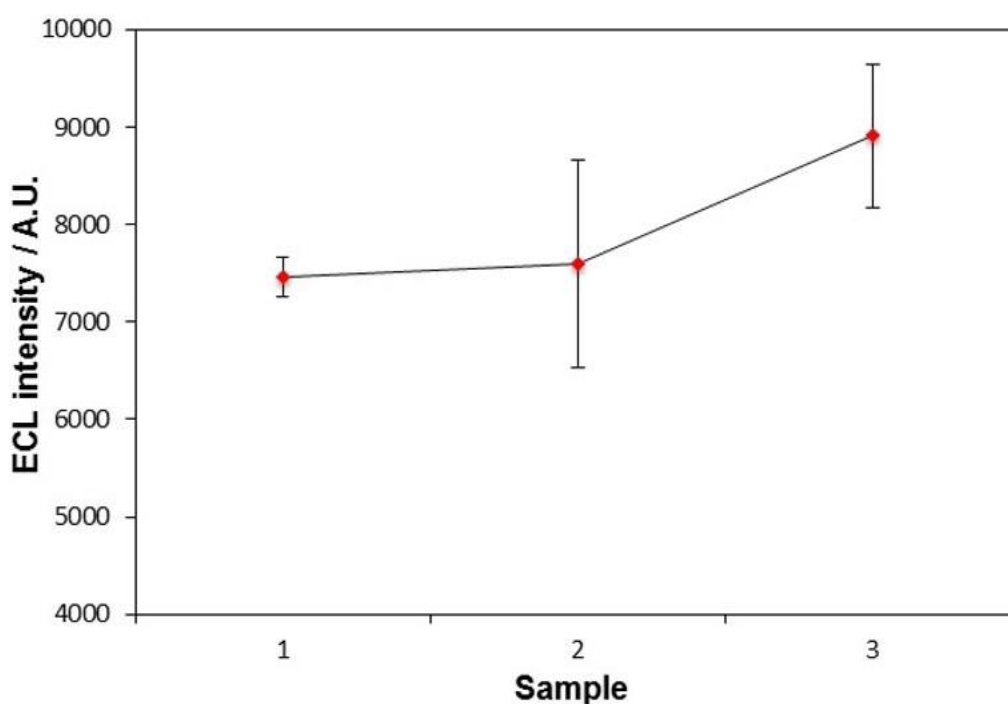


Figure 5.13 - Average ECL response of 800 nm QD/chitosan film in 3 samples of 1 mM $\text{K}_2\text{S}_2\text{O}_8$ in whole blood at a scan rate of 100 mV s^{-1} at $\sim -1.15 \text{ V}$ vs. Ag/AgCl . Error bars represent standard deviations from triplicate data set. PMT input voltage = 0.50 V.

The average intra- and inter-sample relative standard deviation was 8.3 and 10 % respectively. This shows that the ECL behaviour of the NIR QDs is consistent across different whole blood samples.

5.5.1.3 Homocysteine detection

Homocysteine (Hcy) is an α -amino acid that is formed *in vivo* through metabolism of methionine.¹⁷ Typical blood Hcy levels are up to 15 μ M, with concentrations above this resulting in hyperhomocysteinemia.¹⁸ Hyperhomocysteinemia has been linked with pulmonary embolism, stroke, deep vein thrombosis and ischaemic heart disease.¹⁹⁻²¹ This is because Hcy and its cyclic metabolite, homocysteine thiolactone, modify the behaviour of endothelial cells, which can promote vascular injury as their surface becomes a pro, rather than anti-coagulant.^{22, 23} They promote platelet aggregation²⁴ and oxidative stress due to the reactivity of the sulfhydryl group.²⁵ Detection of Hcy tends to be via fluorescence coupled to high-powered liquid chromatography,^{26, 27} electrochemical,^{28, 29} or colorimetric methods.^{30, 31} There are currently no methods for detection of Hcy directly from whole blood samples or using ECL as the detection method. Hcy contains a sulfhydryl group, which are potent radical quenchers,³² and so it was proposed that detection of Hcy could be accomplished through monitoring a decrease in ECL intensity. In order to test this hypothesis, the influence of Hcy concentration on the ECL of NIR QDs in PBS was first investigated (Figure 5.14).

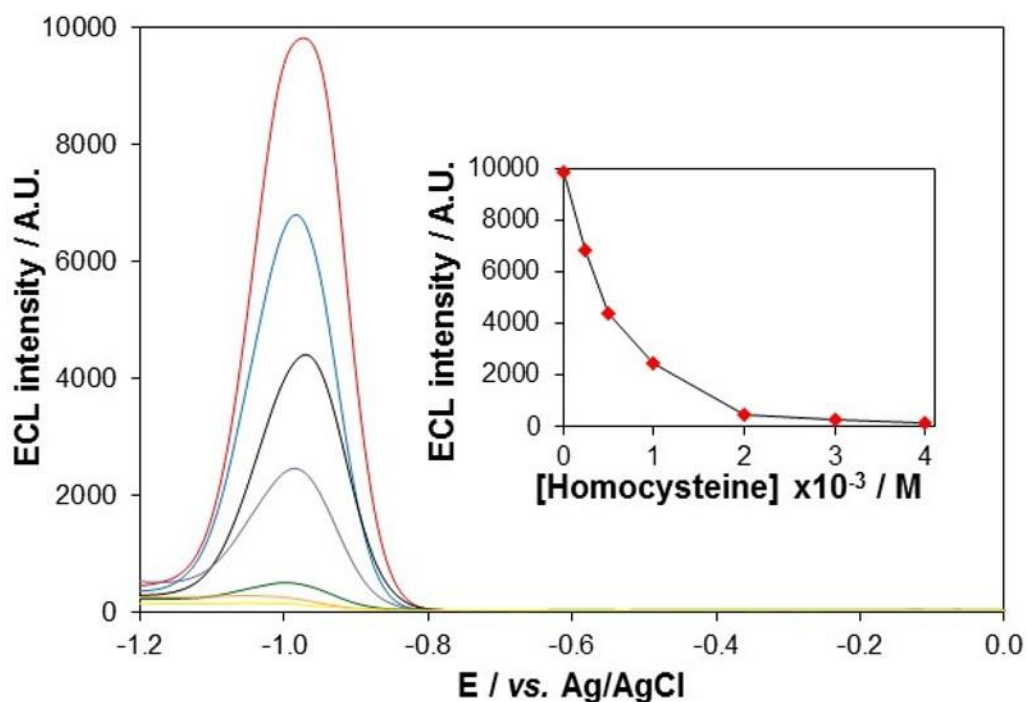
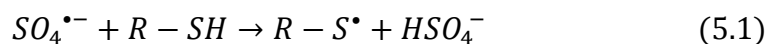


Figure 5.14 - ECL response of 800 nm QD/chitosan film in 1 mM $K_2S_2O_8$ in 0.1 M PBS (red) + 0.25 (blue), 0.5 (black), 1 (purple), 2 (green), 3 (orange) and 4 (yellow) mM Hcy at a scan rate of 100 mV s^{-1} over the potential range $-1.2 \leq v \leq 0 \text{ V vs. Ag/AgCl}$. Inset shows the maximum ECL response of 800 nm QD/chitosan film in these solutions at $\sim -1 \text{ V vs. Ag/AgCl}$. PMT input voltage = 0.65 V.

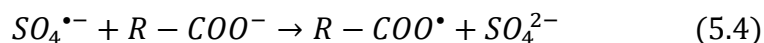
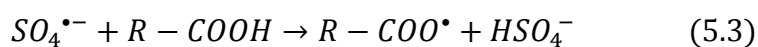
An ECL signal at -1.00 V is observed, which decreases in intensity as the concentration of Hcy increases. The shift in reduction potential compared to whole blood (Figure 5.7) is associated with faster electron transfer between precursor species in PBS as there are fewer interfering species in solution. Hcy inhibits the ECL signal through quenching of the radical precursor species, $SO_4^{\bullet-}$ (equations (5.1) and (5.2)).³²



Where $R=CH_2CH_2CHNH_2COOH$

The sulfhydryl group of Hcy donates a proton to $SO_4^{\bullet-}$ forming a radical thiol species (equation (5.1)), which rapidly dimerises (equation (5.2)).

Alternatively, quenching of $SO_4^{\bullet-}$ can occur via the carboxylic acid moiety of Hcy (equation (5.3) and (5.4)).³³



Where $R=CHNH_2CH_2CH_2SH$

In equation (5.3) a proton is abstracted from the C-H bond forming a carboxyl radical and bisulfate anion. Carboxyl radicals can also be formed through oxidation of carboxylate anion by $SO_4^{\bullet-}$ (equation (5.4)). It is likely that each of these processes contribute to quenching of $SO_4^{\bullet-}$ and therefore reduction in the observed ECL signal, however, it is not clear which is the dominant process.

In order for efficient quenching to occur, the acceptor and donor molecules must be in close contact so that their electron clouds can interact.³⁴ This quenching can be static, which relates to the formation of a ground state donor-acceptor complex, or, more commonly, dynamic, which is diffusion controlled and involves collisions between donor and acceptor molecules, preventing emission. The relationship between emission intensity and quencher is expressed by the Stern-Volmer equation (equation (5.5)), which can be used to calculate the quenching constant of the system.³⁴

$$\frac{I_0}{I} = 1 + K_{SV}[Q] \quad (5.5)$$

Where I_0 is the initial ECL intensity, I the ECL intensity at a specific concentration of quencher $[Q]$, and K_{SV} is the Stern-Volmer quenching constant.

For dynamic quenching, this predicts a linear relationship between I_0/I and $[Q]$ and thus a plot of these parameters has a slope that is equal to K_{SV} , which is the product of the quenching rate constant and the lifetime of the emissive excited state. However, a Stern-Volmer plot of data from Figure 5.14 does not exhibit this linear dependence and instead requires a modification to the Stern-Volmer equation. Previous investigations have shown that the quenching process can be influenced if the emitting species is confined within a polymer film.³⁵⁻³⁷ The so-called *Hindered Access Model* is a two state model that takes into account the fact that some species are accessible and others inaccessible to the quencher.³⁸ Here, this is caused by confinement of the QDs and SO_4^{4-} within the chitosan film, where some species are accessible for quenching and others are isolated from quencher molecules. This modification to the Stern-Volmer equation (equation (5.6)) predicts a linear relationship between $(I_0/I - I)$ and $(1/[Q])$, which yields an intercept equal to f_a^{-1} and a slope of $(f_a K_a)^{-1}$.³⁸

$$\frac{I_0}{I_0 - I} = \frac{1}{f_a} + \frac{1}{f_a K_a [Q]} \quad (5.6)$$

Where f_a is the fraction of accessible species and K_a is the Stern-Volmer quenching constant of this accessible fraction.

Using this modified model, a plot of the data displayed a linear relationship, suggesting that the chitosan polymer is influencing the quenching behaviour in the system (Figure 5.15).

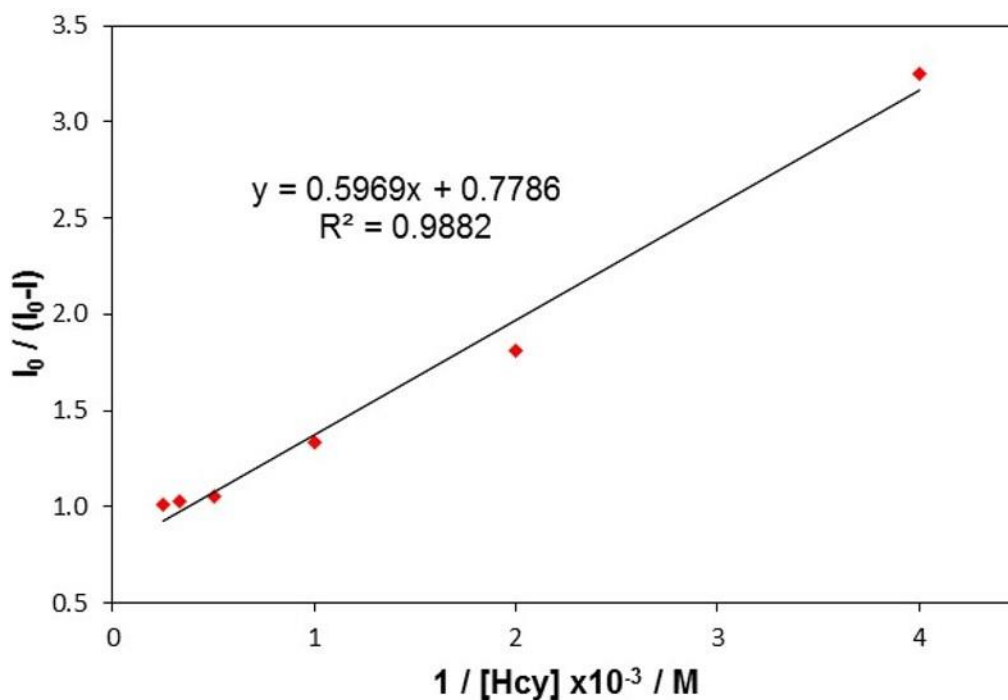


Figure 5.15 - Modified Stern-Volmer plot for 800 nm QD/chitosan film in 0.01 mM $\text{K}_2\text{S}_2\text{O}_8$ with increasing [Hcy].

A linear dependence between 0.25 and 4 mM was observed, with a corresponding K_a value of $1.3 \times 10^3 \text{ M}^{-1}$.

The influence of chitosan on the quenching behaviour was confirmed as a film of bare QDs followed a typical Stern-Volmer relationship (Figure 5.16), yielding a linear dependence of I_0/I on [Q].

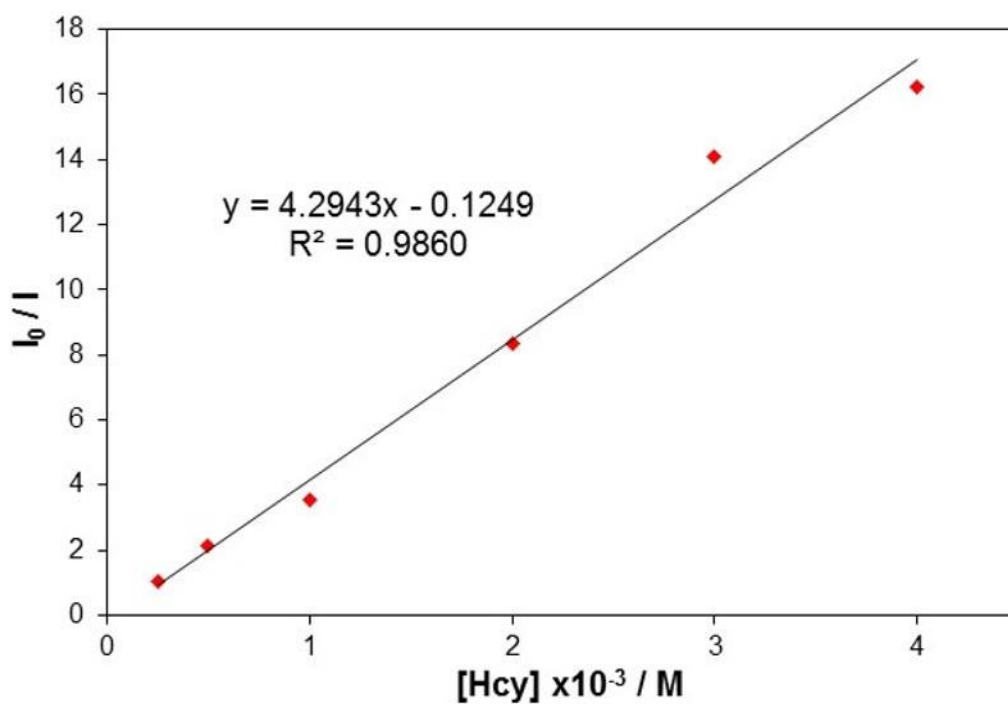


Figure 5.16 - Stern-Volmer plot for a film of bare 800 nm QDs in 0.01 mM $K_2S_2O_8$ with increasing [Hcy].

As Hcy had the ability to quench NIR QD ECL in buffer, the same investigation was carried out in whole blood. The ECL response in blood spiked with increasing Hcy concentrations is shown in Figure 5.17.

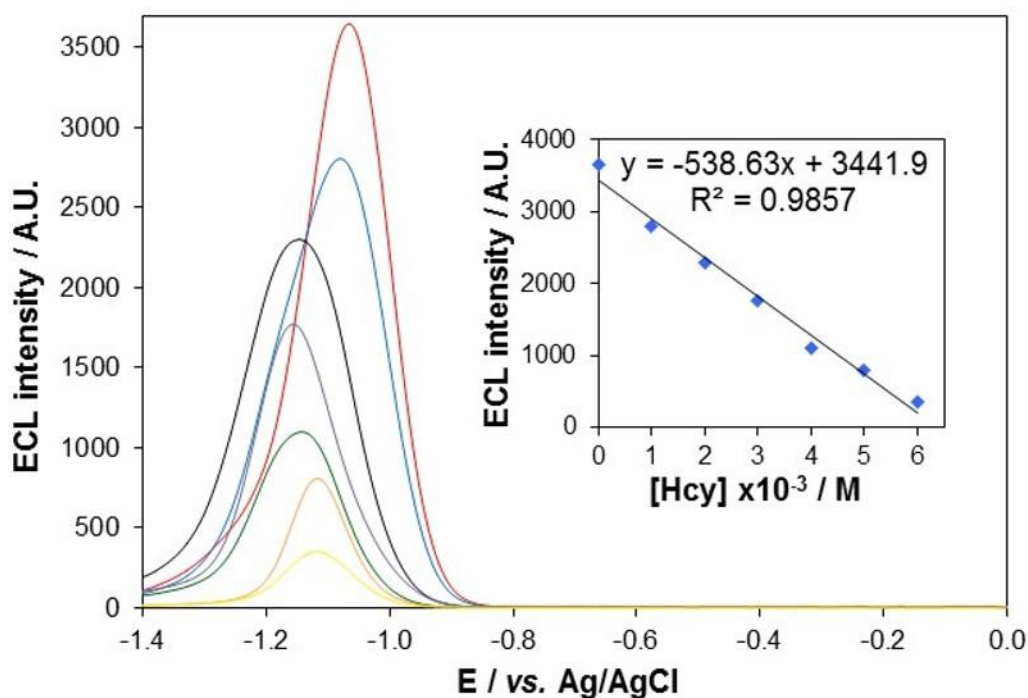


Figure 5.17 - ECL response of 800 nm QD/chitosan film in 1 mM $K_2S_2O_8$ in whole blood (red) + 1 (blue), 2 (black), 3 (purple), 4 (green), 5 (orange) and 6 (yellow) mM Hcy at a scan rate of 100 mV s^{-1} over the potential range $-1.4 \leq v \leq 0 \text{ V vs. Ag/AgCl}$. Inset shows the maximum ECL response of 800 nm QD/chitosan film in these solutions at $\sim -1.15 \text{ V vs. Ag/AgCl}$. PMT input voltage = 0.65 V .

The profile contains an ECL peak at approximately -1.15 V , which decreases in intensity as Hcy concentration increases. Movement of this reductive peak suggests that interference between precursor species and constituents in whole blood is affecting electron transfer in the system. The modified Stern-Volmer plot (Figure 5.18) yields a linear relationship between 1 and 6 mM Hcy, with a K_a value of $1.4 \times 10^2 \text{ M}^{-1}$.

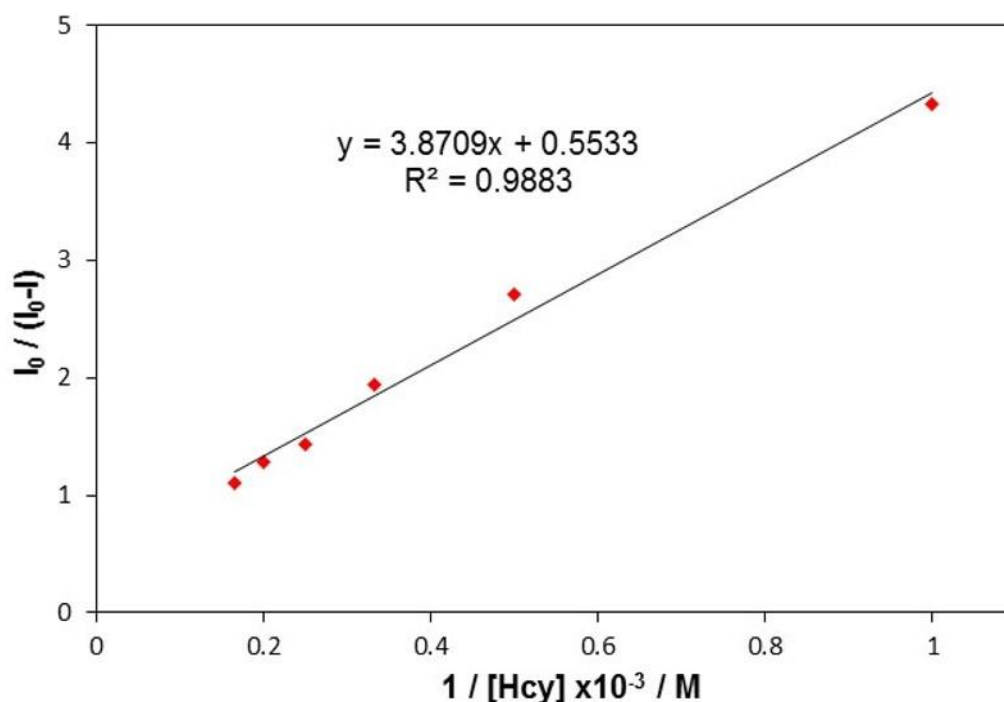


Figure 5.18 - Modified Stern-Volmer plot for 800 nm QD/chitosan film in 1 mM $\text{K}_2\text{S}_2\text{O}_8$ in whole blood with increasing [Hcy].

The quenching rate is approximately 9 times slower than that achieved with Hcy in PBS (from Figure 5.15), indicating that constituents in whole blood are influencing the quenching process. This explains the different relationship between ECL intensity and Hcy concentration observed in blood and PBS (inset, Figures 5.17 and 5.14). This is likely due to the formation of electrostatic interactions between the amine and/or carboxylic acid moieties of Hcy with charged regions of biomolecules (such as albumin) in whole blood and reaction of the sulfhydryl group on Hcy with these species (e.g. alkylation). This will reduce Hcy quenching efficiency as diffusion of this bulkier complex through chitosan will be hindered and reactivity of the sulfhydryl group is diminished. Therefore, its rate of reaction with $\text{SO}_4^{\cdot-}$ at the electrode surface will decrease. The K_a in both buffer and whole blood does not currently allow detection down to clinically relevant levels, however, it is hoped that improvements in biosensor performance would permit this.

This work has shown the applicability of co-reactant NIR QD ECL for the detection of a clinically relevant analyte with direct whole blood analysis.

Significantly, this response has proven to be sensitive to changes in analyte concentration even within this complex matrix. No such systems have been developed previously and this novel biosensor provides evidence that NIR QD ECL systems are capable of selective detection of small biomolecules from whole blood samples.

Furthermore, the ECL response proved sensitive to changes in ECL emitter (QD) concentration, which is very promising for future development of immunoassays with direct whole blood analysis.

5.5.2 Co-reactant free detection

An intense anodic ECL response from NIR QDs without additional co-reactant was detected from whole blood (section 5.4.2), opening up an opportunity for development of a co-reactant free whole blood sensing system.

5.5.2.1 QD concentration

The sensitivity of ECL response in whole blood to changes in QD concentration without an additional co-reactant is highlighted in Figure 5.19.

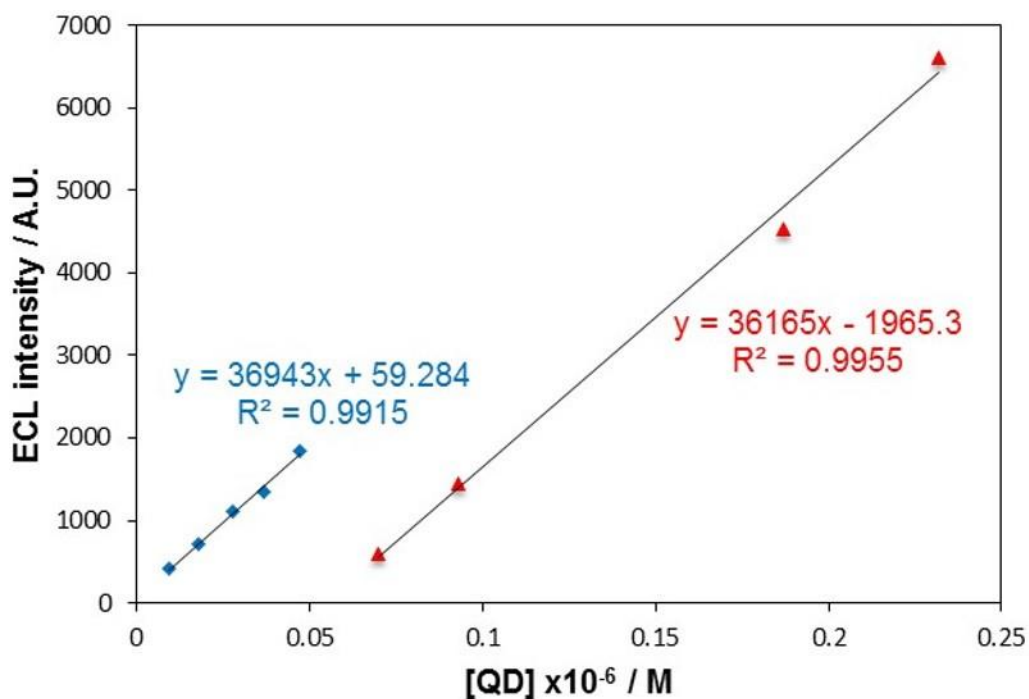


Figure 5.19 - Maximum ECL response of 0.0093-0.047 (blue, PMT input voltage = 1.05 V) and 0.07-0.232 (red, PMT input voltage = 0.75 V) μM 800 nm QD/chitosan film in whole blood at a scan rate of 100 mV s^{-1} at $\sim 1.2 \text{ V vs. Ag/AgCl}$.

This yields two linear ranges (9.3-47 nM and 0.07-0.232 μM) and indicates that maximum sensitivity is achieved using a concentration of 0.232 μM . As expected, these co-reactant free anodic ECL responses are less intense than those achieved in the cathodic region with $\text{K}_2\text{S}_2\text{O}_8$, however, good sensitivity to QD concentration in whole blood was achieved.

5.5.2.2 Response variability

The consistency of response without an additional co-reactant will be affected by the availability of O_2 in solution, which may vary between whole blood samples. Therefore, determination of response precision was required to ensure acceptable reproducibility. Figure 5.20 shows the average ECL response in three whole blood samples.

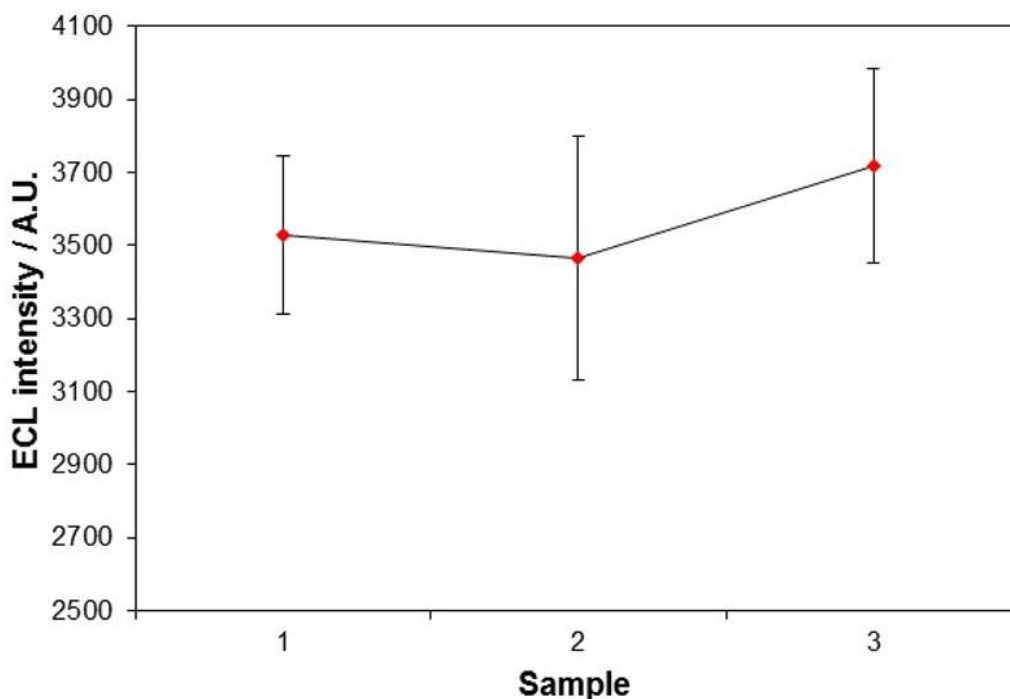


Figure 5.20 - Average ECL response of 800 nm QD/chitosan film in 3 samples of whole blood at a scan rate of 100 mV s^{-1} at $\sim 1.2 \text{ V vs. Ag/AgCl}$. Error bars represent standard deviations from triplicate data set. PMT input voltage = 0.75 V .

The average intra-sample relative standard deviation was 7.60 %. The relative standard deviation between samples was 3.77 %, which is within an acceptable range. This indicates there is improved anodic ECL response consistency from whole blood samples without an additional co-reactant compared to cathodic ECL with $\text{K}_2\text{S}_2\text{O}_8$ (Figure 5.13).

6.4.2.3 Dopamine detection

Dopamine is a catecholamine involved in a wide array of physiological processes.³⁹ It acts within the brain and central nervous system (CNS) as a neurotransmitter and disruption within these systems is linked to a variety of diseases including schizophrenia,⁴⁰ depression,⁴¹ and Parkinson's disease.⁴² Dopamine is not solely involved in the CNS, but also acts on the immune system where it helps to dictate the activity of effector cells,⁴³ the cardiovascular system where it influences factors such as blood pressure and contraction of heart muscles,⁴⁴ and the renal system where it is known to

influence blood supply to the kidney and production of urine.⁴⁵ Detection of dopamine is thus of clinical significance and there are a number of techniques used to do so including voltammetry,^{46, 47} fluorescence,⁴⁸ and ECL.^{49, 50} Detection via ECL is based upon quenching of the response through an energy-transfer process.⁵¹ Therefore, dopamine was selected as an ideal candidate for use in these investigations into whole blood ECL detection as it is often used as a model analyte in ECL studies but has never been examined in blood.

The effect of dopamine concentration on the ECL response of NIR QDs in PBS was examined initially, and is shown in Figure 5.21.

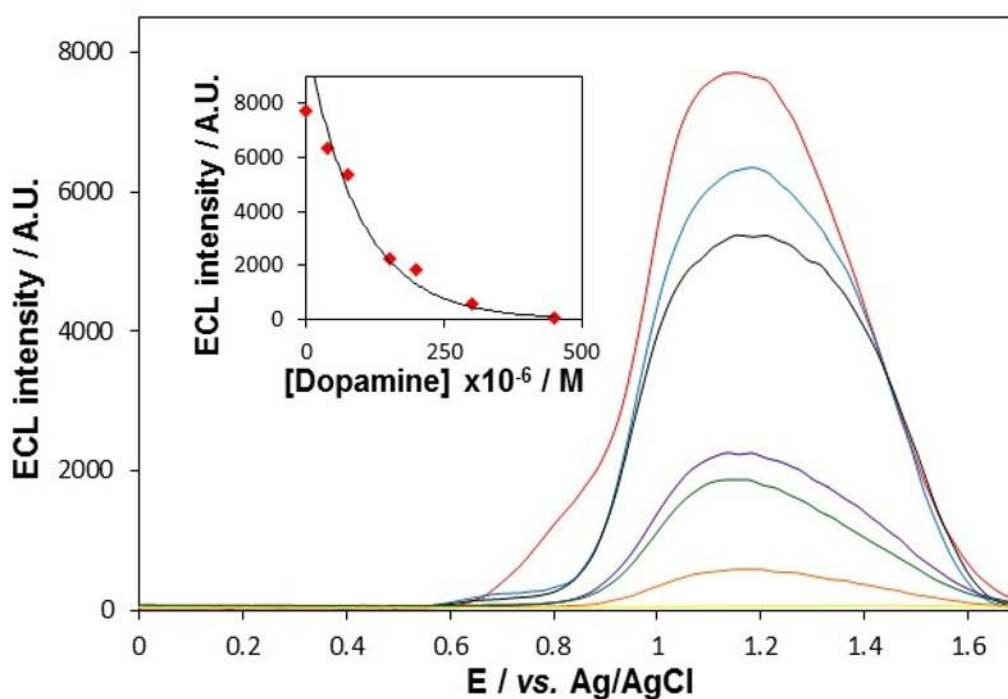


Figure 5.21 - ECL response of 800 nm QD/chitosan film in whole blood (red), 37.5 (blue), 75 (black), 150 (purple), 200 (green), 300 (orange) and 450 (yellow) μM dopamine at a scan rate of 100 mV s^{-1} over the potential range $0 \leq v \leq 1.7 \text{ V vs. Ag/AgCl}$. Inset shows the maximum ECL response of 800 nm QD/chitosan film in these solutions at $\sim 1.20 \text{ V vs. Ag/AgCl}$. PMT input voltage = 0.75 V .

The profile exhibits an oxidative ECL peak at 1.20 V , which decreases in intensity in response to increasing dopamine concentration. Again, a modified

Stern-Volmer equation (equation (5.6)) was used to express the relationship between quencher and ECL intensity (Figure 5.22).

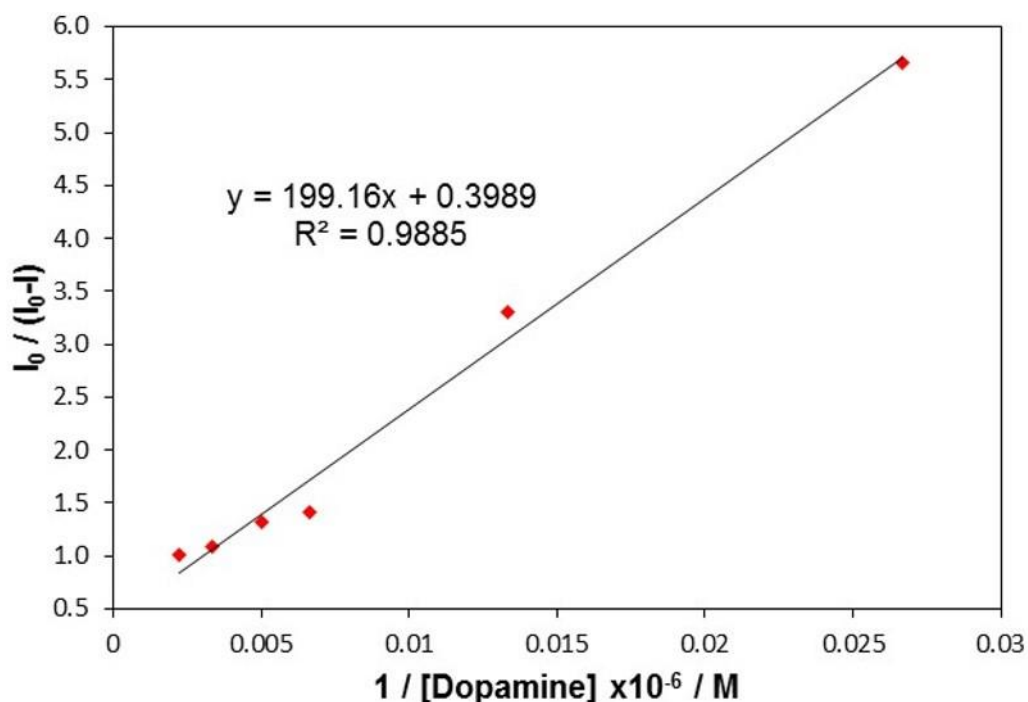


Figure 5.22 - Modified Stern-Volmer plot for 800 nm QD/chitosan film in whole blood with increasing [dopamine].

This yields a linear range of 37.5 to 450 μM dopamine and a K_a of $1.8 \times 10^4 \text{ M}^{-1}$, which specifies dopamine is a more effective quencher of NIR QD ECL emission than Hcy (K_a of $1.3 \times 10^3 \text{ M}^{-1}$ in PBS, section 5.5.1.3). This quenching is a result of an electron transfer process between dopamine and oxidised QDs.⁴⁹ The voltammograms (Figure 5.23) exhibit a small oxidation peak at 0.35 V, which is attributed to the oxidation of dopamine to o-benzoquinone as its peak potential (inset, figure 5.23) is dependent upon dopamine concentration.

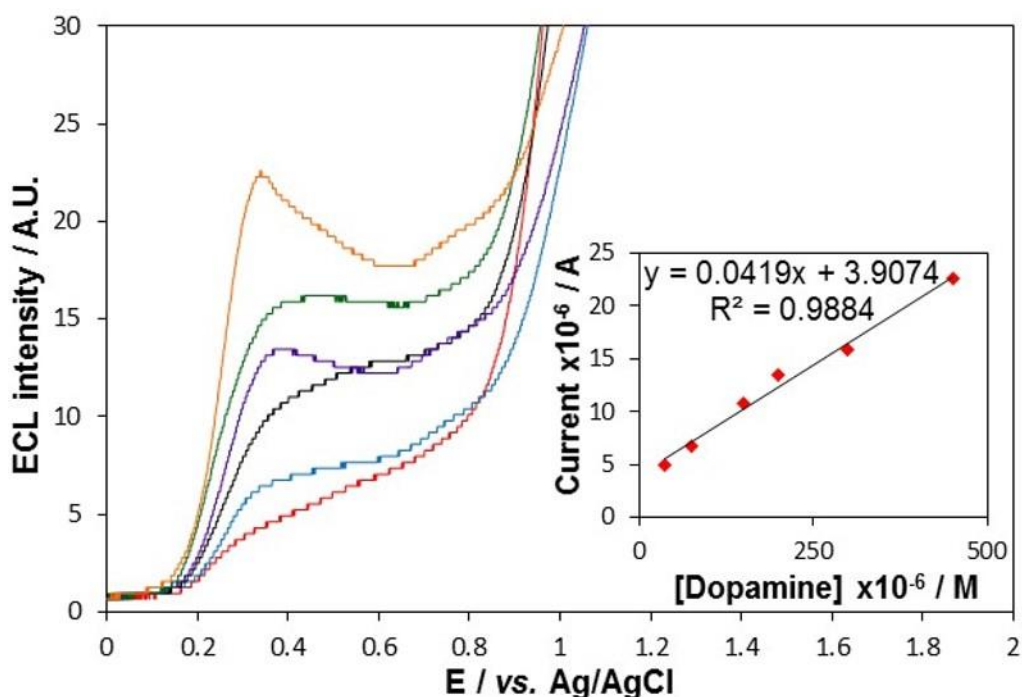


Figure 5.23 - Current response of 800 nm QD/chitosan film in whole blood + 37.5 (red), 75 (blue), 150 (black), 200 (purple), 300 (green) and 450 (orange) μM dopamine at a scan rate of 100 mV s^{-1} over the potential range $0 \leq v \leq 2 \text{ V vs. Ag/AgCl}$. Inset is the linear dependence of this peak current at $0.35 \text{ V vs. Ag/AgCl}$ on [dopamine].

This corresponds to an energy level at approximately -5.10 eV (vs. Ag/AgCl), and therefore transfer of an electron from dopamine to QDs($h^+(1S_h)$) (the hole exists at approximately -5.49 eV) is a favourable process. This results in quenching of the ECL signal, permitting detection of dopamine. As dopamine could effectively quench the ECL of NIR QDs in buffer, detection from whole blood was attempted. Figure 5.24 shows the effect of dopamine concentration on the ECL response of the QD/chitosan film in whole blood.

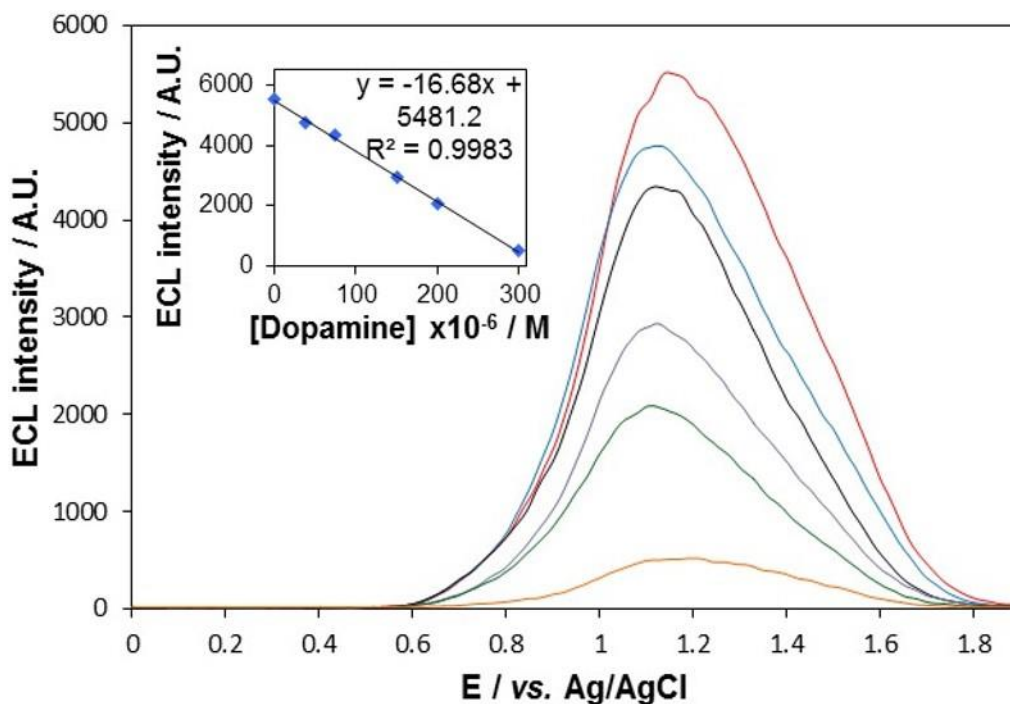


Figure 5.24 - ECL response of 800 nm QD/chitosan film in whole blood + 0 (red), 37.5 (blue), 75 (black), 150 (purple), 200 (green) and 300 (orange) μM dopamine at a scan rate of 100 mV s^{-1} over the potential range $0 \leq v \leq 1.9 \text{ V vs. Ag/AgCl}$. Inset is the linear dependence of this ECL response at $\sim 1.15 \text{ V vs. Ag/AgCl}$ on dopamine concentration. PMT input voltage = 0.75 V .

The profile exhibits an ECL signal at 1.15 V that is linearly dependent on the concentration of dopamine in the whole blood sample over the range $37.5\text{-}300 \mu\text{M}$. The modified Stern-Volmer plot (Figure 5.25) yielded a K_a value of $1.5 \times 10^3 \text{ M}^{-1}$.

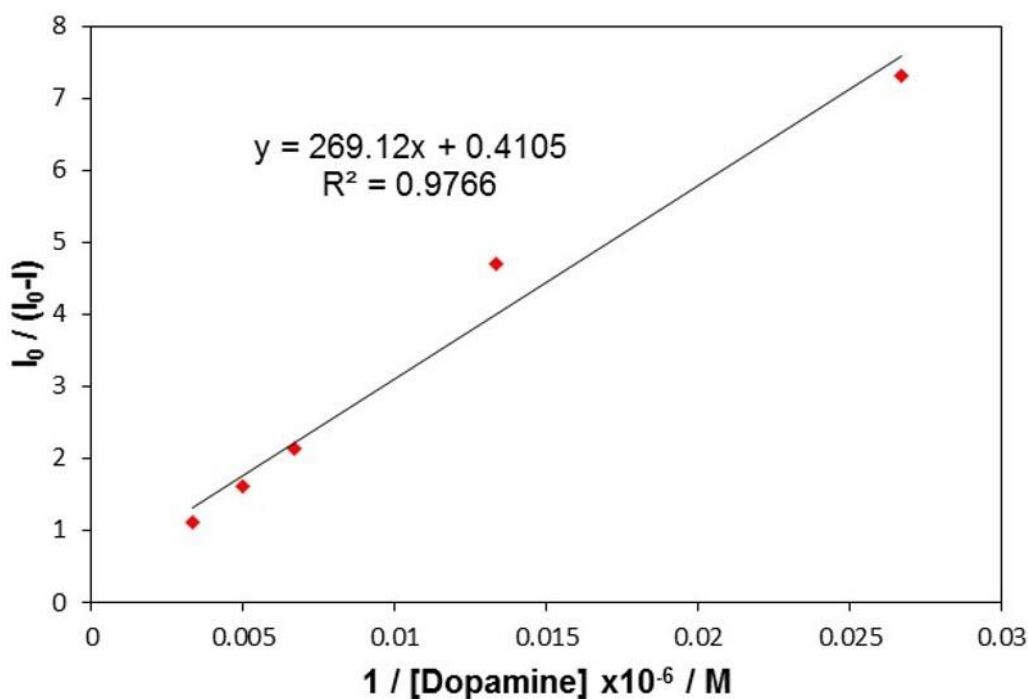


Figure 5.25 - Modified Stern-Volmer plot for 800 nm QD/chitosan film in whole blood with increasing [dopamine].

This rate is approximately 12 times lower than that achieved in buffer, which indicated that de-activation of dopamine quenching ability was occurring. This is likely due to interaction of dopamine with species present in whole blood via electrostatic interactions or hydrogen bonding. This will limit the ability of dopamine to inject an electron into the HOMO of QDs and hinder its diffusion into the film to carry out the quenching process.

Alternative ECL biosensors have low μM dopamine linear concentration ranges.^{49, 50} However, the significance of this biosensor is that ECL detection of dopamine was achieved directly from whole blood and no additional co-reactants were required in the system. It is the first time such a system has been developed and provides further confidence in the ability of these QDs to be effective and responsive ECL emitters in whole blood.

5.6 Conclusion

The aim of this work was to establish the electrochemical properties and ECL performance of NIR QDs in whole blood and to determine whether they were suitable for incorporation into ECL biosensors under such conditions. The electrochemical characteristics of the QDs are similar in whole blood and buffer, with one additional process at -1.15 V in the voltammograms of whole blood. The co-reactant free cathodic ECL signal is suppressed in whole blood, due to quenching of ROS by species in solution. ECL with $K_2S_2O_8$ co-reactant displays a strong signal, which is considerably more intense than that achieved with either 640 or 560 nm QDs, confirming the improved penetrability of 800 nm emission in whole blood. Co-reactant free anodic ECL of the NIR QDs in blood exhibited an intense response at 1.10 V, whereas 640 and 560 nm QDs generated no such detectable signal. Both cathodic and anodic ECL was responsive to the addition of reactive molecules, even in this complex matrix.

Following confirmation that a detectable, responsive ECL signal could be generated in whole blood, a cathodic ECL biosensor for Hcy and a co-reactant free anodic ECL biosensor for dopamine were developed and exhibited good linearity in the mM and μ M range respectively. Both demonstrated altered behaviour in whole blood compared to buffer, which underlines the complex processes that occur in such a matrix. Such findings emphasise the requirement for these investigations into whole blood ECL as the processes involved in light generation are liable to interference from endogenous species. Therefore, this data can be used as both a positive identification of NIR QD ECL generation directly from whole blood and an advisory that it is influenced by matrix components.

Overall, these are the first ECL biosensors to be developed with detection directly from whole blood. This data has demonstrated the penetrability, sensitivity and versatility of NIR QD ECL, which provides an option for the development of innovative biosensors with a particular focus on direct whole blood analysis.

5.7 References

1. D. K. Chatterjee, A. J. Rufaihah and Y. Zhang, *Biomaterials*, 2008, **29**, 937-943.
2. D. K. Sardar, K. L. Nash, J. B. Gruber and A. Sayka, *Biophotonics International*, 2008, **15**, 45.
3. S. Wray, M. Cope, D. T. Delpy, J. S. Wyatt and E. O. R. Reynolds, *Biochimica et Biophysica Acta-Bioenergetics*, 1988, **933**, 184-192.
4. A. Roggan, M. Friebel, K. Doerschel, A. Hahn and G. J. Mueller.
5. M. Friebel, K. Do, A. Hahn and G. Mu, *Journal of biomedical optics*, 1999, **4**, 36-46.
6. C. Woelfle and R. O. Claus, *Nanotechnology*, 2007, **18**, 025402.
7. A. V. Lebedev, V. Pelouch, M. V. Ivanova and D. O. Levitsky, *Hemoglobin*, 2011, **35**, 247-254.
8. A. P. Brown and F. C. Anson, *Analytical Chemistry*, 1977, **49**, 1589-1595.
9. T. Peters Jr, *All about albumin: biochemistry, genetics, and medical applications*, Academic press, 1995.
10. A. Kawakami, K. Kubota, N. Yamada, U. Tagami, K. Takehana, I. Sonaka, E. Suzuki and K. Hirayama, *Federation of European Biomedical Societies Journal*, 2006, **273**, 3346-3357.
11. C. Deng, J. Chen, X. Chen, M. Wang, Z. Nie and S. Yao, *Electrochimica Acta*, 2009, **54**, 3298-3302.
12. P. Di Mascio, M. E. Murphy and H. Sies, *The American journal of clinical nutrition*, 1991, **53**, 194S-200S.
13. B. N. Ames, R. Cathcart, E. Schwiers and P. Hochstein, *Proceedings of the National Academy of Sciences*, 1981, **78**, 6858-6862.
14. R. W. Browne and D. Armstrong, *Methods in Molecular Biology*, 1998, **108**, 347-352.
15. M. Nikinmaa, *An Introduction to Aquatic Toxicology*, Elsevier Science, Waltham, MA, 2014.
16. H. Sies, *European Journal of Biochemistry Reviews*, 1994, **1993**, 101-107.
17. J. P. F. D'Mello and C. A. B. International, *Amino Acids in Human Nutrition and Health*, CAB International, 2012.
18. E. Skibińska, R. Sawicki, A. Lewczuk, J. Prokop, W. Musiał, I. Kowalska and B. Mroczko, *Kardiologia polska*, 2004, **60**, 197-205.
19. C. J. Boushey, S. A. A. Beresford, G. S. Omenn and A. G. Motulsky, *The Journal of the American Medical Association*, 1995, **274**, 1049-1057.
20. J. Danesh and S. Lewington, *Journal of cardiovascular risk*, 1998, **5**, 229-232.
21. D. S. Wald, M. Law and J. K. Morris, *British Medical Journal*, 2002, **325**, 1202.
22. K. Karolczak and B. Olas, *Physiological Research*, 2009, **58**, 623.
23. J. Perła-Kaján, T. Twardowski and H. Jakubowski, *Amino acids*, 2007, **32**, 561-572.
24. V. Rajkumar, P. Ragatzki, A. Sima and J. Levy, *Endocrine*, 1999, **11**, 57-60.
25. J. S. Stamler, J. A. Osborne, O. Jaraki, L. E. Rabbani, M. Mullins, D. Singel and J. Loscalzo, *Journal of Clinical Investigation*, 1993, **91**, 308.

26. A. Araki and Y. Sako, *Journal of Chromatography B: Biomedical Sciences and Applications*, 1987, **422**, 43-52.
27. D. W. Jacobsen, V. J. Gatautis and R. Green, *Analytical biochemistry*, 1989, **178**, 208-214.
28. N. S. Lawrence, R. P. Deo and J. Wang, *Talanta*, 2004, **63**, 443-449.
29. S. A. Pasas, N. A. Lacher, M. I. Davies and S. M. Lunte, *Electrophoresis*, 2002, **23**, 759-766.
30. O. Rusin, N. N. St. Luce, R. A. Agbaria, J. O. Escobedo, S. Jiang, I. M. Warner, F. B. Dawan, K. Lian and R. M. Strongin, *Journal of the American Chemical Society*, 2004, **126**, 438-439.
31. W. Wang, J. O. Escobedo, C. M. Lawrence and R. M. Strongin, *Journal of the American Chemical Society*, 2004, **126**, 3400-3401.
32. L. Dennany, M. Gerlach, S. O'Carroll, T. E. Keyes, R. J. Forster and P. Bertoncello, *Journal of Materials Chemistry*, 2011, **21**, 13984-13990.
33. I. Grgić, B. Podkrajšek, P. Barzaghi and H. Herrmann, *Atmospheric Environment*, 2007, **41**, 9187-9194.
34. J. R. Lakowicz, *Principles of Fluorescence Spectroscopy*, Springer, 2007.
35. S. Deng, T. Zhang, Y. Zhang, D. Shan and X. Zhang, *RSC Advances*, 2014, **4**, 29239-29248.
36. J. H. Clements and S. E. Webber, *The Journal of Physical Chemistry A*, 1999, **103**, 2513-2523.
37. A. R. Eckert, J.-S. Hsiao and S. E. Webber, *The Journal of Physical Chemistry*, 1994, **98**, 12025-12031.
38. N. S. Allen, *Photochemistry and Photophysics of Polymeric Materials*, Wiley, 2010.
39. K. Neve, *The Dopamine Receptors*, Humana Press, 2009.
40. N. R. Swerdlow and G. F. Koob, *Behavioral and brain sciences*, 1987, **10**, 197-208.
41. E. Dailly, F. Chenu, C. E. Renard and M. Bourin, *Fundamental & clinical pharmacology*, 2004, **18**, 601-607.
42. H. Bernheimer, W. Birkmayer, O. Hornykiewicz, K. Jellinger and F. Seitelberger, *Journal of the neurological sciences*, 1973, **20**, 415-455.
43. S. Basu and P. S. Dasgupta, *Journal of neuroimmunology*, 2000, **102**, 113-124.
44. L. I. Goldberg, *Pharmacological reviews*, 1972, **24**, 1-29.
45. M. F. Lokhandwala and F. Amenta, *The FASEB journal*, 1991, **5**, 3023-3030.
46. Y. Zhao, Y. Gao, D. Zhan, H. Liu, Q. Zhao, Y. Kou, Y. Shao, M. Li, Q. Zhuang and Z. Zhu, *Talanta*, 2005, **66**, 51-57.
47. Y. Wang, Y. Li, L. Tang, J. Lu and J. Li, *Electrochemistry Communications*, 2009, **11**, 889-892.
48. V. S. Y. Lin, C.-Y. Lai, J. Huang, S.-A. Song and S. Xu, *Journal of the American Chemical Society*, 2001, **123**, 11510-11511.
49. R. Cui, Y.-P. Gu, L. Bao, J.-Y. Zhao, B.-P. Qi, Z.-L. Zhang, Z.-X. Xie and D.-W. Pang, *Analytical chemistry*, 2012, **84**, 8932-8935.
50. L. Li, H. Liu, Y. Shen, J. Zhang and J.-J. Zhu, *Analytical chemistry*, 2011, **83**, 661-665.
51. X. Liu, H. Jiang, J. Lei and H. Ju, *Analytical chemistry*, 2007, **79**, 8055-8060.

*Chapter 6 – Development of a cholesterol biosensor
based on electrogenerated chemiluminescence of 800
nm CdSeTe/ZnS quantum dot*

6.1 Introduction

The burden of high cholesterol levels on healthcare services worldwide is becoming a widely recognised and increasing problem. There is clear evidence this is related to over-eating and lack of exercise, which are driving the current global obesity epidemic.¹ Hypercholesterolemia (total blood cholesterol concentrations above 5mM)² results in the accumulation of this cholesterol on artery walls, leading to their hardening, thinning and chronic inflammation (atherosclerosis).³ Patients suffering from this indisposition are at a proven risk of developing more serious cardiac related diseases such as ischaemic heart disease^{4, 5}, stroke⁶ and peripheral vascular disease⁷. Detection of elevated cholesterol levels, affecting as much as 50% of the UK general population,⁸ is key in implementing a strategic health plan to reduce total cholesterol blood concentrations and minimise the risk of progression to more serious diseases. Literature in this area indicates that it is levels of high density and low density lipoproteins that are most strongly indicative of cardiovascular disease risk.⁹⁻¹¹ Low levels of high density lipoproteins (HDL) and high levels of low density lipoproteins (LDL) are associated with an increased risk of CVD.¹² This is because oxidation of LDL tends to promote the development of atherosclerosis,¹³ whereas HDL has a host of benefits that fight its onset.¹⁴ Levels of these lipoproteins can be estimated via their associated cholesterol concentrations.¹⁵ As such, the requirement for accurate, robust and selective biosensors for cholesterol detection is of clear clinical importance.

A number of cholesterol detection methods based on spectrophotometric¹⁶, HPLC¹⁷ and gas-liquid chromatography¹⁸ have previously been reported. However, these tend to require expensive equipment, extensive sample preparation and suffer from poorer sensitivity and selectivity when compared to enzymatic based biosensors. The majority of cholesterol biosensors incorporate cholesterol oxidase (ChOx) into their design and use electrochemical detection (amperometric) of H₂O₂, produced as a by-product

in the ChOx-catalysed oxidation of cholesterol in the presence of oxygen¹⁹⁻²³. The presence of ChOx infers excellent inherent selectivity, avoiding the need for lengthy sample preparation procedures and reducing costs. However, interference from other analytes present in the sample, as with any analysis, can lead to error in interpretation.

As outlined in Chapter 1, ECL has been used extensively as a detection method in biosensing. This has allowed the development of a variety of ECL-based biosensors for cholesterol detection. Marquette et al²⁴ developed a biosensor based on the ECL of a luminol/H₂O₂ system, with ChOx immobilised in a membrane through which cholesterol samples were passed. Generation of H₂O₂ in the presence of cholesterol resulted in the emission of ECL from luminol, allowing detection down to 0.6 nM. Ballesta-Claver et al²⁵ created a disposable sensor that incorporated synthesised luminol copolymers onto which ChOx was covalently attached. In the presence of cholesterol, production of H₂O₂ resulted in the generation of ECL from these conducting polymers that showed a linear response to increasing cholesterol concentrations.

Integration of nanomaterials for ECL enhancement has been extensively reviewed (section 1.1.4.2 and 1.2). NIR QDs have exhibited sensitivity towards H₂O₂ (section 3.4.2.1) and have been shown to generate intense, responsive ECL signals directly from whole blood (Chapter 5). As such, the aim of work presented in this chapter was to develop an enzymatic biosensor for cholesterol based on the NIR ECL of these QDs, and to achieve detection directly from whole blood samples.

6.2 Experimental

6.2.1 Apparatus

Electrochemical measurements were carried out using a CH instrument model 760D electrochemical analyser. All experiments were carried out using a conventional three-electrode assembly, consisting of a 3 mm diameter GC working electrode, Pt wire counter electrode and Ag/AgCl reference electrode. GC electrodes were cleaned by successive polishing using 1, 0.3 and 0.05 μM alumina slurry, followed by sonication in ethanol and water, respectively, for 30 mins. The electrodes were then dried under a flow of N_2 gas. CV was carried out at a scan rate of 100 mV s^{-1} and sample interval of 1 mV across a potential range outlined in each figure. Measurements involving simultaneous detection of light and current utilised a CH instrument model 760D connected to a Hamamatsu H10723-20 PMT. The input voltage to the PMT was + 5 V and the control voltage was set between 0.5 and 1.05 V depending on the required sensitivity. During electrochemical experiments, the cell was kept in a light-tight Faraday cage in a specially designed holder configuration where the working electrode was positioned directly above the PMT window. All measurements were made at room temperature.

6.2.2 Materials

Core-shell CdSeTe/ZnS quantum dots (Qdot® 800 ITK™ organic quantum dots, 1 μM in decane) were purchased from Invitrogen. Chitosan (medium molecular weight, 75-85% de-acetylated), phosphate buffered saline (PBS, pH 7.4), hydrogen peroxide (H_2O_2), cholesterol, cholesterol oxidase (ChOx) from *Streptomyces sp.*, Triton X-100, 2-propanol, glutaraldehyde (25 %, aqueous), sodium cyanoborohydride (NaCNBH_3), sodium bicarbonate, Tween 20, glucose, urea, citric acid and 2-(dimethylamino)ethanethiol (DAET) were all purchased from Sigma-Aldrich and used as received. All other reagents used

were of analytical grade, and all solutions were prepared in milli-Q water (18 mΩ cm).

Human serum samples were obtained from Dublin City University following ethical approval and stored at -20°C until use.

Bovine whole blood was obtained from Wishaw Abattoir Ltd (185 Caledonian Road, Wishaw, Lanarkshire, ML2 0HT) and stored in aliquots at -20°C. Aliquots were defrosted at room temperature on the day of analysis and used immediately.

6.2.3 Methods

Preparation of water soluble CdSeTe/ZnS core-shell QDs

The method followed was similar to that developed by Woelfle and Claus²⁶. 0.5 mL of 0.5 M DAET in methanol was mixed with 0.25 mL of the CdSeTe/ZnS QDs in decane (1 μM). N₂ was bubbled through the solution for 5 mins, which was then sealed and left stirring overnight in the dark at room temperature. The QDs were then precipitated with an excess of acetone followed by centrifugation at 5000 rpm for 6 mins. The filtrate was removed and the precipitate was re-dispersed in 0.25 mL of distilled water. These water-soluble QDs were centrifuged for a further 6 mins at 3000 rpm to remove any impurities and then stored in darkness at 4°C.

Preparation of CdSeTe/ZnS core-shell QD-chitosan composite film

A 0.1 % chitosan solution was prepared in 1 % acetic acid and sonicated for 5 mins. The QD/chitosan composite was prepared by mixing aliquots of the water-soluble QDs with the chitosan solution in a 1:1 (v/v) ratio and mixing for 30 s. 3 μL (unless otherwise stated) of this composite was then carefully cast

onto the electroactive portion of a GC electrode, with mixing of the composite for 10 s between electrodes. The film was allowed to dry for 1 h at 4°C.

QD concentration in the film was altered by mixing the water-soluble QDs with a suitable volume of water prior to mixing in a 1:1 (v/v) ratio with chitosan.

Cholesterol and ChOx solution preparation

A 10 mM stock solution of cholesterol was prepared in Triton X-100:2-propanol:0.1 M PBS (pH 7.4) (1:1:8 (v/v) ratio); this required heating for full dissolution. Aliquots of this stock solution were diluted in Triton X-100:2-propanol:0.1 M PBS (pH 7.4) (1:1:8 (v/v) ratio) to achieve the required working concentration. The solution was stored at 4°C when not in use.

A 10 mg/mL ChOx stock solution was prepared on the day of use by dissolving 1 mg of ChOx in 100 µL of distilled water. 10 µL of this ChOx stock solution was added to 990 µL of the cholesterol solutions at varying concentrations, vortexed, and left mixing in an incubator at 45°C (unless otherwise stated) for 75 mins (again, unless otherwise stated). The as prepared QD-chitosan composite films were immersed in these solutions and the ECL signal measured.

Preparation of spiked interference samples

A 5 mM cholesterol solution was prepared to which 10 mM urea, 10 mM glucose or 1 mg/mL citric acid was added. This solution was then incubated with ChOx as outlined above and the ECL response of the QD/chitosan film was then monitored.

Preparation of spiked human serum samples

Human serum was mixed 1 to 1 with cholesterol solutions at different concentrations containing 0.1 mg/mL ChOx. These solutions were mixed and left to incubate for 1 h at 45 °C and then analysed by ECL.

Preparation of CdSeTe/ZnS core-shell QD-chitosan-ChOx composite film – immobilisation via adsorption

The QD-chitosan film and 10 mg/mL ChOx stock solution were prepared as before. After the film had dried, the modified GC electrode was incubated in 10 mg/mL ChOx for 1 h at 4 °C.

Preparation of CdSeTe/ZnS core-shell QD-chitosan-ChOx composite film – glutaraldehyde cross-linking

3 µL of the 0.23 µM 800 nm CdSeTe/ZnS QDs were drop-cast onto the electrode and allowed to dry in the dark at 4°C. 4 µL of 0.05% chitosan was drop-cast onto the GC electrode and left to dry for 1 h at 4°C. This electrode was then incubated with 25 µL of 10% glutaraldehyde in 0.1 M bicarbonate buffer (pH 8.4) for 1 h at room temperature. The electrode was then rinsed with distilled water, followed by incubation in 10 mg/mL ChOx (in 50 mM NaCNBH₃ in 0.1 M bicarbonate (pH 8.4)) for 3 h at room temperature. The electrode was then thoroughly washed in 0.01% Tween 20 (in 0.1 M PBS) and rinsed with distilled water.

Preparation of whole blood samples

Whole blood samples were mixed 1 to 1 with cholesterol solutions at different concentrations containing 0.2 mg/mL ChOx. These solutions were mixed and left to incubate for 2 h at room temperature and then analysed by ECL.

6.3 Cholesterol detection using NIR QD ECL

6.3.1 Viability of the biosensor

H₂O₂, in this case produced as a by-product of the enzymatic oxidation of cholesterol, can act as a co-reactant for the production of ECL from NIR QDs. The resulting ECL profile exhibits a double peak (Figure 3.16) and the intensity of peak 2 (at -1.35 V vs. Ag/AgCl) has exhibited a reproducible linear dependence on H₂O₂ concentration (Figure 3.18). This previous research provided evidence for the H₂O₂ sensitivity of NIR QD ECL, which should have the ability to detect cholesterol based on the dependence of this H₂O₂ concentration on the enzymatic oxidation, and hence concentration of cholesterol. As such, the basis of this biosensor is outlined in Figure 6.1.

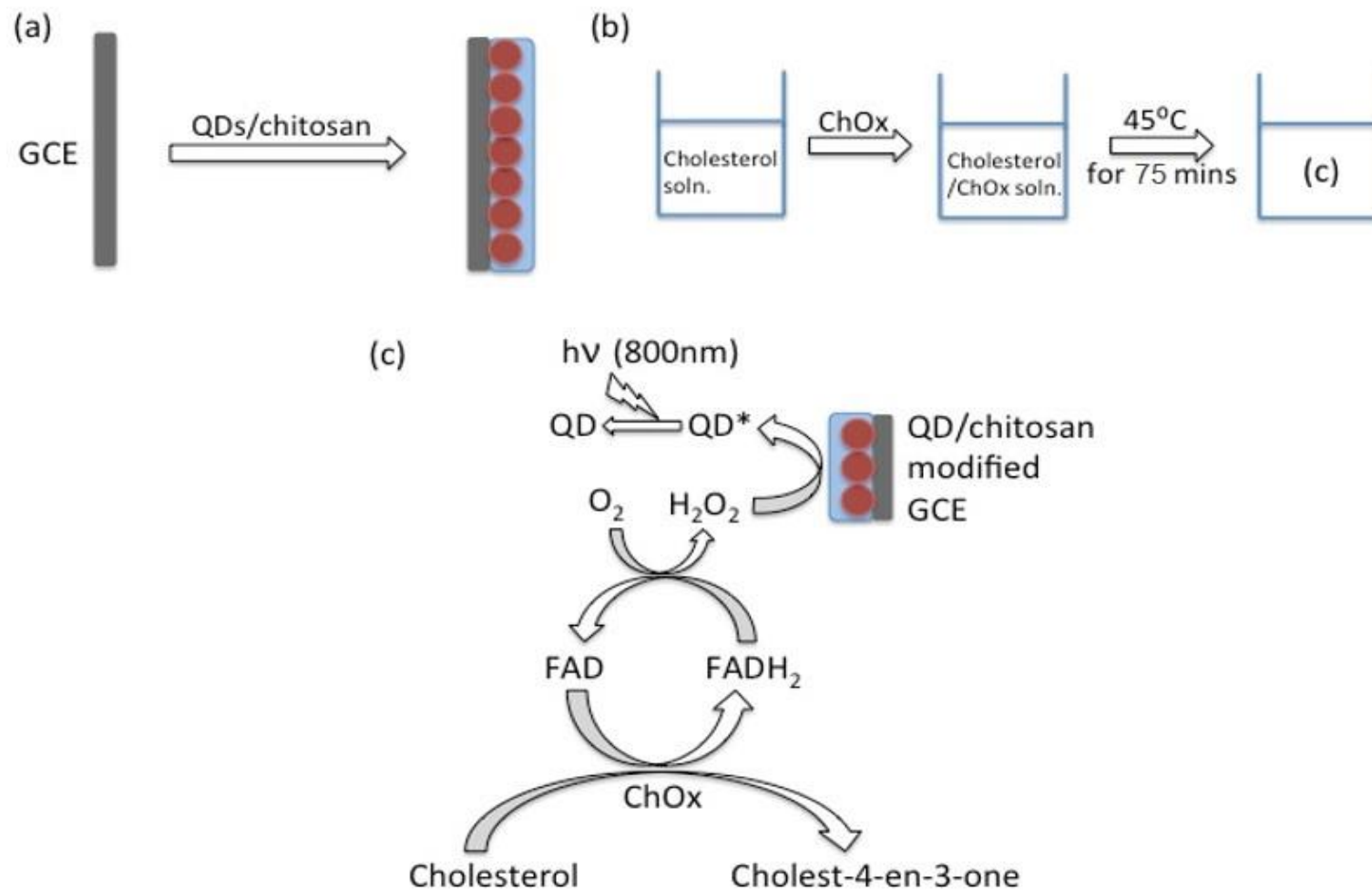


Figure 6.1 – (a) Modification of GC electrode with 800 nm QD/chitosan film, (b) preparation and incubation of cholesterol samples with ChOx and (c) ChOx-catalysed oxidation of cholesterol producing H_2O_2 by-product and its subsequent interaction with NIR QDs to generate an ECL signal.

The outcome of this process should be an increase in ECL intensity at -1.35 V in the presence of cholesterol, which is shown in Figure 6.2.

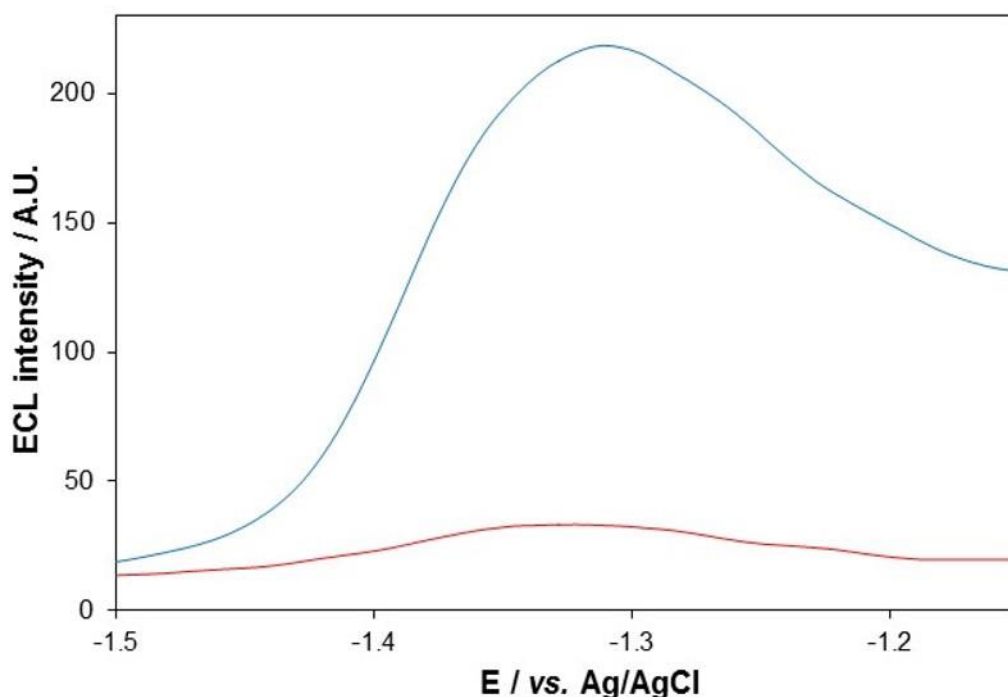


Figure 6.2 – ECL response of 800 nm QD/chitosan film in 0.1 M PBS (red) and 5 mM cholesterol (blue) incubated with 0.1 mg/mL ChOx at 45°C for 75 mins at a scan rate of 100 mV s⁻¹ over the potential range -1.5 ≤ v ≤ -1.1 V vs. Ag/AgCl. PMT input voltage = 0.50 V.

A significant increase in ECL intensity is observed in the presence of cholesterol. This demonstrates successful production of H₂O₂ as a by-product of ChOx-catalysed oxidation of cholesterol, and subsequent interaction of this co-reactant with NIR QDs to enhance their ECL signal. This suggests that this system is a viable method for detecting cholesterol.

6.3.2 Mechanism and kinetics of H₂O₂ production

ChOx is a monomeric flavoenzyme that belongs to the family of oxidoreductases.²⁷ It catalyses the transfer of electrons from the CH-OH group of steroids containing a 3β-hydroxyl group to its co-factor flavin adenine dinucleotide (FAD), and the isomerisation of this oxidised steroid to a Δ⁴-3-

ketosteroid.²⁷ ChOx structure consists of two loops and involves two domains, a FAD co-factor binding domain and a cholesterol binding domain. The FAD domain comprises α -helices sandwiching a central mixed β -pleated sheet, whilst the steroid domain consists largely of a β -pleated sheet.²⁸ The active site is buried deep within this hydrophobic internal structure between these two domains, with opening of loop regions allowing sequestration of cholesterol into the active site from the aqueous environment.²⁸ It is suggested that a histidine residue acts as the proton acceptor from the C₃-hydroxyl group of the steroid and can consequently stabilise the dienolic intermediate during isomerisation.²⁹

In the presence of ChOx, cholesterol is oxidised and H₂O₂ produced in the process outlined in Figure 6.3.³⁰

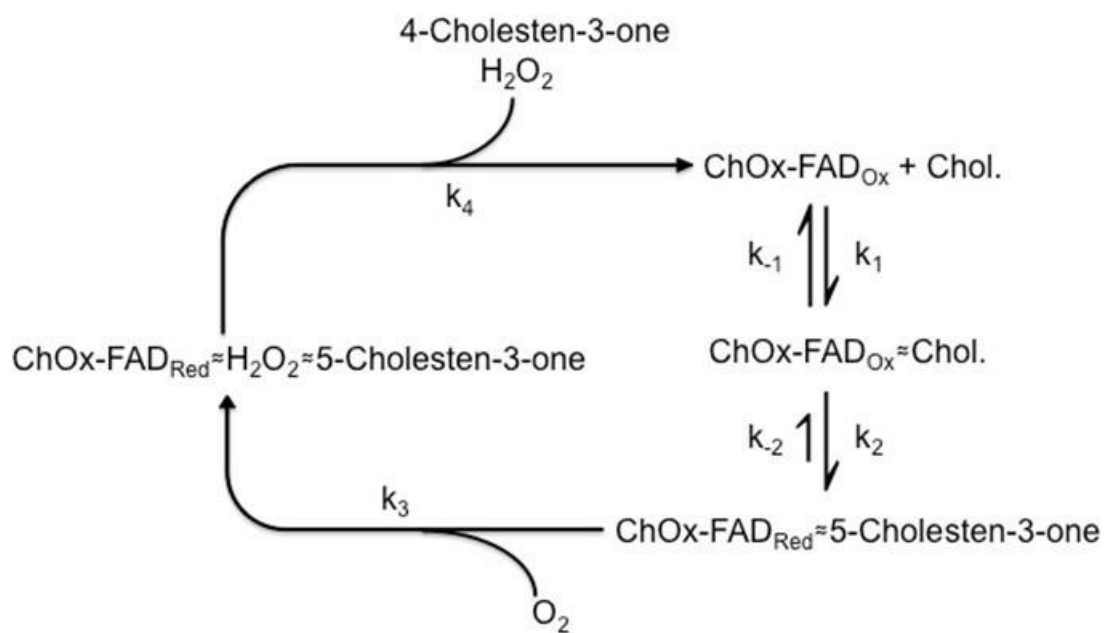


Figure 6.3 - Mechanism of action of the ChOx-catalysed oxidation of cholesterol. Adapted from Pollegioni *et al.*³⁰

The cholesterol molecule must bind to the active site of the enzyme at a rate, k_1 . An oxidised flavin, present in the FAD-binding domain that forms the roof of the active site, can then accept hydrogen from the C₃-(OH) of cholesterol to form 5-cholesten-3-one and reduced flavin (rate, k_2). This process is in

competition with the dissociation of the enzyme-substrate complex pre substrate oxidation (rate, k_{-1}) and is essentially reversible. These processes have the relative rates $k_1 \gg k_{-1} > k_2 \gg k_{-2}$.³⁰ O_2 then enters the system as the substrate for re-oxidation of flavin and is reduced to form H_2O_2 and $E-FAD_{Ox}$ – 5-cholesten-3-one at rate, k_3 . 5-cholesten-3-one then undergoes isomerisation in the active site to form the final product 4-cholesten-3-one, resulting in dissociation of the enzyme-substrate complex, with the release of H_2O_2 and regeneration of the enzyme ready to bind with another cholesterol molecule.

The initial rate of H_2O_2 production is governed by the binding and oxidation of cholesterol (k_1 and k_2) and by the availability of O_2 (k_3). Overall, it is determined by the turnover number (k_{cat}) of the enzyme, which comprises k_1 - k_3 and the regeneration of the enzyme, k_4 , and is defined as the maximum number of substrate molecules that the enzyme can convert to product per active site per unit time.³¹ Therefore, a number of factors will influence H_2O_2 concentration in solution and these must remain as constant as possible (except cholesterol concentration) in order for a stable ECL response to be obtained from this system. Table 6.1 displays the ECL response of the QD/chitosan film in three separate cholesterol/ChOx solutions.

Table 6.1 – The ECL response of 800 nm QD/chitosan film in three solutions of 3 mM cholesterol/0.1 mg/mL ChOx incubated at 45°C for 75 mins at a scan rate of 100 mV s⁻¹ at a potential of ~-1.35 V vs. Ag/AgCl. PMT input voltage = 0.50 V.

Solution	ECL response at ~-1.35 V vs. Ag/AgCl.	% RSD
1	234.7	1.91
2	237.8	
3	229.0	

The data has a % RSD within an acceptable range, illustrating H_2O_2 production and the kinetics of its subsequent oxidation and interaction with QDs are occurring at a consistent rate between sample solutions.

6.3.3 Optimisation of experimental conditions

As the presence of cholesterol yielded an increase in ECL intensity (Figure 6.2), the experimental conditions that maximised H₂O₂ production (monitored through an increase in ECL intensity at -1.35 V) were investigated (Figure 6.4).

From Figure 6.4 (a), maximum ECL intensity was apparent after 75 mins incubation, followed by a decrease in intensity with longer incubation times. This data shows that H₂O₂ concentration in solution increases (up to 75 mins) as a greater number of interactions between cholesterol and ChOx can occur over the duration of the experiment. However, it appears the decomposition of H₂O₂ into O₂ and H₂O dominates over its production with incubation greater than 75 mins, indicating the rate of H₂O₂ production decreases over time.

Figure 6.4 (b) illustrates the effect of incubation temperature on the ECL response. Temperature is known to influence enzyme activity as it can alter enzyme conformation, affecting the availability of the active site for substrate binding.³² The temperature profile of ChOx shows an increase in activity from room temperature up to 45°C, followed by a loss of activity at higher temperatures. This demonstrates that active site availability for cholesterol binding is optimised at 45°C (for an incubation period of 75 mins), which is in close agreement with manufacturer data.³³ At higher temperatures, enzyme de-naturation and loss of activity can take place because of irreversible changes to its conformation.³⁴

Figure 6.4 (c) shows an increase in ECL intensity from 0.02 to 0.1 mg/mL ChOx that is indicative of elevated H₂O₂ levels in solution. At higher enzyme concentrations, there are a larger number of molecules available for interaction with cholesterol and therefore the likelihood of a successful collision and binding event occurring between the two is greater.³⁵ As a result, more cholesterol molecules will be oxidised and a higher concentration of H₂O₂ by-product will be produced, which can then interact with QDs to generate a

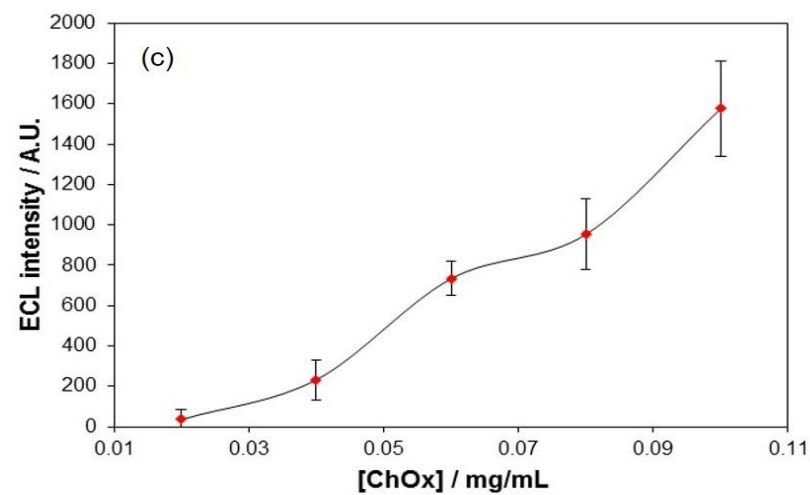
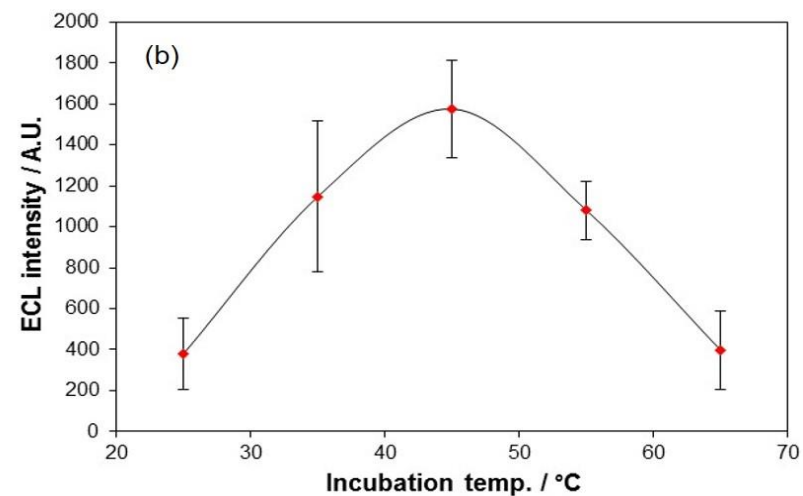
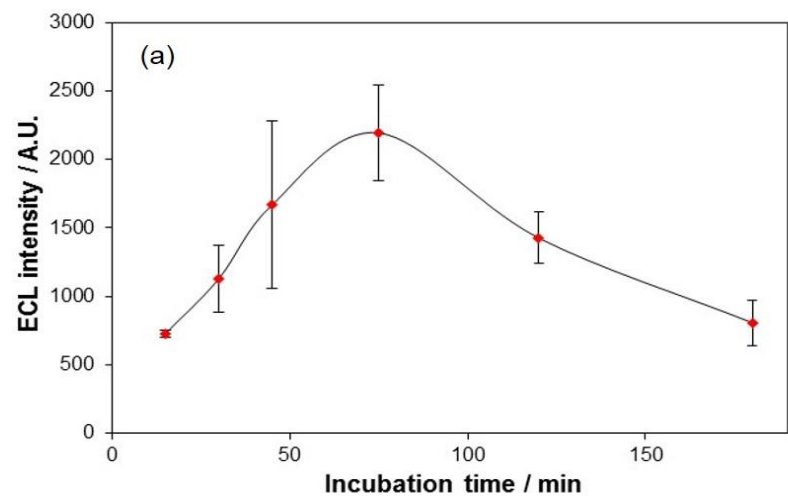


Figure 6.4 – Average ECL response at ~ -1.35 V vs. *Ag/AgCl* of 800 nm QD/chitosan film in 5mM cholesterol with varied (a) incubation time, (b) incubation temperature and (c) [ChOx]. PMT input voltage = 0.70 V.

stronger ECL signal. The high end of the investigated range was limited by the concentration of the stock solution.

The influence of pH on ECL intensity was also examined and is shown in Figure 6.5.

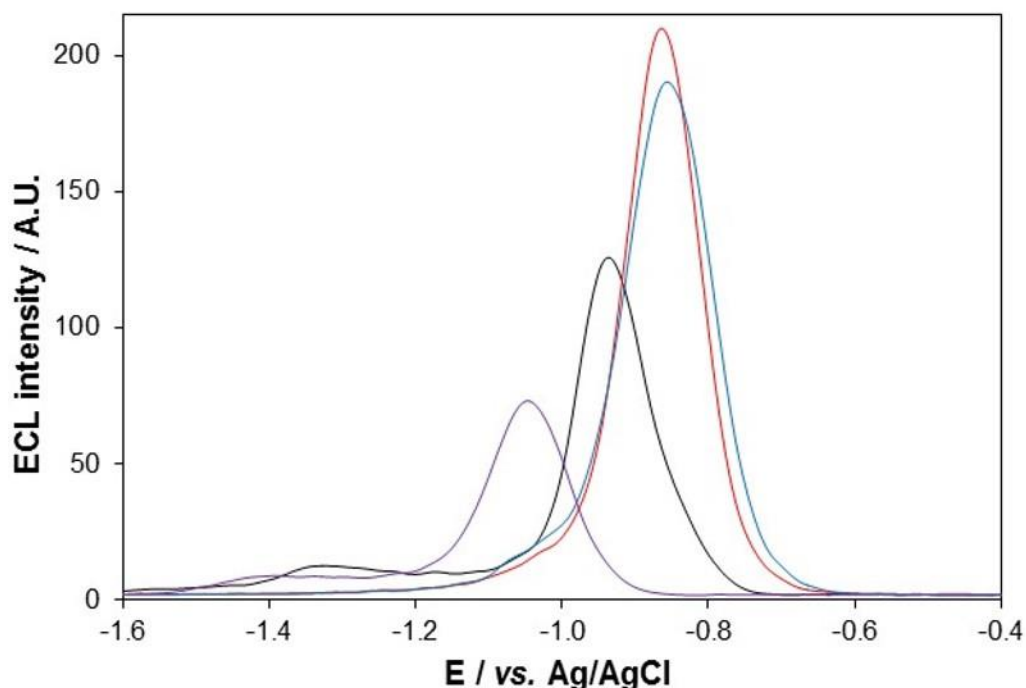
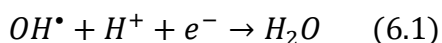


Figure 6.5 - ECL response of 800 nm QD/chitosan film in 5 mM cholesterol at pH 1 (red), 5 (blue), 7.4 (black) and 10 (purple) at a scan rate of 100 mV s⁻¹ over the potential range -1.6 ≤ v ≤ -0.4 V vs. Ag/AgCl. PMT input voltage = 0.50 V.

In acidic conditions a single reductive ECL peak at -0.90 V is observed, whereas a double peak is seen in neutral and basic conditions. The potential shift in appearance of the ECL peaks has been discussed previously (section 4.3.3.2). In acidic conditions a peak at -1.35 V is not observed, likely caused by rapid conversion of OH[•] into H₂O diminishing its concentration at the electrode surface available for ECL reactions (equation (6.1)).



Alterations in pH are thought to affect substrate binding through modification of acidic and basic side chains within the active site.³⁵ This can lead to

conformational changes in the structure of the active site, changing its accessibility for substrate molecules. This is likely contributing to the increase in intensity of peak 1 under acidic conditions. Additionally, as reduction of O_2 to H_2O_2 is a proton coupled electron transfer, its rate in acidic conditions is likely higher, increasing the concentration of H_2O_2 produced. An increase in the porosity of the chitosan film may also be contributing to the increase in intensity. Protonation of its amino group causes repulsion between neighbouring $-^+NH_3$ sites and permits easier diffusion of co-reactant molecules towards the electrode surface. As maximum ECL intensity of the H_2O_2 sensitive peak was achieved in pH 7.4, it was used for further sensor development.

6.3.4 Dependence of NIR QD ECL on cholesterol concentration

Incorporating the most sensitive film and system parameters (section 4.3.1 and 4.3.4 respectively) with the experimental conditions optimised in the previous section allowed detection of cholesterol using the NIR QD ECL biosensing system outlined in Figure 6.1. The dependence of ECL intensity on cholesterol concentration is shown in Figure 6.6.

ECL intensity (at -1.35 V vs. Ag/AgCl) shows a stable linear dependence on cholesterol concentration from 0.25 – 5 mM, demonstrating successful application of this biosensor for cholesterol detection in buffer. At higher cholesterol concentrations, a negative deviation from linearity was observed, which could be the result of substrate saturation of the enzyme. Under such circumstances, the rate of enzyme-catalysed reaction reaches a maximum as all available active sites are occupied by substrate molecules.³⁵ The achieved linear dependency is within a clinically relevant range, which will help minimise sample preparation requirements.

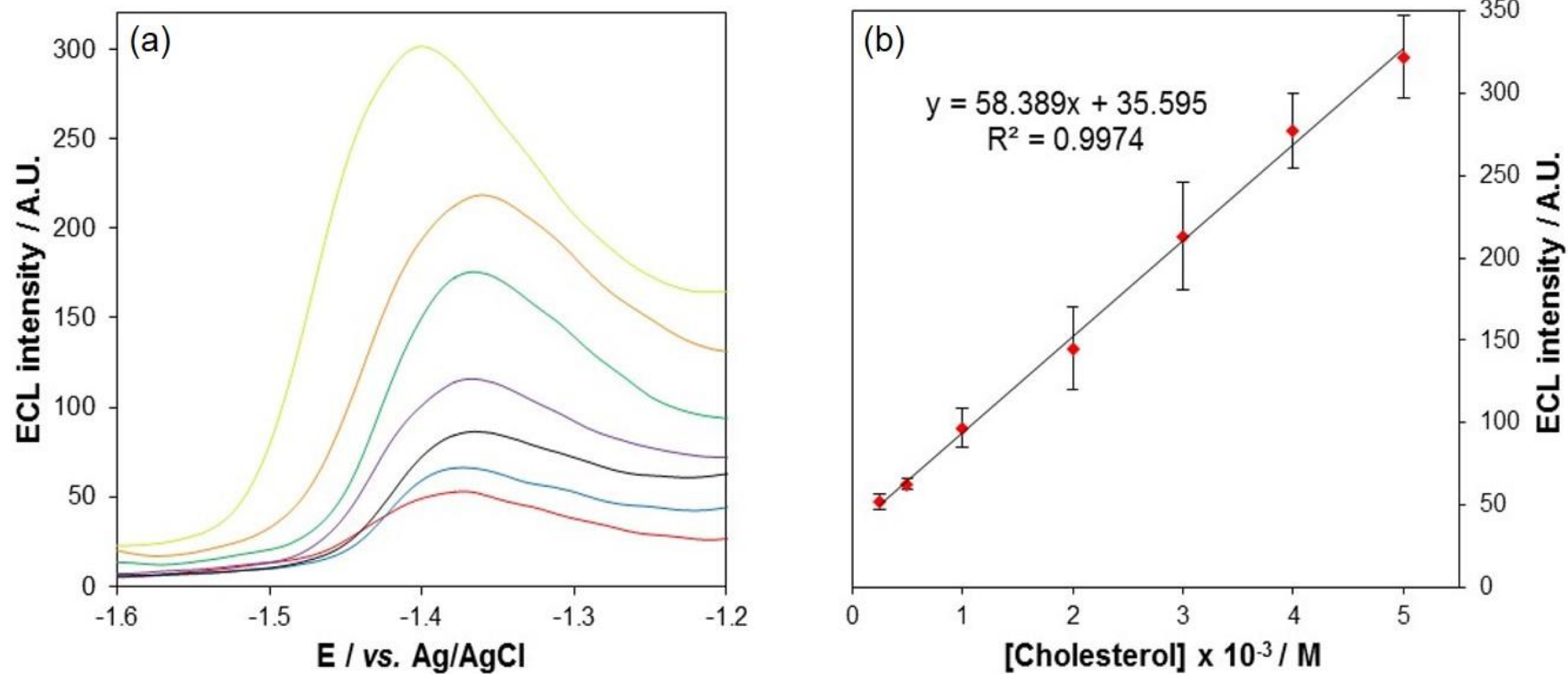


Figure 6.6 – (a) Typical ECL response of 800 nm QD/chitosan film in 0.25 (red), 0.5 (blue), 1 (black), 2 (purple), 3 (green), 4 (orange) and 5 (yellow) mM cholesterol at a scan rate of 100 mV s⁻¹ over the potential range -1.6 ≤ v ≤ -1.2 V vs. Ag/AgCl and (b) the linear dependence of NIR QD ECL on [cholesterol]. Error bars represent standard deviations from triplicate data set. PMT input voltage = 0.50 V.

This increase in ECL intensity is accompanied by an increase in peak current at a similar potential (~ -1.40 V) (Figure 6.7).

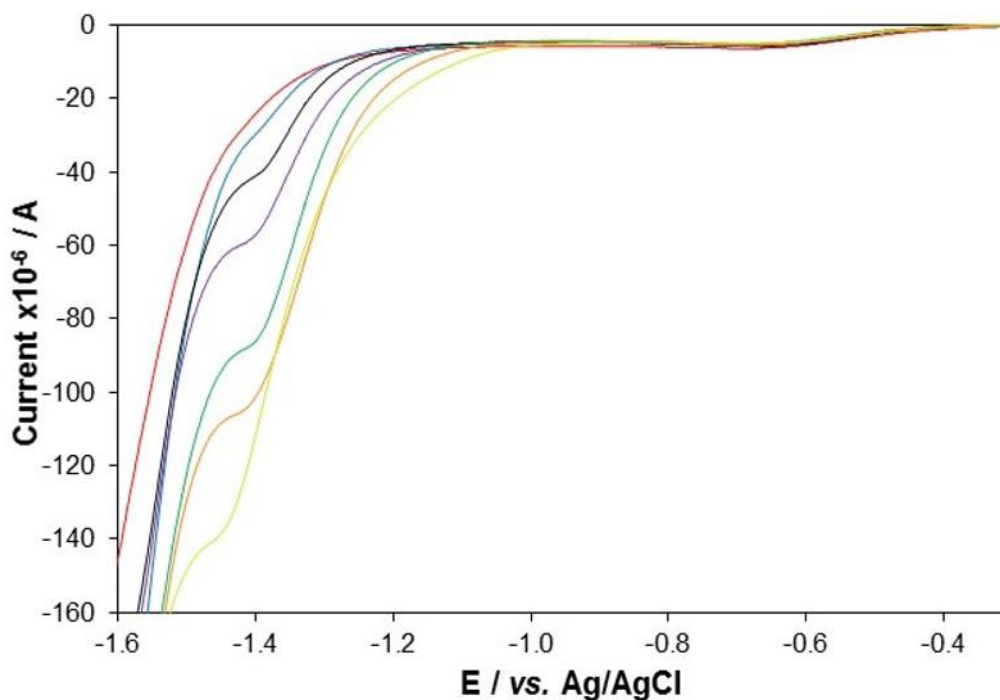


Figure 6.7 - Typical current response of 800 nm QD/chitosan film in 0.25 (red), 0.5 (blue), 1 (black), 2 (purple), 3 (green), 4 (orange) and 5 (yellow) mM cholesterol at a scan rate of 100 mV s^{-1} over the potential range $-1.6 \leq v \leq -0.3$ V vs. Ag/AgCl.

The voltammogram contains a reduction peak at -0.70 V and another at -1.40 V. The reduction peaks at approximately -0.70 and -1.40 V have previously been related to O_2 and H_2O_2 reduction processes respectively (section 2.3.2.2). This is in good agreement with the voltammograms shown here, with the first reduction process unaffected by changes in cholesterol concentration and peak current at -1.40 V decreasing with increasing cholesterol concentration. This signifies that H_2O_2 concentration is dependent upon cholesterol concentration in this system.

6.3.5 Consistency of response from multiple biosensors

Figure 6.3 highlights a number of factors that will influence production of H_2O_2 as a by-product of cholesterol oxidation. These include the number and

availability of active sites, binding of cholesterol, electron transfer to the co-factor and subsequent transfer to O₂, and finally dissociation of the ChOx-cholesten-3-one complex with associated release of H₂O₂. Additionally, this product must diffuse from solution to the ECL active area for precursor formation and generation of an ECL signal. These processes were shown to occur at a consistent rate between solutions (Table 6.1). The response of three separate biosensors was examined (Figure 6.8). This was to ensure consistency of these processes, which should allow maintenance of the linear dependency of ECL intensity on cholesterol concentration.

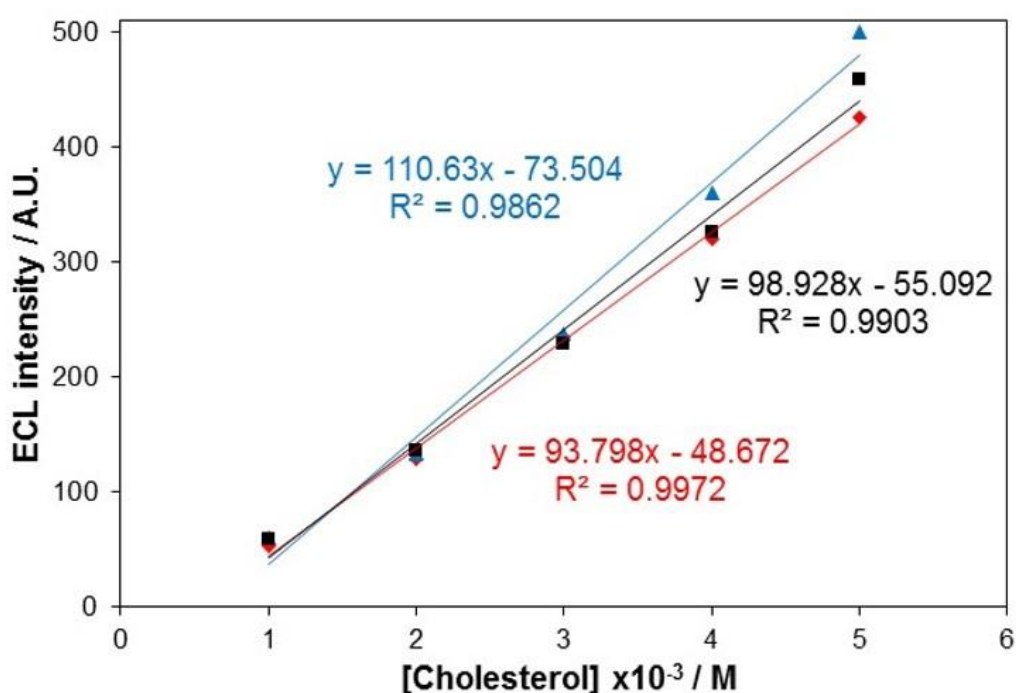


Figure 6.8 - ECL response from 3 separate 800 nm QD/chitosan film biosensors in increasing [cholesterol] at ~ -1.35 V vs. Ag/AgCl and a scan rate of 100 mV s^{-1} . PMT input voltage = 0.50 V.

A consistent linear dependence on cholesterol concentration was observed with each biosensor, demonstrating good stability of the ECL response. The % RSD at each point is outlined in Table 6.2.

Table 6.2 - ECL intensities from 3 separate 800 nm QD/chitosan film biosensors in increasing [cholesterol] and the % RSD between intensities at each concentration point. PMT input voltage = 0.50 V.

[Cholesterol] / mM	Max. ECL intensity @ ~ -1.35 V vs. Ag/AgCl			% RSD
	Biosensor 1	Biosensor 2	Biosensor 3	
1	53.3	60.7	58.6	6.63
2	128.6	133.2	136.3	2.92
3	234.7	237.8	229	1.91
4	320.8	359.6	326.5	6.24
5	426.2	500.6	458.1	8.09
Avg. % RSD				5.16

The data shows a % RSD value at each concentration point and a total average % RSD between the three biosensors within an acceptable range. This confirms that the enzymatic production of H_2O_2 and its subsequent action as co-reactant for generation of NIR QD ECL are consistent processes between multiple biosensors.

6.3.6 Biosensor stability

As the basis of this biosensor is ECL emission from NIR QDs, their response stability was established over a period of three weeks (Figure 6.9).

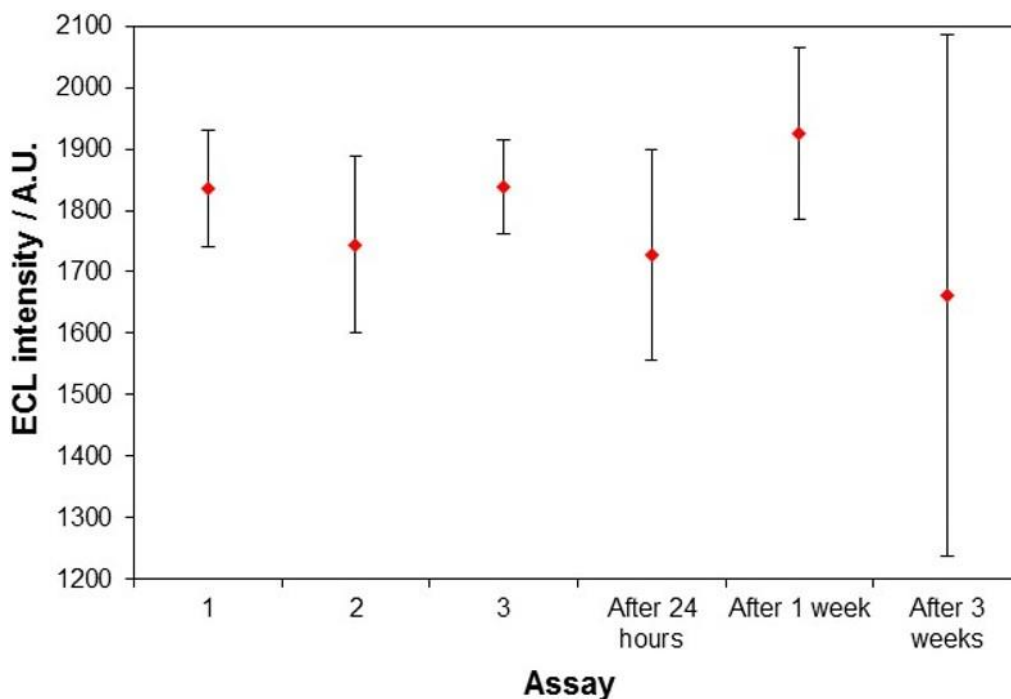


Figure 6.9 – Average ECL response of 800 nm QD/chitosan film on day 1 (assays 1,2+3), after 24 hours, after 1 week and after 3 weeks. Error bars represent standard deviations from 6 data points. PMT input voltage = 0.70 V.

The data shows good stability of ECL intensity over the three week period. Variations in response between these assays is shown in Table 6.3.

Table 6.3 – Average ECL intensities from six 800 nm QD/chitosan films assayed on different days and the % RSD between them. PMT input voltage = 0.70 V.

Assay day	Avg. ECL intensity	% RSD
x (1)	1834.7	2.93
x (2)	1744.5	
x (3)	1837.3	
x+1	1727.8	3.11
x+7	1925.5	4.55
x+21	1662.5	5.83

Within a single day, the inter-assay variability was 2.93 %. After one day, one week and 3 weeks, the % RSD between average ECL intensities was 3.11, 4.55 and 5.83 %, respectively. Consistency of response remains constant across the examined period, however, the variation at three weeks has an unacceptable % RSD of 25.49 % across six data points. This indicates that reproducibility of 800 nm QD ECL suffers after storage for three weeks. This is likely due to QD aggregation that will influence their concentration in the chitosan film. These results show that the shelf-life of these NIR QDs is less than three weeks when stored at 4°C.

6.3.7 Effect of interferences on response

The specificity of this biosensor was investigated through spiking of cholesterol sample solutions with common interferences found in biological samples. This will help determine the selectivity of the system as well as provide information on the compatibility of this biosensor for whole blood analysis, which will contain a range of impurities. Glucose, citric acid and urea were selected as the interfering species. Glucose was chosen as H₂O₂ is produced as a by-product of its oxidation³⁶ and any non-specific enzymatic catalysis of this process by ChOx should register as an increase in ECL intensity at the monitored potential. Its normal concentration in blood is between 3.5-6.1 mM.³⁷ Citric acid is known to interact with OH[•] to form organic radicals³⁸ and could therefore interrupt generation of the ECL signal. It is regularly used as an anticoagulant constituent for the collection of blood specimens, typically at concentrations of 0.02 mg/mL.³⁹ It is also found in the blood where it takes part in the citric acid cycle.⁴⁰ Urea exists at high concentrations in blood (normal concentration between 2.5-7.1 mM)⁴¹ and is documented as a weak OH[•] scavenger.⁴² The effect of these interferences on the ECL response of this biosensor is shown in Figure 6.10.

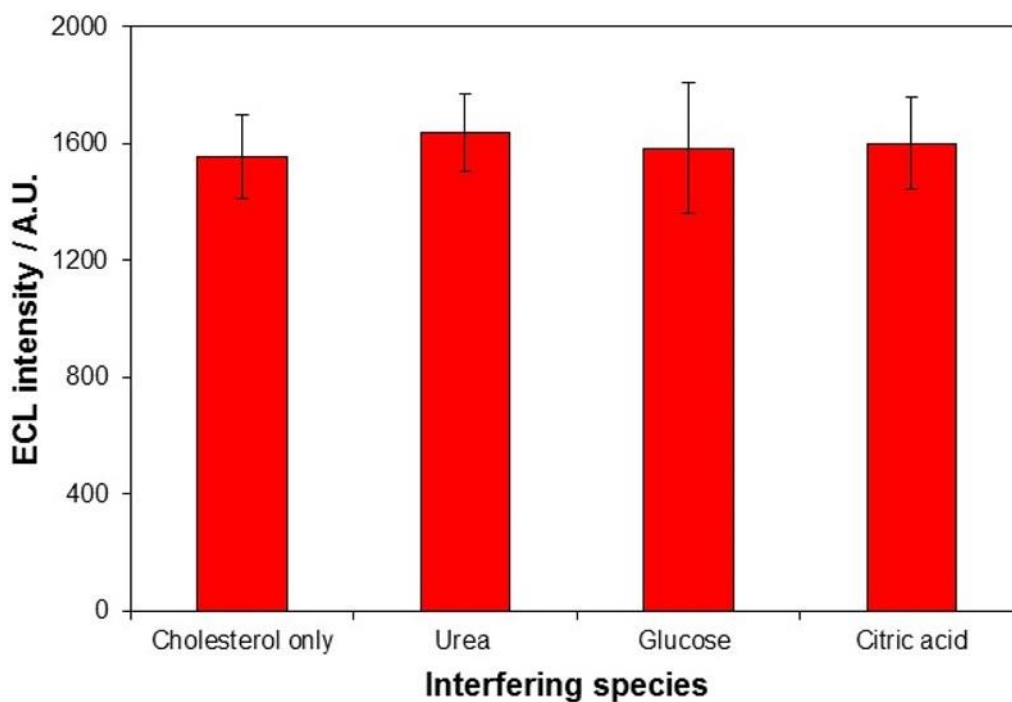


Figure 6.10 - Average ECL response of 800 nm QD/chitosan biosensor in 5 mM cholesterol with 10 mM urea, 10 mM glucose and 1 mg/mL citric acid at \sim -1.35 V vs. Ag/AgCl. Error bars represent standard deviations from triplicate data set. PMT input voltage = 0.70 V.

The intensity of the ECL response remains constant following addition of each interfering species. The % RSD between the average cholesterol only ECL intensity and with urea, glucose and citric acid are 3.62, 1.34 and 2.07 %, respectively. This shows good specificity of the biosensor, suggesting it is suitable for detection of cholesterol from biological fluids.

6.3.8 Detection from human serum samples

As the interference study showed good selectivity of the developed cholesterol biosensor, detection from a more complex matrix (human serum) was attempted. This was done as it should provide a good indication of the detection capability of the biosensor in a biological sample. The dependence of NIR QD ECL on cholesterol concentration in spiked human serum samples is shown in Figure 6.11.

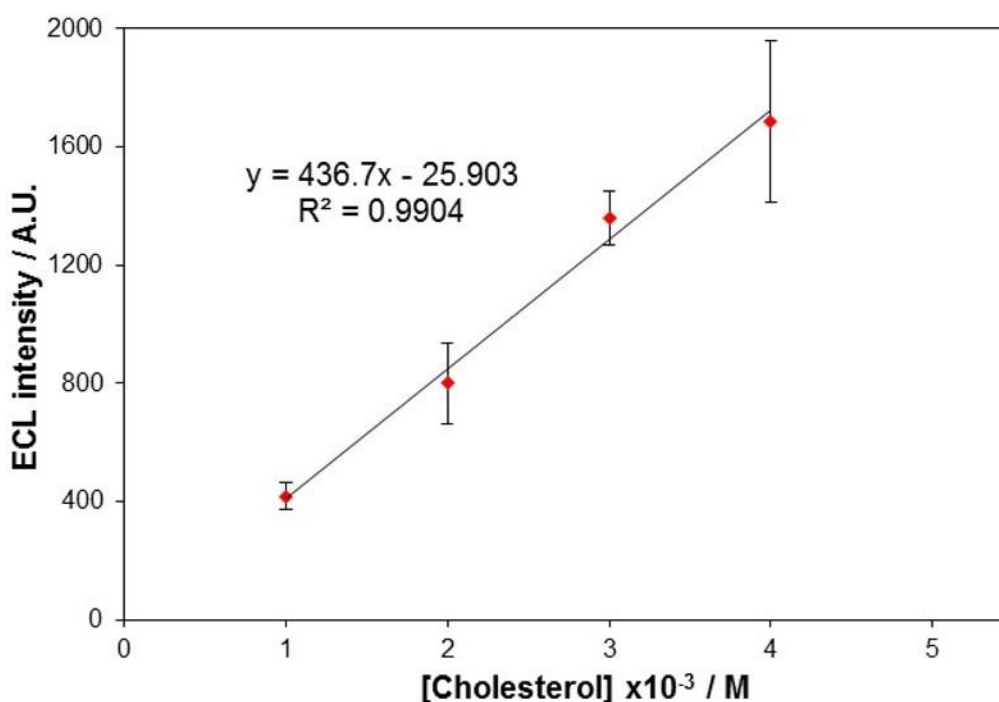


Figure 6.11 - Dependence of the ECL response with respect to [cholesterol] for the 800 nm QD/chitosan film in spiked human serum samples at ~ -1.35 V vs. Ag/AgCl. . Error bars represent standard deviations from triplicate data set. PMT input voltage = 0.70 V.

A linear ECL response between 1 and 4 mM cholesterol was obtained, which highlights the sensitivity of NIR QD ECL to a clinically relevant analyte within a biological matrix. The smaller linear range of the biosensor in human serum is likely caused by poorer solubility of cholesterol in this matrix compared to the optimised buffer conditions. It is possible that quenching of OH^{\bullet} by a species in solution is taking place, however, it is unclear why this process would occur to any greater extent at higher cholesterol concentrations. This data shows that detection of cholesterol from human serum can be accomplished using NIR QD ECL.

6.3.9 Summary

Overall, this data shows successful application of NIR QD ECL for the selective detection of cholesterol from buffer and biological matrix with a clinically relevant linear range. Response consistency was good both within a single biosensor and between multiple biosensors, providing confidence in the

reproducibility of this system. This work also confirms that enhancements in NIR QD ECL can be achieved with small concentrations of co-reactant that have been produced via biological processes, implying biocompatibility of the biosensor. This is the first cholesterol biosensor based on NIR ECL detection, with emission at this wavelength opening up opportunities for whole blood analysis.

6.4 Towards whole blood analysis

6.4.1 Viability of the system

The documented ability of NIR QDs to generate an intense, responsive ECL signal in whole blood (Chapter 5) and development of a selective, reliable cholesterol biosensor capable of detection from biological matrix (section 6.3) permitted investigations into its application with direct blood analysis. The ECL response in H_2O_2 spiked whole blood was first attempted (Figure 6.12).

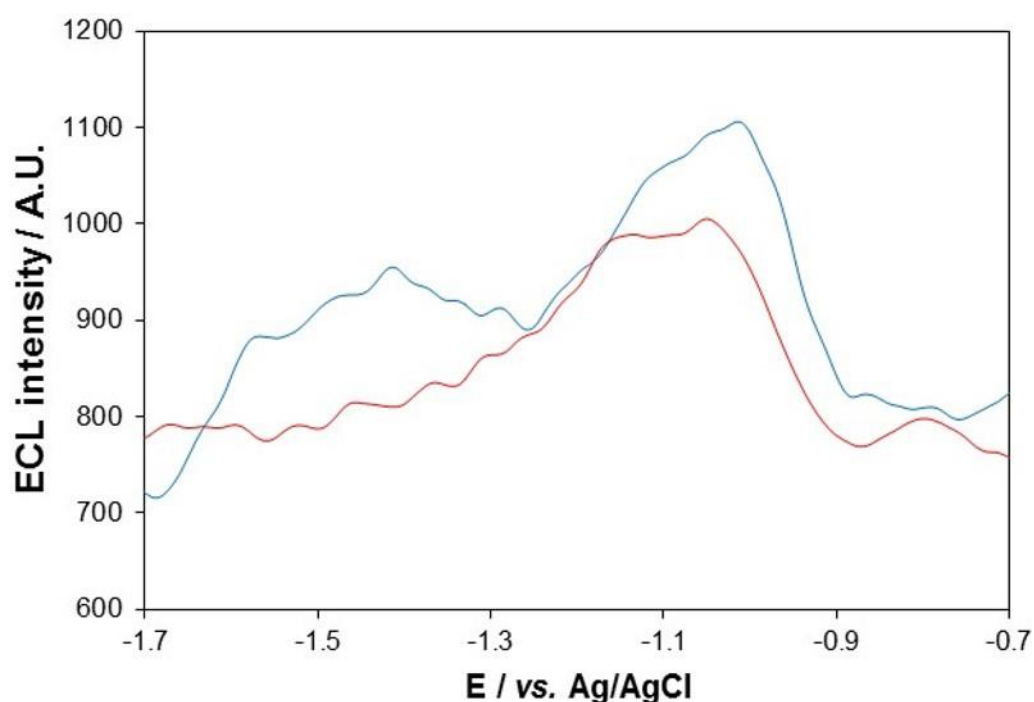


Figure 6.12 - ECL response of 800 nm QD/chitosan film in whole blood (red) and spiked with 1 mM H_2O_2 (blue) at a scan rate of 100 mV s^{-1} over the potential range $-1.7 \leq v \leq -0.7$ V vs. Ag/AgCl. PMT input voltage = 1.00 V.

The ECL profile in whole blood exhibits a single peak at -1.00 V, as seen previously (section 5.4.1.1). Following addition of H₂O₂ a small second peak is seen at approximately -1.40 V, consistent with the ECL signal known to be sensitive to H₂O₂ (section 3.4.2.1). This implies that NIR QD ECL is responsive to H₂O₂ in whole blood at this concentration. Therefore, the ECL response of the developed NIR QD biosensor in cholesterol spiked whole blood was examined (Figure 6.13).

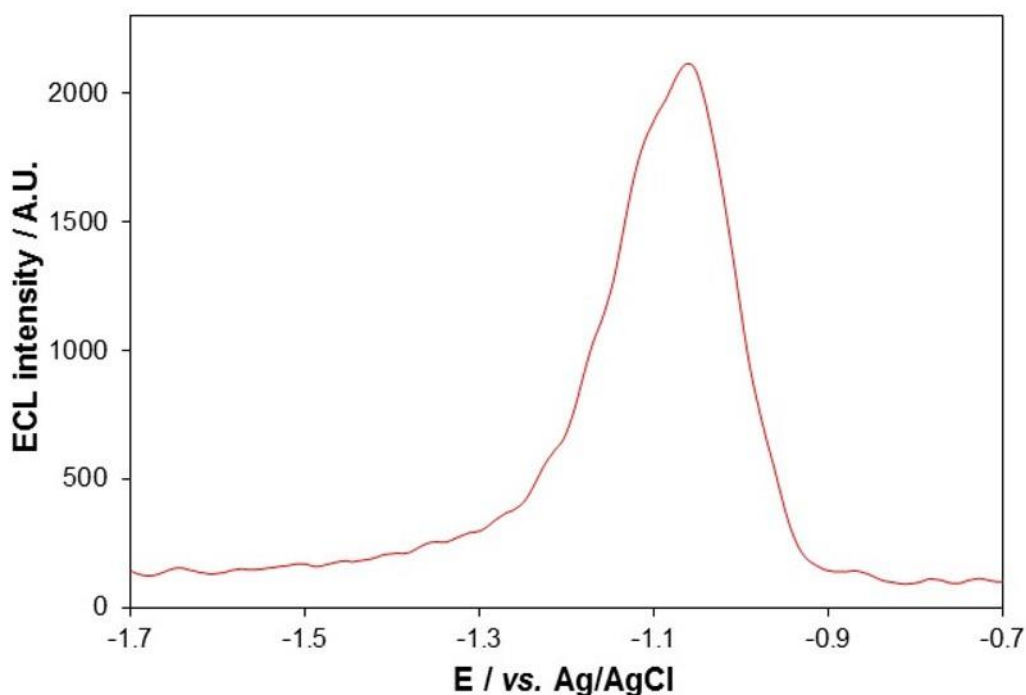


Figure 6.13 - ECL response of 800 nm QD/chitosan biosensor in whole blood spiked with 5 mM cholesterol at a scan rate of 100 mV s⁻¹ over the potential range -1.7 ≤ v ≤ -0.7 V vs. Ag/AgCl. PMT input voltage = 1.00 V.

The ECL profile exhibits a complete loss of the second, H₂O₂ sensitive peak previously observed at ~-1.40 V. The initial ECL peak is still present in the profile. Loss of peak 2 indicates that interaction between OH[•] and QDs(e⁻(1S_e)) is inhibited in whole blood. This is due to quenching of OH[•] by free radical scavengers present naturally in blood (e.g. glutathione,⁴³ melatonin,⁴⁴ vitamin C⁴⁵), which has been shown to occur in co-reactant free cathodic systems (section 5.4.1.1) when the concentrations of H₂O₂ are very low.

The H₂O₂ concentrations being produced in this biosensing system appear not to be sufficient to overcome quenching by whole blood species. Therefore, no dependence of ECL intensity on cholesterol concentration was observed. In order to minimise the effect of this quenching, immobilisation of the enzyme on the electrode surface was attempted. The aim of this was to concentrate the production of H₂O₂ in the immediate vicinity of the film so that its diffusion through whole blood to the ECL active area was minimised and its effective concentration in this region was maximised. This should increase the concentration of OH[•] available at the electrode surface for interaction with NIR QDs and permit generation of the H₂O₂ sensitive ECL peak.

6.4.2 Enzyme immobilisation

Enzyme immobilisation on chitosan films has been used regularly as a successful method in the development of electrochemical biosensors.⁴⁶⁻⁵⁰ The majority of these systems utilise the amine groups on the surface of chitosan for cross-linking via glutaraldehyde. Enzyme immobilisation via adsorption is also commonly implemented and has been reviewed very recently.⁵¹ Chitosan is well suited for immobilisation via adsorption due to its protonated amino groups creating anchor points for electrostatic interactions with the enzyme. Additionally, biocompatibility is maximised via enzyme immobilisation in this manner because no additional reactants are required. As such, this method was chosen for initial investigations into ChOx immobilisation.

6.4.2.1 Immobilisation via adsorption

An alteration in experimental design was required for enzyme immobilisation, as incubation of an enzyme-modified 800 nm QD/chitosan film in cholesterol solutions cannot be implemented due to water-solubility of the QDs. Consequently, the incubation step was removed from the procedure. These investigations were originally carried out in buffer to determine the viability of each method. The average ECL response of the enzyme modified NIR

QD/chitosan films in increasing cholesterol concentrations is shown in Figure 6.14.

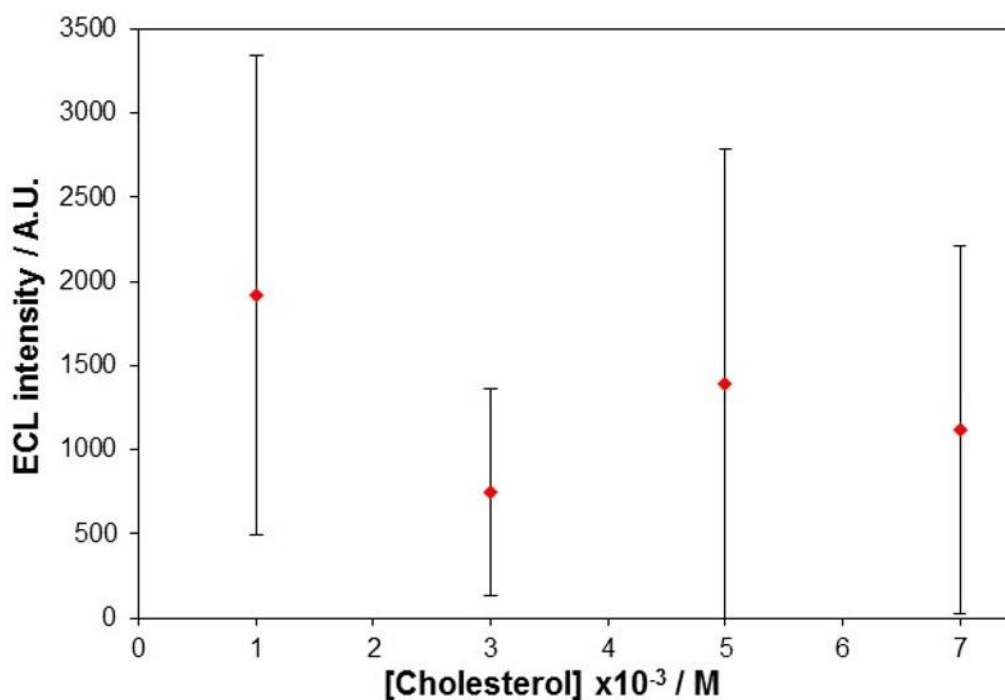


Figure 6.14 - Average ECL response at ~ -1.35 V vs Ag/AgCl of the 800 nm QD/chitosan/ChOx biosensor in increasing [cholesterol]. Error bars represent standard deviations from triplicate data set. PMT input voltage = 0.70 V.

The data shows no clear ECL dependence of the enzyme modified film on cholesterol concentration and a large variation in response at each data point (average % RSD at each concentration is 88.98 %). The detection of a signal indicates H₂O₂ is being produced when the modified electrodes were prepared in this manner. However, inconsistency of this response suggests that enzyme bioactivity is not stable between modified electrodes, which will cause changes in the efficiency of ChOx-catalysed cholesterol oxidation and subsequent variation in H₂O₂ concentration at the electrode surface.

Enzyme immobilisation on a solid support can have both positive and negative effects on its bioactivity.⁵² Often a decrease in activity is due to distortion of enzyme conformation through interactions with the solid support.⁵² Less often, these same processes can lead to enhancement of enzyme activity through

stabilisation of an enzyme in an activated form.⁵³ The activity is affected in this way as the 3D structure of an enzyme determines the availability of its binding site for a substrate. In solution, its mobility allows conformation in its most accessible form, whereas immobilisation can hinder this free movement and 'lock' an enzyme in a less favourable conformation.⁵⁴ The nature of interactions between enzyme and immobilisation matrix will determine what form this takes, as well as affecting enzyme flexibility and its solvation, which will influence bioactivity.⁵⁴ It appears the interactions forming between ChOx and chitosan, likely electrostatic interactions between protonated amine groups on chitosan and negative moieties on the surface of the enzyme, are not doing so consistently between films, causing variations in bioactivity and an irreproducible ECL response.

6.4.2.2 Immobilisation via glutaraldehyde cross-linking

It has been reported that immobilisation via multi-point covalent attachment can prevent damaging conformational changes and act as a scaffold for stabilisation of the enzyme in an activated form.^{52, 54} This highlights the benefits of a more-targeted approach to immobilisation than adsorption, where control over the process is minimal. For that reason, immobilisation via glutaraldehyde cross-linking was attempted. The reaction scheme for this process is outlined in Figure 6.15.

The first stage in glutaraldehyde cross-linking is nucleophilic attack of a terminal carbonyl on glutaraldehyde by a primary amine on chitosan. A Schiff base is then formed following elimination of water. This is a reversible process and as such a reducing agent (NaCNBH_3) is used to reduce the double bond of the Schiff base and prevent gradual dissociation of the imine. The same mechanism occurs at the opposing terminal carbonyl of glutaraldehyde for binding of the enzyme. Reaction with a number of functional groups on the surface of the enzyme is possible (amines, phenols, imidazole).⁵⁵ However, cross-linking via ϵ -amine groups on lysine residues is believed to

predominate.⁵⁵⁻⁵⁷ These groups are located on the protein surface due to polarity of the amine group.⁵⁸ They have a pK_a of >9.5 but it is assumed that the low percentage of non-protonated amines present at physiological pH are sufficient to react with glutaraldehyde.⁵⁸

These reactions are documented as occurring with minimum reversibility between pH 7 – 9, so were carried out under slightly basic conditions for both this reason and to minimise protonation of primary amine groups.⁵⁹ Low concentrations of glutaraldehyde have been shown to induce intramolecular cross-linking rather than the sought product.⁶⁰ Therefore, higher concentrations were used. The ECL profiles and intensity dependence of the QD/chitosan/ChOx film modified in this way on cholesterol concentration is shown in Figure 6.16.

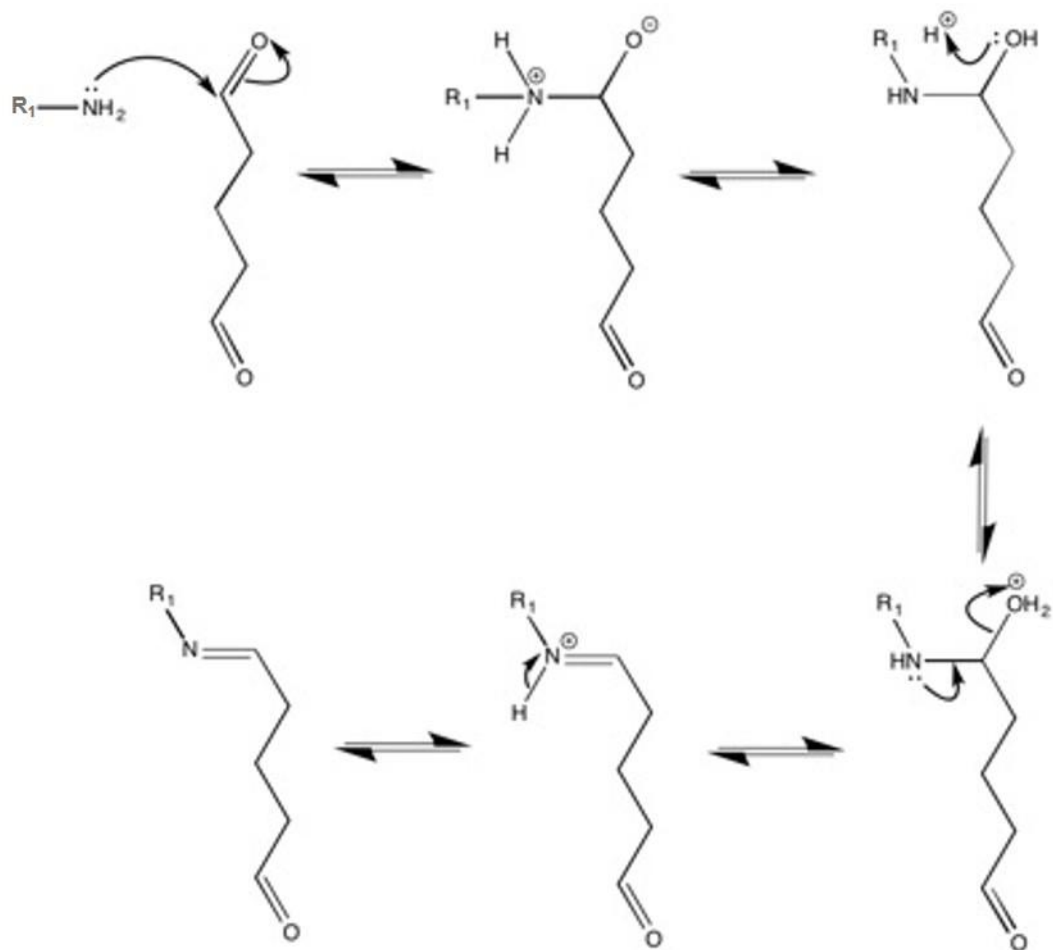


Figure 6.15 – Mechanism of glutaraldehyde activated amine-amine crosslinking.

An ECL response at -1.40 V is observed that exhibits sensitivity to cholesterol from 0 to 7 mM. Stability of response is significantly better using this method of immobilisation compared to adsorption, indicating superior consistency of enzyme bioactivity when immobilised in this manner. An increase in linear range up to 7 mM (compared to 5 mM with enzyme in solution) was accomplished, representing a change in enzymatic behaviour following immobilisation. This extended range is ideal for biosensor application as it permits detection in patients exhibiting hypercholesterolemia (total blood cholesterol concentrations above 5mM).² The linearity of ECL response is superior using the initial system (Figures 6.1 and 6.6 (b)). However, the exhibited ECL dependency of the enzyme immobilised electrode on cholesterol concentration provided assurances that enzyme activity was retained. Such a system was therefore deemed viable for detection of cholesterol through the production of H₂O₂ as a by-product of its oxidation.

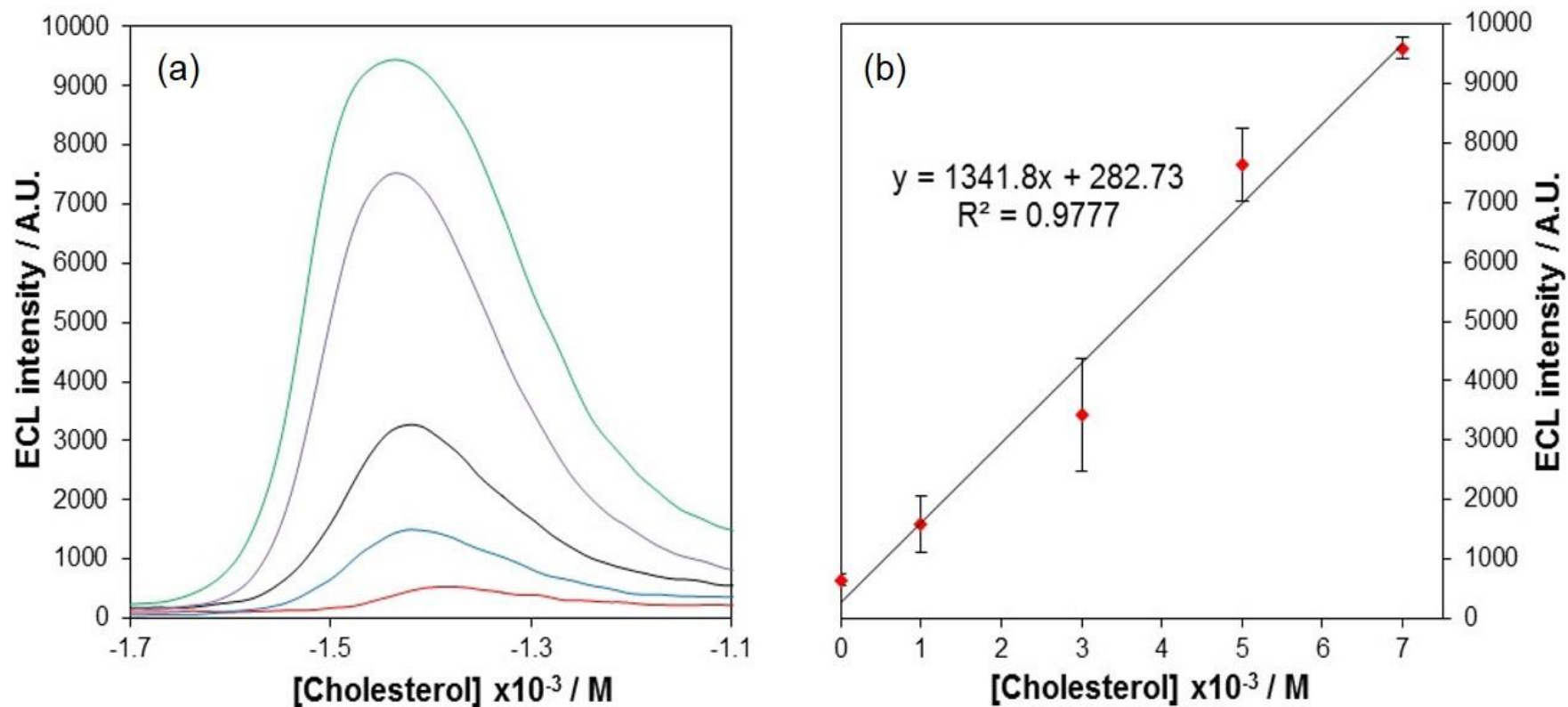


Figure 6.16 - (a) Typical ECL response of 800 nm QD/chitosan/ChOx biosensor in 0 (red), 1 (blue), 3 (black), 5 (purple) and 7 (green) mM cholesterol at a scan rate of 100 mV s^{-1} over the potential range $-1.7 \leq v \leq -1.1 \text{ V}$ vs. Ag/AgCl and (b) the linear dependence of NIR QD ECL on [cholesterol]. Error bars represent standard deviations from triplicate data set. PMT input voltage = 0.85 V.

6.4.2.3 Enzyme immobilised biosensor – whole blood analysis

As the NIR QD biosensor with enzyme immobilisation via glutaraldehyde cross-linking was sensitive to alterations in cholesterol concentration in buffer, its application in whole blood was attempted. The ECL profile of this biosensor in 5 mM cholesterol is shown in Figure 6.17.

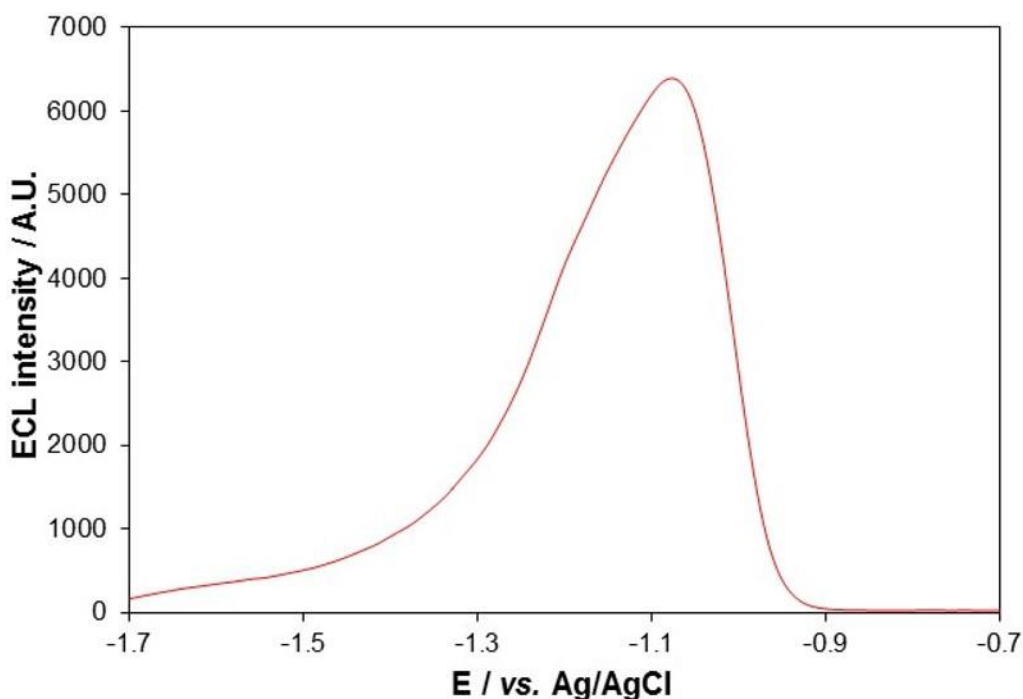


Figure 6.17 - ECL response of 800 nm QD/chitosan/ChOx biosensor in whole blood spiked with 5 mM cholesterol at a scan rate of 100 mV s^{-1} over the potential range $-1.7 \leq v \leq -0.7 \text{ V vs. Ag/AgCl}$. PMT input voltage = 1.00 V.

This profile is very similar to that observed with the previous biosensor in whole blood (Figure 6.13), exhibiting a single peak at approximately -1.10 V and the disappearance of the H_2O_2 sensitive peak at -1.40 V. This means that quenching of OH^\bullet by whole blood species is still occurring to such an extent that no ECL response can be generated. Either the concentration of H_2O_2 produced at the electrode surface is not sufficiently greater with the enzyme immobilised system, or OH^\bullet scavenging in the blood sample is more severe than expected. For that reason, the peak potential at -1.40 V for the QD/chitosan/ChOx electrode in increasing cholesterol concentrations (in

buffer, Figure 6.18) was investigated and compared to those attained with ChOx in solution (Figure 6.7).

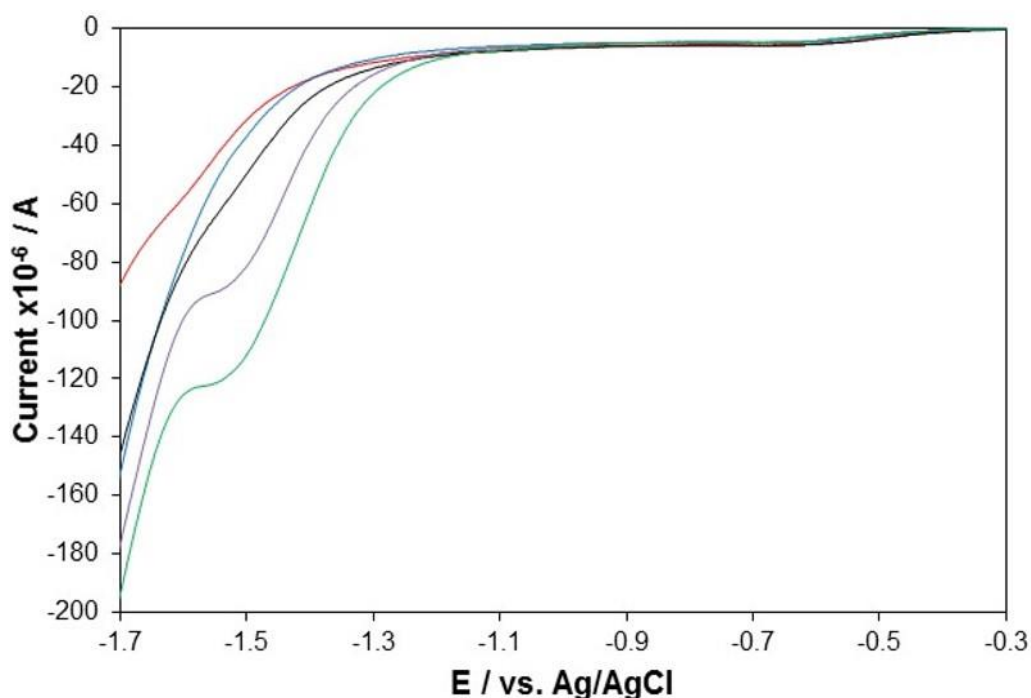


Figure 6.18 - Typical current response of 800 nm QD/chitosan/ChOx biosensor in 0 (red), 1 (blue), 3 (black), 5 (purple) and 7 (green) mM cholesterol at a scan rate of 100 mV s⁻¹ over the potential range $-1.7 \leq v \leq -0.3$ V vs. Ag/AgCl.

A very similar voltammogram is observed (compared to Figure 6.7) with a small, unresponsive peak at -0.70 V and a larger, cholesterol sensitive peak at -1.50 V. The peak potentials at comparable cholesterol concentrations are smaller with this system compared to the initial system, indicating production of higher concentrations of H₂O₂ at the electrode surface has not been achieved through immobilisation of ChOx. The reason for this appears to be a combination of two factors: the required removal of an incubation step at the enzymes optimal temperature (45°C), which will limit both the activity of ChOx and the number of cholesterol molecules that can be oxidised, and the presence of an additional insulating layer of enzyme on the surface of the electrode, inhibiting diffusion of H₂O₂ to the electroactive region of the electrode. The result is no increase in effective H₂O₂ concentration at the

electrode surface and no observable ECL response (at -1.40 V) in whole blood due to radical quenching.

6.4.3 Future developments

This data has highlighted one of the main problems associated with whole blood analysis, namely the presence of interfering species in such a complex matrix that can influence the observed response. As a technique that often requires the interaction of radical species, ECL generation in this system has been shown to be susceptible to quenching by free-radical scavengers in whole blood. The most attainable solution to this problem is improvement in the sensitivity of NIR QD ECL to H₂O₂. Antioxidant efficiency for OH[•] consumption is not 100 %, ⁶¹ as it has been shown that radicals exist in the blood at pM concentrations. ^{62, 63} H₂O₂ produced in this biosensing system should increase the OH[•] concentration, however, it must still be at concentrations below the limit of detection (LOD) for these NIR QDs as no ECL response is observed. Improving this LOD through enhancements in ECL performance, which has been reviewed in section 1.1.4.2, should permit its detection at significantly lower concentrations that will hopefully allow generation of a responsive signal in whole blood.

6.5 Conclusions

An operational biosensor for the detection of cholesterol was developed using NIR QD ECL. This biosensor demonstrated a clinically relevant linear range and a selective, stable response that was capable of cholesterol quantification in human serum samples with an analysis time of less than 40 s. This is the first such enzymatic biosensor that utilises NIR QD ECL as the detection technique.

Previous work has shown the sensitivity of these ECL emitters to H₂O₂ concentration (section 3.4.2.1) and this was exploited for the basis of the biosensor. ChOx-catalysed oxidation of cholesterol in the presence of O₂

creates H_2O_2 at a concentration dependent upon cholesterol levels in the sample. As such, monitoring of H_2O_2 through NIR QD ECL intensity was used to infer cholesterol concentration in solution. The inherent specificity of enzymatic reactions created a selective biosensing system that was not affected by the presence of other small molecules (glucose, urea, citric acid).

The successful development of this biosensor and the demonstrated ability of NIR QDs to generate a strong ECL signal in whole blood (chapter 5) meant direct blood analysis was attempted. Quenching of OH^\bullet by species in whole blood prevented the appearance of an ECL peak that was linearly dependent on H_2O_2 concentration. Biosensor development through enzyme immobilisation did not overcome this problem. For this reason, application of the developed biosensors with direct blood analysis was not successful in its current form. It is envisaged that enhancements in NIR QD ECL sensitivity has the potential to permit detection in whole blood.

This work has highlighted the applicability of ECL with direct whole blood analysis requires superior system sensitivity when compared to analysis in buffer or human serum. It also suggests that detection limits in these sample matrices are not representative of those that can be attained in whole blood using the same system. This is significant as the vast majority of publications in the biosensing field are based on detection from buffer and human serum/plasma samples. Clearly this is only problematic for biosensors that are aimed towards whole blood analysis, however, this is the first time that complications associated with ECL biosensing from whole blood samples has been demonstrated. This information should aid in future development of whole blood ECL detection systems, which may require system modifications to improve sensitivity and stability.

6.6 References

1. J. S. Stern and A. Kazaks, *Obesity: A Reference Handbook*, ABC-CLIO, 2009.
2. P. Durrington, *The Lancet*, 2003, **362**, 717-731.
3. J. P. Koval, *Cholesterol in Atherosclerosis and Coronary Heart Disease*, Nova Science Pub Incorporated, 2005.
4. W. P. Castelli and K. Anderson, *The American Journal of Medicine*, 1986, **80**, 23-32.
5. M. Ezzati, A. D. Lopez, A. Rodgers, S. Vander Hoorn and C. J. L. Murray, *The Lancet*, 2002, **360**, 1347-1360.
6. R. Collins, J. Armitage, S. Parish, P. Sleight and R. Peto, *Lancet*, 2004, **363**, 757-767.
7. K. E. Aspry, J. W. Holcroft and E. A. Amsterdam, *American journal of preventive medicine*, 1995, **11**, 336-341.
8. *High Cholesterol - Diagnosis*,
<http://www.nhs.uk/Conditions/Cholesterol/Pages/Diagnosis.aspx>,
Accessed 10/19, 2013.
9. D. J. Gordon, J. L. Probstfield, R. J. Garrison, J. D. Neaton, W. P. Castelli, J. D. Knoke, D. R. Jacobs, S. Bangdiwala and H. A. Tyroler, *Circulation*, 1989, **79**, 8-15.
10. W. P. Castelli, R. J. Garrison, P. F. Wilson, R. D. Abbott, S. Kalousdian and W. B. Kannel, *Journal of the American Medical Association*, 1986, **256**, 2835-2838.
11. R. O. Bonow, *Circulation*, 2002, **106**, 3140-3141.
12. P. Mathieu, P. Pibarot, É. Larose, P. Poirier, A. Marette and J.-P. Després, *The international journal of biochemistry & cell biology*, 2008, **40**, 821-836.
13. R. Stocker and J. F. Keaney, *Physiological reviews*, 2004, **84**, 1381-1478.
14. M. Navab, S. T. Reddy, B. J. Van Lenten and A. M. Fogelman, *Nature Reviews Cardiology*, 2011, **8**, 222-232.
15. Y. Cui, R. S. Blumenthal, J. A. Flaws, M. K. Whiteman, P. Langenberg, P. S. Bachorik and T. L. Bush, *Archives of Internal Medicine*, 2001, **161**, 1413-1419.
16. A. Kenny, *Biochemical Journal*, 1952, **52**, 611.
17. W. W. Wong, D. L. Hachey, L. L. Clarke, S. Zhang, M. Llaurador and W. G. Pond, *Applied radiation and isotopes*, 1994, **45**, 529-533.
18. E. Agulló and B. S. Gelós, *Food research international*, 1996, **29**, 77-80.
19. X. Tan, M. Li, P. Cai, L. Luo and X. Zou, *Analytical biochemistry*, 2005, **337**, 111-120.
20. J.-C. Vidal, J. Espuelas, E. Garcia-Ruiz and J.-R. Castillo, *Talanta*, 2004, **64**, 655-664.
21. A. Crumbliss, J. Stonehuerner, R. Henkens, J. Zhao and J. O'Daly, *Biosensors and Bioelectronics*, 1993, **8**, 331-337.
22. M. Guo, J. Chen, J. Li, L. Nie and S. Yao, *Electroanal*, 2004, **16**, 1992-1998.
23. S. Brahim, D. Narinesingh and A. Guiseppe-Elie, *Analytica chimica acta*, 2001, **448**, 27-36.

24. C. A. Marquette, S. Ravaud and L. J. Blum, *Analytical Letters*, 2008, **33**, 1779-1796.
25. J. Ballesta-Claver, J. Ametis-Cabello, J. Morales-Sanfrutos, A. Megía-Fernández, M. Valencia-Mirón, F. Santoyo-González and L. Capitán-Vallvey, *Analytica chimica acta*, 2012, **754**, 91-98.
26. C. Woelfle and R. O. Claus, *Nanotechnology*, 2007, **18**, 025402.
27. G. Gadda, G. Wels, L. Pollegioni, S. Zucchelli, D. Ambrosius, M. S. Pilone and S. Ghisla, *European journal of biochemistry*, 1997, **250**, 369-376.
28. Q. K. Yue, I. J. Kass, N. S. Sampson and A. Vrieling, *Biochemistry*, 1999, **38**, 4277-4286.
29. J. Li, A. Vrieling, P. Brick and D. M. Blow, *Biochemistry*, 1993, **32**, 11507-11515.
30. L. Pollegioni, G. Wels, M. S. Pilone and S. Ghisla, *European Journal of Biochemistry*, 1999, **264**, 140-151.
31. M. Campbell and S. Farrell, *Biochemistry*, Cengage Learning, 2014.
32. F. Bettelheim, W. Brown, M. Campbell and S. Farrell, *Introduction to General, Organic and Biochemistry*, Cengage Learning, 2009.
33. Sigma-Aldrich, *C8649 - Cholesterol Oxidase from Streptomyces sp.*, <http://www.sigmaaldrich.com/catalog/product/sigma/c8649?lang=en®ion=GB>, Accessed 13/08/2014, 2014.
34. E. E. A. Enger, *Concepts in Biology*, Rex Bookstore, Inc., 2007.
35. S. Seager and M. Slabaugh, *Organic and Biochemistry for Today*, Cengage Learning, 2013.
36. A. S. G. Huggett and D. A. Nixon, *The Lancet*, 1957, **270**, 368-370.
37. F. He, F. Feng, S. Wang, Y. Li and D. Zhu, *Journal of Materials Chemistry*, 2007, **17**, 3702-3707.
38. C. Corvaja, P. L. Nordio and G. Giacometti, *Transactions of the Faraday Society*, 1966, **62**, 3400-3402.
39. J. Jespersen, R. M. Bertina and F. Haverkate, *Laboratory Techniques in Thrombosis - A Manual*, Springer, 2000.
40. A. K. Olson, B. Bouchard, X.-H. Ning, N. Isern, C. Des Rosiers and M. A. Portman, *American Journal of Physiology-Heart and Circulatory Physiology*, 2012, **302**, H1086-H1093.
41. D. D. Wilson, *McGraw-Hill Manual of Laboratory and Diagnostic Tests*, McGraw-hill, 2007.
42. G. Cohen, *Photochemistry and photobiology*, 1978, **28**, 669-674.
43. T. Hennet, E. Peterhans and R. Stocker, *The Journal of general virology*, 1992, **73**, 39-46.
44. D. X. Tan, L. C. Manchester, R. Hardeland, S. Lopez-Burillo, J. C. Mayo, R. M. Sainz and R. J. Reiter, *Journal of pineal research*, 2003, **34**, 75-78.
45. S. J. Padayatty, A. Katz, Y. Wang, P. Eck, O. Kwon, J.-H. Lee, S. Chen, C. Corpe, A. Dutta and S. K. Dutta, *Journal of the American College of Nutrition*, 2003, **22**, 18-35.
46. M. E. Ghica, R. Pauliukaite, O. Fatibello-Filho and C. Brett, *Sensors and Actuators B: Chemical*, 2009, **142**, 308-315.
47. X.-L. Luo, J.-J. Xu, Y. Du and H.-Y. Chen, *Analytical Biochemistry*, 2004, **334**, 284-289.

48. Y. Yang, H. Yang, M. Yang, G. Shen and R. Yu, *Analytica Chimica Acta*, 2004, **525**, 213-220.
49. B. Wang, X. Ji, H. Zhao, N. Wang, X. Li, R. Ni and Y. Liu, *Biosensors and Bioelectronics*, 2014, **55**, 113-119.
50. R. Devi and C. S. Pundir, *Sensors and Actuators B: Chemical*, 2014, **193**, 608-615.
51. T. Jesionowski, J. Zdarta and B. Krajewska, *Adsorption*, 2014, **20**, 801-821.
52. R. C. Rodrigues, C. Ortiz, Á. Berenguer-Murcia, R. Torres and R. Fernández-Lafuente, *Chemical Society Reviews*, 2013, **42**, 6290-6307.
53. C. Mateo, J. M. Palomo, G. Fernandez-Lorente, J. M. Guisan and R. Fernandez-Lafuente, *Enzyme and Microbial Technology*, 2007, **40**, 1451-1463.
54. F. Secundo, *Chemical Society Reviews*, 2013, **42**, 6250-6261.
55. A. Habeeb and R. Hiramoto, *Archives of biochemistry and biophysics*, 1968, **126**, 16-26.
56. H. H. Weetall, *Analytical chemistry*, 1974, **46**, 602A-615a.
57. A. H. Korn, S. H. Fearheller and E. M. Filachoine, *Journal of Molecular Biology*, 1972, **65**, 525-529.
58. I. Migneault, C. Dartiguenave, M. J. Bertrand and K. C. Waldron, *Biotechniques*, 2004, **37**, 790-806.
59. K. Okuda, I. Urabe, Y. Yamada and H. Okada, *Journal of fermentation and bioengineering*, 1991, **71**, 100-105.
60. O. R. Zaborsky and C. Chemical Rubber, *Immobilized enzymes*, CRC press Cleveland, 1973.
61. P. Stocker, J.-F. Lesgards, N. Vidal, F. Chalier and M. Prost, *Biochimica et Biophysica Acta-General Subjects*, 2003, **1621**, 1-8.
62. W. Dröge, *Physiological reviews*, 2002, **82**, 47-95.
63. Y. J. H. J. Taverne, A. J. J. C. Bogers, D. J. Duncker and D. Merkus, *Oxidative medicine and cellular longevity*, 2013, **2013**, 1-15.

*Chapter 7 – Designing an immunoassay for whole blood
analysis*

7.1 Introduction

Immunoassays are highly selective and sensitive methods for the detection of target analytes based on the high binding affinity of a specific antibody (Ab) for its target analyte (antigen). The resulting interaction of these two components causes a small biological, chemical or physical alteration in the system that can be monitored by a transducer and may be used to quantify the concentration of analyte in a sample. Optical^{1, 2} or electrochemical^{3, 4} monitoring of these changes are usually employed, although some mass⁵ and temperature sensitive devices⁶ are used. These can directly detect Ab-antigen binding or monitor a reaction following the binding event. Incorporation of an Ab into a system confers unparalleled specificity, stability and flexibility,⁷ as they exist for a wide range of clinically relevant analytes. Development have been extensive since construction of the first radioisotope based immunoassays in the 1960's,^{8, 9} as advances in the field have yielded improvements in sensitivity, specificity, stability and biocompatibility.¹⁰

The inherent sensitivity of ECL lends itself perfectly to monitoring of Ab-antigen binding following integration of an ECL active component into the system. This is usually achieved through conjugation of an ECL active species with an Ab, which is then used in a sandwich type immunoassay as a labelled secondary Ab. A variety of bio-conjugation techniques are used to accomplish this, including EDC/NHS click chemistry,¹¹ amine cross-linking¹² and avidin-biotin binding.¹³ A number of immunoassays that use ECL as their detection method have been developed for a wide variety of analytes, which are outlined in chapter 1. From this review, only a handful of these biosensors incorporate near infra-red (NIR) emitters into their design, none of which have achieved detection in whole blood. The future of immunoassay design now lies in accessing more analytes through ultrasensitive (fM-aM) detection, development of multi-analyte systems and design of immunosensors capable of real time or point of care (POC) diagnostics.¹⁰ The superb sensitivity associated with ECL has already been demonstrated, with detection limits in

the atto and femto-molar range accomplished,¹⁴⁻¹⁶ whilst the biocompatibility of QDs combined with their size tunable emission wavelength ensures they are ideal materials for multi-analyte detection. This work has already shown the ability of water-soluble NIR QDs to generate a detectable ECL signal in whole blood (chapter 5), which is far more sensitive than that achieved using visible region QDs. Therefore, these NIR QDs lend themselves to POC diagnostics, which requires direct whole blood analysis and minimal sample pre-treatment. As such, NIR ECL could play a significant role in the future development of immunoassays.¹⁷

The aim of this work was to utilise the inherent sensitivity of the ECL technique with the increased penetrative capability of NIR QD emitters to develop a sensitive immunoassay capable of analysis from whole blood samples. Work in Chapter 6 highlighted the influence species in whole blood can have on the observed ECL intensity and the requirement for improvements in NIR QD ECL sensitivity in these conditions. Therefore, the use of an alternative biosensor design (immunoassay rather than enzymatic biosensor) with a more sensitive co-reactant ($K_2S_2O_8$, as determined in section 4.3.2.1) was proposed as a more suitable method for ECL detection with analysis in whole blood.

7.2 Experimental

7.2.1 Apparatus

Electrochemical measurements were carried out using a CH instrument model 760D electrochemical analyser. All experiments were carried out using a conventional three-electrode assembly, consisting of a 3 mm diameter GC working electrode, Pt wire counter electrode and Ag/AgCl reference electrode. GC electrodes were cleaned by successive polishing using 1, 0.3 and 0.05 μM alumina slurry, followed by sonication in ethanol and water, respectively, for 30 mins. The electrodes were then dried under a flow of N_2 gas. CV was carried out at a scan rate of 100 mV s^{-1} and sample interval of 1 mV across a potential range outlined in each figure. For DPV, the increment potential was 4 mV, amplitude 50 mV, pulse width 50 ms, sample width 16.7 ms and pulse period 0.5 s across a potential range outlined in each figure. Electrochemical impedance spectroscopy was carried out on a CH instrument model 760D electrochemical analyser using the same three-electrode assembly as above. The measurements were performed in a 10 mM solution of $\text{K}_4\text{Fe}(\text{CN})_6^{3-/4-}$ in 0.1 M PBS at pH 7.4. The bias potential was set at 0.26 V and the frequency range was between 0.01 and 100000 Hz with signal amplitude of 5 mV. Measurements involving simultaneous detection of light and current utilised a CH instrument model 760D connected to a Hamamatsu H10723-20 PMT. The input voltage to the PMT was + 5 V and the control voltage was set between 0.5 and 1.05 V depending on the required sensitivity. During electrochemical experiments, the cell was kept in a light-tight Faraday cage in a specially designed holder configuration where the working electrode was positioned directly above the PMT window. All measurements were made at room temperature.

7.2.2 Materials

Core-shell CdSeTe/ZnS QDs (Qdot® 800 ITK™ organic quantum dots, 1 μM in decane, Qdot® 800 ITK™ carboxyl quantum dots, 8 μM in buffer, Qdot®

800 Streptavidin conjugate quantum dots, 1 μM in buffer) were purchased from Invitrogen. Anti-human IgG (H+L) antibody produced in goat-biotin conjugate (1.5 mg/mL in buffer) was purchased from Novex. Chitosan (medium molecular weight, 75-85% de-acetylated), phosphate buffered saline (PBS, pH 7.4), potassium persulfate ($\text{K}_2\text{S}_2\text{O}_8$), 2-(dimethylamino)ethanethiol (DAET), glutaraldehyde, sodium cyanoborohydride (NaCNBH_3), sodium bicarbonate, Anti-human IgG (Fab specific) antibody produced in goat (2.3 mg/mL in buffer), IgG from human serum (4.8 mg/mL in buffer), $\text{K}_4\text{Fe}(\text{CN})_6^{3-}$, H_2O_2 , Tween 20, *N*-(3-Dimethylaminopropyl)-*N'*-ethylcarbodiimide hydrochloride (EDC), *N*-Hydroxysuccinimide (NHS), MES hydrate and Centriscart-I centrifugal ultrafiltration units 100 kDa MWCO were all purchased from Sigma-Aldrich and used as received. All other reagents used were of analytical grade, and all solutions were prepared in milli-Q water (18 m Ω cm).

Bovine whole blood was obtained from Wishaw Abattoir Ltd (185 Caledonian Road, Wishaw, Lanarkshire, ML2 0HT) and stored in aliquots at -20 °C. Aliquots were defrosted at room temperature on the day of analysis and used immediately.

7.2.3 Methods

Preparation of water soluble CdSeTe/ZnS core-shell QDs

The method followed was similar to that developed by Woelfle and Claus¹⁸. 0.5 mL of 0.5 M DAET in methanol was mixed with 0.25 mL of the CdSeTe/ZnS QDs in decane (1 μM). N_2 was bubbled through the solution for 5 mins, which was then sealed and left stirring overnight in the dark at room temperature. The QDs were then precipitated with an excess of acetone followed by centrifugation at 5000 rpm for 6 mins. The filtrate was removed and the precipitate was re-dispersed in 0.25 mL of distilled water. These water-soluble QDs were centrifuged for a further 6 mins at 3000 rpm to remove any impurities and then stored in darkness at 4°C.

Preparation of CdSeTe/ZnS core-shell QD-chitosan composite film

A 0.1 % chitosan solution was prepared in 1 % acetic acid and sonicated for 5 mins. The QD/chitosan composite was prepared by mixing aliquots of the water-soluble QDs with the chitosan solution in a 1:1 (v/v) ratio and mixing for 30 s. 3 μ L of this composite was then carefully cast onto the electroactive portion of a GC electrode, with mixing of the composite for 10 s between electrodes. The film was allowed to dry for 1 h at 4°C.

QD concentration in the film was altered by mixing the water-soluble QDs with a suitable volume of water prior to mixing in a 1:1 (v/v) ratio with chitosan.

Ab immobilisation via physisorption

The 2.4 mg/mL stock solution of Ab was diluted to the required concentration in bicarbonate buffer (pH 8.4). Clean GC electrodes were then immersed in this Ab solution and left to incubate for 1 h at 4°C. The electrodes were then thoroughly washed in 0.01% Tween 20 (in 0.1 M PBS) and rinsed with distilled water.

Ab immobilisation via glutaraldehyde cross-linking

3 μ L of 0.05% chitosan was drop-cast onto a GC electrode and left to dry for 1 h at 4°C. This electrode was then incubated with 25 μ L of 10% glutaraldehyde in 0.1 M bicarbonate buffer (pH 8.4) for 1 h at room temperature. The electrode was then rinsed with distilled water, followed by incubation with Ab (at required concentration) in 50 mM NaCNBH₃ (in 0.1 M bicarbonate buffer) for 3 h at room temperature. The electrode was then thoroughly washed in 0.01% Tween 20 (in 0.1 M PBS) and rinsed with distilled water.

Antigen binding

The as-prepared Ab functionalised GC electrodes (by either physisorption or glutaraldehyde cross-linking) were first incubated in 1 mg/mL BSA to block non-specific binding sites for 45 mins at 4°C. The electrode was then thoroughly washed in 0.01% Tween 20 (in 0.1 M PBS) and rinsed with distilled water. This was followed by incubation in the required concentration of antigen (diluted in 0.1 M PBS) for 2 h at 37 °C. A blank sample electrode was attained by incubation in 0.1 M PBS containing no antigen. The electrodes were thoroughly washed in 0.01% Tween 20 (in 0.1 M PBS) and rinsed with distilled water.

Fabrication of 'Switch off' – The steric hindrance model immunosensor

3 µL of the QD-chitosan composite film was drop-cast onto a GC electrode and allowed to dry for 1 h at 4°C. Ab immobilisation was then carried out following the physisorption or glutaraldehyde cross-linking protocols outlined above. Antigen binding was then carried out as above. The ECL response of this QD-chitosan-Ab-antigen modified electrode was then monitored.

Fabrication of 'Switch off' – An alternative approach to the steric hindrance model immunosensor

Ab immobilisation was carried out via physisorption or glutaraldehyde cross-linking (as outlined above), followed by incubation with BSA and antigen, respectively (as outlined in *Antigen binding* section). Finally, the electrode was incubated in a 0.05 µM solution of the NIR QDs (diluted in 0.1 M PBS) for 1 h at 4°C. This Ab-antigen-QD modified electrode was thoroughly washed in 0.01% Tween 20 (in 0.1 M PBS) and rinsed with distilled water, followed by monitoring of its ECL response.

QD-Ab conjugation – EDC/NHS cross-linking

A 1 mL solution containing 100 μ L Qdot® 800 ITK™ carboxyl QDs, 200 μ L EDC in 0.1 M PBS, 50 μ L NHS in 0.1 M PBS (at final working concentrations of 0.05 μ M, 0.2 M and 0.1 M respectively unless otherwise stated in Table 7.1) and 650 μ L MES buffer (pH 5.5) was prepared and mixed gently in the dark for 1 h at room temperature. All solutions were prepared immediately prior to mixing. To this, 1 mL of 1 mg/mL (unless otherwise stated in Table 7.1) Anti-human IgG (Fab specific) antibody produced in goat was added and gently mixed in the dark for 2 h at room temperature. This solution was then added to a Centriscart-I centrifugal ultrafiltration unit with 100 kDa MWCO and washed with 0.1 M PBS (pH 7.4) multiple times through centrifugation at 3500 rpm for 10 mins. The prepared QD-Ab conjugate was then used immediately.

QD-Ab conjugation – avidin-biotin binding

The selected concentration of Qdot® 800 Streptavidin conjugate (diluted in 0.1 M PBS) was mixed with the selected concentration of Anti-human IgG (H+L) antibody produced in goat-biotin conjugate (diluted in 0.1 M PBS) and gently stirred for 1 h at room temperature. The prepared QD-Ab conjugate was then used immediately.

Fabrication of 'Switch on' – A sandwich type immunoassay

Ab immobilisation (via physisorption) and antigen binding were carried out as previously described. This Ab-antigen modified electrode was then incubated in the QD-Ab conjugate (prepared via avidin-biotin binding) for 2 h at 37 °C to allow binding to occur. This modified electrode was then thoroughly washed in 0.01% Tween 20 (in 0.1 M PBS) and rinsed with distilled water to remove any unbound Ab/QDs. The ECL response from this electrode was then obtained. EIS at each stage of electrode modification was carried out to determine its effect on electrode resistance.

Fabrication of 'Switch on' – A sandwich type immunoassay from whole blood

Ab immobilisation via physisorption was carried out as described previously, followed by incubation in 1 mg/mL BSA for 45 mins at 4°C. A whole blood sample diluted 1:1 with 0.1 M PBS was then spiked with 0.5 mg/mL human IgG. The Ab-functionalised electrode was incubated in this spiked solution for 2 h at room temperature followed by washing in 0.01% Tween 20 and rinsing with distilled water. This modified electrode was then incubated in QD-Ab conjugate (0.5 µM and 0.75 mg/mL respectively) for a further 2 h at room temperature followed by the same washing procedure. The Ab-antigen-Ab-QD modified electrode was then immersed in a whole blood sample containing 100 mM $K_2S_2O_8$ and its ECL response was acquired.

7.3 Immunoassay development

7.3.1 Viability of response

The basis of many ECL immunoassays is the ability of the system to detect very low concentrations of the ECL emitter, which is brought into contact with the electrode surface through biological recognition events. The detection capabilities of this system were examined to ensure a detectable ECL response from low concentration NIR QDs was achievable. Using the conditions optimised in chapter 4, a pM linear range was achieved (Figure 7.1)

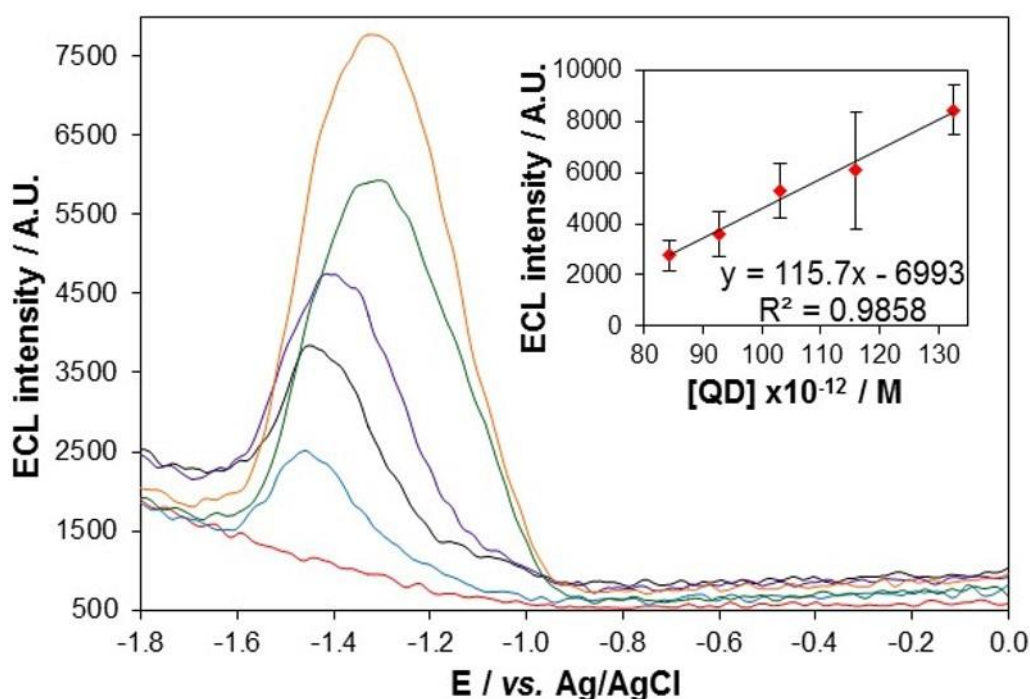


Figure 7.1 – Typical ECL response of 0 (red), 84.4 (blue), 92.8 (black), 103.1 (purple), 116 (green) and 132.6 (orange) pM 800 nm QD/chitosan film in 100 mM $K_2S_2O_8$ at a scan rate of 100 mV s^{-1} over the potential range $-1.8 \leq v \leq 0 \text{ V vs. Ag/AgCl}$. Inset shows the dependency of ECL intensity on [QD] at $\sim -1.30 \text{ V vs. Ag/AgCl}$. Error bars represent standard deviations from triplicate data set. PMT input voltage = 1.00 V.

An ECL signal at approximately -1.30 V was observed, which shifted towards more negative potentials as the QD concentration decreases. There is no longer an excess of QDs available for electron injection at the electrode surface, and as such a delay in the potential of maximum ECL intensity arises.

The likelihood of a collision and electron transfer reaction occurring between ECL precursors is greatly decreased, accounting for the large fronting nature of the ECL peaks, particularly at the lowest concentrations. The pM linear range signified this system was capable of emitting a detectable ECL signal with very low concentrations of NIR QDs.

7.3.2 Selection of immunoassay design

There are two main assay designs used within ECL biosensors that can be broadly categorised into 'switch on' or 'switch off' techniques (Figure 7.2). In the 'switch on' design, a primary Ab is immobilised on an electrode surface and the target antigen is then allowed to bind. The ECL response is 'switched on' when a labelled secondary Ab brings an ECL active species into contact with the electrode surface through secondary binding. Its intensity is governed by the concentration of bound analyte as this dictates the number of ECL active species in contact with the electrode surface. With the 'switch off' design, the ECL active species is immobilised directly on the electrode surface, followed by Ab immobilisation. Antigen binding results in the formation of a bulky biomolecule complex that has the ability to hinder diffusion of co-reactant species to the ECL active zone. This causes a decrease in ECL intensity, which is dependent upon antigen concentration as this dictates the level of steric hindrance experienced by the co-reactant molecules.

The aim of this section of work was to compare these assay designs and select the optimum based on sensitivity, specificity and reproducibility. Human immunoglobulin G (HIgG) was selected as the target for proof of concept studies, as there are a number of visible region ECL based detection systems for this analyte that can be used for comparison.¹⁹⁻²² The conditions optimised in chapter 4 were used to ensure maximum sensitivity was achieved.

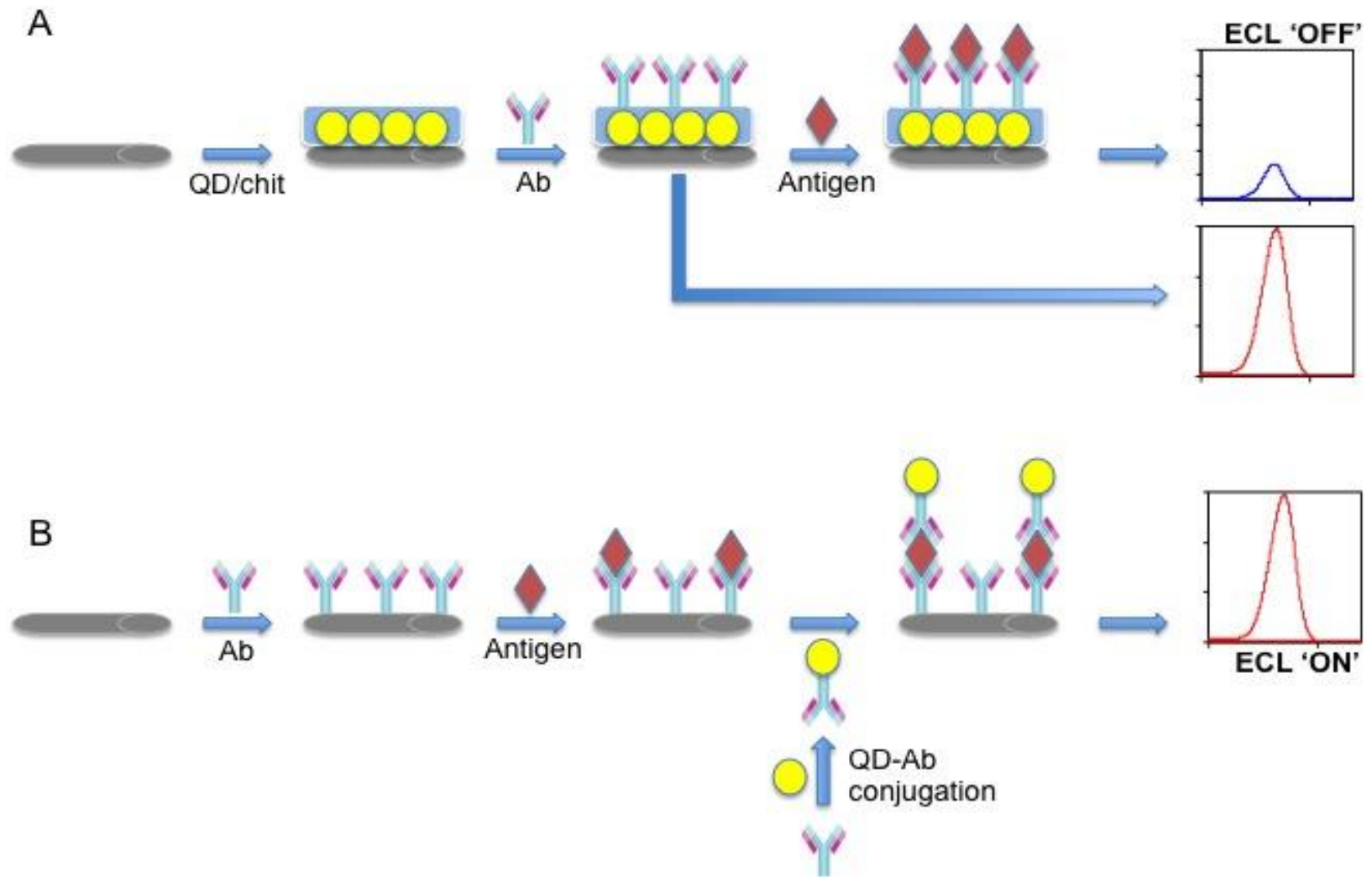


Figure 7.2 - ECL 'OFF' (A) and ECL 'ON' (B) immunoassay designs.

7.3.2.1 'Switch off' design – The steric hindrance model

The basis of this model is a decrease in ECL intensity as the concentration of target analyte increases. The formation of bulky Ab-antigen bioconjugates increases steric hindrance at the electrode surface, inhibiting diffusion of co-reactant molecules to the ECL active area. Figure 7.3 outlines the effect of increasing Ab concentration on the observed ECL signal.

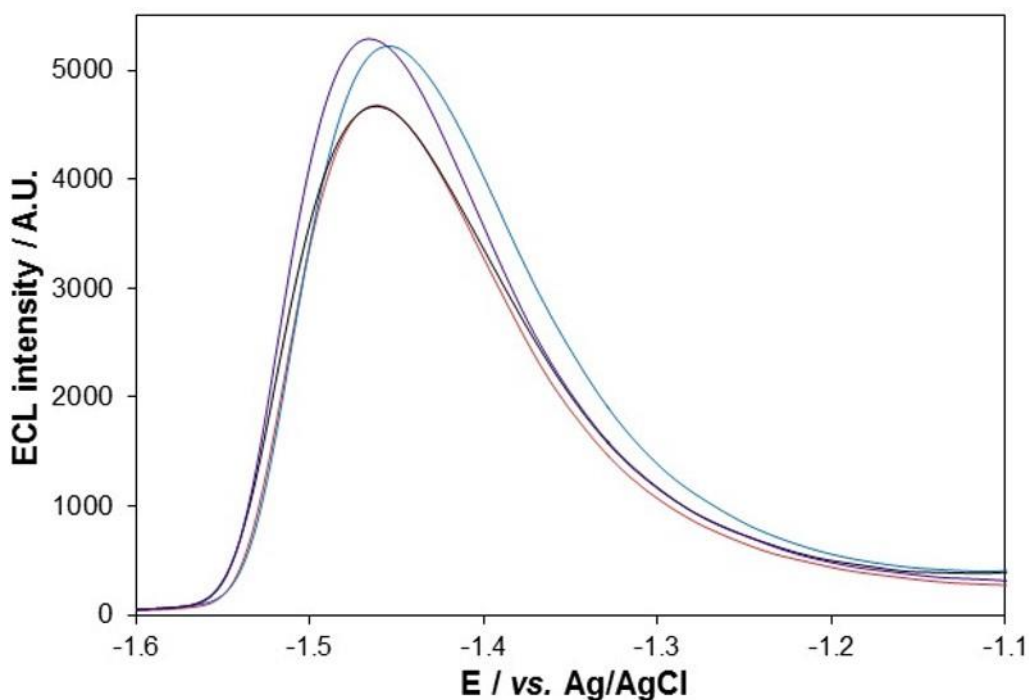


Figure 7.3 - ECL response of 800 nm QD/chitosan film with 0 (red), 2.3 (blue), 0.23 (black) and 0.00023 (purple) mg/mL HIgG Ab in 10 mM H₂O₂ at a scan rate of 100 mV s⁻¹ over the potential range -1.6 ≤ v ≤ -1.1 V vs. Ag/AgCl. PMT input voltage = 0.95 V.

The ECL peak at -1.45 V is related to ECL generation from QD/OH[•] interactions (section 3.4.2.1). Immobilisation of Ab on the electrode surface does not result in a decrease in ECL intensity, which would be expected if steric hindrance was influencing the transport of co-reactant molecules. In this system, electrochemical interactions between positively charged amine groups on the surface of chitosan and negatively charged carboxylic acid moieties present on the Ab should form, allowing immobilisation in this way. The disadvantage of this method is that Ab orientation cannot be controlled,

which can result in poor surface coverage and loss of binding activity if the active site is not accessible. It is possible that Ab immobilisation via physisorption does not provide sufficient surface coverage to hinder co-reactant diffusion. Therefore, a well-established glutaraldehyde cross-linking method for Ab immobilisation, which has been used previously for chitosan-biomolecule conjugation,²³⁻²⁵ was attempted. A comparison of these immobilisation methods is shown in Figure 7.4.

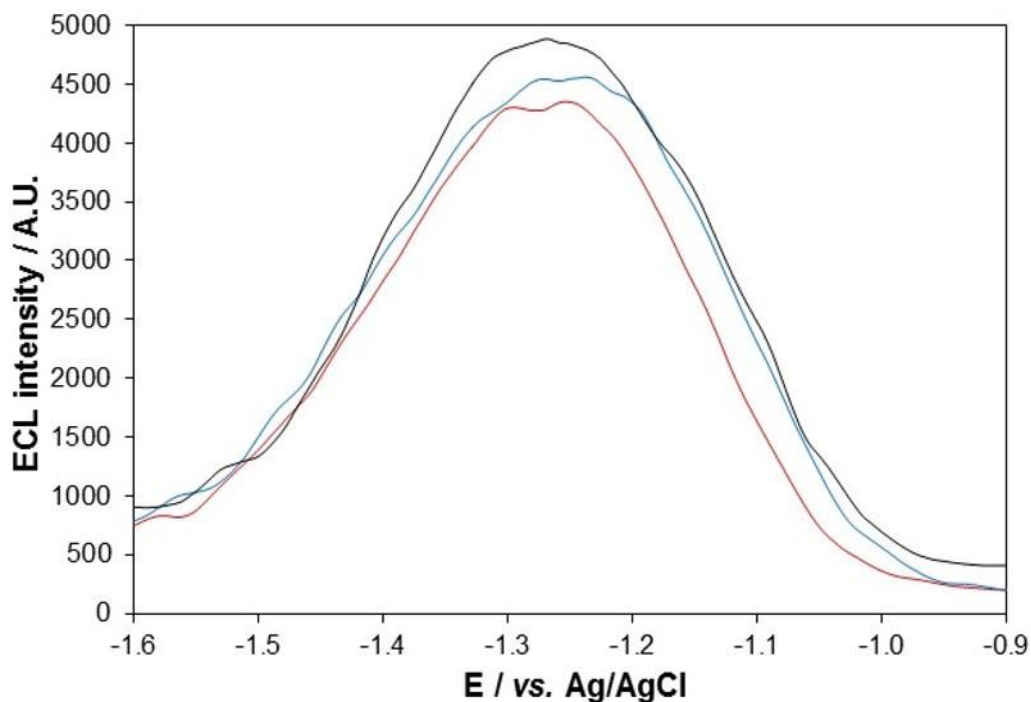


Figure 7.4 - ECL response of 800 nm QD/chitosan film with no Ab (red), Ab immobilised via physisorption (blue) and Ab immobilised via glutaraldehyde cross-linking (black) in 20 mM $K_2S_2O_8$ at a scan rate of 100 mV s^{-1} over the potential range $-1.6 \leq v \leq -0.9 \text{ V vs. Ag/AgCl}$. PMT input voltage = 0.95 V.

No change in ECL intensity was observed, regardless of the Ab immobilisation method used. This specifies that the presence of Ab on the electrode surface is not capable of preventing the movement of co-reactant molecules to the ECL active area. Antigen was then allowed to bind to immobilised Ab to determine whether the formation of a bulkier Ab-antigen bioconjugate had a greater influence on ECL intensity (Figure 7.5).

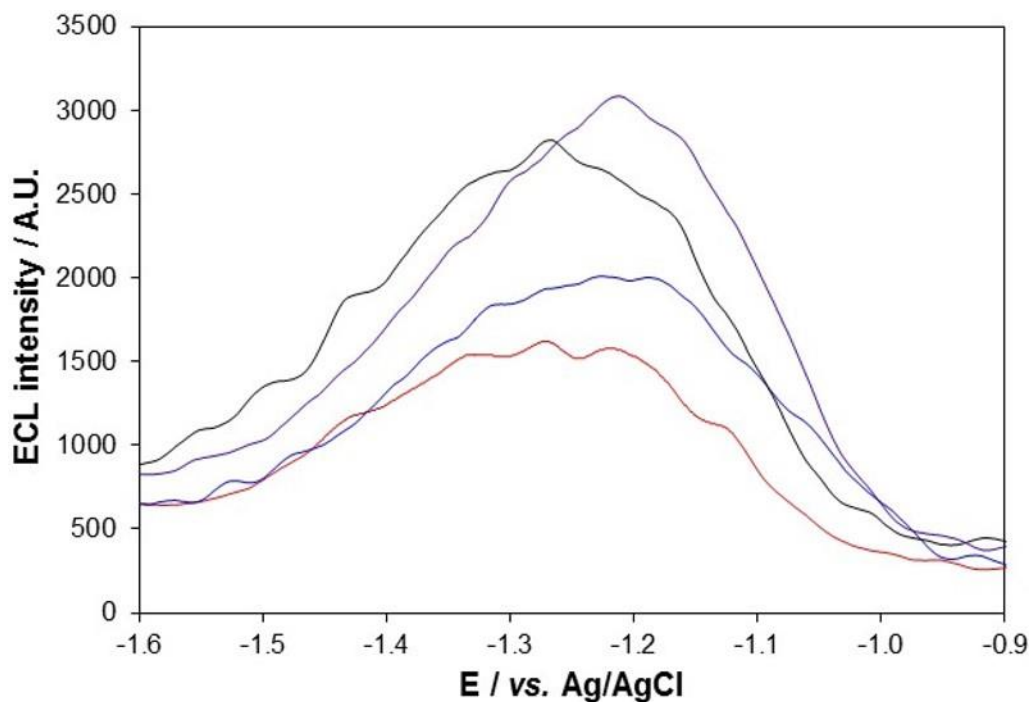


Figure 7.5 - ECL response of 800 nm QD/chitosan film with Ab immobilised via physisorption (red) + 2 mg/mL antigen (blue) and Ab immobilised via glutaraldehyde cross-linking (black) + 2 mg/mL antigen (purple) in 20 mM $K_2S_2O_8$ at a scan rate of 100 $mV s^{-1}$ over the potential range $-1.6 \leq v \leq -0.9$ V vs. Ag/AgCl. PMT input voltage = 0.95 V.

A decrease in ECL intensity was not observed following introduction of antigen into the system, suggesting that steric hindrance was not affecting NIR QD ECL intensity. Poor Ab surface coverage using the physisorption method should be improved via glutaraldehyde cross-linking, which has been used extensively for Ab immobilisation in this way.²⁶⁻³⁰ The strong affinity between Ab and antigen (typical association constants under physiological conditions of $10^8 - 10^{12} M^{-1}$)³¹ should ensure binding takes place. Thus, the lack of any influence on ECL intensity indicates that co-reactant molecules are able to penetrate the biomolecule layer at a rate capable of maintaining an excess of co-reactant precursor species at the electrode surface. A possible explanation for this is that NIR QD sensitivity may not be sufficient to detect minute changes in co-reactant concentration. At this time, this immunoassay design is not suitable for antigen detection using NIR QD ECL.

7.3.2.2 'Switch off' design – An alternative approach to the steric hindrance model

This approach is based on the requirement of an ECL emitting species to be in contact with the electrode surface to allow precursor formation. The design of this assay is displayed in Figure 7.6. An Ab is immobilised onto the electrode surface and its antigen is allowed to bind. This modified electrode is then incubated in the ECL active species and the observed ECL intensity should be governed by the number of bound antigen species as this will determine the biomolecule film thickness and electron transfer kinetics.

Electron transfer between donor (electrode) and acceptor (QD) can only occur if their orbitals are overlapping or if they are electronically coupled so that charge can flow between them.³² The rate of single-step electron transfer between electronically coupled donors and acceptors decreases exponentially with distance and is strongly influenced by the electronic characteristics of the bridging material.³³ In this case, the bridging material consists of a selection of amino acids, which make up the structure of an Ab and antigens. The exact nature of electron transfer from donor to acceptor through biomolecules is not currently known, but is thought to include electron hopping and electron tunneling components. Electron hopping uses redox active intermediates in the Ab structure, such as amide bonds, amino acid side chains or organic/inorganic co-factors with suitable redox potentials, as relay sites for electron transfer to the donor.³³ The rate of electron hopping is only weakly dependent on distance and is more sensitive to the nature of the bridging material. Electron tunneling tends to be a single step electron transfer process between directly overlapping orbitals of the donor and acceptor or with help from solvent molecules.³³ The rate of electron transfer of this process is strongly distance dependent. Charge transport through an Ab is known to be an efficient process, which allows them to act as bridging species, whilst antigen binding has been shown to decrease electrical conductivity through blocking of certain charge conducting groups in the Ab structure.³⁴

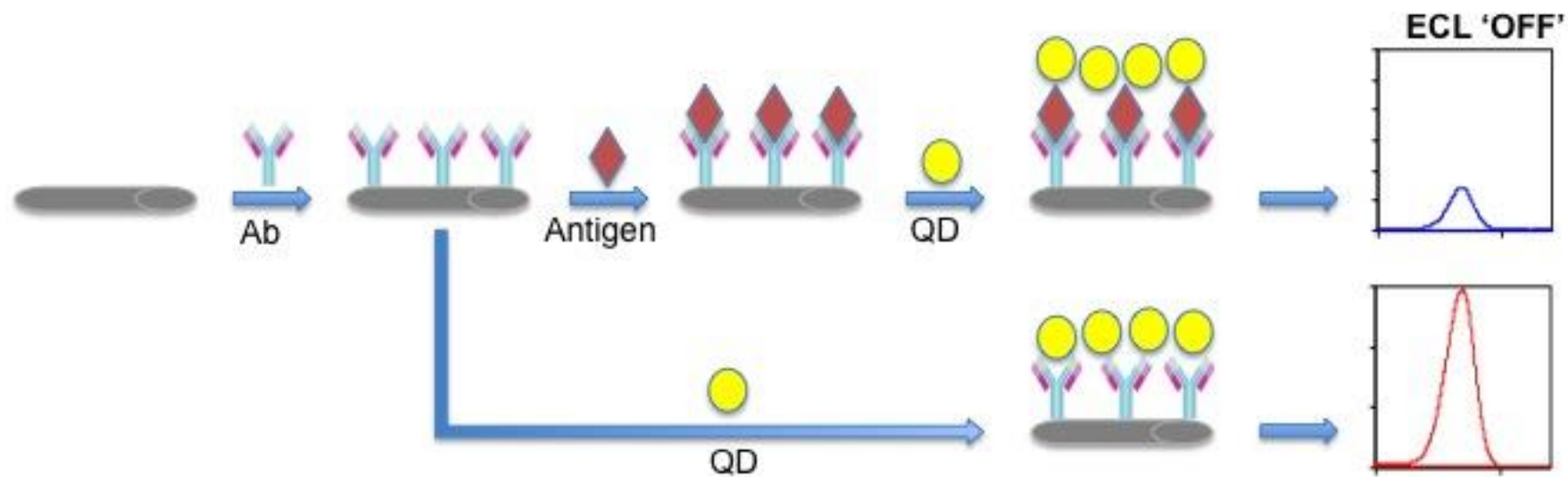


Figure 7.6 - Modified 'switch off' immunoassay design.

The concentration of ECL precursor species, and the resulting ECL intensity, is maximised when heterogeneous electron transfer is most rapid, i.e. when the species are in direct contact with the electrode surface. Attachment of an insulating biomolecule layer on the electrode surface will decrease the electrical conductivity of the system, even though Ab are efficient charge transporters. This electrical conductivity will be further decreased following antigen binding. The result is a decrease in electron transfer rate at each step of biomolecule immobilisation, which is caused by a combination of an increased distance between the donor and acceptor and a decrease in electron transfer efficiency as film conductivity falls. The average distance between the electrode surface and ECL emitter, and the electrical conductivity of the immobilised biomolecule layer will therefore be dependent upon the Ab surface coverage of the electrode and the number of bound antigen species. An increase in antigen concentration will cause a decrease in electron transfer rate between the electrode surface and the acceptor molecule on the surface of the film, provided Ab surface coverage is kept constant. Additionally, formation of co-reactant precursor species will be inhibited as the rate of diffusion of co-reactant molecules will decrease through a thicker film.³⁵ This will manifest itself in a decreased ECL intensity as the formation of precursor species is inhibited.

Electrostatic interactions can form between positively charged QDs and negatively charged moieties on the surface of Ab and antigens (usually present on the side chain of an acidic residue)³⁶, permitting electron transfer between them. The large size of NIR QDs should ensure that a biomolecule layer on the electrode surface will prevent their direct contact with it. As a result, the generation of reduced QDs will be dependent upon the electron transfer rate through the biomolecule layer, which in turn will be dictated by the Ab concentration (kept constant) and the antigen concentration (varied), as discussed above. Therefore, it was proposed that a biosensor based on this design could be used for antigen quantification through monitoring of the ECL

response. The effect of increasing Ab concentration on the ECL response is shown in Figure 7.7.

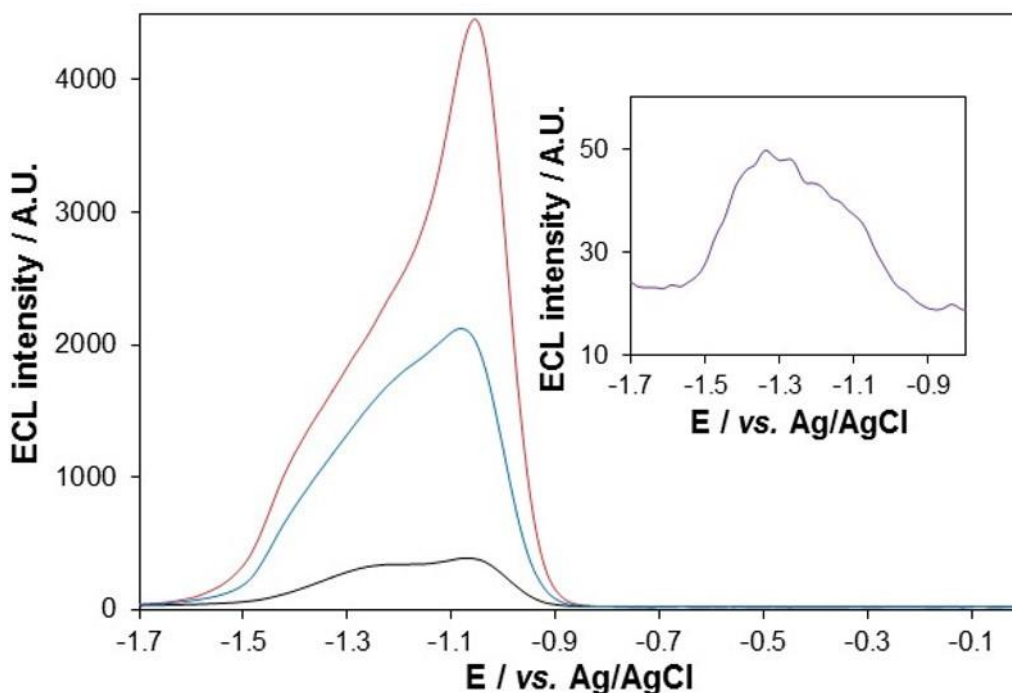


Figure 7.7 - ECL response of 800 nm QDs on a GC electrode pre-incubated with 0 (red), 0.00023 (blue), 0.023 (black) and 0.23 (inset, purple) mg/mL HlgG Ab in 20 mM $K_2S_2O_8$ at a scan rate of 100 mV s^{-1} over the potential range $-1.7 \leq v \leq 0 \text{ V}$ vs. Ag/AgCl. PMT input voltage = 0.55 V.

The broad peak with ECL maximum at -1.10 V decreases in intensity as the concentration of Ab on the electrode surface increases. This shifts to approximately -1.30 V with high Ab loading (0.23 mg/mL) due to strong inhibition of electron transfer under such conditions. This confirms that successful immobilisation of Ab via physisorption has been achieved and its presence on the electrode surface has created an insulating layer that is impeding the formation of precursor species available for excited state generation. At lower Ab concentrations, poorer surface coverage allows direct contact between the electrode surface and QDs, which explains the significantly higher intensities observed at very low Ab concentrations.

Ideally, the surface coverage should be high so that any changes in response are solely the result of antigen binding, rather than inconsistencies in the uniformity of the Ab layer. This data indicated that an Ab concentration of 0.23 mg/mL provided the best surface coverage and this concentration was therefore used to investigate the effect of antigen binding on the ECL response (Figure 7.8).

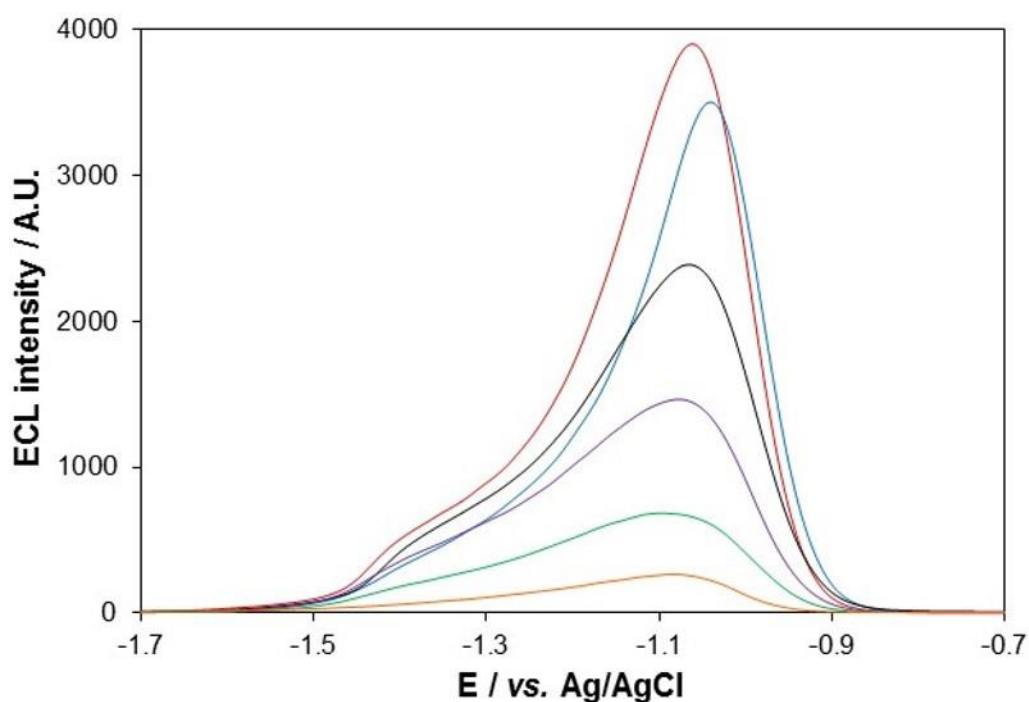


Figure 7.8 – ECL response of 800 nm QDs on a GC electrode pre-incubated with 0.23 mg/mL HlgG Ab + 0 (red), 0.00005 (blue), 0.0005 (black), 0.005 (purple), 0.05 (green) and 0.5 (orange) mg/mL HlgG in 1 mM $K_2S_2O_8$ at a scan rate of 100 mV s^{-1} over the potential range $-1.7 \leq v \leq -0.7 \text{ V vs. Ag/AgCl}$. PMT input voltage = 0.75 V.

An increase in antigen concentration resulted in decreased ECL intensity due to slower electron transfer kinetics. This allowed detection down to 50 ng/mL HlgG. System specificity was studied through incorporation of BSA to block any non-specific binding sites (Figure 7.9).

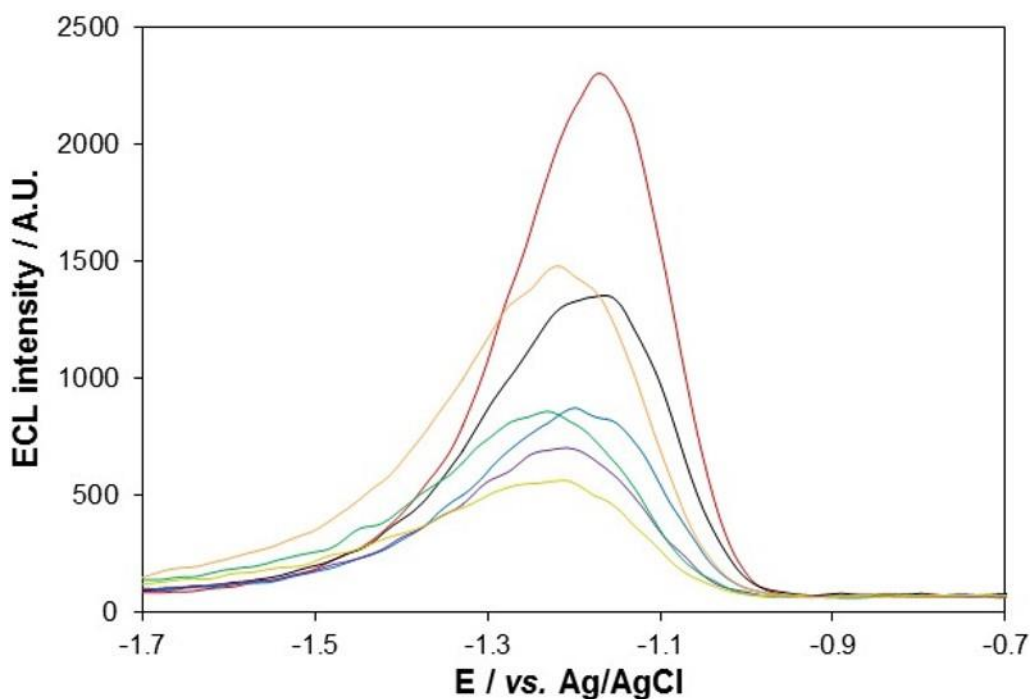


Figure 7.9 - ECL response of 800 nm QDs on a GC electrode pre-incubated with 0.23 mg/mL HlgG Ab and 1 mg/mL BSA + 0 (red), 0.00016 (blue), 0.0008 (black), 0.004 (purple), 0.02 (green), 0.1 (orange) and 0.5 (yellow) mg/mL HlgG in 1 mM $K_2S_2O_8$ at a scan rate of 100 mV s^{-1} over the potential range $-1.7 \leq v \leq -0.7 \text{ V vs. Ag/AgCl}$. PMT input voltage = 0.75 V.

A small shift in reductive ECL peak potential to approximately -1.15 V is caused by the decrease in film conductivity following immobilisation of BSA. The ECL response does not follow any obvious trend. However, Ab-antigen binding appears to be taking place as the signal is consistently lower when analyte at any concentration is present. This data shows that the majority of antigen binding seen in Figure 7.8 was through non-specific interactions with the electrode surface, rather than with the active site of its Ab. As a result, the sensor loses sensitivity to changes in antigen concentration following blocking of non-specific sites and the observed trend in ECL intensity is lost. This implies that although Ab-antigen binding appears to be taking place, it is not doing so consistently at each electrode. This may be caused by poor orientation of Ab on the electrode surface due to uncontrolled immobilisation, which can limit the accessibility of its active site.³⁷ Variations in QD-biomolecule interactions between films may also influence the rate of electron

transfer, since the strength of the interaction is a factor that dictates efficiency of the electron transfer reaction.³⁸ The non-specificity of these interactions may limit the applicability of this assay design. To improve the uniformity of the Ab layer, glutaraldehyde cross-linking to the electrode surface was carried out (Figure 7.10).

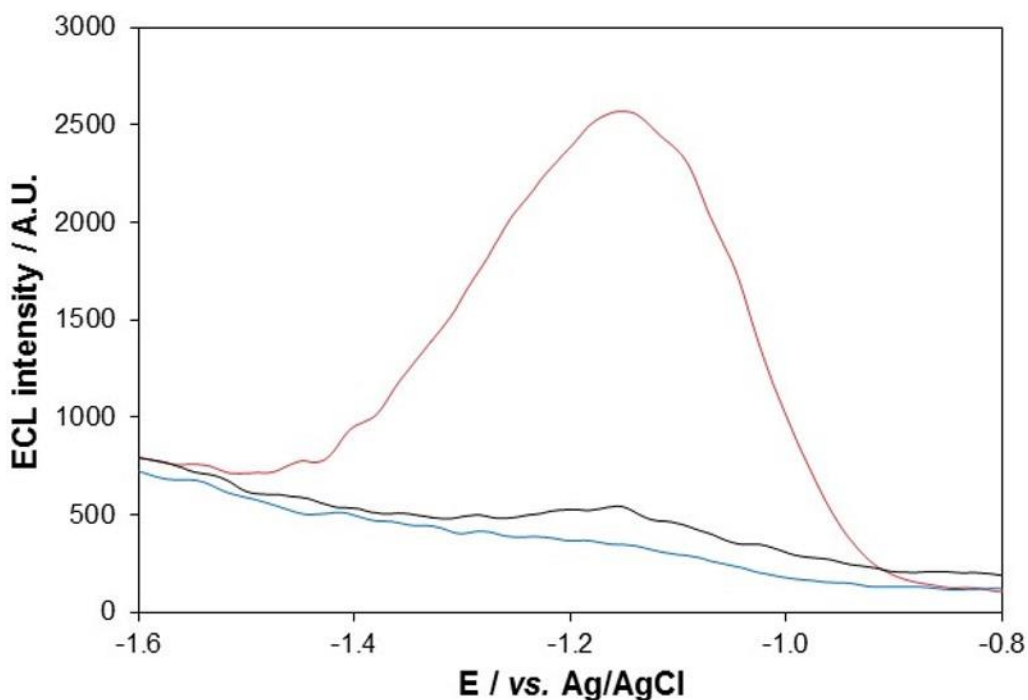


Figure 7.10 - ECL response of 800 nm QDs on a GC electrode pre-incubated with 0 (red) and 0.0023 mg/mL (blue) HIgG Ab immobilised via glutaraldehyde cross-linking and with 0.5 mg/mL HIgG (black) in 100 mM $K_2S_2O_8$ at a scan rate of 100 mV s^{-1} over the potential range $-1.6 \leq v \leq -0.8 \text{ V vs. Ag/AgCl}$. PMT input voltage = 1.05 V.

With no Ab present, an ECL response at -1.15 V was observed, which decreased significantly in intensity following Ab immobilisation, indicating a successful procedure. The GC electrode was amine functionalised using a film of chitosan, which provided anchor points for Ab immobilisation. However, unmodified chitosan is not particularly conductive³⁹ and following modification with a layer of insulating Ab molecules a film with poor electron transfer properties appears to form. Only a very weak ECL response can be detected following incubation of these modified electrodes in QDs, as the creation of precursor species is severely inhibited. This method of Ab immobilisation is

therefore not suitable for use with this assay design as electron transfer is inhibited to such an extent that sensitive ECL detection is not possible.

The requirement for a selective response to variations in antigen concentration was not met using this assay design. Whether this was due to poor uniformity of immobilised Ab on the electrode surface, variations in uncontrollable QD-biomolecule interactions, or both, is currently unknown. Taking this into consideration, further development with this assay protocol was not carried out. However, this work did confirm that Ab immobilisation can successfully be achieved via physisorption or glutaraldehyde cross-linking and that Ab-antigen binding is taking place under these experimental conditions. It also underlined the sensitivity of NIR QD ECL to changes in film conditions, which provided assurances in their biosensing ability using an alternative assay design.

7.3.2.3 'Switch on' design – A sandwich type immunoassay

To improve the specificity of interactions between QDs and the biomolecule layer, QD-Ab labelling was implemented and this conjugate was integrated into a sandwich type immunoassay design. These are the most commonly developed immunoassays and have been used with ECL monitoring to achieve detection limits in the atto and femto molar range. The two main challenges with these systems are consistent immobilisation of Ab on the electrode surface and efficient conjugation of the ECL emitter to a secondary Ab. The former is regularly achieved through simple physisorption directly onto the electrode surface or via covalent bonding between a substrate on the electrode surface and a functional group on the Ab. This usually takes the form of glutaraldehyde cross-linking between two amine groups or EDC/NHS coupling between an activated carboxylic acid group and an amine. QD-Ab conjugation is usually accomplished using these same covalent chemistries⁴⁰ or via avidin-biotin interactions.⁴¹

Previous work in this chapter confirmed that physisorption and glutaraldehyde cross-linking can be used to immobilise Ab on the GC electrode surface. However, the glutaraldehyde method in its current form does not create a system that is conducive to sensitive analyte detection owing to poor charge transport through the film and biomolecule layer. As layer thickness will be greater (three layers of biomolecules as opposed to two) using a sandwich type immunoassay, efficient charge transport through the film is required to allow electron transfer with the QDs (brought into contact with the electrode surface following biological recognition events). Therefore, for this initial proof of concept study, physisorption was selected as the Ab immobilisation method.

For QD-Ab bioconjugation via EDC/NHS coupling or avidin-biotin binding, QDs with alternative ligand passivation layers were required. For EDC/NHS coupling, QDs coated with a polymer that has surface carboxylic acid residues were used (QD-COOH) and for avidin-biotin binding, streptavidin-coated QDs (QD-av) were required. The voltammograms from DPV of these alternative QDs are shown in Figure 7.11.

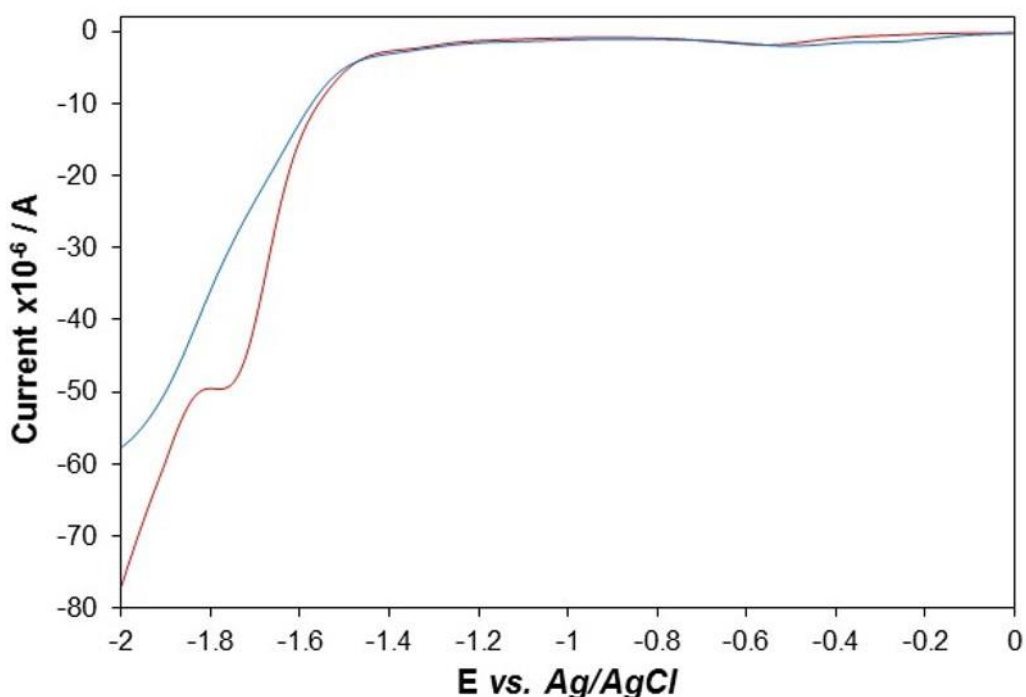


Figure 7.11 - Current response from film of bare 800 nm QD-COOH (red) and QD-av (blue) in 0.1 M PBS over the potential range $-2 \leq v \leq 0$ V vs. Ag/AgCl.

Both sets of QDs exhibit a reduction peak at -0.6 V, which is attributed to reduction of O₂ (section 2.3.2.1). An additional reduction peak at -1.75 V is seen with QD-COOH, which is similar to that detected previously (section 2.3.2.1), indicating it is associated with a secondary reduction process of the QDs. This peak is not seen with QD-av, which is likely due to passivation with a biomolecule layer with greater resistance to electron transfer. The electrochemical behaviour of these QDs is clearly influenced by their passivation layer, which is likely to affect their ECL properties.

These QDs must emit a detectable ECL signal in order to be useful for antigen detection. Confirmation of ECL emission from these QDs was therefore required (Figure 7.12).

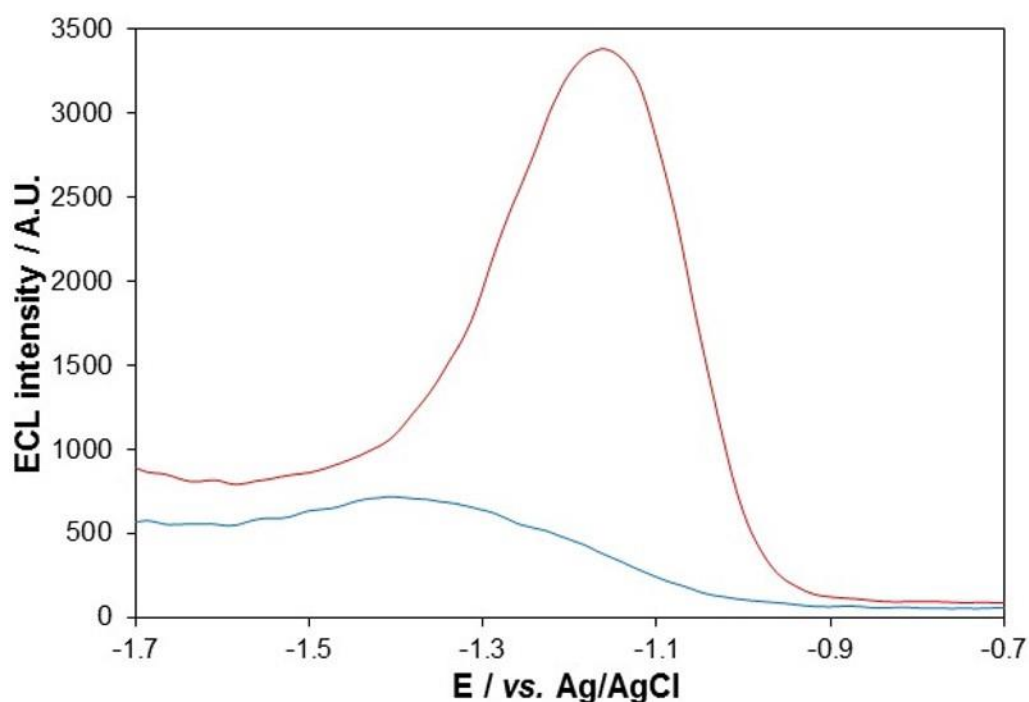


Figure 7.12 - ECL response from film of bare 0.1 μM 800 nm QD-COOH (red) and 0.1 μM 800 nm QD-av (blue) in 100 mM $\text{K}_2\text{S}_2\text{O}_8$ at a scan rate of 100 mV s^{-1} over the potential range $-1.7 \leq v \leq -0.7$ V vs. Ag/AgCl. PMT input voltage = 0.75 V.

QD-COOH exhibits a reductive ECL peak that appears at -0.80 V and reaches a maximum at -1.15 V. QD-av ECL appears at -0.85 V and has a maximum intensity at -1.35 V. This peak is 4.5 times weaker than that seen with QD-

COOH. Under identical experimental conditions, regular NIR QDs produce a signal that is too intense for detection (as it would damage the PMT) and this signifies that ECL sensitivity of these QDs is influenced by their surface passivation. The order of sensitivity for these passivated QDs is regular NIR QD>QD-COOH>QD-av. The observed trend originates in the ease of electron injection into these QDs. DAET (used to passivate the regular NIR QDs) is a short chain thiol ligand that is positively charged, whereas carboxylated QDs are passivated with a polymer layer (unknown composition) with surface –COO⁻ groups. This thicker, negatively charged coating will hinder the injection of electrons into the QD core and the appearance of ECL and its efficiency will be affected. QD-av are passivated with 5-10 covalently bound streptavidin protein molecules. Passivation with a layer of biomolecules will significantly affect electron transfer kinetics due to increased resistance to QD electron injection and an increased distance between the electrode surface and the QD itself. Formation of QDs(e⁻(1S_e)) will be harder, accounting for the small increase in ECL onset potential, and the substantially slower electron transfer kinetics explains the large decrease in ECL intensity. Although intensity is adversely affected using these alternative 800 nm QDs, a detectable ECL response is apparent, enabling their use in these assays.

This data shows that QD-Ab conjugation will cause a decrease in ECL intensity as the biomolecule layer surrounding each QD becomes larger. Monitoring of the decrease in ECL signal following conjugation can therefore be used as a simple tool to determine the most efficient conjugation protocol. Table 7.1 outlines the percentage decrease in ECL intensity following QD-Ab conjugation with a variety of conditions investigated.

Table 7.1 - % loss of ECL signal in 100 mM K₂S₂O₈ after QD-Ab conjugation via avidin-biotin binding and EDC/NHS coupling.

QD-av		
Parameter	Variable	% loss ECL signal
Ab concentration (mg/mL)	0.15	-0.4
	0.3	57.7
	0.75	62.8
QD concentration (μM)	0.1	34.9
	0.2	35.5
	0.5	65.1
QD-COOH		
Parameter	Variable	% loss ECL signal
EDC:NHS ratio	1:1	1.4
	2:1	17.6
	4:1	17.2
EDC concentration (M)	0.1	4.0
	0.2	38.8
	1	38.5
Ab concentration (mg/mL)	0.0001	13.5
	0.01	8.4
	1	10.6
QD concentration (μM)	0.4	11.5
	0.8	12.0
	1.6	8.9

From Table 7.1 it can be seen that QD-Ab conjugation via EDC/NHS coupling did not appear to be particularly successful. This may be due to poor QD surface coverage with carboxylic acid residues, poor activation of these prior to Ab binding or hydrolysis of intermediate products. Conjugation efficiency appears to be most dependent upon a high EDC concentration and a large excess of EDC compared to NHS. Slightly acidic conditions (pH 5.5) were used to minimise the likelihood of intermediate hydrolysis, however, the conjugation procedure was not as efficient as conjugation via avidin-biotin binding.

This method was considerably more successful, which is due to the high affinity of these species for one another and the simplicity of the binding procedure. The avidin-biotin interaction is one of the strongest non-covalent interactions currently known (dissociation constant of approximately 1.3×10^{-15} M) and is stable over a wide range of pH and temperatures.⁴² Table 7.1 reveals that increasing Ab concentration had the largest effect on QD coverage as more Ab molecules were present for binding to the QD surface. The highest examined QD concentration exhibited the largest % decrease in ECL, indicating the most favourable QD:Ab ratio for binding occurs with Ab and QD concentrations of 0.75 mg/mL and 0.5 μ M respectively. The Ab concentration was limited by that of the stock solution. Lower QD concentrations were attempted, however, the resulting ECL signal prior to conjugation was very weak, even under optimal sensing conditions (chapter 4). For that reason, these concentrations were not deemed suitable for incorporation into an immunoassay.

Table 7.1 highlights the optimal method for Ab conjugation with these NIR QDs. This information can be used for all future immunoassay development that integrates them into their design.

Electrochemical impedance spectroscopy (EIS) was used to monitor the growth of the biomolecule layer on the electrode surface to ensure successful Ab immobilisation, antigen binding and secondary Ab binding. This technique

is based on the electrical circuit shown in Figure 7.13 and examines the relationship between various sources of impedance in the system in relation to signal frequency.

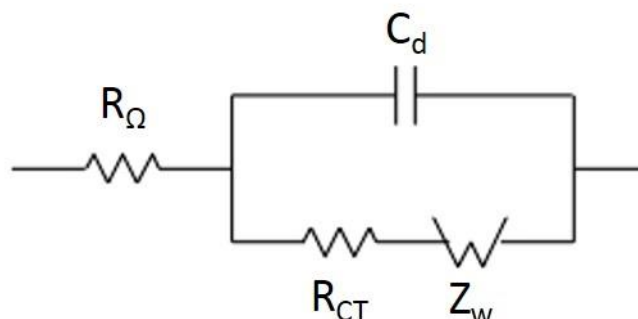


Figure 7.13 – Electrical circuit in EIS. R_{Ω} is solution resistance, R_{CT} is resistance to charge transfer, C_d is the double layer capacitance and Z_w is Warburg impedance (resistance to mass transfer)

At low frequencies, Warburg impedance dominates over all other sources of resistance in the system and this is observed as a straight line in the spectra that is indicative of diffusion control. At very high frequency, the double layer capacitance offers no impedance and thus the only resistance in the system is R_{Ω} . As the frequency drops, impedance from the double layer capacitance begins to increase and the resistance to charge transport becomes important. At lower frequencies (but still at values where R_{CT} and C_d dominate over Z_w) the impedance offered by the double layer capacitance is very high and resistance to charge transfer is the dominant factor.⁴³ This relationship manifests itself in the semi-circular region observed in EIS spectra with radius determined by resistance to charge transfer. It is expected that as the biomolecule layer on the electrode surface is formed, the transfer of electrons from the electrode surface to the electroactive species will become increasingly inhibited. This is due to slower charge transfer through a thicker biomolecule layer, which has been discussed previously (section 7.3.2.2). Therefore, as the biosensor is fabricated the size of the semi-circular region in the EIS spectra should increase. This is observed in Figure 7.14.

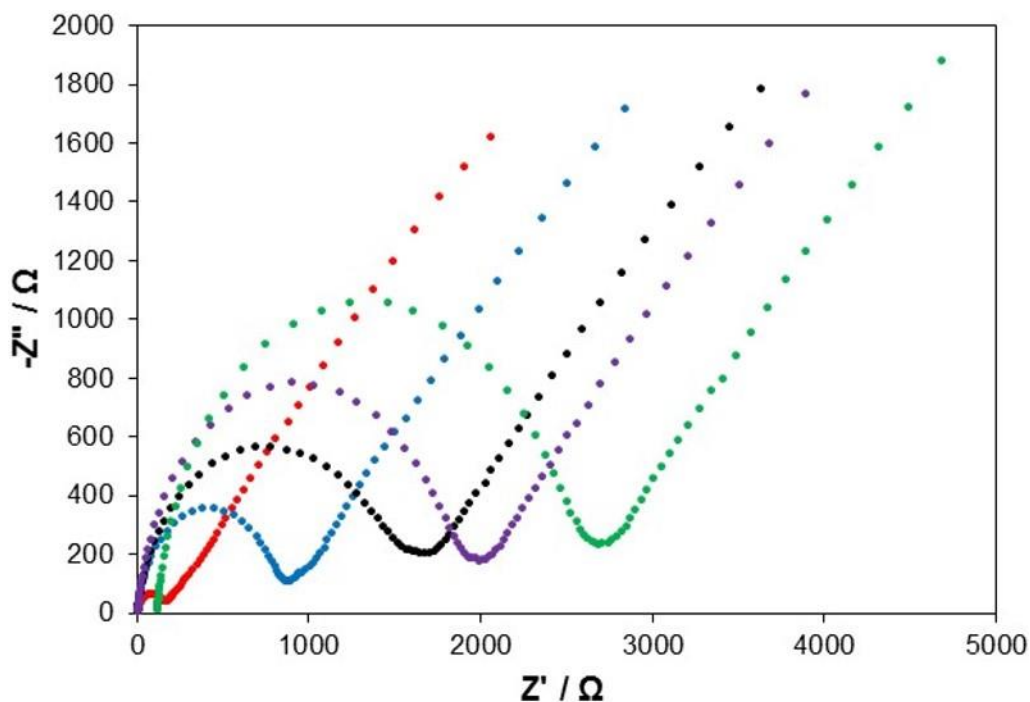


Figure 7.14 - EIS spectra for a blank GC electrode (red), + 0.23 mg/mL HlgG Ab (blue), + 1 mg/mL BSA (black), + 0.5 mg/mL HlgG antigen (purple) and + QD-Ab conjugate (green) over a frequency range of 0.01 – 100000 Hz and a signal amplitude of 5 mV.

The blank GC electrode shows an almost straight line, which is representative of diffusion limited electron transfer at the electrode surface as there almost no resistance to charge transfer. The semicircular region increases in size following Ab immobilisation, as this biomolecule layer inhibits charge transfer in the system. Further increases in electron transfer resistance are exhibited following BSA, antigen and QD-labelled secondary Ab binding, due to an increasing thickness and resistance to electron transfer through the biomolecule layer. The value of R_{Ω} is determined from the x-axis intercept of the semi-circle in the high frequency region (where Z' tends to zero) and in this system is approximately 14 Ω . R_{CT} can be determined from extrapolating the end of the semi-circular region to the x-axis and these values are shown in Table 7.2.

Table 7.2 – Values of R_{CT} determined from EIS spectra following electrode modification.

Modified electrode	R_{CT} / Ω
Blank	186
Ab only	886
Ab + BSA	1685
Ab + BSA + Ag	1980
Ab + BSA + Ag + Qd-Ab	2700

This data highlights the increase in charge transfer resistance associated with increasing the thickness of the biomolecule layer and confirms that fabrication of the immunosensor was successful. Therefore, an ECL response should be produced following binding of the QD labelled secondary Ab. The QD-Ab conjugate prepared using optimum conditions was used for detection of HlgG (Figure 7.15).

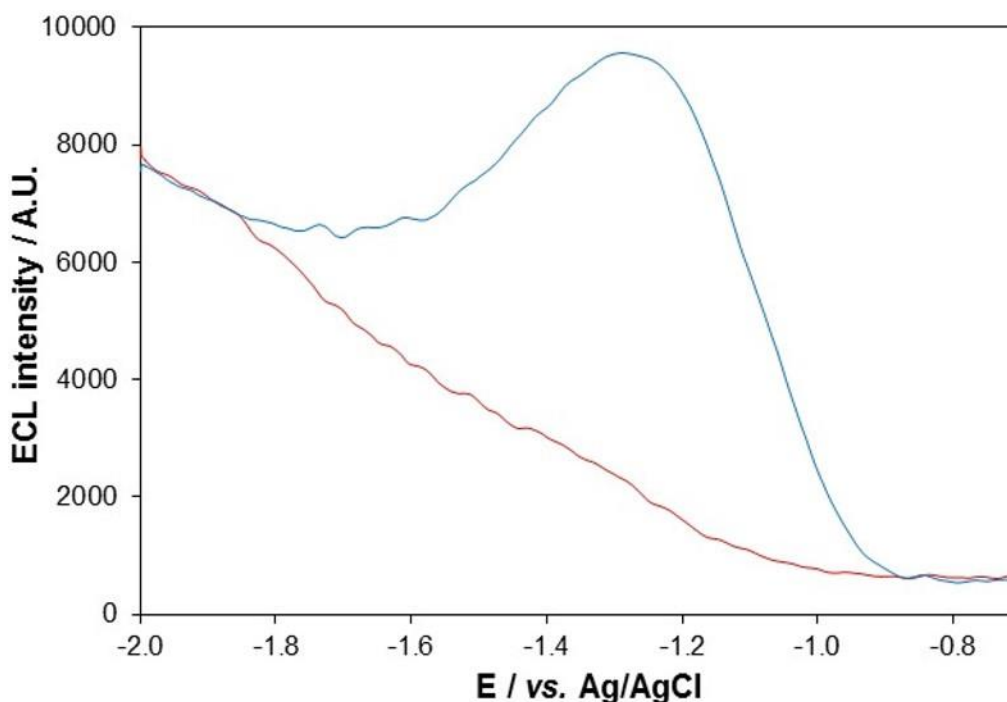


Figure 7.15 - ECL response of sandwich immunoassay biosensor using 0.5 μ M-0.75 mg/mL QD-Ab conjugate with 0 (red) and 0.5 mg/mL (blue) HlgG in 100 mM $K_2S_2O_8$ at a scan rate of 100 $mV s^{-1}$ over the potential range $-2 \leq v \leq -0.7$ V vs. Ag/AgCl. PMT input voltage = 1.05 V.

A strong reductive ECL peak at -1.25 V in the presence of 0.5 mg/mL HIgG was observed. The % RSD between triplicate assays at this concentration was 1.06 %, demonstrating a good stability of biosensor response. Figure 7.16 shows the ECL response during fabrication of this biosensor, confirming that ECL generation is reliant upon the presence of NIR QDs through binding of the labelled secondary Ab.

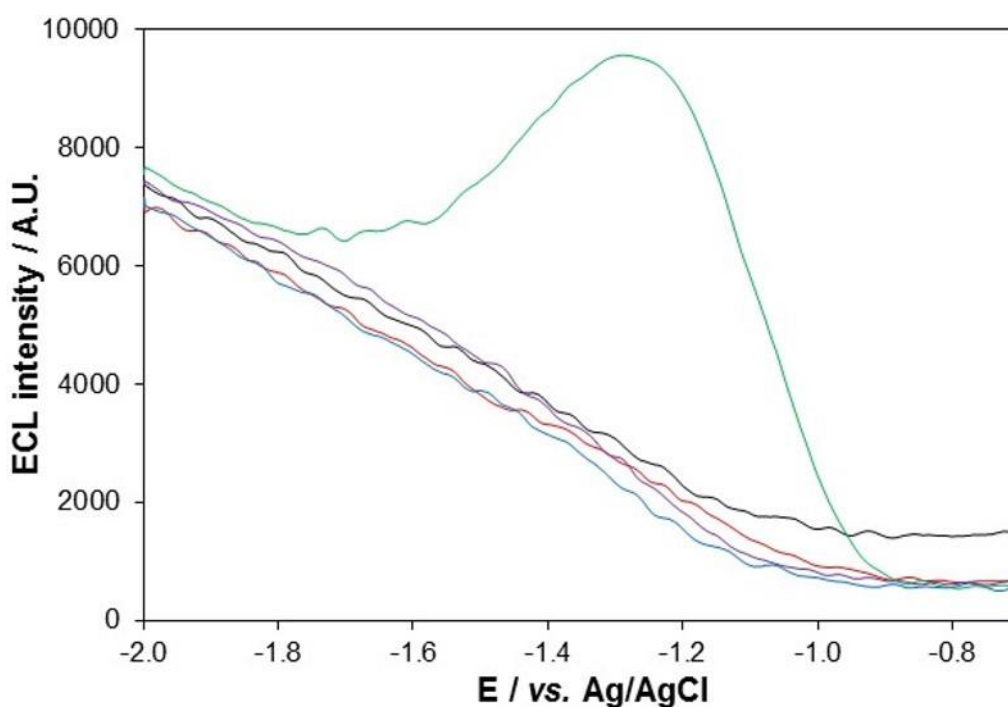


Figure 7.16 - ECL response of blank GC electrode (black), Ab functionalised electrode (red), Ab+BSA functionalised electrode (black), Ab+BSA+antigen functionalised electrode (purple) and Ab+BSA+antigen+QD-Ab conjugate functionalised electrode (green) in 100 mM $K_2S_2O_8$ at a scan rate of 100 mV s^{-1} over the potential range $-2 \leq v \leq -0.7\text{ V vs. Ag/AgCl}$. PMT input voltage = 1.05 V.

An ECL signal was only detected using this sandwich type immunoassay design following binding of the QD labelled secondary Ab. This demonstrates that QD reduction is possible via electron transfer through the biomolecule layer and that QDs are present at sufficient concentration to elicit a response.

This data shows that NIR QD ECL can be used to detect HlgG using a sandwich type immunoassay that integrates NIR QD-Ab conjugates (from Table 7.1) and optimised ECL detection conditions (chapter 4).

Whole blood detection

A key objective of this work was to establish the whole blood detection capability of a NIR QD ECL immunosensor. As detection of HlgG was successfully accomplished in buffer (Figure 7.16), application of this immunoassay design with direct whole blood analysis was attempted. The ECL response of this biosensor under these conditions is shown in Figure 7.17.

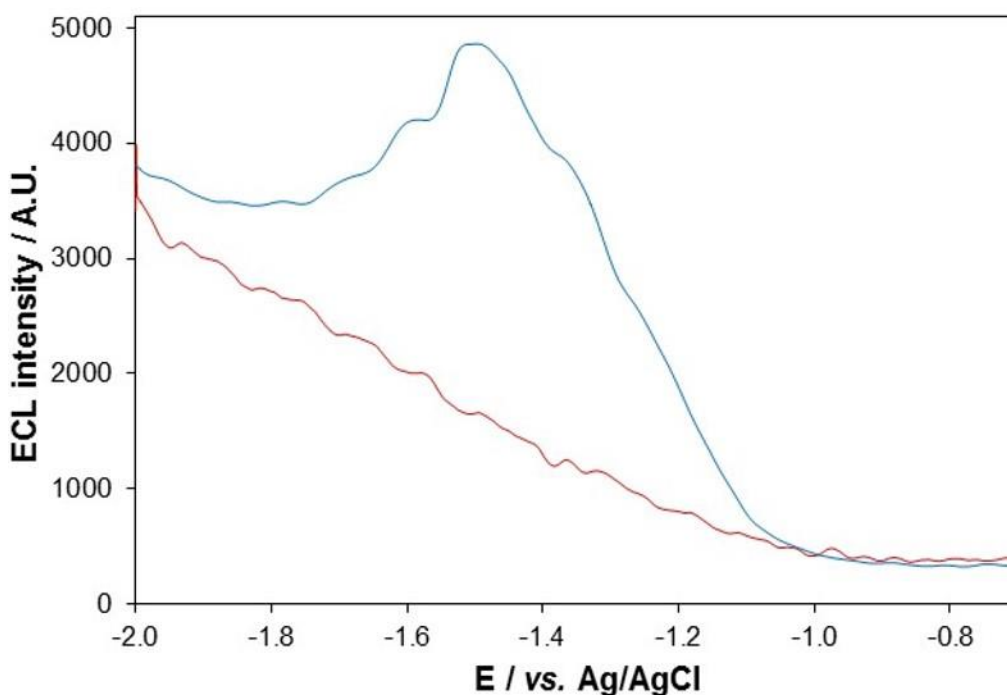


Figure 7.17 - ECL response of sandwich immunoassay biosensor using 0.5 μ M-0.75 mg/mL QD-Ab conjugate with 0 (red) and 0.5 mg/mL (blue) HlgG in whole blood with 100 mM $K_2S_2O_8$ at a scan rate of 100 mV s⁻¹ over the potential range $-2 \leq v \leq -0.7$ V vs. Ag/AgCl. PMT input voltage = 1.05 V.

In the presence of 0.5 mg/mL HlgG, a reductive ECL peak is observed at -1.45 V, which is not apparent in the blank, indicating it results from biological

recognition interactions that are linking NIR QDs to the electrode surface. The peak is less intense and shifted to more negative potentials than that seen in buffer. This is likely due to interruption of Ab-antigen binding by species in blood, a small degree of light and co-reactant radical quenching and slower electron transfer kinetics in whole blood.

The work described in chapter 5 showed that NIR QDs can generate an intense ECL signal in whole blood with $K_2S_2O_8$ co-reactant, whilst this work is an indicator of their potential use as ECL labels in sandwich type immunoassays with direct whole blood analysis.

A detectable ECL signal could not be observed for HIgG concentrations below 0.5 mg/mL and the response in whole blood was not reproducible. This may be caused by poor efficiency of ECL generation under these charge transport limited conditions or due to ineffective Ab-antigen binding because of poor Ab orientation on the electrode surface, which limits the availability of its binding site. In the future, it is likely these deficiencies can be overcome through optimisation of biosensor design. This is discussed in the following section.

7.4 Future developments

This work has shown the potential capability of a NIR QD ECL immunosensor with detection from whole blood. This proof-of-concept system requires further research to enhance sensitivity, stability and specificity. The key area for development of this system lies in improvements in its reproducibility and sensitivity, the origin of which can likely be found in three distinct areas. Firstly, modification of the electrode film could allow an increase in electron transfer kinetics, which would ensure more efficient generation of an ECL signal. Enhancements in charge transport properties and QD ECL intensity have been achieved through incorporation of additional nanomaterials, such as graphene, carbon nanotubes (CNTs) and gold nanoparticles (Au NPs) into biosensor design, which has been reviewed in section 1.1.4.2.

Secondly, optimisation of the Ab immobilisation procedure should permit an increase in biosensor sensitivity and reproducibility through better orientation of the Ab on the electrode surface and superior Ab surface coverage. This will increase the number and availability of binding sites for interaction with antigen, which should in turn increase the number of QD-labelled secondary Ab able to bind to the electrode surface. By their nature, nanocomposite materials with excellent charge transport properties also have large surface to volume ratios due to their nanoscale dimensions. This permits high Ab loading, which will increase the number of active sites available for antigen binding. Recent work by Yan *et al.* employed a Au NP covered graphene composite to increase the surface area and conductivity of their electrode, allowing higher Ab loading.⁴⁴ This was incorporated into a POC biosensor with a carcinoembryonic antigen (CEA) detection limit of 0.3 pg/mL. Incorporation of poly (diallyldimethylammonium chloride) into a similar Au NP-graphene system allowed for an enhanced LOD for CEA (2 fg/mL) based on ECL quenching of $[\text{Ru}(\text{bpy})_3]^{2+}$ by QDs.⁴⁵ A similar approach was used by Wu *et al.*, where Au NPs were loaded onto the surface of graphite oxide to create an excellent Ab immobilisation matrix with the added benefit of improved electrical conductivity.⁴⁶ This yielded a detection limit for prostate specific antigen (PSA) of 0.5 pg/mL. CNTs have also been used for Ab immobilisation due to their large surface to volume ratio, high conductivity and rigid shape that can be used as a template for Ab immobilisation.⁴⁷ Sardesai *et al.* took advantage of these properties to generate a multi-analyte biosensor for interleukin-6 and PSA with detection limits of 0.25 and 1 pg/mL respectively.⁴⁸ Multi-walled CNTs were used as the immobilisation matrix for concanavalin A, allowing efficient binding and a detection limit for K562 cells of 600 cells/mL.⁴⁹ These examples highlight the benefits of using nanocomposite for Ab immobilisation. Higher Ab loading, better alignment and faster electron transfer kinetics combine to ensure these materials are ideal for enhancement of immunoassay ECL performance.

Thirdly, significant enhancements in ECL intensity have been accomplished through secondary Ab labelling with multiple ECL emitting species. The advantage being that, for a given antigen concentration, the effective concentration of ECL species in contact with the electrode surface is increased significantly because binding of a single secondary Ab brings several labels with it. An increase in ECL active species loading on secondary Ab was successfully used by Wang *et al.*, who integrated multiple CdTe/CdS QDs onto a silica nanosphere/secondary Ab probe resulting in enhancement of ECL intensity of 3.5-fold when compared to binding of a single QD labelled secondary Ab probe.⁵⁰ With this amplified system, a HlgG detection limit of 87 fg/mL was possible. An alternative system using amplification through increased QD loading on secondary Ab was developed through the use of a nanoporous PtRu alloy as the immobilisation matrix for CdTe QDs and secondary Ab.¹² This alloy permitted attachment of multiple QDs and Ab molecules, increasing ECL intensity 4.67-fold compared to a single QD label. PtFe nanoparticle alloys have been used with similar success for functionalisation with several CdTe QDs as sensitive ECL labels.⁵¹ Combining this QD functionalised alloy with graphene nanosheets yielded an extremely sensitive (LOD=15 aM) system for DNA detection. An alternative DNA sensor used nanoporous Au as the matrix for immobilisation of multiple ECL labels (carbon QDs).⁵² This paper-based biosensor permitted a DNA LOD of 0.86 aM, because of the significant enhancement in ECL intensity of the label.

From this review, it is clear there are a number of options available for enhancing the sensitivity and stability of this biosensor. Improving the charge transport properties and Ab immobilisation matrix can be achieved through integration of nanomaterials such as graphene, Au NPs and CNTs, which have been shown to improve these biosensor elements leading to enhancements in ECL performance. Creation of multi-label ECL probes will increase the number of ECL active species brought into contact with the electrode surface and have been used previously with great success. This provides confidence that ECL generated from the NIR QDs employed within this biosensor can be sufficiently

enhanced using these modifications to allow significant improvements in immunoassay performance.

7.5 Conclusions

Integration of a NIR QD-labelled secondary Ab into a sandwich type immunoassay protocol permitted detection of HIgG in buffer and whole blood. It is believed that further development of this biosensor will allow significant enhancements in ECL performance, as has been shown in other similar systems.

Three alternative immunosensing platforms for HIgG that integrated NIR QDs into their design were investigated. A classical 'switch off' protocol that relied on inhibiting the diffusion of co-reactant species to the electrode surface through increased steric hindrance did not enable antigen detection. This may have been caused by insensitivity of the ECL signal to very small changes in co-reactant concentration. A modified version of this protocol was developed, which has not been used previously. This design was based on changes in electron transfer kinetics associated with biomolecule layer formation. This system showed promise as a detection method, but required improvements in Ab surface coverage and active site availability, as well as greater control over QD-biomolecule layer interactions. This implied that a traditional sandwich type immunoassay would be a more suitable immunoassay design. Optimisation of QD-Ab conjugation was accomplished, based on the principle that ECL intensity was influenced by the nature and thickness of the QD passivation layer. An ECL response was only obtained following antigen and QD labelled secondary Ab binding, exhibiting advanced specificity over previous assay designs in this chapter.

The aim of this work was to develop a NIR QD ECL immunoassay detection system that was capable of analysis directly from whole blood samples. For the first time, an ECL signal was detected using a sandwich type immunoassay design and analysis from blood. Although in its early stages, this research sets

a precedent that suggests eligibility of NIR QDs as ECL active species for target analyte detection directly from whole blood. It is hoped that optimisation of this work can aid in the development of novel ECL biosensors with whole blood analysis.

7.6 References

1. J. Li and M. J. Sailor, *Biosensors and Bioelectronics*, 2014, **55**, 372-378.
2. K. Campbell, P. Barnes, S. A. Haughey, C. Higgins, K. Kawatsu, V. Vasconcelos and C. T. Elliott, *Analytical and bioanalytical chemistry*, 2013, **405**, 7753-7763.
3. Y. W. Hartati, S. N. Topkaya, I. P. Maksum and M. Ozsoz, *Advances in Analytical Chemistry*, 2013, **3**, 20-27.
4. T. Bryan, X. Luo, P. R. Bueno and J. J. Davis, *Biosensors and Bioelectronics*, 2013, **39**, 94-98.
5. R. Gabl, E. Green, M. Schreiter, H. D. Feucht, H. Zeininger, R. Primig, D. Pitzer, G. Eckstein and W. Wersing, *Sensors*, 2003, **2**, 1184-1188.
6. B. Xie, M. Mecklenburg, B. Danielsson, O. Öhman, P. Norlin and F. Winquist, *Analyst*, 1995, **120**, 155-160.
7. D. Wild, *The Immunoassay Handbook*, Elsevier, 2005.
8. R. S. Yalow and S. A. Berson, *Nature*, 1959, **184**, 1648-1649.
9. R. P. Ekins, *Clinica Chimica Acta*, 1960, **5**, 453-459.
10. E. P. Diamandis and T. K. Christopoulos, *Immunoassay*, Elsevier Science, 1996.
11. X. Li, R. Wang and X. Zhang, *Microchimica Acta*, 2011, **172**, 285-290.
12. Y. Zhang, S. Ge, S. Wang, M. Yan, J. Yu, X. Song and W. Liu, *Analyst*, 2012, **137**, 2176-2182.
13. S. Wang, E. Harris, J. Shi, A. Chen, S. Parajuli, X. Jing and W. Miao, *Physical Chemistry Chemical Physics*, 2010, **12**, 10073-10080.
14. X.-B. Yin, Y.-Y. Xin and Y. Zhao, *Analytical chemistry*, 2009, **81**, 9299-9305.
15. W. Miao and A. J. Bard, *Analytical chemistry*, 2004, **76**, 5379-5386.
16. M. Zhao, Y. Zhuo, Y. Chai, Y. Xiang, N. Liao, G. Gui and R. Yuan, *Analyst*, 2013, **138**, 6639-6644.
17. L. Chen and H. Han, *Microchimica Acta*, 2014, **181**, 1485-1495.
18. C. Woelfle and R. O. Claus, *Nanotechnology*, 2007, **18**, 025402.
19. Y. R. Kim, H. J. Seo, J. W. Oh, H. Lim, T. H. Kim and H. Kim, *Electroanalysis*, 2013, **25**, 1056-1063.
20. L. L. Li, K. P. Liu, G. H. Yang, C. M. Wang, J. R. Zhang and J. J. Zhu, *Advanced Functional Materials*, 2011, **21**, 869-878.
21. H. Qi, Y. Zhang, Y. Peng and C. Zhang, *Talanta*, 2008, **75**, 684-690.
22. W. Yun, X.-Y. Wang, P. Dong, J.-K. Zhu, Y. Xu, P.-G. He and Y.-Z. Fang, *Chinese Journal of Analytical Chemistry*, 2009, **37**, 8-12.
23. M. Albarghouthi, D. A. Fara, M. Saleem, T. El-Thaher, K. Matalka and A. Badwan, *International journal of pharmaceutics*, 2000, **206**, 23-34.
24. S.-B. Zhang, Z.-S. Wu, M.-M. Guo, G.-L. Shen and R.-Q. Yu, *Talanta*, 2007, **71**, 1530-1535.
25. S. Wang, L. Ge, X. Song, J. Yu, S. Ge, J. Huang and F. Zeng, *Biosensors and Bioelectronics*, 2012, **31**, 212-218.
26. S. Xu, Y. Liu, T. Wang and J. Li, *Analytical chemistry*, 2011, **83**, 3817-3823.
27. Q. Wang, B. Zhang, X. Lin and W. Weng, *Sensors and Actuators B: Chemical*, 2011, **156**, 599-605.

28. H. Dai, X. Wu, H. Xu, Y. Wang, Y. Chi and G. Chen, *Electrochimica Acta*, 2009, **54**, 4582-4586.
29. P. Yan, Q. Tang, A. Deng and J. Li, *Sensors and Actuators B: Chemical*, 2014, **191**, 508-515.
30. L.-j. Wang and C.-j. Jia, *Journal of Instrumental Analysis*, 2012, **7**, 018.
31. D. S. Hage and J. Cazes, *Handbook of Affinity Chromatography, Second Edition*, Taylor & Francis, 2005.
32. N. J. Turro, V. Ramamurthy and J. C. Scaiano, *Principles of Molecular Photochemistry: An Introduction*, University Science Books, 2009.
33. M. Cordes and B. Giese, *Chemical Society Reviews*, 2009, **38**, 892-901.
34. S. K. Vashist, I. Kaur, R. P. Bajpai, L. M. Bharadwaj, R. Tewari and R. Raiteri, *Journal of Zhejiang University Science B*, 2006, **7**, 683-685.
35. H. N. Choi, S. H. Yoon, Y. K. Lyu and W. Y. Lee, *Electroanalysis*, 2007, **19**, 459-465.
36. C. J. v. Oss and M. H. V. v. Regenmortel, *Immunochemistry*, Marcel Dekker, Inc., New York, 1994.
37. F. Secundo, *Chemical Society Reviews*, 2013, **42**, 6250-6261.
38. I. Bertini, *Biological Inorganic Chemistry: Structure and Reactivity*, University Science Books, 2007.
39. J. B. Marroquin, K. Y. Rhee and S. J. Park, *Carbohydrate polymers*, 2013, **92**, 1783-1791.
40. I. L. Medintz, H. T. Uyeda, E. R. Goldman and H. Mattoussi, *Nature materials*, 2005, **4**, 435-446.
41. E. R. Goldman, E. D. Balighian, H. Mattoussi, M. K. Kuno, J. M. Mauro, P. T. Tran and G. P. Anderson, *Journal of the American Chemical Society*, 2002, **124**, 6378-6382.
42. G. T. Hermanson, *Bioconjugate techniques*, Academic press, 2013.
43. A. J. Bard and L. R. Faulkner, *Electrochemical Methods: Fundamentals and Applications*, Wiley, 2nd Edition, 2000.
44. J. Yan, M. Yan, L. Ge, S. Ge and J. Yu, *Sensors and Actuators B: Chemical*, 2014, **193**, 247-254.
45. T. Hao, Z. Guo, S. Du and L. Shi, *Sensors and Actuators B: Chemical*, 2012, **171**, 803-809.
46. L. Wu, M. Li, M. Zhang, M. Yan, S. Ge and J. Yu, *Sensors and Actuators B: Chemical*, 2013, **186**, 761-767.
47. P. Bertonecello, A. J. Stewart and L. Dennany, *Analytical and bioanalytical chemistry*, 2014, **406**, 5573-5587.
48. N. P. Sardesai, J. C. Barron and J. F. Rusling, *Analytical chemistry*, 2011, **83**, 6698-6703.
49. Z. Chen, Y. Liu, Y. Wang, X. Zhao and J. Li, *Analytical chemistry*, 2013, **85**, 4431-4438.
50. J. Wang, H. Han, X. Jiang, L. Huang, L. Chen and N. Li, *Analytical chemistry*, 2012, **84**, 4893-4899.
51. F. Liu, W. Deng, Y. Zhang, S. Ge, J. Yu and M. Yan, *Microchimica Acta*, 2014, **181**, 213-222.
52. Y. Wang, S. Wang, S. Ge, S. Wang, M. Yan, D. Zang and J. Yu, *Analytical Methods*, 2013, **5**, 1328-1336.

Chapter 8 – Conclusions and future work

8.1 Conclusions and future work

ECL biosensors have shown great promise in the diagnostic industry because of their benefits over more conventional detection techniques. Superb sensitivity combined with biomolecule induced specificity create a method that is well suited for the detection of low concentration analytes in complex matrices. Biosensor performance has been enhanced through integration of nanomaterials that exhibit superior electronic and optical properties. Of particular interest are QDs, which can generate intense ECL signals in a variety of sensor designs at a wavelength governed by their size. The unique size-tunable properties of QDs are caused by quantum confinement of their excitons in all three dimensions, which influences their electronic structure and creates a band gap that is dependent upon their size. Tuning this emission into the NIR region has potential benefits for biosensing applications as maximum light penetration through biological samples and minimum autofluorescence at this wavelength are apparent. This is well suited for point of care (POC) detection that requires whole blood analysis and minimal sample preparation.

For these reasons, the aim of this work was to establish the electrochemical properties and ECL performance of 800 nm CdSeTe/ZnS QDs in a typical aqueous environment and in whole blood; a complex matrix that comprises a variety of species capable of influencing electrochemical behaviour. This was to act as the groundwork for development of ECL biosensors with direct blood analysis.

The electrochemical and optical properties of QDs illustrated size dependence and these results were used to estimate the band gap energy for a series of QDs. A number of QD electron transfer processes were observed in the voltammograms that were associated with electron or hole injection into the HOMO and LUMO levels. However, estimation of the quasi-particle gap indicated not all electron transfer events were visualised using these techniques. Importantly, NIR ECL emission was confirmed from 800 nm

CdSeTe/ZnS QDs, which was deemed to originate from the core rather than surface states. To confirm this is the case with all co-reactants, determination of ECL emission wavelength in each of these systems should be carried out.

The cathodic and anodic ECL characteristics of NIR QDs were investigated and used to predict their electronic structure. An ECL signal was generated in both regions without additional co-reactants, indicating dissolved O_2 and its reduction products could successfully undergo rapid, energetic electron transfer with QDs to form an excited state. The electrogenerated precursors were attributed to different reactive oxygen species (ROS); in the cathodic region, hydroxyl radicals (OH^\bullet) and other ROS were involved, and in the anodic region superoxide ($O_2^{\bullet-}$) was the major precursor species. A more intense signal was detected in the anodic region, even though electron transfer kinetics in this system were likely slower, suggesting a greater proportion of $O_2^{\bullet-}$ was available for interaction with QDs. In the cathodic region, a double peak profile was observed that was attributed to alternative ECL pathways involving different reactive oxygen species (ROS). Formation of these energetic intermediates at different potentials manifested itself in multiple peaks following interaction with QDs.

Enhancements in cathodic and anodic ECL were achieved following addition of co-reactants. The mechanism of ECL formation with these species was established and the electronic interactions required for excited state formation examined. Addition of H_2O_2 co-reactant resulted in the same double peak profile obtained with O_2 and was related to similar production pathways. It was shown that the second ECL peak in the profile was sensitive to H_2O_2 concentration, whereas the first was not. A single peak profile was observed with $K_2S_2O_8$ co-reactant. The loss of a double peak was related to the strength of the oxidising species, $SO_4^{\bullet-}$, and subsequent rapid electron transfer kinetics with reduced QDs. This pathway dominated production of ECL in this system and a single peak was observed. The fast rate of homogeneous electron transfer between the precursor species meant $K_2S_2O_8$ generated the strongest

enhancement in ECL intensity of all investigated co-reactants. In the anodic region, the electronic interactions involved in excited state formation with TPA and $\text{Na}_2\text{C}_2\text{O}_4$ co-reactants should permit strong enhancement of ECL intensity compared to $\text{O}_2^{\cdot-}$. However, this was only observed with TPA. Indirect oxidation of $\text{C}_2\text{O}_4^{2-}$ and subsequent consumption of QD precursors in this process inhibited ECL intensity and $\text{Na}_2\text{C}_2\text{O}_4$ was not deemed a suitable co-reactant with these QDs.

To fully exploit the versatility of QDs, alternative co-reactant systems could be investigated to ascertain their influence on ECL intensity. Of particular interest would be a more biocompatible co-reactant in the anodic region, as TPA is not well-suited for use with biological samples.

A variety of system parameters were optimised to obtain maximum ECL performance. Chitosan was selected as the polymer for film construction as it provided suitable stabilisation of QDs and did not interfere overly with the ECL process. Improvements in the electrical properties of this film should enhance electron transfer kinetics and ECL generation. Modification of this polymer film is a key area for furthering the development of NIR QD ECL performance. Significantly, ECL generation at physiological pH exhibited maximum sensitivity due to the stability of precursor species in these conditions. This is ideal for biosensing applications, particularly with direct blood analysis. Superior ECL performance was also observed using a glassy carbon (GC) electrode, indicating this material should be used to achieve maximum sensitivity.

Following optimisation of system parameters, the electrochemical characteristics and ECL performance of 800 nm CdSeTe/ZnS QDs in whole blood were investigated. This work was a fundamental objective of the thesis as it examined the applicability of NIR QDs in the environment in which their integration into ECL biosensing systems is based, but in which their behaviour has never been investigated.

In both the cathodic and anodic regions an ECL response was observed directly from whole blood that was significantly more intense than that achieved using visible region QDs. This confirmed the superior penetrative ability of NIR ECL emission through whole blood and demonstrated the benefits of these materials for biosensing applications. The cathodic ECL signal without additional co-reactant was very weak due to quenching of radical species by free radical scavengers in blood. This highlighted the difficulties involved in detection from complex matrices. However, this signal was sensitive to the addition of co-reactant ($K_2S_2O_8$), generating an intense ECL signal that demonstrated the ability of NIR QD ECL to respond to these reactive molecules, even within a sample that includes a variety of interfering species. A strong oxidative ECL signal was obtained with O_2 co-reactant due to the greater stability of $O_2^{\cdot-}$ in whole blood. Addition of TPA resulted in a small increase in ECL intensity, however, an alternative co-reactant with better biocompatibility would be more suited for use with whole blood samples.

The sensitivity of NIR QD whole blood ECL to changes in environment allowed examination of their capability to detect clinically relevant analytes in these conditions. A cathodic homocysteine biosensor using $K_2S_2O_8$ co-reactant and a co-reactant free anodic dopamine biosensor were developed based on ECL quenching mechanisms. These are the first NIR ECL biosensors with application directly in whole blood. The ECL behaviour of NIR QDs demonstrated altered behaviour in these samples compared to buffer, caused by interaction of species involved in the ECL process with interferences in whole blood. This emphasised the importance of investigating ECL analysis in blood and further examination of the ECL properties of NIR emitting materials in this matrix should be carried out to fully understand the mechanism of action and consequence of these interactions. This work illustrated the ability of NIR QD ECL to produce a sensitive, intense ECL signal in whole blood and applied this capacity to the detection of clinically relevant analytes.

This characteristic of NIR QDs permitted their integration into a cholesterol biosensor with the aim of detection directly from clinical samples. A stable, selective and reproducible biosensor was developed that was based on enhancement of NIR QD ECL by H_2O_2 . This co-reactant was produced as a by-product of the cholesterol oxidase (ChOx) catalysed oxidation of cholesterol and thus an increase in ECL intensity accompanied an increase in cholesterol concentration. A clinically relevant linear range between 0.25-5 mM was achieved and detection from human serum samples was possible. Application of this biosensor in whole blood samples was not accomplished due to quenching of radical precursor species (OH^{\bullet}) involved in ECL generation. Attempts were made to minimise the effect on ECL intensity of these quenching processes by immobilising the enzyme on the electrode surface, however, these were unsuccessful. This indicated that the H_2O_2 sensitivity of this system was insufficient to detect the low levels that will be apparent due to quenching in whole blood. It is envisaged that future improvements in the ECL performance of NIR QD systems through increasing electrical conductivity and optimising biomolecule immobilisation should permit significant enhancements in sensitivity. This should advance the detection capabilities of these systems for very low concentration target analytes.

To further the investigation and development of whole blood NIR QD ECL biosensing systems, a selection of immunoassay designs that exploited the ability of $\text{K}_2\text{S}_2\text{O}_8$ to generate intense NIR QD ECL signals were studied. Detection of human immunoglobulin G (HIgG) via 'switch off' techniques confirmed successful antibody (Ab) immobilisation and antigen binding, but did not exhibit a reproducible response following fabrication of the biosensor. To improve specificity and stability of response, a classical sandwich type immunoassay was used. An ECL signal was only observed following formation of the QD-labelled immunocomplex, signifying successful construction of the biosensor. This system was then used to detect HIgG directly from a whole blood sample. The sensitivity and reproducibility of this biosensor requires further development, however, this work provides confidence that NIR QD ECL

can be used for the detection of clinically relevant analytes with whole blood analysis.

In conclusion, work in this thesis has shown that integration of NIR QDs into ECL biosensing systems is a very promising route for the development of novel biosensors designed for whole blood analysis. The modification and optimisation opportunities available for such systems ensures continuous and effective advancements in performance are achievable. As healthcare progresses towards the digital era, the requirement for rapid analysis of an array of biomarkers from clinical samples must be met by advances in biosensor technology. This work has demonstrated that NIR ECL detection is a viable method that is well-suited for such an application.

Appendix

Appendix 1

Published articles:

P. Bertocello, A. J. Stewart and L. Dennany, *Analytical and bioanalytical chemistry*, 2014, **406**, 5573-5587.